ISSN 0289-842X

RIKEN Accelerator Progress Report

1983

vol. 17

理化学研究所
the Institute of Physical and Chemical Research

RIKEN Accelerator Progress Report
January-December 1983

理化学研究所
the Institute of Physical and Chemical Research
Wako-shi, Saitama, 351-01 JAPAN

Editors

Y. Awaya	Y. Gono
M. Imamura	T. Inamura
H. Kamitsubo	M. Odera
E. Yagi	

This volume contains recent information of the accelerators at RIKEN (IPCR), informal reports and abstracts of papers which will be published at scientific meetings or in publications by staff members, guests, and visitors.

CONTENTS

2. Atomic and Solid-State Physics

Page

5. Instrumentation

6. Miscellaneous

IV. ACCELERATOR DEVELOPMENT

V. RADIATION MONITORING

AUTHOR INDEX

I. INTRODUCTION

Since collaborative research works using the160 cm cyclotron started in 1967 at the Institute of Physical and Chemical Research (RIKEN), experimental studies on nuclear physics, atomic and solid state physics, radiochemistry, material engineering, radiation chemistry and radiation biology have been extensively carried out. The main facilities being dedicated to these research works are the 160 cm cyclotron, the variable frequency linear accelerator (RILAC) and the electrostatic accelerator (TANDETRON) of 1 MV.

During the past one year the cyclotron was in good condition as before. A small computer was introduced to aid the operation of the cyclotron. The RILAC has been in steady operation in this period. Various kinds of ions of both gaseous and solid materials were accelerated in the frequency range of 17 to 30 MHz. Test acceleration was succeeded at 45 MHz. Beam dynamical behavior of the ions in the RILAC was studied and acceleration efficiency was improved considerably. The TANDETRON has been in steady operation in this period.

A majority of the research works have been carried out with heavy ions. In the field of nuclear physics a considerable progress has been made in development of the instruments such as a neutron multiplicity filter, a helium jet transport system and a superconducting solenoid. Experiments with these new tools as well as a Compton-suppressed spectrometer using large BGO crystals now under construction have partly been started this year and are expected to be more extensive in future. In addition to these, experiment has also started to solve a long-standing puzzle on low angular momentum cutoff in fusion reactions.

Atomic Processes Laboratory was organized in April, 1983, to promote research works on atomic physics theoretically and experimentally. In this year most of the experimental works were made using various kinds of heavy ions from the RILAC. By the measurement of X-rays, Auger-electrons and recoil ions, multiple ionization mechanism and dynamical process of highly charged ions were investigated. In addition to these atomic collision experiments, study of beam-foil spectroscopy has started this year and its first report is given in this volume. Some theoretical activities also began to work from this year mainly in the field of heavy particle collision, rearrangement collisions and electron-molecule collisions.

The perturbed angular correlation method was applied to investigate the electronic states in magnetic oxides. Emission Mössbauer spectroscopy of ^{119}Sn using cyclotron-produced ^{119}Sb was extended in this period to *in situ* measurement on solid state-aqueous solution interfaces. Depth profiling of surface hydrogen was made by measuring the recoil protons from the Rutherford scattering with incident Ar ions and also by measuring high energy gamma-rays from ^{15}N-induced reactions on hydrogen and deuterium nucei. From these measurement the growth mechanism of amorphous Si:H layer was analyzed. The first determination of the lattice location of hydrogen in a bcc metal has been made by the channeling method using a nuclear reaction ^{11}B + p. The success of this technique is believed to open a new possibility for investigating the isotope dependence of the site occupancy of hydrogen atoms.

As to the irradiation effects on materials, the ion implantation effect, the ion mixing and the helium embrittlement of nuclear materials have been studied. In addition, irradiation creep experiment on fusion reactor materials was started with 16 MeV proton beam.

In charged particle activation analysis, the detection limits were considerably lowered by improving the chemical separation procedures after irradiation as well as the detection system. Contamination of light elements in GaAs, Sb-doped Si and other semiconductor materials of industrial importance were successfully determined. Bromoperiodol labeled with ^{77}Br was prepared for the study on the dopamine receptor in the brain. In the field of radiation chemistry, photoemission spectra along a N-ion induced trajectory in helium gas were studied.

Construction of the separated sector cyclotron is in progress. During the past one year the last sector magnet was completed at the factory. Fabrication of the power supplies for the sector magnets as well as trim coils is now under way. Construction of the cyclotron vault was almost finished.

Hiromichi Kamitsubo

H. Kamitsubo
Editor

II. OPERATION OF ACCELERATORS

1. Cyclotron Operation

S. Fujita, K. Ogiwara, H. Takebe, S. Kohara,
K. Ikegami, T. Kageyama, and I. Kohno

During the period from Oct. 23, 1982 to Oct. 22, 1983 the cyclotron was operated on the 24 h a day basis. Statistics of machine operation time is shown in Table 1. The total operation time of 4096.0 h is 3 % (269.3 h) shorter than that of the last year. This decrease in operation time is due to decreased ratio of net beam time to scheduled beam time. Figure 1 shows the net beam time obtained from the difference of reading of time meter over the past 11 years.

Table 2 shows the beam time allotment to various activities in this period. The scheduled beam time was increased by 185 h compared with that of the last year. For the new study of Test of track detector and Single event upset in the LSI memory, 137 h was allotted in

Table 1. Cyclotron operation

	Oscillator	Ion-source	Beam
Reading of time meter on Oct. 23, 1982	76325.3	80614.2	45692.5
Reading of time meter on Oct. 22, 1983	81388.5	85751.2	49788.5
Difference	5063.2	5137.0	4096.0
Percentage of 365 days	57.8 %	58.6 %	46.8 %
Schedule in this period			
Beam time	234 (days)		
Overhaul and installation work	54		
Periodical inspection and repair	27		
Vacation and holidays	50		

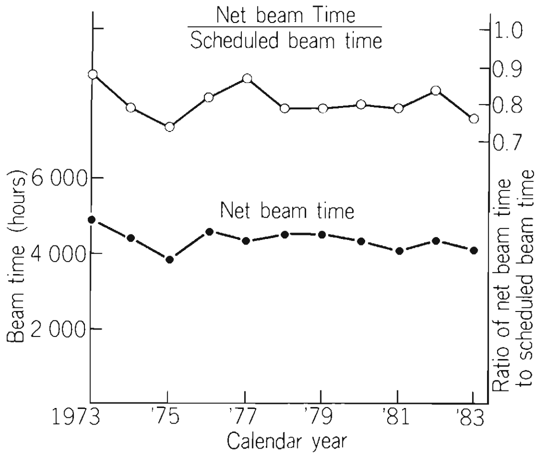

Fig. 1. Net beam time and the ratio of net beam time to scheduled beam time.

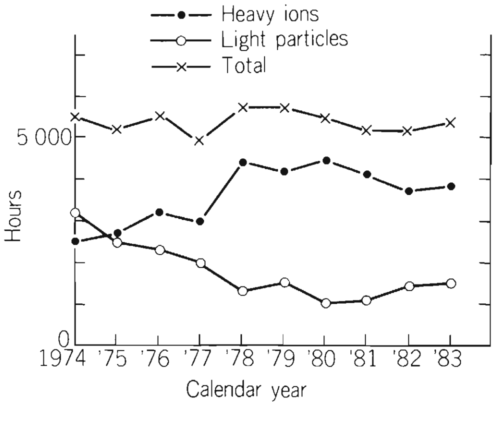

Fig. 2. The cyclotron beam time history.

this scheduled beam time.

Table 3 shows the distribution of the scheduled beam time among particle accelerated. Ions such as $^{9}Be^{3+}$ and $^{6}Li^{2+}$ were newly accelerated and several experiments were performed by using these ion beams. In this period, the beam times for deuteron, $^{7}Li^{2+}$, O^{5+} and newly accelerated ions were increased in contrast to the decrease for N^{5+}, $^{20}Ne^{6+}$, and $^{13}C^{4+}$.

Figure 2 shows the beam time of heavy and light ions over the past 9 years. Although the request for heavy ion beam was slightly, i.e. 96 h, increased, the ratio of heavy ion beam time to light ion beam time was almost the same as that of the last year. The cyclotron was operated to accelerate heavy ions for more than 70 % of total scheduled beam time in the past 6 years.

Table 2. Scheduled beam time and subjects of activity in the period XVIII.

	Subject	Heavy ion	Light particle	Total
Nucl. Phys.	Nuclear reaction	2689 (h)	95 (h)	2784 (h)
	In-beam spectroscopy	478	0	478
	RI production	54	304	358
Fields others than Nucl. Phys.	Nuclear chemistry	0	397	397
	Radiation biology	123	44	167
	Radiation chemistry	288	0	288
	Solid state physics	46	70	116
	Atomic collision	60	94	154
	Study of radiation damage	0	250	250
Outside users	Study of radiation damage	0	159	159
	RI production	0	67	67
	Test of track detector	0	19	19
	Single event upset in the LSI memory	118	0	118
Total		3833	1522	5355
Percent in total		71.6 %	28.4 %	100 %
Maintenance, operation and engineering				
	Exchange of ion sources		88 (h)	
	Machine inspection and repair		648	
	Total		736	

Table 3. Distribution of beam time among particles accelerated.

Particle	(h)	(%)	Particle	(h)	(%)
p	529	9.9	N^{5+}	600	11.2
d	115	2.1	O^{5+}	1102	20.6
$^{3}He^{2+}$	189	3.5	$^{20}Ne^{6+}$	308	5.8
$^{4}He^{2+}$	689	12.9	$^{13}C^{4+}$	134	2.5
$^{7}Li^{2+}$	151	2.8	$^{18}O^{5+}$	108	2.0
$^{12}C^{4+}$	474	8.9	$^{9}Be^{3+}$ [a]	93	1.7
N^{4+}	767	14.3	$^{6}Li^{2+}$ [a]	96	1.8
			Total	5355	100

a) Newly accelerated ions.

II-2. RILAC Operation

Y. Miyazawa, M. Hemmi, T. Inoue, T. Kambara, M. Yanokura,
M. Kase, T. Kubo, E. Ikezawa, K. Kihara,* and S. Toku*

The Riken heavy ion linear accelerator, RILAC, has been in steady operation in this period and various kinds of ion beams were transported to various targets. Table 1 gives statistics of operation in the period Sept. 1, 1982 – Aug. 31, 1983. The beam time of 167 days used for the experimental works includes three days of unscheduled shut down of RILAC. Therefore, the beam time which has actually been available to the user was 98.2% of the scheduled time. Figure 1 shows statistics of ions used in this period. It is clear that most of the users preferred the beam of Ar^{4+} ions and of N^{2+} ions to heavier projectiles. Percentage of the beam time for the experiment in the total machine time was 64% for Ar^{4+} ions and 25 % for N^{2+} ions. $^{15}N^{2+}$ ion beam was also supplied to the user. Its beam has been utilized to the analysis of hydrogen contents in some materials. A ten percent enriched ^{15}N gas was fed to the ion source to get the $^{15}N^{2+}$ ion beam. In order to increase the energy of ion having mass larger than that of argon, it is necessary to get highly charged ions. A pulsed arc power supply$^{1)}$ for PIG source was installed in a 500kV high voltage terminal of the injector in the spring of 1983. By use of the pulsed power supply, Kr^{8+} (88.7 MeV) and Xe^{9+} (108 MeV) ions were accelerated and used in some experiments. A charge stripper, which is installed in the beam line between cavity No. 6 and SW magnet, was frequently used at the request of users. Carbon foil of the stripper has thickness of 10 microgram/cm^2 and is 15 mm in diameter.

Table 1. Statistics of operation in the period Sep. 1, 1982 – Aug. 31, 1983.

Beam time	167 days	45.8 %
Overhaul and improvement work	46	12.6
Periodical inspection and repair	39	9.9
Scheduled shut down	113	31.0
Total	365	100.0

Beam line C of the beam transport system is in line with the acceleration axis of the linac, so that small amount of undesired beam with different charge states will be present in the beam arriving the target in this course. To avoid the mixing of undesired beams in the main beam, a compact deflection magnet$^{2)}$ (CD) was installed in the beam line C.

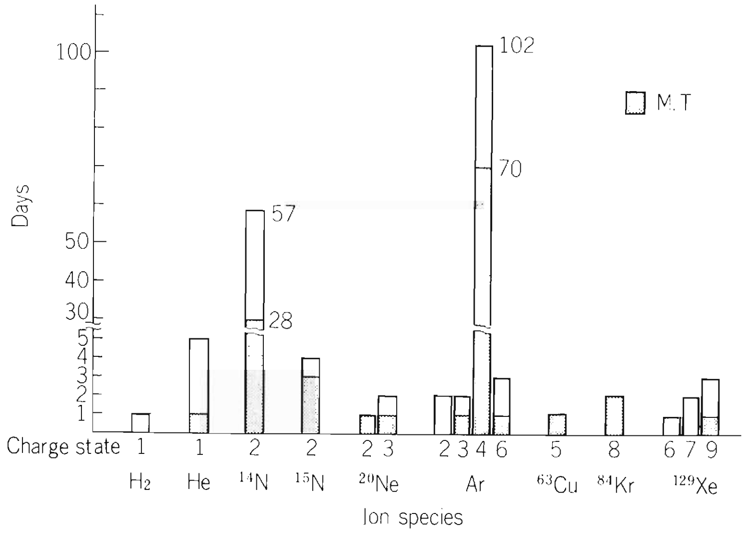

Fig. 1. Statistics of Ion Used in the period Sept. 1, 1982 – Aug. 31, 1983.

---

* Sumijyu examination and inspection corporation.

Many improvements were done to get simple and stable operation of the linac. Total accelerating voltage of 16 MV was obtained easily by use of an automatic rf voltage recovering circuit,$^{3)}$ which instantaneously changes mode of excitation of the cavities to suppress continuation of discharge, in the case when the acceleration voltage was lost by sparking during operation of the linac. There is no need of step by step adjustment of RF parameters by the operators to get the accelerating voltage. The divider resistance of accelerating column of injector was changed from 5×10^9 ohm to 1.75×10^9 ohm. The reason for the change is to avoid the abrupt potential change of accelerating electrodes when a stray beam hits them. The beam injected to the linac became stable by this improvement.

The linac cavity had several troubles in this period : a quadrupole magnet in a drift tube (DT/II-13) had insulation failure in its tape coil and the beam was accelerated without this magnet excited in operation of the linac; silver strips (thickness 0.2mm) inserted between the inner conductor of the coaxial section of cavity and the base of the drift tube supporting horizontal piece melted with heat generated by rf current at positions of poor contact. The melted contact strips in the cavities No. 3 and No. 4 were replaced by beryllium copper strips. It is expected that the beryllium copper strips can withstand the repeated thermal stress which is supposed to cause the poor contact in the case of the silver sheets.

References
1) M. Hemmi and Y. Miyazawa: p. 173 in this report.
2) M. Hemmi, Y. Miyazawa, and S. Motonaga: p.171 in this report.
3) T. Kubo: RIKEN Accel. Progr. Rep., 16, 168 (1982).

II-3. TANDETRON-Operation

H. Sakairi, E. Yagi, T. Kobayashi, and T. Urai

In one year from the November of 1982 the machine was operated for 76 days in total. The machine time showed a decrease against the previous year. It was caused by partial reconstruction of the room which took 3 months. Except this period the machine has been working almost satisfactorily.

Subjects of the experimental studies were as follows:

(1) Lattice location of Sn atoms implanted into Al crystals,
(2) Lattice location of H atoms in Ta and V crystals,
(3) Depth profiles of H atoms in amorphous solids of Si,
(4) Depth profiles of Au atoms in ZnSe crystals,
(5) Radiation damage in Cd-implanted GaP crystals,
(6) Blistering of stainless steel surfaces by He Implantation.

For studies of (1), (4), (5), and (6) $^{4}He^{+}$ ions were used and for those of (2) and (3), $^{11}B^{+}$ ions.

The largest trouble in this year occured in the cesium ion gun of the sputter ion source. A canal conducting Cs vapour from a furnace to the ionizer, which provides primary Ce ions for sputtering, corroded to have a hole. A new gun prepared by us has operated without any trouble.

A remote switching system to change the polarity of a magnet was designed and constructed, which chooses the ion source to be used between a duoplasmatron and the sputter ion source. A similar system was prepared for another magnet to select a course for the accelerated beam. Both systems have operated well.

To install a new beam transporting system for an electron microscope for the study of radiation damage, an ion optical apparatus are being prepared. It is scheduled to be completed at the end of fiscal year 1983.

Many works of repair and improvement of the TANDETRON and the surrounding instruments was collaborated by the work shop.

II-4. Implanter Operation

M. Iwaki

The RIKEN 200 kV Low Current Implanter is described in details in the previous report.[1] This machine has been utilized in the fields of modification of surface layers of materials such as metals, insulators and semiconductors. Main items under practice are as follows:

(1) Compositions and structure of ion-implanted pure irons
(2) Mechanical and electrochemical properties of ion-implanted pure irons and steels
(3) Compositions and structure of ion-implanted diamonds
(4) Electrical and electrochemical properties of ion-implanted diamonds
(5) Compositions and structure of ion-implanted graphites
(6) Electrochemical properties of ion-implanted graphites
(7) Ion beam mixing of Ti deposited Cu and Ni
(8) Ion beam mixing of GaAlAs-GaAs
(9) Annealing of ion-implanted GaP.

In order to perform modification of materials, many kinds of elements were used for implantation, which were given in a table in the previous report.[1] Additional other elements implanted are shown in Table 1, which also presents the typical beam current obtainable from the feeding materials charged in the furnaces of the Nielsen type ion source. Recently this machine has been operated almost everyday and the need for operation with some kinds of target materials and implanted species is showing the tendency to increase still more.

Table 1. Typical beam current obtained by the RIKEN 200 kV Low Current Implanter.

Element	Current (μA)	Charged materials
F	10	BF_3
Na	10	NaCl
Ca	5	$CaCl_2$
Mn	20	$MnCl_2$
Fe	20	$FeCl_2$
Kr	5	Elem.

In order to develope many works which require a high current ion beam to get a high production rate of specimens, a high current ion implanter is now under construction by the help of Special Coordination Funds for Promoting Science and Technology. Figure 1 shows the schematic layout of this RIKEN 200 kV High Current Implanter, which is a modified Lintott High Current Machine (Series III). The Lintott machine with a well-known Freeman type ion source is designed to be floating at post-acceleration potential and a target chamber at ground potential. The 40 kV accelerator is contained in an isolated terminal mounted on insulators from a base frame. This terminal can float at 0~160kV to give the post-acceleration.

The modified implanter has the advantages of having

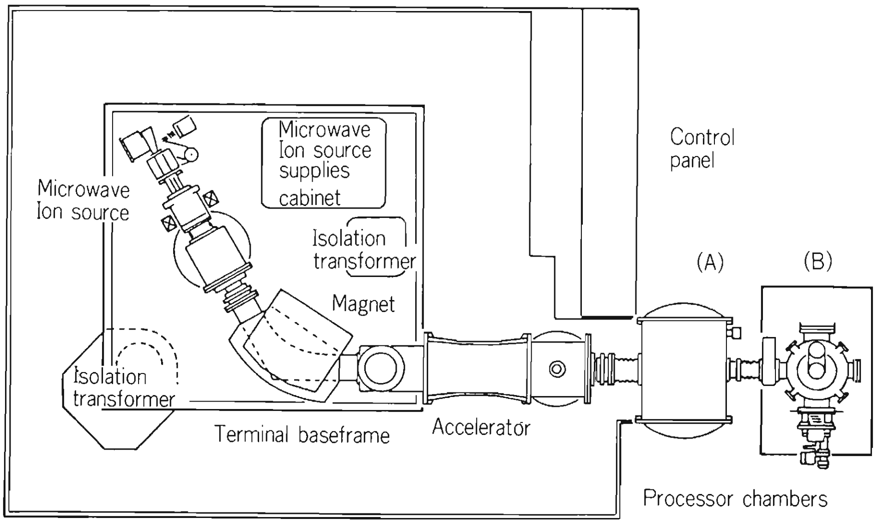

Fig. 1. Schematic drawing of RIKEN 200 kV High Current Implanter.

own microwave ion source (produced by Hitachi Ltd.) and owning two target chambers. The microwave discharge ion source has a comparatively long life time due to lack of hot-filament, which restricts the life time of a Freeman type ion source usually used in obtaining a high current ion beam. In its operation, it is easy to discharge feeding materials at their low flow rate. During the discharge of metal chlorides, the chloride ions and radicals in the plasma do not consume any component of this microwave ion source and might prevent metal to deposit on the inner walls of the discharge chamber by bombarding and chemically cleaning the walls. Therefore, this ion source is considered to be suitable for production of metallic ions.

The ion beam extracted from the ion source at the maximum voltage of 40 kV is a ribbon beam and the ion trajectries are parallel in the vertical plane and divergent in the holizontal plane. The divergent beam from the ion source enters the analysing magnet, which has a rotatable entrance pole. This enables the beam to be focussed into the resolving slit without the use of any electrostatic focussing lenses. The magnet is capable of bending ions with masses up to 130 at full extraction voltage of 40 kV and larger masses at decreased extraction voltages.

The post-acceleration of the beam is achieved across a single acceleration gap set in the center of a stainless steel chamber. The arrangement enabled the X-rays emitted during the post-acceleration up to 160 kV to be shielded in the close neighborhood of the origin of the X-rays. The beam shutter after the post-acceleration gap and before the processor gate valve is electrically isolated and is used to measure beam current by magnetically suppressing secondary electrons.

Processor chamber A, which is placed at the original position of a Lintott implanter, has nine target holders for performing ion implantation at the ambient temperature. Maximum implanted area of the sheet is $150 \times 240\ \mathrm{mm}^2$ for each target holder. Processor B installed at the end of the beam line has two types of target holders. One can be utilized for ion implantation in a sheet of $50 \times 40\ \mathrm{mm}^2$ at controlled temperature from liquid nitrogen temperature up to 500 °C. The other enables ion implantation in a cylinder, of which maximum size is 100 mm in diameter and 50 mm in length.

This high current implanter will easily perform modification of material surface-layers.

Reference

1) M. Iwaki: RIKEN Accel. Progr. Rep., 15, 7 (1981).

III. RESEARCH ACTIVITIES

1. Nuclear Physics

1. Possible Evidence for Lower Critical Angular Momentum in Complete Fusion

T. Nomura, H. Kudo, S. Kohmoto, K. Sueki, and T. Kubo

NUCLEAR REACTIONS $^{12}C(^{16}O, xnypz\alpha\gamma)$, E = 70 – 120 MeV, natural target; $^{24}Mg(\alpha, xnypz\alpha\gamma)$, E = 30 – 50 MeV, enriched target; measured E_γ, I_γ. Evaporation calculation; experimental evidence for the existence of lower ℓ_{cr} in fusion.

The existence of a lower cutoff ($\ell_{cr}^{<}$) in angular momentum that limits the complete fusion cross section in a heavy-ion reaction has been predicted by the time-dependent Hartree-Fock (TDHF) calculation[1] as well as by the semiclassical coupled-channels model calculations.[2] However, no clear experimental evidence for $\ell_{cr}^{<}$ has so far been found. A main difficulty in the experimental search for $\ell_{cr}^{<}$ lies in the fact that the expected magnitude of the effect influences only a small fraction of the reaction cross section. We should therefore look for observables that are sensitive to the existence of $\ell_{cr}^{<}$.

It is well known that high-spin states in a highly excited light nucleus preferentially decay by the evaporation of α-particles, and that low-spin states deexcite mainly by the emission of nucleons.[3] When the evaporation residues resulting from the fusion reaction are classified by the number of α-particles evaporated in the decay chain of the compound nucleus, those nuclei produced without the emission of α-particles originate mainly from lowest-spin states in the compound nucleus. The yield of such residual nuclei is therefore considered to have high sensitivity to test the possible existence of $\ell_{cr}^{<}$ as shown in Fig. 1, where the yields of ^{24}Na and ^{25}Na produced in the $^{12}C(^{16}O, 3p)$ and $^{12}C(^{16}O,3pn)$ reactions, respectively, are found to originate from compound states with spin values lower than 10 ħ, while the yield of ^{23}Na, for instance, comes mainly from states with much higher spins. The TDHF calculations predict $\ell_{cr}^{<} \simeq 3$ ħ at the bombarding energy of 80 MeV, 11 ħ at 90 MeV and 15 ħ at 100 MeV[4].

We have measured cross sections of residual nuclei using the technique of γ-ray spectroscopy in the bombardment of a thick natural carbon target with ^{16}O-beam of 70 – 120 MeV. There are two reasons for using the thick target in the γ-ray measurement. One is to prevent residual nuclei from recoiling out of the target, so that the yield estimate becomes reliable. Another is to decrease the Doppler shift (broadening) in the prompt spectra as far as possible. Special attention was paid to the yield of Na isotopes ($^{21\text{-}25}$Na) to see a possible effect of $\ell_{cr}^{<}$. The nuclei ^{22}Na and ^{24}Na are kown to have low spin isomers at the first excited states. The isomer ratio of these nuclei is also expected

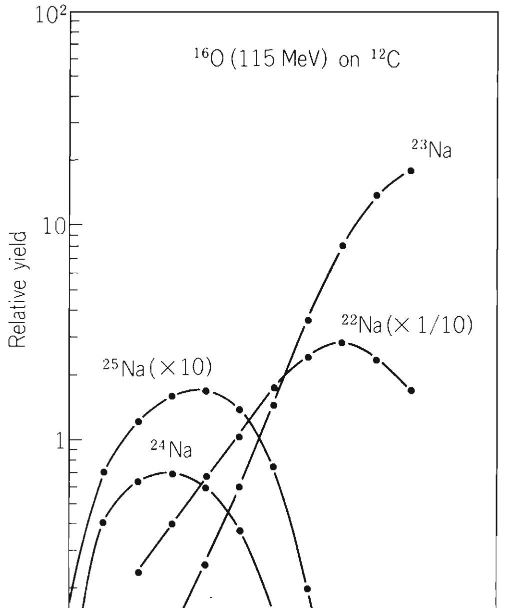

Fig. 1. Product cross sections of some Na isotopes in the bombardment of ^{12}C with 115 MeV ^{16}O beam as a function of angular momentum of the compound nucleus. They are calculated by the code GROGI2.

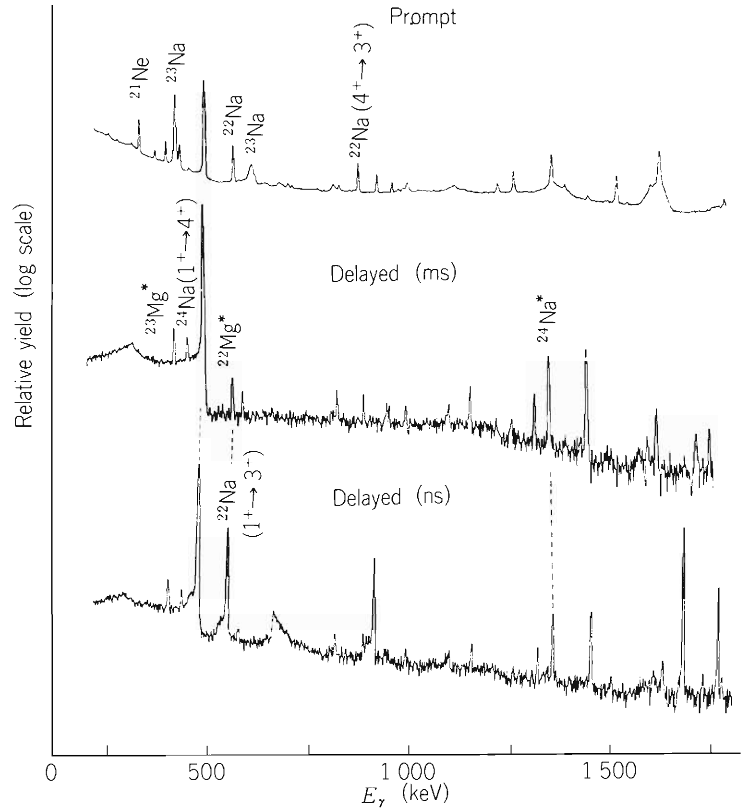

Fig. 2. A part of the γ-ray spectra taken in the 110 MeV ^{16}O bombardment of a natural thick carbon target. The assignment of dominant γ-rays belonging to either Na isotopes or related nuclei are given. Note that the energy scale is only correct for the prompt spectrum and the delayed spectrum in the ms region, and that it is slightly different for the delayed spectrum in the ns region.

to be influenced seriously by the existence of $\ell_{cr}^{<}$. For comparison, the yields of the same residual nuclei were also measured in the ^{24}Mg + α reaction at 30 – 50 MeV, which forms the same compound nucleus but is believed not to have non-zero value of $\ell_{cr}^{<}$.

Gamma rays resulting from the above reactions were measured with a 80 cm^3 Ge(Li) detector. In addition to prompt γ-rays, delayed spectra were taken in the nanosecond range using the cyclotron natural beam bursts as well as in the millisecond range using the pulsed ion source. A purpose of measuring the delayed spectra in the ns range is to estimate the yield of the 1$^+$ isomer ($t_{1/2}$ = 243 ns) in ^{22}Na, while that of the delayed spectra in the ms region is to see the 1$^+$ isomer ($t_{1/2}$ = 20.2 ms) in ^{24}Na and the decay of other activities having rather short half-lives produced in various reactions. Typical examples of the measured γ-ray spectra are shown in Fig. 2.

A preliminary analysis of the results yields the experimental excitation functions of some γ-rays in Na isotopes as shown in Fig. 3. They were deduced from the difference of the thick target yeilds at various energies in the case of the ^{16}O-induced reaction. It should be noted that the product cross sections in the ^{24}Mg + α reaction have been multiplied by a factor of $(\lambdabar_0/\lambdabar_\alpha)^2$, where $\lambdabar_0$ and $\lambdabar_\alpha$ are the relative wavelengths in the ^{16}O- and α-induced reactions, respectively, at the same excitation energies of the compound nucleus. Therefore, the values of the product cross sections (σ) should be equal to each other if the residual nuclei are originated from the decay of the compound nuclei having the same distributions of angular momenta. The following points should be noted.

(1) The yields of γ-rays belonging to ^{25}Mg and ^{24}Na^m in the ^{16}O-induced reaction are much smaller than those of the same γ-rays in the α-induced reactions. Since these isotopes are mainly produced from low-spin states in the compound nucleus, this fact indicates that low angular momenta in the entrance channel do not contribute to the formation of the compound nucleus in the case of the ^{16}O + ^{12}C reaction. Note that ^{25}Mg has the similar spin dependence as ^{25}Na because it is produced by the same three-nucleon emission.

(2) The yields of the 5/2$^+$ → 3/2$^+$ γ-ray in ^{23}Na as well as those of the 4$^+$ → 3$^+$ plus 5$^+$ → 3$^+$ γ-rays in ^{22}Na are nearly equal to each other in both the ^{16}O-

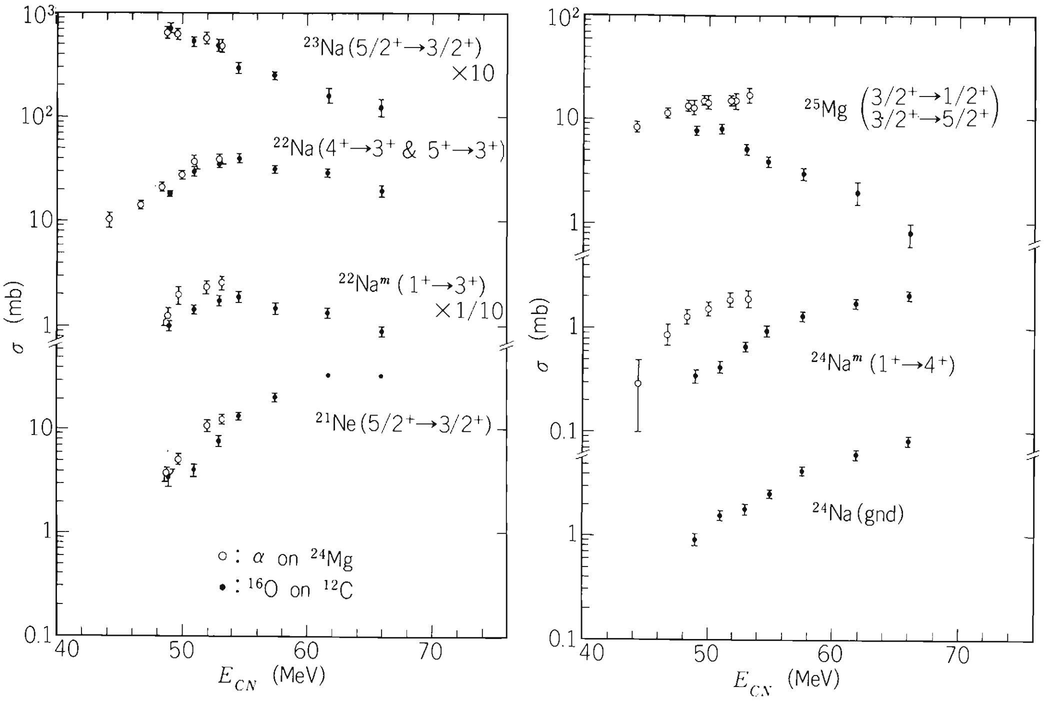

Fig. 3. Excitation functions of some γ-rays in various isotopes measured in the $^{16}O + ^{12}C$ reaction (closed circles) and in the $^{24}Mg + \alpha$ reaction (open circles). Note that the yields for the α-induced reaction are multiplied by the factor explained in the text.

and α-induced reactions. Since these isotopes are not sensitive to $\ell_{cr}^{<}$, this indicates that the upper critical angular momentum for fusion is nearly the same in both reactions.

(3) The values of σ for the $1^+ \rightarrow 3^+$ γ-ray in $^{22}Na^m$ and $5/2^+ \rightarrow 3/2^+$ γ-ray in ^{21}Ne are also smaller in the $^{16}O + ^{12}C$ system, although the difference is not so large as the case of ^{25}Mg and $^{24}Na^m$. The $1^+ \rightarrow 3^+$ γ-ray in $^{22}Na^m$ represents the low-spin yield of ^{22}Na, and should be somewhat sensitive to the existence of $\ell_{cr}^{<}$. The nucleus ^{21}Ne is produced by the three-nucleon emission in addition to one α particle, and must have the similar spin dependence as ^{25}Mg. The smaller product cross section of these isotopes in the $^{16}O + ^{12}C$ reaction is therefore understood also by the existence of $\ell_{cr}^{<}$.

A more detailed analysis is now in progress.

References

1) S. E. Koonin, K. T. R. Davies, V. Maruhn-Rezwani, H. Feldmeir, S. J. Drieger, and J. W. Negele: Phys. Rev., C15, 1359 (1977).
2) R. A. Broglia, C. H. Dasso, G. Pollarollo, and A. Winther: Phys. Rev. Lett., 40, 707 (1978).
3) T. Nomura, J. Delaunay, C. Tosello, and N. Bendjaballah: Nucl. Phys., A305, 262 (1978).
4) Y. Yamaji: Private communication.

III-1-2. Re-evaluation of Friction Coefficients for Deep Inelastic Heavy-Ion Collisions

S. Yamaji and A. Iwamoto

NUCLEAR REACTIONS Microscopic calculation of friction, linear response theory.

It is necessary to take into account the effect of the lifetime of particle-hole states to treat the discrete spectrum in the microscopic calculation of friction coefficients for heavy-ion reactions using the formalism of linear response theory.[1)]

Our previous works[2)-4)] have introduced one free parameter Γ to take into account its effect in the independent particle model (IPM).

In the present report, we have done a numerical calculation of friction coefficients with new formalism, which Jensen et al.[5)] have derived, approximating the particle-hole Green function in the response function by the coherent term of one-body operators. We call this approximation the coherent term approximation (CTA). Since the expression for the friction coefficients, which is given in detail in Ref. 6, differs much between these two models (IPM and CTA), the calculated results for CTA are compared with the previous ones for IPM.[3),4)]

Three kinds of the shape parameters, the relative distance R, deformation δ and mass number of projectile-like nucleus A_1 are taken. Three diagonal friction coefficients γ_{RR}, $\gamma_{\delta\delta}$ and $\gamma_{A_1A_1}$ are calculated as a function of these shape parameters.

(1) Radial-radial friction coefficients γ_{RR}

In Fig. 1, we show friction γ_{RR} for the system ^{64}Zn + ^{196}Pt as a function of the relative distance R between two nuclei for several values of temperature T. From this figure, one sees that γ_{RR} for CTA depends more sensitively on temperature than that for IPM and that it increases with increase of temperature. Although the strength of γ_{RR} for CTA at temperature of about 2 MeV, that is, the typical temperature in deep inelastic collisions, is still smaller than that for IPM, calculations for CTA and IPM give γ_{RR} of the same order of magnitude and reproduce the order of magnitude of the proximity friction (shown by the dot-dashed line) in the surface region of R = 12 ~ 14 fm.

(2) Deformation-deformation friction coefficients $\gamma_{\delta\delta}$

Figure 2 shows $\gamma_{\delta\delta}$ calculated for the system ^{64}Zn + ^{196}Pt as a function of R for several values of T. The results for both cases give the same order of magnitude and about half of the proximity friction, which was estimated in Ref. 4. It can also be seen from this figure that $\gamma_{\delta\delta}$ for CTA depends more strongly on T and R than that for IPM.

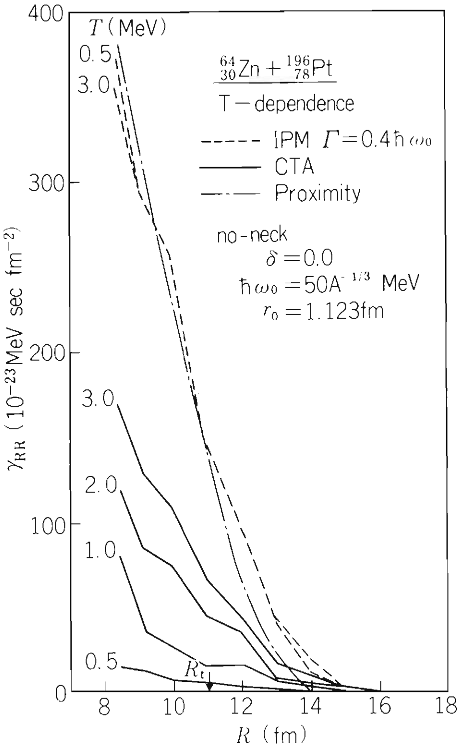

Fig. 1. The radial-radial friction coefficient γ_{RR} for the system ^{64}Zn + ^{196}Pt as a function of the relative distance R between two nuclei for several values of the temperature T.

The solid and dashed lines correspond to the calculated results by the method of coherent terms approximation (CTA)[5)] and by the independent particle model (IPM) with the smearing width $\Gamma = 0.4\,\hbar\omega_0$[2)-4)], respectively. The dot-dashed line shows the proximity friction. The deformation δ of two nuclei is set to be zero and the neck formation is not included. The oscillator parameter $\hbar\omega_0$ is taken to be 50 $A^{-1/3}$ MeV in the same way as in Ref. 4. The touching distance shown by the arrow is estimated to be 11.1 fm by the relation R_t = 1.123 × $(A_1^{1/3} + A_2^{1/3})$ fm.

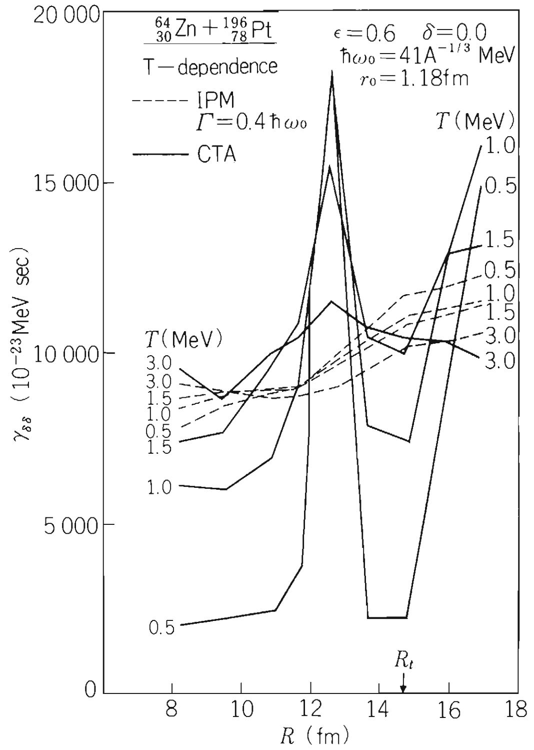

Fig. 2. The deformation-deformation friction coefficient $\gamma_{\delta\delta}$ for the system ^{64}Zn + ^{196}Pt as a function of the relative distance R for several values of T.

The solid and dashed lines correspond to the calculated results for CTA and IPM with $\Gamma = 0.4\hbar\omega_0$, respectively. The deformation δ is set to be zero and the neck-parameter ϵ defined in Ref. 3 is taken to be 0.6. The oscillator parameter $\hbar\omega_0$ is taken to be 41 $A^{-1/3}$ MeV.

(3) Mass asymmetry-mass asymmetry friction coefficients $\gamma_{A_1A_1}$

We calculated $\gamma_{A_1A_1}$ for ten systems given in Ref.3. We plot here the inverse of $\gamma_{A_1A_1}$ instead of $\gamma_{A_1A_1}$ as a function of R as in Ref.3. This is done because $1/\gamma_{A_1A_1}$ is equal to mass diffusion coefficient per unit temperature D_A/T in the transport equation, if we neglect the coupling between mass transfer motion and other motions and assume overdamped motion for mass transfer.

Some examples of D_A/T are shown as a function of R in Fig.3. Since the friction $\gamma_{A_1A_1}$ for IPM depends very weakly on T, the calculated values of $\gamma_{A_1A_1}$ for IPM are plotted only for the average temperature. Although the dependence of $\gamma_{A_1A_1}$ for CTA on T is stronger than that for IPM, it is still too weak to reproduce the dependence of the experimental values on temperature for the cases of ^{40}Ar + ^{197}Au and ^{40}Ar + ^{232}Th reactions. The shape of two touching nuclei when mass exchange occurs seems to be more important to reproduce such temperature dependence of D_A/T.

It can be concluded that both calculations for IPM and CTA reproduce the experimental values of friction coefficients within one order of magnitude, although the friction coefficients on the basis of Ref.5(CTA) depend more strongly on the temperature and configuration than our previous ones (IPM).[3,4]

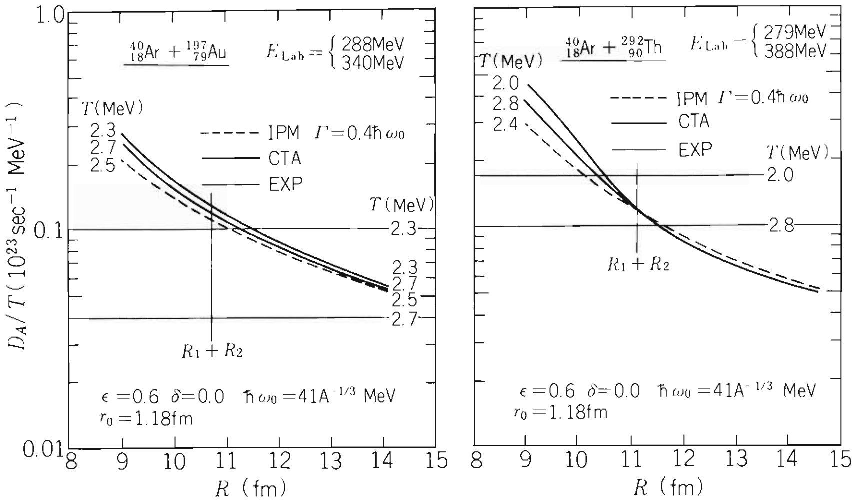

Fig. 3. The calculated mass diffusion coefficient per unit temperature as a function of the relative distance R up to the distance where the neck-radius becomes zero.

The solid and dashed lines correspond to the calculated results for CTA and IMP with $\Gamma = 0.4\hbar\omega_0$, respectively. The experimental values are shown by horizontal lines. The numbers at the calculated solid lines and experimental values[7),8)] show the values of temperature estimated from the two experimental data of different incident energies. The results for IPM are calculated at the average temperature. The vertical lines show the position of two touching spheres, which is estimated by the relation $R = 1.18 \times (A_1^{1/3} + A_2^{1/3})$ fm.

References

1) H. Hofmann and P.J. Siemens: Nucl. Phys., A275, 464 (1977).
2) K. Sato, A. Iwamoto, K. Harada, S. Yamaji, and S. Yoshida: Z. Phys. A-Atoms and Nuclei, 288, 383 (1978).
3) S. Yamaji, A. Iwamoto, K. Harada, and S. Yoshida: Phys. Lett., 108B, 433 (1981).
4) A. Iwamoto, K. Harada, S. Yamaji, and S. Yoshida: Z. Phys. A-Atoms and Nuclei, 302, 149 (1981).
5) A.S. Jensen, J. Leffers, K. Reese, H. Hofmann, and P.J. Siemens: Phys. Lett., 117B, 5 (1982).
6) S. Yamaji and A. Iwamoto: Z. Phys. A-Atoms and Nuclei, 313, 161 (1983).
7) S. Ayik, B. Schürman, and W. Nörenberg: ibid., 279, 145 (1976).
8) G. Wolschin and W. Nörenberg: ibid., 284, 209 (1978).

III-1-3. Effects of Two Particle - Two Hole Excitations on the Mass Distributions in the ^{16}O + ^{40}Ca Reaction

S. Yamaji and M. Tohyama*

NUCLEAR REACTION DIC calculation of mass distributions.
^{16}O + ^{40}Ca time-dependent coupled-cluster approximation.

The time-dependent Hartree-Fock (TDHF) theory has been extensively applied to analysis of heavy ion collisions and has succeeded to reproduce the total kinetic energy loss and mean values of the mass distributions etc.

The variances of mass distributions calculated in the TDHF, however, are always an order of magnitude smaller than observed values.$^{1)}$ This result suggests the importance of two-body collisions, which are not included in the standard TDHF. One way to include their effect is to use the time-dependent coupled-cluster approximation (TDCCA) proposed by Hoodbhoy et al.$^{2)}$

We previously applied this method to the analysis of mass distribution in heavy ion collisions.$^{3)}$ The calculation showed that the variances of the mass distributions in TDCCA are very much enhanced as compared with those in TDHF, while both approximations give similar results to the expectation values of the mass distributions. This calculation$^{3)}$ was, however, only limitted to one-dimensional collisions.

In the present note, we report on the calculation extended to treat realistic collisions. Here, we give a brief discription of our treatment. The detail is given in Ref. 3.

The equations to be solved numerically are derived by taking the lowest-order terms of the two particle-two hole amplitude in TDCCA:

$$i\frac{\partial}{\partial t}\varphi_\nu(t) = h(t)\,\varphi_\nu(t) \qquad (1)$$

$$i\frac{d}{dt}\langle\rho_1\rho_2|S_2|\nu_1\nu_2\rangle_A = \langle\rho_1\rho_2|V|\nu_1\nu_2\rangle_A. \qquad (2)$$

The first equation determines the time-evolution of the single-particle basis, where h(t) is the Hartree – Fock(HF) Hamiltonian. We assume that the particle states $\varphi_\rho(t)$ also obey the same equation as the hole states $\varphi_\nu(t)$. The indices ν and ρ denote hole and particle states, respectively. The second equation specifies the time-evolution of the two particle-two hole amplitude $<\rho_1\rho_2|S_2|\nu_1\nu_2>_A$.

Then, the mean number $\bar{N}_R$ of particles and the variance σ_R^2 of the mass distribution in the right fragment can be expressed in terms of the right-hand overlap integrals of single particle wave functions and two particle-two hole amplitudes at the time when two fragments are well separated in the final stage of the collision.$^{3)}$

We have performed numerical TDCCA calculations for the collision 320 MeV ^{16}O + ^{40}Ca on the basis of the Skyrme force TDHF-code with axial symmetry.$^{4)}$

The initial densities of two fragments are obtained by summing the square of the static Hartree-Fock wave functions over all hole states. The orbitals of the hole states are 0s and 0p for ^{16}O and 0s, 0p, 0d and 1s for ^{40}Ca. The initial particle states, which are restricted to 0d and 1s orbitals for ^{16}O and to 0f and 1p orbitals for ^{40}Ca, are obtained from the static Hartree-Fock potential. The time-evolution of particle states are assumed to obey the same TDHF equation as that for the hole states.

We use the δ-function $V(\vec{r},\vec{r}') = V_0\delta(\vec{r}-\vec{r}')$ as the residual interaction. The strength V_0 is adjusted so that the depth of one-body potential obtained by folding the residual interaction with the density reproduces approximately that of the HF potential. We get $V_0 = -400$ MeV fm^3, if we use the value of 0.17 fm^{-3} for the density and of – 50 MeV for the depth of HF potential, and get $V_0 = -530$ MeV fm^3, if we use the value of 0.15 fm^{-3} for the density and of –60 MeV for the depth of HF potential.

With this residual interaction of strength – 400 ~ 530 MeV fm^3, the increase of σ_R^2 due to the extention of the space for neutron particle states of ^{16}O to 0f – 1p shells is found to be less than 3 percent and the increase of σ_R^2 due to the extention of the space for neutron particle states of ^{40}Ca to 0g – 1d –2s shells is found to be less than 6 percent.

Concerning the calculated results, inclusion of two particle-two hole excitations gives only a few percent change to the net mass exchange of TDHF. However, as shown in Fig. 1, the variances are enhanced very much in

---

* Institut für Theoretishe Physik, Giessen University, West Germany.

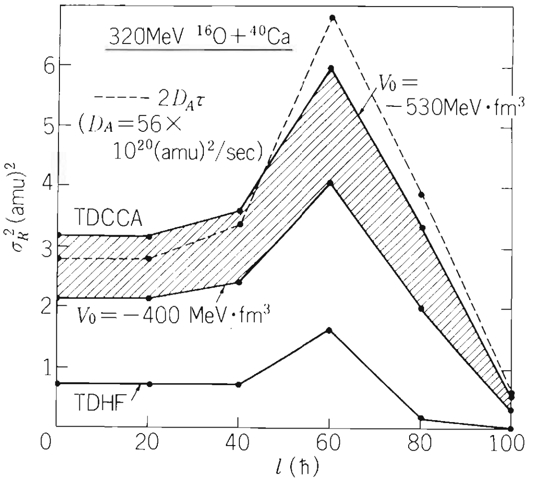

Fig. 1. The variance σ_R^2 versus the initial angular momentum ℓ for the 320 MeV ^{16}O + ^{40}Ca reaction.

TDCCA. As an example, in DIC with the initial angular momentum $\ell = 80\hbar$, σ_R^2(TDCCA) is 2.0 ~ 3.4 (amu)^2, while σ_R^2(TDHF) is 0.18 (amu)^2. The nonvanishing two particle-two hole amplitudes are found to oscillate with the time period (0.05 ~ 0.1) × 10^{-21} sec and have the absolute value of 0.001 ~ 0.01. Although each term which is proportional to the square of two particle-two hole amplitude in the summation of the expression σ_R^2 is very small, it is found to contribute coherently.

For lack of observed values for this reaction, the calculated values are compared with the empirical values of σ_R^2 estimated by the use of the relation $\sigma_R^2 = 2D_A\tau$$^{5)}$ which can well reproduce observed mass distributions for heavy systems with the mass difusion coefficient $D_A \sim A \times 10^{20}$ (amu)^2/sec, where A is the total mass number of the composite system and τ is the collision time. The relation $\sigma_R^2 = 2D_A\tau$ can be extrapolated to lighter systems.$^{6)}$ The collision time τ is calculated by TDHF in the present work, defining it as the interval during which the minimum density along the symmetry axis between the fragments exceeds 1/4 of nuclear matter density. The TDCCA results shown by the shaded area are slightly smaller than the empirical one shown by the dashed line in Fig. 1. Considering V_0 to be an adjustable parameter, small increase of V_0 from the values used here yields the empirical values.

To summarize, the realistic calculation with two-body collisions reproduces the order of magnitude of empirical values of σ_R^2 for the 320 MeV ^{16}O + ^{40}Ca reaction, although one-dimensional calculations could show only that σ_R^2 increases, if the effect of two-body collisions is included.

References

1) K. T. R. Davies and S. E. Koonin: Phys. Rev. C, 23, 2042 (1981).
2) P. Hoodbhoy and J. W. Negele: ibid., C19., 1971 (1979).
3) M. Tohyama and S. Yamaji: Phys. Lett., 123B, 16 (1983).
4) K. T. R. Davies: unpublished.
5) W. U. Schröder and J. R. Huizenga: An. Rev. Nucl. Sci., 27, 465 (1977).
6) S. Yamaji, A. Iwamoto, K. Harada, and S. Yoshida: Phys. Lett., 108B, 433 (1981).

III-1-4. Fusion and Evaporation Phenomena in Heavy-Ion Reaction of Relatively Light-Mass System

M. Magara,* K. Sueki, Y. Hamajima,* H. Nakahara,
H. Kudo, and I. Kohno

NUCLEAR REACTIONS ^{62}Ni(^{14}N,X), E_{lab}= 40 – 120 MeV, total reaction cross sections, fusion cross sections, excitation functions of residues, calculation of evaporation.

In heavy-ion reactions, formation of a compound nucleus and its decay from high angular momentum states are most fundamental problems to be clarified. Many papers have been published on these problems$^{1)}$ and most of them concluded that the ordinary statistical evaporation model was applicable to explain the excitation function of compound-like residues even without taking into account the critical angular momentum 1_{cr} for fusion and the angular momenta carried away by emitted particles.$^{2)}$ The aim of this work is to understand the effect of those angular momenta on excitation functions of compound-like residues.

As a reaction system, ^{14}N + ^{62}Ni was chosen and two kinds of experiments were performed; namely, observation of excitation functions of compound-like residues by the radiochemical technique and that of fusion cross sections by a $\Delta E - E$ counter telescope consisting of a gas proportional counter and a surface barrier detector. Details of the former experiment were reported in the previous progress report.$^{3)}$ Some of the results are shown in Fig. 1 for ^{73}Se, ^{72}As, ^{71}As, and ^{70}As by filled circles. The solid lines were drawn through the data points to guide the eye. They are cumulative cross sections including those of β-decay precursors. For the study of fusion cross sections, a self-supporting enriched ^{62}Ni target of 600 μg/cm^2 thickness was bombarded with 115 MeV and 96 MeV ^{14}N beams, and products were observed at lab angles of 3 to 26 degrees. Elastic scattering data were also taken over the same lab angles in order to get the maximum angular momentum, 1_{max}, of the reaction. Results of the fusion cross section study are shown in Fig. 2 by open circles. From the elastic scattering data, grazing angles were deduced by the quarter-point method, and 1_{cr}'s and total reaction cross sections σ_t were evaluated with the classical approximation, the latter values being given in Fig. 2 by filled circles. Total reaction cross section data were fitted by the classical relationship $\sigma_t = \pi R^2\ (1\text{-}B/E_{cm})$ as shown by the solid line. The dotted line shows the theoretical fusion cross sections predicted by Bass, and the broken line is drawn through the data points with the assumption that the incident energy dependence of fusion cross sections obeys the prediction of the Bass model.$^{4)}$ From the solid line and the broken line were evaluated the 1_{max} and 1_{cr} values used in the evaporation calculations discussed below.

Two kinds of computer codes were used to test the effect of angular momenta on the formation cross sections of compound-like residues. They were ALICE code and GROGI2 code. In the two codes, transmission coefficients are calculated with the same optical parameters, and the energy dependence of level densities are treated similarly. However, in ALICE code, variation of angular momentum distributions emitted particles is either completely neglected or approximately treated by assuming that a certain kind of emitted particles always carries away a fixed amount of angular momenta. In this code, the internal excitation energy is given by subtraction of the rotational energy from the total excitation energy. In GROGI2 code, angular momenta are treated rigorously by calculating angular momentum distribution of the residual nucleus after each particle evaporation. In Fig. 1, results of ALICE code calculation in which 1_{cr} values are fed in as the maximum angular momentum for fusion are shown by dotted and dot-dashed lines. The former are the results of calculations with complete neglect of angular momentum balance and the latter are the results with assumption that neutrons, protons, and alpha particles always carry away $1\hbar$, $1\hbar$, and $4\hbar$ angular momenta. Agreement with the experimental data is extremely poor and even the peak energies can not be reproduced. The dashed lines show the results of GROGI2 calculations in which 1_{cr} values are fed in. Although the absolute cross sections and high energy tails of the excitation function curves (e.g. in ^{73}Se) are not reproduced well, the peak

---

* Faculty of Science, Tokyo Metropolitan University.

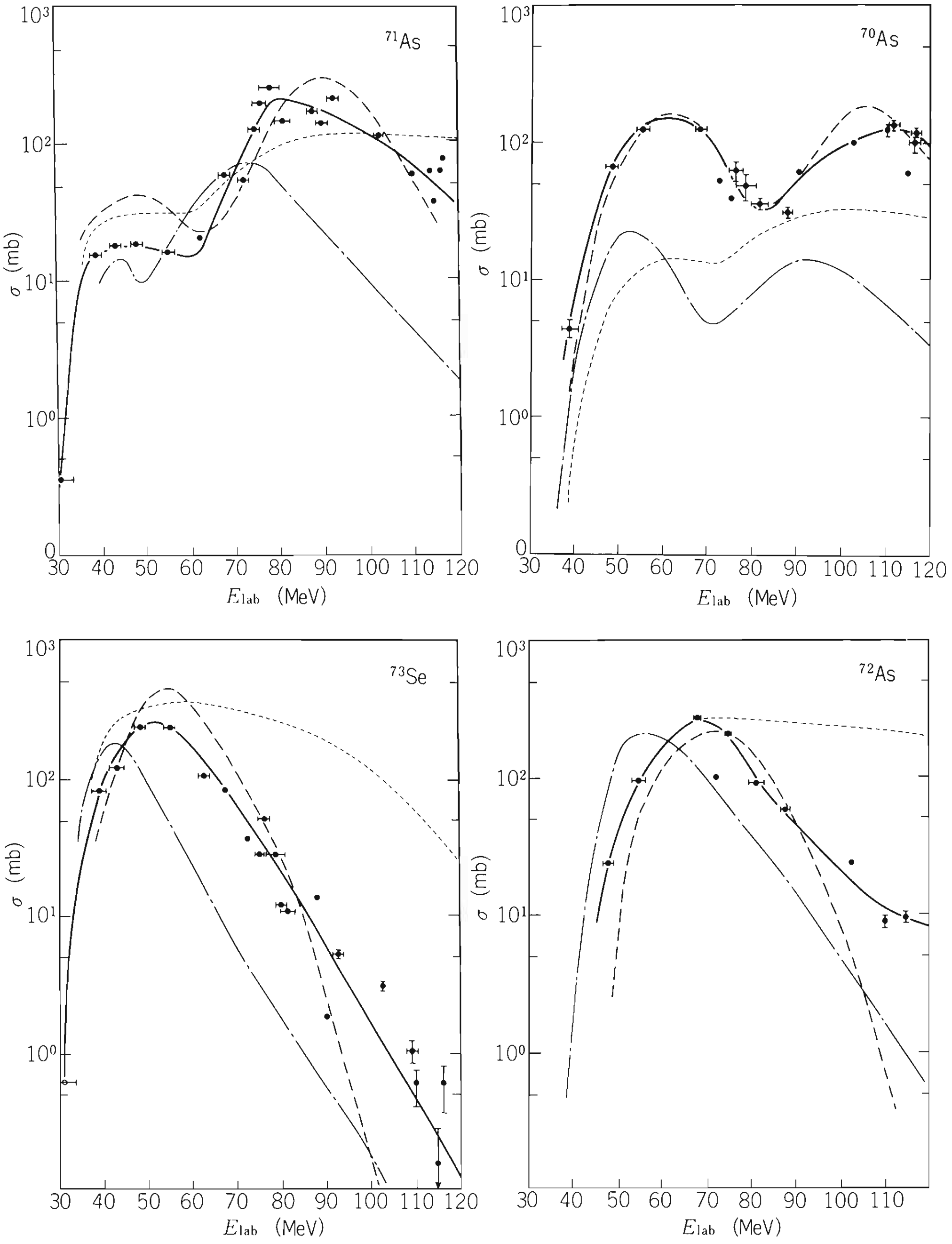

Fig. 1. Excitation functions of compound-like residues prodcued by the ^{14}N on ^{62}Ni. Filled circles show the results of experiments and the solid lines are drawn through the data points to guide the eye. The dotted and dot-dashed lines are the results calculated by use of ALICE code with complete neglect of the angular momentum balance and with the assumption that emitted particles carry away angular momenta, n = 1ħ, p = 1ħ, and α = 4ħ, respectively. The dashed lines are the results of GROGI2 code calculation.

energy and general trend of the experimental data are better reproduced. Any further adjustment of parameters such as pairing energies was not attempted. The GROGI2 calculations were also performed by using l_{max} values instead of l_{cr} values. Use of an incorrect maximum angular momentum for fusion in the entrance channel was found to affect primarily alpha particle emissions. In Fig. 3, angular distributions of the residual nucleus after neutron, proton, and alpha particle emission from the compound nucleus are depicted. The solid and dashed lines show the results of calculations when the l_{cr} and l_{max} are used, respectively.

As a conclusion, the excitation functions of compound-like residues produced in heavy-ion reactions can be understood well by the ordinary statistical evaporation model if angular momenta in the entrance and exit

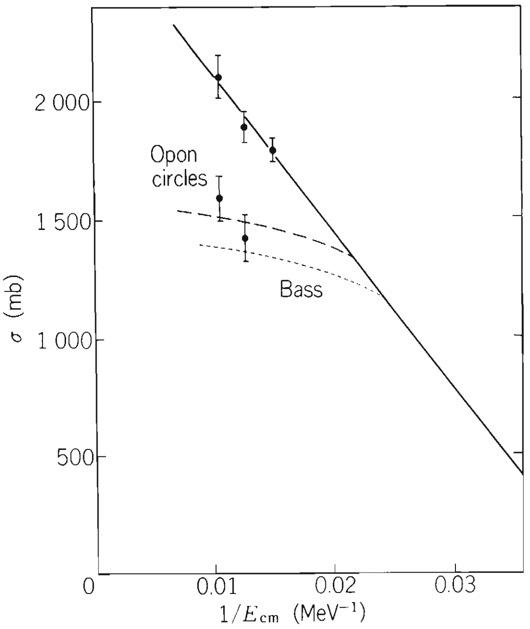

Fig. 2. The filled and open circles are, respectively, total and fusion cross sections obtained from the measurement with the ΔE – E counter telescope. The solid line shows the best fit to the data of total reaction cross sections by use of the classical relationship. The dotted line shows fusion cross sections predicted by Bass and the broken line is drawn through the data points with the assumption that the incident energy dependence of fusion cross sections obeys the Bass model.

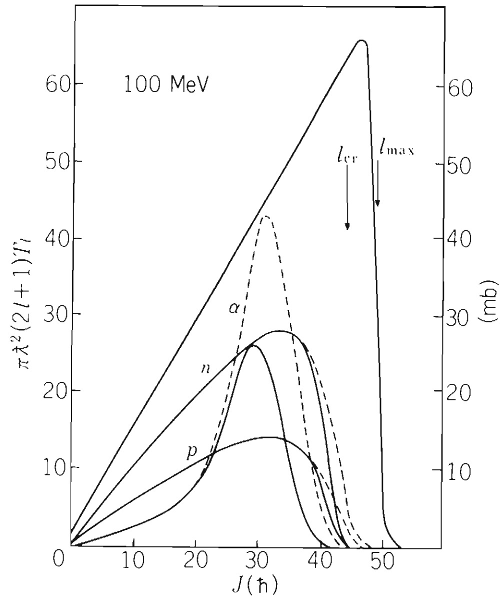

Fig. 3. The angular momentum distribution of the compound nucleus (thick solid line), and those of the daughter nuclei after a neutron, proton, and alpha particle emission from the compound nucleus when incident energy is 100 MeV. The thin solid and dashed lines show how angular momentum distributions will change if the 1_{cr} and 1_{max} are fed into the GROGI2 code as the input of the maximum angular momentum for fusion, respectively.

channels are rigorouly treated. The effect of pre-equilibrium emission on cross sections was found inconspicuous for most of the products investigated in this work except for ^{73}Se. No assumption of extraordinary emission of alpha particles was required in the analysis unlike that postulated in heavier reaction systems.

References

1) M. Langevin, J. Barreto, and C. Détraz: Phys. Rev., C14, 152 (1976) etc.
2) P. Misaelides: Radiochim. Acta, 28, 1 (1981).
3) K. Sueki, Y. Hamajima, M. Takahashi, Y. Nagame, H. Nakahara, and I. Kohno: RIKEN Accel. Progr. Rep., 16, 9 (1982).
4) R. Bass: Nucl. Phys., A231, 45 (1974).

III-1-5 Effective Moment of Inertia of Medium-Mass Fissioning Nuclei

G. X. Liu*

NUCLEAR REACTIONS ^{118}Sn(^{14}N,f), E = 120 MeV; ^{118}Sn(^{20}Ne,f), E = 135 MeV; measured angular distributions of fission fragments, fission cross sections; deduced J_{eff}.

Angular distributions of fission fragments have been measured in ^{14}N- and ^{20}Ne- induced reactions on ^{118}Sn to deduce an effective moment of inertia at the saddle point of relatively light fissioning nuclei. A self-supporting ^{118}Sn target of about 400 μg/cm^2 thickness was bombarded with 120 MeV ^{14}N and 135 MeV ^{20}Ne ions from the cyclotron. Fission fragments were detected with mica track detectors. The preliminary analysis of the ^{14}N + ^{118}Sn data yields the angular distribution shown in Fig. 1, from which we obtain $\sigma_f = 2.0 \pm 0.4$ mb.

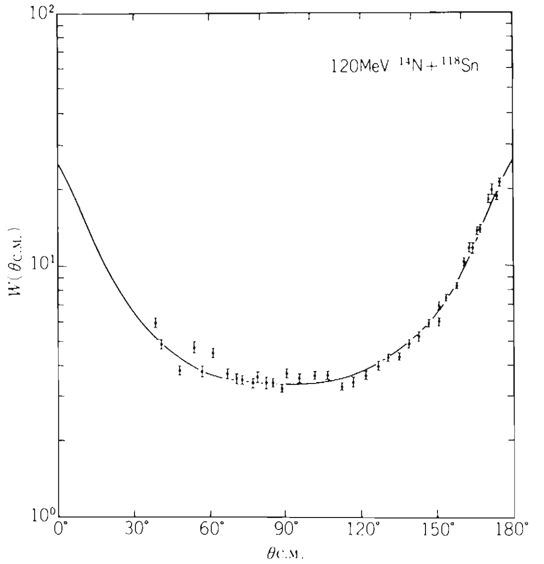

Fig. 1. Angular distribution of the fission fragments from the ^{14}N + ^{118}Sn reaction at 120 MeV. The data are converted to those of the centre-of-mass system (under the assumption of compound nucleus formation).

An effective moment of inertia is deduced to be about $J_0/J_{eff} = 1.6 \pm 0.2$, where J_0 is the moment of inertia of a rigid spherical nucleus, following the prescription of Ref. 1. The above value is close to that of similar light fissioning nuclei ^{132}Xe as described in Ref. 2. More detailed analysis is now in progress.

References

1) K. G. Kuvatov et al.: Yad. Fiz., 14, 79 (1971).
2) H. Blok and B. D. Pate: Z. Phys., A281, 255 (1977).

---

* On leave of absence from Institute of Modern Physics, Academia Sinica, Lanzhou, China.

III-1-6. High-Lying Proton Single-Particle States in Heavy Nuclei

E. Takada, M. Ishihara, Y. W. Lui,* Y. Mihara,*
T. Murakami,** Y. Toba,* and R. E. Tribble*

NUCLEAR REACTIONS $^{208}Pb(\alpha,t)^{209}Bi$ at E = 60 MeV and $^{208}Pb(^{3}He,d)^{209}Bi$, measured energy spectra for $\theta = 4^{\circ} - 35^{\circ}$, studied single-particle strengths.

Proton stripping reactions were used to investigate single-particle proton states at high energy regions of 5–10 MeV excitation in ^{209}Bi and other nuclei. Contrary to the studies of deep-hole states, which existed numerously, studies of highly-lying particle states have been rare so far.$^{1)}$ Of particular interest are location, width and strength of high angular momentum states such as $1j_{5/2}$, $1i_{11/2}$ in ^{209}Bi. Such information will help to extend basic knowledge on shell structure of nuclei, e.g., on locations of $n\hbar\omega$ states with large n, shell structure at $2\hbar\omega$ excitation, and systematics of ℓ-s splitting. While high-lying particle strength is generally distributed over a wide range of excitation energy, the spreading for those high-spin states may be relatively confined because of their large angular momenta. Using stripping reactions with large ℓ mismatch, one can thus hope to locate high-spin single-particle strengths at continuum regions. Previously we have tested$^{2)}$ availability of a heavy-ion reaction, (^{12}C, ^{11}B), in populating those strengths. Here we report on experiments using (α, t) reactions. Measurements with a (^{3}He, d) reaction were also made for comparison.

A 60 MeV α beam and a 75 MeV ^{3}He beam from the AVF cyclotron at Texas A & M University were used to bombard self-supporting ^{208}Pb foils of more than 99% isotopical enrichment. The outgoing tritons and deutrons, respectively, were momentum-analysed via the ESP-110 magnetic spectrograph with a focal plane detector consisting of a position sensitive proportional gas counter and a backing E counter of plastic scintilator. Spectra spanning E_x = 0 to 18 MeV were measured at several angles from 4° to 35°. The angular opening typically used was 1.7°. The energy calibration was obtained from the low-lying states of ^{209}Bi. Cross sections for the low-lying states in the (α,t) reaction were consistent with the results of Perry et al.$^{3)}$ within experimental errors.

Typical spectra obtained for the (α, t) and (^{3}He,d) reactions on ^{208}Pb are shown in Fig. 1. The triton spectrum in Fig. 1(a) shows anticipated selective enhancement for high-spin states as seen in the strong populations of the low-lying levels of $h_{9/2}$ (0.0 MeV) and $i_{13/2}$(1.6 MeV). It also shows some prominent bumps at higher excitation energies. Preliminary DWBA analysis on angular distributions indicates high ℓ dominance for these bumps. A deutron spectrum from the ^{208}Pb (^{3}He,d)^{209}Bi shown in Fig. 1(b) exhibits a contrary trend in favour of low-spin final states such as $p_{3/2}$(3.1 MeV) and $f_{7/2}$(0.9 MeV) levels. The spectrum at higher excitation has a large continuum contribution presumably due to ^{3}He breakup process, and the

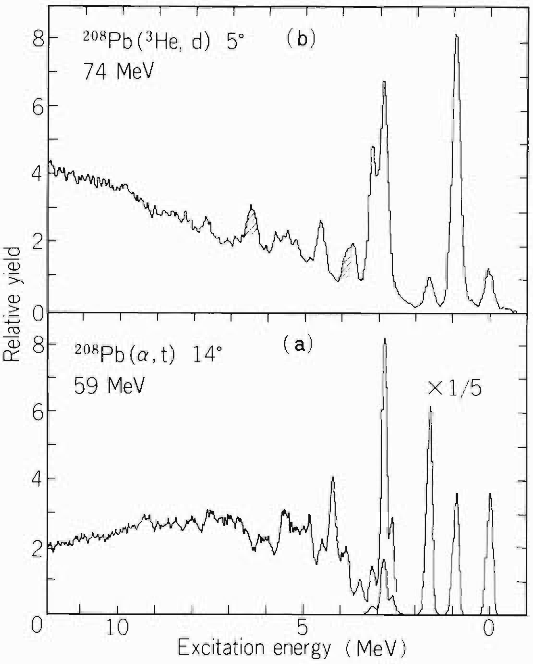

Fig. 1. Typical spectra of (a) ^{208}Pb (α,t) ^{209}Bi reaction and (b) $^{208}Pb(^{3}He, d)$ ^{209}Bi reactions. Hatched peaks are due to contamination in the target.

---

* Present address: Texas A & M University, Cyclotron Institute, College Station, Texas 77843.

** Present address: University of Washington, Nuclear Physics Laboratory, Seattle, Washington 98195.

strengths corresponding to the bump structures observed in the (α,t) reaction are week.

Detailed quantitative analyses on highly-lying states are somewhat hampered by uncertainties about background estimation and contamination of carbon and oxygen in the target. Analyses in terms of DWBA are being pursued by noting the selectivity difference between the (α,t) and (^{3}He,d) reactions. Preliminary results indicate that about 50 to 80% fractions of $i_{11/2}$ and $j_{15/2}$ single particle strengths are located in the energy region of E_x – 4.0 to 7.6 MeV.

References

1) S. Gales, C.P. Massole, S, Fortier, E. Gerlic, J. Guillot, E. Hourani, J. M. Maison, J. P. Schapira, B. Zweiglinski, P. Martin, and V. Comparat: Phys. Rev. Lett., 48, 1593 (1982).

2) M. Ishihara, E. Takada, T. Murakami, E. Unglicht, Y. W. Lui, R. Trible, Y. Toba, and Y. Mihara: REKEN Accel. Progr. Rep., 16, 15 (1982).

3) R. Perry, A. Nadasen, D. L. Hendrie, P. G. Proos, and N. S. Chant: Phys. Rev., C 24, 1471 (1981).

III-1-7. Chemical Effects on Internal Conversion of Outer-Shell Electrons in ^{125}Te

T. Miura, Y. Hatsukawa, K. Endo, H. Nakahara,
A. Hashizume, M. Fujioka, and E. Tanaka*

RADIOACTIVITY ^{125}I; Implanted into Cu, Zn, Sn; measured L, M, N, O - CE, Mössbauer spectra; deduced 5s electron density at nucleus.

Chemical effects on internal conversions of outer-most shell electrons were investigated by several groups in the past.$^{1)}$ In the case of nuclear magnetic dipole (M1) transition, the internal conversion coefficient α is dominated by the matrix elements which for low and moderate transition energies are proportional to the magnitudes of the s-orbital electron wave functions near the nucleus $\sum_{ns} |\psi_{ns}(0)|^2$. Therefore, one expects that the internal conversion coefficient of valence s-shell electrons is proportional to their charge density near the nucleus and, in general, differ slightly for different chemical states of the same element.

For experiments of this type with a high resolution β-ray spectrometer, it is necessary that the transition energy is less than about 50 keV for the conversion lines of the electrons in the outer-most shell to be separated from that due to electrons in the next-inner shells. We have already reported the chemical effect on the internal conversion process in ^{119}Sn.$^{2)}$ In the present study we chose the 35.46 keV M1 transition of ^{125}Te that follows the decay of ^{125}I ($T_{1/2}$ = 60d). In this case the energy of conversion electron is so low that high resolution measurement of the conversion electron spectra becomes extremely difficult, and the most essential problem is how to prepare a source sufficiently thin, e.g. 10 μg/cm^2.

The source sample in this work were prepared by implanting ^{125}I into metals (Cu, Zn and Sn) by means of the electromagnetic isotope separator Tohoku. Implantation of the radioactive ^{125}I was carried out at the terminal potential of 20 kV at room temperature. The dose rate was 3 x 10^8 atoms/cm^2·sec at the focal plane of A = 125. From the radioactivity of the implanted sample, the number of implanted ^{125}I atom was determined to be 3 x 10^{13} atoms/cm^2 (~100 μCi/cm^2). After implantation, in order to identify the chemical state of the implanted sample, emission Mössbauer spectra were measured by keeping both source and absorber (96% enriched Zn^{125}Te) at liquid nitrogen temperature.

The internal conversion spectra were observed with the high-resolution iron-free β-ray spectrometer at RIKEN and INS with the instrumental momentum resolution of 0.10% for the O-shell conversion of 35.46 keV transition. A gas-flow proportional counter having a thin Mylar window of 4 μm thick was used as a detector. The L, M, N, and O conversion lines of the 35.46 keV transition were measured. In Fig. 1 are shown the conversion electron spectra in the region of N and O lines from the source of Sn substrate. The N_I line and O line with energy difference of 156 eV could be clearly resolved from each other. The relative conversion intensity ratio O/N_I was evaluated using the computer code, ACSEMP$^{3)}$ whose function was essentially a least-

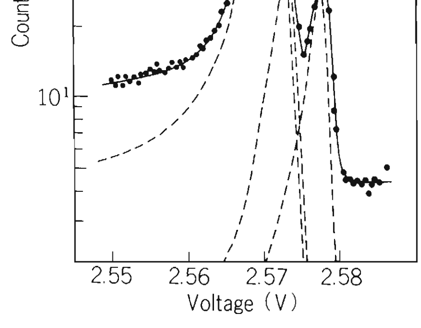

Fig. 1. The N and O conversion lines of 35.46 keV M1 transition in ^{125}Te (Sn). The solid curve is the result of the least-squares fit, yielding the components shown by dashed lines.

---

* Faculty of Science, Tohoku University.

squares analysis of the spectra using empirical profiles.

Results of the analyses of three different sources are listed in Table 1. Each of the Mössbauer spectra of Zn, Cu, and Sn sources showed a single line indicating a unique implantation site. If the effect of the change in 5s electron density on the inner s-electron densities is small, one can deduce the 5s electron density at the nucleus from the observed O/N_I ratio by using the formula ($O_I \longleftrightarrow 5s, N_I \longleftrightarrow 4s$)

$$|\psi_{5s}(0)|_x^2 = |\psi_{4s}(0)|^2 \cdot (O/N_I) \qquad (1)$$

where $|\psi_{5s}(0)|_x^2$ is the 5s electron density at the nucleus for the chemical state x and $|\psi_{4s}(0)|^2$ is the 4s electron density of the Te atom. It is noted that in Eqn. (1) the observed O shell line is treated as a pure O_I line, i.e. the $O_{II,III}$ conversion is neglected relative to the O_I conversion. We used the relativistic value of Band et al.[4] for the theoretical 4s density $|\psi_{4s}(0)|^2 = 928$ a.u. in Eqn. (1). The 5s electron densities at the nucleus, thus evaluated are listed in Table 1. The results show that the zinc atoms around the tellurium atom cause the reduction of the valence s-electron density at nucleus by about 10% when compared to the case of tin atoms surrounding the tellurium atom.

Table 1. Experimentally determined conversion line intensity ratios and electron densities for the 35.46 keV M1 transition in ^{125}Te for various metal matrices.

Source	O/N_I	$\|\psi_{5s}(0)\|^2$
Sn	0.138 ± 0.003	128 ± 3
Cu	0.128 ± 0.004	119 ± 4
Zn	0.119 ± 0.007	110 ± 6

References

1) See, for example, J.P. Bocquet, Y.Y. Chu, O.C. Kistner, M.L. Perlman, and G.T. Emery: Phys. Rev. Lett., 17, 809 (1966); B. Martin and Schulé: Phys. Lett., 46B, 367 (1973).
2) H. Muramatsu, T. Miura, H. Nakahara, M. Fujioka, E. Tanaka, and A. Hashizume: RIKEN Accel. Progr. Rep., 16, 91 (1982); Phys. Rev. B, (in press).
3) M. Fujioka and M. Takashima: J. Phys., 40, C2-32 (1979).
4) I. M. Band and V. I. Fomichev: Atom. Data and Nucl. Data Table, 23, 295 (1979).

III-1-8. High-Spin States of Er Isotopes in the Interacting Boson Model

N. Yoshida, A. Arima,* and T. Otsuka**

(NUCLEAR STRUCTURE interacting boson model, high-spin states.)

The interacting boson model (IBM) which treats pairs of particles as s- (monopole) and d- (quadrupole) bosons has been successful in describing low-lying collective states in spherical, deformed and transitional nuclei.[1] The particle-plus-core model is widely used to explain the properties of high-spin states which couples particles in high-j intruder orbitals to a core which represents collective motion of particles in other orbitals. When one uses the IBM core, one can describe ground- and excited bands in various kinds of nuclei in a unified way by varying the parameters in the hamiltonian. In a previous work, we used the IBM to describe high-spin states of the Ba and Ce isotopes—transitional nuclei.[2] In that case, we took into account two fermions in $0h_{11/2}$ and obtained a fairly good agreement of energies and B(E2) values between the calculation and experiment.

In the work we here report on, we describe high-spin states of deformed nuclei. In the model, we treat the particles in the intruder orbital explicitly as fermions, and consider that the particles in other orbitals are represented by IBM bosons. The hamiltonian is

$$H = H^B + H^F + H^{int} \tag{1}$$

where H^B is a boson hamiltonian which can be written as

$$\begin{aligned} H^B = {} & \varepsilon_d d^\dagger \cdot \tilde{d} + \kappa(d^\dagger s + s^\dagger \tilde{d} + \chi[d^\dagger \tilde{d}]^{(2)}) \cdot \\ & (d^\dagger s + s^\dagger \tilde{d} + \chi[d^\dagger \tilde{d}]^{(2)}) + \frac{1}{10}\kappa' \left([d^\dagger \tilde{d}]^{(1)} \cdot \right. \\ & \left. [d^\dagger \tilde{d}]^{(1)}\right) + \frac{1}{4}\kappa''(s^\dagger s^\dagger - d^\dagger \cdot d^\dagger) \cdot \\ & (ss - \tilde{d} \cdot \tilde{d}), \end{aligned} \tag{2}$$

and H^F is a fermion hamiltonian with one- and two-body interactions:

$$H^F = \varepsilon^F \hat{n}^F + \frac{1}{2} \sum_J g^{(J)} ([a_j^\dagger a_j^\dagger]^{(J)} \cdot [\tilde{a}_j \tilde{a}_j]^{(J)}). \tag{3}$$

As for H^{int}, the interaction between bosons and fermions, we take

$$\begin{aligned} H^{int} = {} & x(d^\dagger s + s^\dagger \tilde{d}) \cdot [a_j^\dagger \tilde{a}_j]^{(2)} + y[d^\dagger \tilde{d}]^{(2)} \cdot [a_j^\dagger \tilde{a}_j]^{(2)} \\ & + Z^{(0)} \left\{ [a_j^\dagger a_j^\dagger]^{(0)} s - s^\dagger [\tilde{a}_j \tilde{a}_j]^{(0)} \right\} \\ & + Z^{(2)} \left\{ [a_j^\dagger a_j^\dagger]^{(2)} \cdot \tilde{d} - d^\dagger \cdot [\tilde{a}_j \tilde{a}_j]^{(2)} \right\}, \end{aligned} \tag{4}$$

where $s^\dagger$, $d^\dagger$, and $a_j^\dagger$ are s-boson, d-boson and fermion creation operators, respectively. s is s-boson annihilation operator, while $\tilde{d}$ and $\tilde{a}_j$ are tensor operators whose components are related to those of d-boson and fermion annihilation operators, d, a_j, by

$$\tilde{d}_m = (-1)^{2-m} d_{-m} \tag{5}$$

and

$$\tilde{a}_{jm} = (-1)^{j-m} a_{j-m} \ . \tag{6}$$

The first two terms on the right-hand side of Eqn. (4) give the quadrupole-quadrupole interaction between bosons and fermions. The third and the fourth terms change a boson into a pair of fermions and vice versa. They represent the monopole- and quadrupole interactions between the particles in the intruder orbital and those in other orbitals. The boson hamiltonian and the boson-fermion interaction are phenomenologically determined so as to reproduce the energy levels obtained by experiment. B(E2) values and quadrupole moments are calculated using an E2 operator

$$T^{(E2)} = q^B(d^\dagger s + s^\dagger \tilde{d} + \chi[d^\dagger \tilde{d}]^{(2)}) + q^F[a_j^\dagger \tilde{a}_j]^{(2)} \tag{7}$$

B(M1) values and magnetic dipole moments can be calculated using

$$\begin{aligned} T^{(M1)} = {} & m^B[d^\dagger \tilde{d}]^{(1)} \\ & + m'^B \left\{ [[d^\dagger s]^{(2)} [d^\dagger \tilde{d}]^{(1)}]^{(1)} + [[d^\dagger \tilde{d}]^{(1)} \right. \\ & \left. [s^\dagger \tilde{d}]^{(2)}]^{(1)} \right\} + m^F[a_j^\dagger \tilde{a}_j)^{(1)} \end{aligned} \tag{8}$$

The model is applied to the Er isotopes. In this case the intruder orbital is $0i_{13/2}$ for neutrons. For the moment, we allow up to three bosons to change into fermions. The maximum number of fermions is therefore six. Calculation is being carried out.

References

1) A. Arima and F. Iachello: Ann. Rev. Nucl. Part. Sci., 31, 75 (1981); and references therein.

2) N. Yoshida, A. Arima, and T. Otsuka: Phys. Lett., 114B, 86 (1982).

---

* Department of Physics, University of Tokyo.

** Japan Atomic Energy Research Institute.

III-1-9. Multiple Coulomb Excitation of ^{161}Dy and ^{163}Dy

T. Inamura, A. Hashizume, M. Ohshima,* E. Minehara,*
S. Kikuchi,* and H. Kumahora**

NUCLEAR REACTIONS ^{161,163}Dy(^{58}Ni, ^{58}Ni$'\gamma$), E = 250 MeV; measured E_γ, $I_\gamma(\theta)$, $\gamma\gamma$coin., $\gamma\gamma$DCO, lifetimes; deduced levels, J, π.

Multiple Coulomb-Excitation Experiment on ^{161}Dy and ^{163}Dy has been carried out with a 250 MeV ^{58}Ni beam from the JAERI 20-UR tandem accelerator. We have identified members of the ground-state rotational band up to spin 25/2. We have also measured lifetimes of these states which, when taken together with γ-ray branching and mixing ratios, have enabled absolute B(M1) and B(E2) values to be determined in a model-independent way.

As shown in the case of ^{167}Er whose ground-state rotational band is built on the neutron orbital $i_{13/2}$, $7/2^+[633]$,[1] a considerable effect of rotational perturbation on B(M1) is likely to be observed even at low rotational frequency. The nucleus ^{161}Dy possesses the neutron orbital $i_{13/2}$, $5/2^+[642]$, while ^{163}Dy possesses $f_{7/2}$, $5/2^-[523]$. These nuclei would exhibit contrasting behavior of the rotational perturbation effect on transition probabilities as well as on level energies because of considerably different orbital angular momenta.

Figure 1 shows the ground-state rotational band of ^{163}Dy observed in the present experiment. Levels above $15/2^-$ have newly been established. For ^{161}Dy, levels up to $33/2^+$ are known, but lifetimes have been reported only up to the $9/2^+$ state.[2] Detailed analyses are in progress.

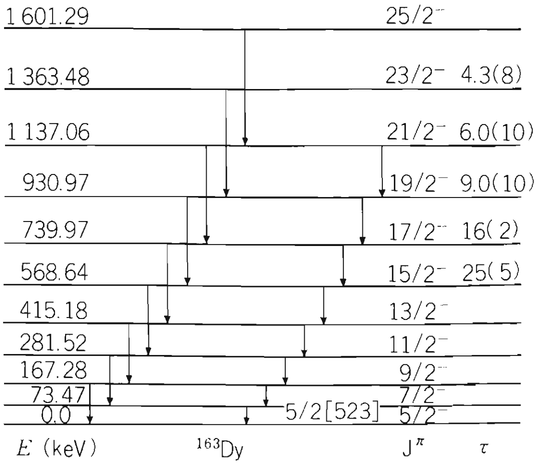

Fig. 1. The ground-state of rotational band of ^{163}Dy. Nuclear lifetime τ are given in units of psec. Numbers in parentheses indicate the statistical uncertainties in the least significant figure.

References
1) M. Ohshima, E. Minehara, M. Ishii, T. Inamura, and A. Hashizume: J. Phys. Soc. Japan, 52, 2959 (1983).
2) Nuclear Data Sheets, 13, 493 (1974).

---

* Japan Atomic Energy Research Institute, Tokai.
** Dept. of Physics, Hiroshima University.

III-1-10. Angular Distributions of Gamma-Rays from Dy under Transient Magnetic Field

A. Hashizume, N. Sakai, and K. Asai

NUCLEAR REACTION Dy(^{40}Ar, ^{40}Ar$'\gamma$), E = 48 MeV; measured $\gamma(\theta)$, natural targets. Transient Magnetic Field.

In the decelerating process of recoil-ions produced by Coulomb excitation, the ions receive extremely large magnetic field when the medium is the polarized ferromagnetic materials. This magnetic field interacts with spins of the recoil nuclei and causes Lamour precession of de-exciting γ-rays emitted from the recoils. The origin of this strong magnetic field has been the subject of the study for these several years, and it is believed that the mechanism proposed by Lindhard and Winther could be one of the origins in the low velocity region of the recoils. For higher velocity, several phenomelogical relations were proposed for the relations between the velocity and the transient magnetic field. One of the simplest relations is [1)]

$$B(v, Z) = aZ(v/v_0)\chi,$$

where v_0 is the Bohr velocity, χ is the magnetization of the foil and a is a parameter which must be determined by experiments. To study such transient field and g-factors a goniometer for the γ-ray angular distribution was installed in the experimental area of RILAC.[2)] When a natural dysprosium target evaporated on an iron foil of 6 μm in thickness was bombarded with 48 MeV Ar^{4+} ions, the γ-rays emitted from 1st and 2nd excited states in dysprosium nuclei were observed. Figure 1 shows preliminary results of the angular distribution of 169 keV γ-ray emitted from the 4$^+$ state in ^{164}Dy when magnetic fields up and down with respect to the beam direction were applied. Observed $\Delta\theta$ depends on Larmour frequency and life-time of the excited state. The g-factor of the 4$^+$ state in ^{164}Dy is not known. It is expected that the factor is slightly different from that of 2$^+$ state,[3)] becauses ^{164}Dy is a deformed nucleus. However, transient field which is velocity dependent must be known to deduce the g-factor. We are now studying the field using known g-factor of dysprosium and other kind of targets.

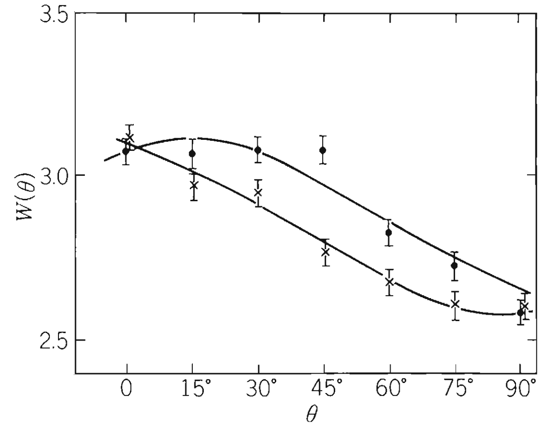

Fig. 1. Field up and down angular distribution for 169 keV γ-rays from the 4$^+$ state in ^{164}Dy.

References

1) J. L. Eberhardt, R. E. Horstman, P. C. Zalm, H. A. Doubt, G. Van Middelkoop: Hyperfine Inter., 3, 195 (1977).
2) A. Hashizume, N. Sakai, K. Asai, H. Kumagai, and Y. Yamada: p. 129 in this report.
3) O. Haüsser, H. R. Andrews, D. Ward, N. Rud, P. Taras, R. Nicole, J. Keinonen, P. Skensved, and C. V. Stager: Nucl. Phys., A406, 339 (1983).

III-1-11. Spin Polarizaiton of Residual Nucleus in ^{6}Li-Induced Reaction

K. Ieki, M. Ishihara, T. Inamura, S. Kohmoto,
K. Sueki, and H. Kudo

NUCLEAR REACTION ^{197}Au(^{6}Li, $\alpha\gamma$), E = 49 MeV; measured γ ray circular polarization; dependence on threshold energy of scattered γ rays.

Circular polarization of gamma-rays emitted from residual nucleus in the ^{197}Au(^{6}Li, α) reaction was measured at E = 49 MeV and $\theta_{lab.} = 40°$ to determine the polarization of the target-like fragment. A comparison is made with previous result$^{1)}$ on the ^{159}Tb(^{7}Li,α) reaction, where the polarization has strong dependence on α-particle energy that cannot be explained by naive triton cluster transfer picture. The experimental method used was the same as described previously$^{1)}$ except for the choice of the threshold energy E_γ^{th} of scattered γ rays. In the previous study of ^{7}Li-induced reaction, E_γ^{th} was set at 210 keV because lower energy γ rays gave fairly small analyzing power. However, when the projectile is light like Li, transferred angular momentum ℓ_{tr} and γ-ray multiplicity M_γ may be so small that neglect of low energy γ rays may affect the results significantly. In the present study, E_γ^{th} was set to be minimum to accept low energy γ rays as much as possible.

In figure 1, the results of spin polarization P_z are shown as a function of α-particle energy E_α for three values of E_γ^{th} which were set in offline analysis. The effect of E_γ^{th} on P_z is rather weak in the region of $E \leq 35$ MeV, but it is significant at highest E_α, even changing the sign of P_z. The observed variation with E_γ^{th} may be related to γ-deexcitation process. When ℓ_{tr} is smaller than spin cutoff parameter, statistical γ transitions at early stage tend to cascade towards final states with higher spins ($I_f > I_i$) while γ transitions at lower excitations may exhibit usual stretched nature ($I_f < I_i$). Since statistical γ rays have higher energies than stretched transitions, choice of E_γ^{th} may affect relative weight between the two types of γ rays. In the higher E_α region, smallest ℓ_{tr} is expected and this effect will occur most drastically.

By setting E_γ^{th} at minimum, values of P_z are fairly constant at $P_z \simeq -0.4$ within statistical errors. The negative polarization corresponds to positive deflection angle as is expected for direct-type process. The energy spectra whose shape are Gaussian, peaked at the energy corresponding to the velocity of beam are considered to be the effect of kinematical matching conditions. This is indeed indicative of a direct reaction mechanism such as breakup fusion process.

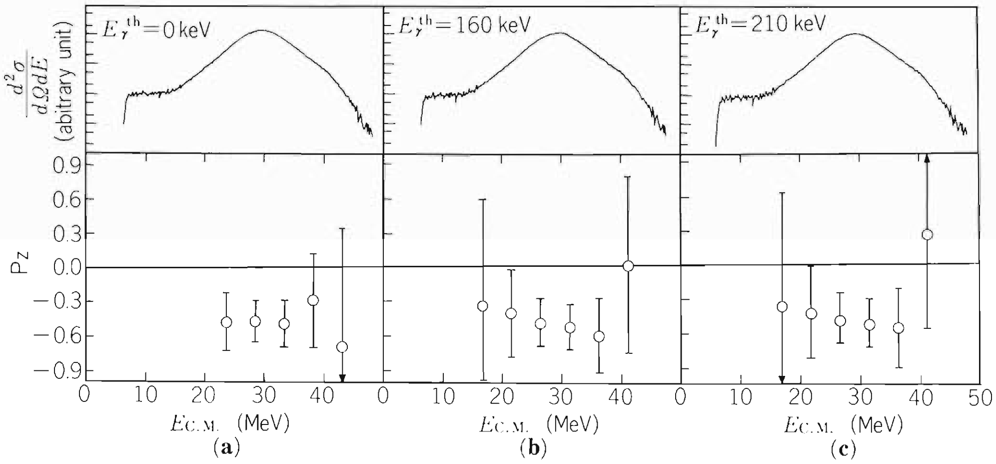

Fig. 1. Energy spectra and spin polarization for the ^{197}Au(^{6}Li,α) reaction. Threshold energy E_γ^{th} of scattered γ rays is set to be (a) 0 keV, (b) 160 keV, (c) 210 keV, respectively.

Reference
1) K. Ieki, M. Ishihara, T. Inamura, S. Kohmoto, H. Utsunomiya, K. Sueki, and H. Kudo: RIKEN Accel. Progr. Rep., 16, 28 (1982).

III-1-12. Correlation between Angular Anisotropy of Fission Fragment and Its Mass in the System of 16 MeV p+^{238}U

Y. Hamajima,* K. Sueki, H. Nakahara,
and I. Kohno

NUCLEAR FISSION ^{238}U (p, nxf), E = 16 MeV; measured complementary fragment kinetic energies; deduced $<E_K>$ (m), σ_{E_K}(m), Y(m) and correlation between angular anisotropy of fission fragment and its mass.

According to Bohr's channel theory, the angular distribution of fission fragments are mostly determined by the properties of the nucleus at the saddle point if the K quantum number at the saddle point is conserved during the deformation of the nucleus from the saddle to the scission point and if the fission fragments separate along the nuclear symmetry axis.$^{1)}$ Extensive studies have been performed with respect to the angular distributions of fission fragments$^{2)}$ and, as far as the angular distributions are concerned, Bohr's theory has been proved correct. Therefore, if the final fate of mass division is determined near the saddle point, some correlation is expected between the final fragment mass and its angular distribution. In 1982, Kudo *et al.* reported in the 15 MeV p + ^{232}Th system that some correlation existed between the angular anisotropy and the fragment mass and that the experimental data could be well reproduced with the assumption of two kinds of saddle points, one leading to symmetric mass division and another to asymmetric division.$^{3)}$

In the present work the correlation between the angular anisotropy of a fission fragment and its mass is further examined in the 16 MeV p + ^{238}U system.

The U target was prepared by vacuum evaporation of UF_4 onto a carbon film of about 50 μg/cm^2 in thickness. The target thickness was about 0.1 mg/cm^2. The target was bombarded with 16 MeV p beams from the cyclotron. The coincident complementary fragments were detected with two 60 μm gold-silicon surface barrier detectors. The solid angle of one detector was collimated to be 0.56 msr and the other, with 21.8 msr. More than 93% of events detected with the smaller collimated detector were coincident with the other detector. Three parameters were stored and recorded on a magnetic tape: two corresponding to the kinetic energies of the complementary fragments and another one to the time-of-flight difference between the two fission fragments in order to check accidental coincidence events.

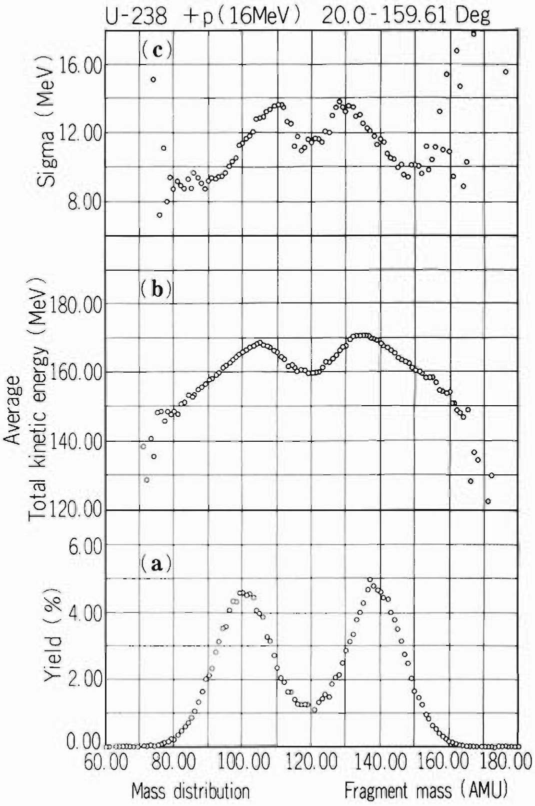

Fig. 1. Results for proton-induced fission of ^{238}U observed at laboratory angle of 20°. (a) The postneutron-emission mass distribution, (b) Average total preneutron-emission kinetic energy as a function of mass. See text for discussion in the cause of the asymmetric distribution, (c) Root-mean-square width of total kinetic energy distribution as a function of fragment mass. The abnormal values for masses smaller than 80 and larger than 150 might have resulted from poor statistics.

---

* Faculty of Science, Tokyo Metropolitan University.

The data were analysed with an off-line computer. The fragment pulse heights were, event-by-event, converted into fragment kinetic energies and provisional masses through an iteration procedure using the mass-dependent energy calibration method of Schmitt *et al.*,$^{4),5)}$ the mass and momentum conservation relations and the ^{252}Cf calibration data.

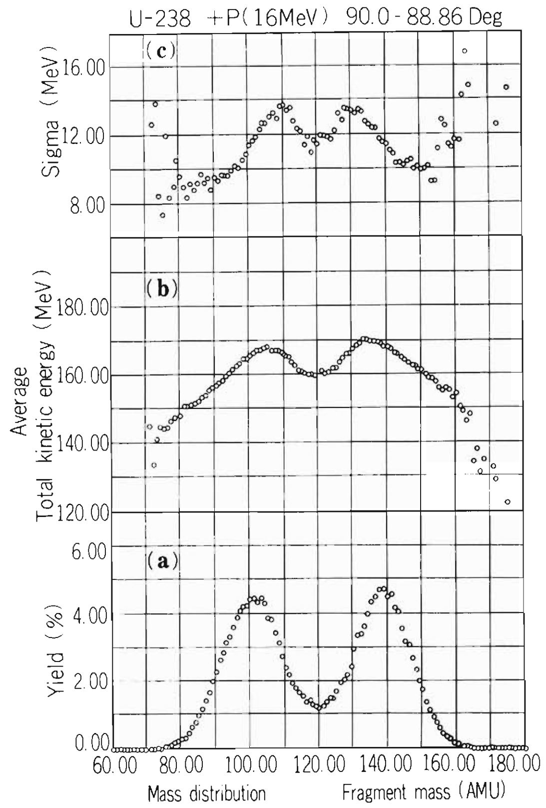

Fig. 2. Results for proton-induced fission of ^{238}U observed at laboratory angle of 90°. See Fig. 1. for explanation of Figs. (a), (b) and (c).

The preliminary results observed at laboratory angle of 20° are shown respectively in Fig. 1 a), b), and c), on the mass distributions, average total fragment kinetic energy distributions and root-mean-square widths of total fragment kinetic energy distributions. In Fig. 2 a), b), and c) are also shown those taken at 90°. The total kinetic energy averaged over the fragment mass distribution was several MeV lower than that from Viola's systematics.$^{6)}$ The asymmetric total kinetic energy distribution might have resulted from an inaccurate correction for neutron emission and/or that of energy loss in the target material. The preliminary analysis yielded no correlation between the angular anisotropy and fragment mass at this bombarding energy. More detailed analysis of the data is now in progress.

References

1) A. Bohr: Proc. of First United Nations Conf. on the Peaceful Uses of Atomic Energy, II, 911 (1955).
2) R. Vandenbosch and J. R. Huizenga: in Nuclear Fission, Academic, New York (1973).
3) H. Kudo, Y. Nagame, H. Nakahara, K. Miyano, and I. Kohno: Phys. Rev. C, 25, 909 (1982).
4) H. W. Schmitt, W. K. Kiker, and C. W. Williams: Phys. Rev., 137, B837 (1965).
5) H. W. Schmitt, J. H. Neiler, and F. J. Walter: ibid., 141, 1147 (1966).
6) V. E. Viola, Jr.: Nucl. Data Sheets, A1, 391(1966).

III-1-13. Fission in ^{14}N Induced Reactions on ^{238}U at 120 MeV

K. Sueki, M. Magara,* Y. Hamajima,*
H. Kudo,** H. Nakahara, and I. Kohno

NUCLEAR REACTIONS ^{238}U(^{14}N,X) fission, measured cross sections of total reaction and fission, angular distributions and angular correlations of fission fragments.

For reactions of highly fissionable target nuclei, where essentially all the fusion phenomena are accompanied by fission, it is possible to obtain the fusion cross section by observing angular correlations of fission fragments.$^{1)}$ The fission events preceded by incomplete transfer of the linear momenta of the incident particles to the target can be separated from those of fusion-fission by angular correlation studies. The amount of the average angular momenta given to the fissioning nuclei can also be estimated from the observation of angular distributions of fission fragments with respect to the direction of incident particles.

In the present experiment we have studied the reactions resulting from the bombardment of a ^{238}U target with ^{14}N ions and observed pairs of fission fragments in coincidence by using a small 30 μm thick SSD (0.5 msr) and a position-sensitive SSD (20 deg.), both placed in the reaction plane.

Beams of 120 MeV ^{14}N ions were provided by the cyclotron. The target consisted of 150 μg/cm^2 ^{238}UF$_4$ material evaporated onto a 50 μg/cm^2 carbon foil. The angular distribution of elastic scattering events were also observed in order to get the information on the total reaction cross section and the grazing angular momentum.

Some of the results are summarized in Table 1. The grazing angle was determined in the elastic scattering from which the interaction radius, R_{int}, the grazing angular momentum, ℓ_{gr}, and the total reaction cross section, σ_R, were evaluated with the classical approximation.

The fission-fragment angular distribution observed in the lab system is shown in Fig. 1(a). The total fission cross section, σ_f, integrated over this distribution was 1515 mb. The angular distribution in the CM system shown in Fig. 1(b) was obtained on the very crude

Table 1. Measured characteristics of the 120 MeV ^{14}N + ^{238}U reaction system.

θ_{gr}	56.2	±	0.5	deg
R_{int}	12.46	±	0.07	fm
gr	64	±	1	ħ
σ_R	1755	±	38	mb
σ_f	1515	±	50	mb

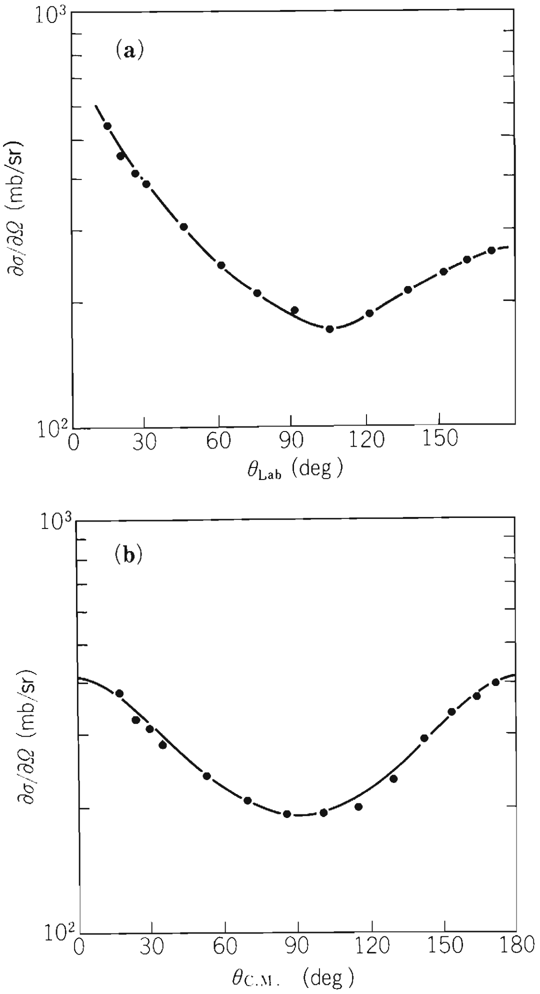

Fig. 1. The angular distribution of fission fragments at 120 MeV ^{14}N + ^{238}U. (a) lab system, (b) CM system.

---

* Faculty of Science, Tokyo Metropolitan University.

** Present address: Faculty of Science, Niigata University.

assumption that all the observed fission events originated from complete-fusion-fission and that only symmetric fission took place. A more accurate conversion from the lab system to the CM system is now in progress.

The angular correlation data observed with one detector at $\psi_1 = 90^\circ$ with respect to the beam direction are shown in Fig. 2. There are clearly two components in the angular correlation data. One is due to the complete-fusion-fission whose events are centered around the angle $\theta_{12} = 160^\circ$ which is very close to the angle, indicated by an arrow, expected from full-momentum-transfer. The other is due to the fission preceded by incomplete linear momentum transfer from the projectile to the target. Fragments from the latter events fall on large θ_{12}. When the data are analyzed into two components on the assumption that each has a Gaussian distribution as shown by a solid and a dashed curve in Fig. 2, the incomplete-fusion-fission amounts to about 10 % of the total fission events. Similar fractions were also obtained even when ψ_1 was varied from 20° to 90°. Therefore, the fusion-fission cross section, which is approximately equivalent to the fusion cross section, amounts to about 1360 mb. From the present data, the cross sections of various reaction mechanisms can be divided into the following fraction of the total:

Incomplete linear momentum transfer;

$$(\sigma_R - 0.9\sigma_f)/\sigma_R \simeq 0.22$$

Incomplete linear momentum transfer followed by fission; $0.1\sigma_f/\sigma_R \simeq 0.09$

Complete linear momentum transfer;

$$0.9\sigma_f/\sigma_R \simeq 0.78.$$

Where the incomplete-fusion-fission cross section is located in the σ_ℓ vs. ℓ plane is unknown yet. It requires the knowledge of the ℓ dependence of the fission barrier and the excitation energy of the fissioning nucleus. As a next step, we are trying to observe the excitation energy of the fissioning nucleus by coincidence experiments between the emitted light particles and fission fragments.

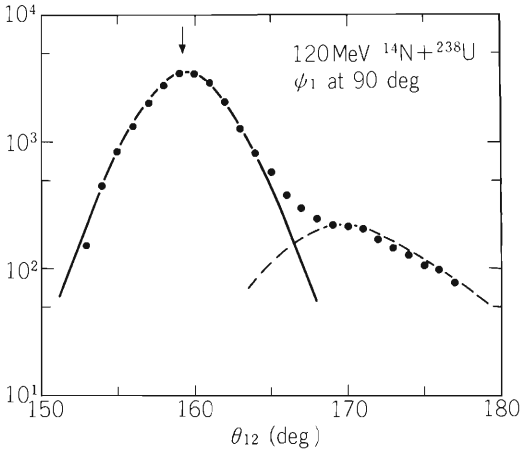

Fig. 2. Fission-fragments angular correlation for the system of 120 MeV $^{14}N + ^{238}U$ with the fixed detector at $\psi_1 = 90^\circ$. The solid line is a Gaussian distribution centering around the angle corresponding to the full-momentum-transfer, and the dashed line shows the residual area. The arrow indicates the predicted correlation angle for full-momentum-transfer.

Reference

1) T. S. Sikkeland, E. L. Haines, and V. E. Viola, Jr.: Phys. Rev., 125, 1350 (1962); V. E. Viola, Jr., B. B. Back, K. L. Wolf, T. C. Awes, C. K. Gelbke, and H. Breuer: Phys. Rev. C, 26, 178(1982).

III-1-14. Isomeric Transitions of ^{211m}Po and ^{212m}Po

H. Kudo, T. Nomura, K. Sueki,
Y. Gono, and M. Magara*

NUCLEAR REACTION ^{208}Pb(α,n)^{211m}Po, $E_\alpha = 20 - 30$ MeV, ^{209}Bi(α,p)^{212m}Po, $E_\alpha = 30 - 40$ MeV, isomeric transition, He-jet transport, $\alpha - \gamma$ coincidence, γ-decay branching ratios.

(1) Isomeric transition of ^{211m}Po

^{211}Po is known to have a high spin isomer whose spin and parity is assigned as $J^\pi = 25/2^+$.[1] This isomeric state deexcites through α-decay with a half-life of 25.2 s (See Fig. 1). However, a possible competing γ-decay of the isomeric state has not been observed yet, the upper limit of the isomeric transition being reported to be less than 0.2 % relative to the α-decay. We have measured the branching ratio of γ-decay of the isomeric state by use of a hellium-jet transport system which has recently been fabricated.[2] We used the reaction ^{208}Pb(α,n)^{211m}Po at $E_\alpha = 20 - 24$ MeV for production of ^{211m}Po. The half life (0.516 s) of the ground state is fairly short compared with that of the isomeric state. After decaying out of the ground state that was produced directly from the nuclear reaction ^{208}Pb(α,n)^{211g}Po, we measured the α-decays from the isomeric state as well as from the ground state which was possibility repopulated after the isomeric γ-ray transitions. A part of the observed α-spectra is shown in Fig. 2, in which the 7.450 MeV peak is clearly seen. The decay curve of this peak is also shown in the upper part of Fig. 2. Comparing yields of known abundant α-particles of ^{211m}Po with that of the 7.450 MeV α-particles, we obtained the branching ratio of γ-decay of ^{211m}Po as 0.016 ± 0.004 %.

The isomeric γ-ray transition is considered to take place between the $25/2^+$ and $17/2^+$ states (see Fig. 1) with $E_\gamma = 35.3$ keV. Taking into account the internal

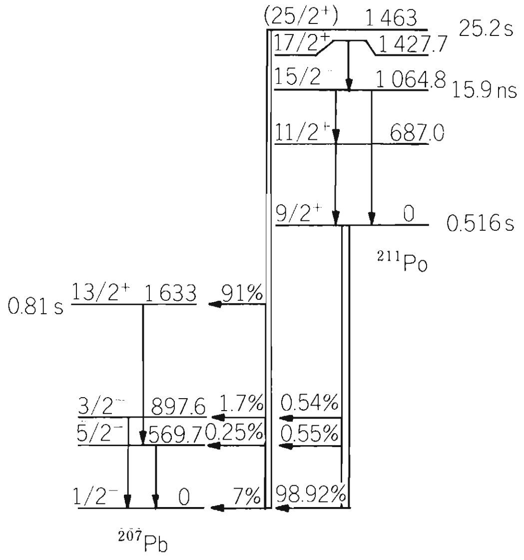

Fig. 1. Partial decay scheme of ^{211m}Po and ^{211g}Po.

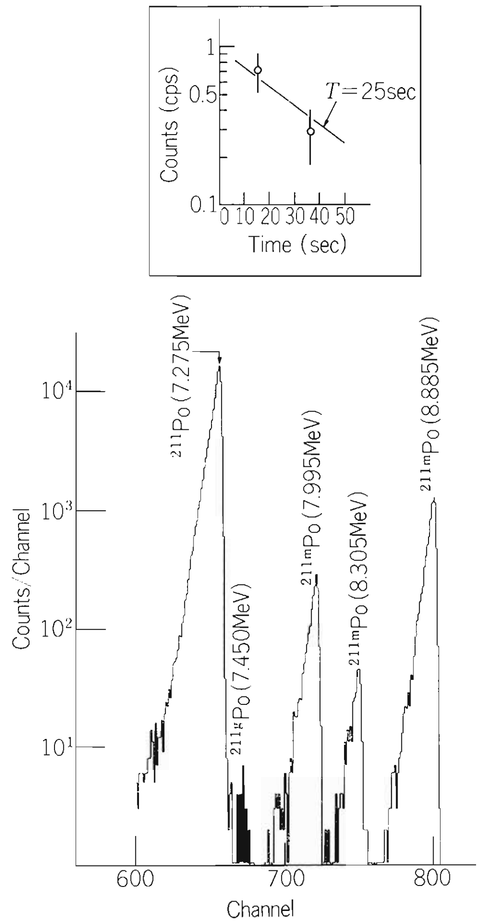

Fig. 2. A part of α-spectra of ^{211m}Po and ^{211g}Po (lower part) and the decay curve of the 7.450 MeV peak (upper part).

---

* Faculty of Science, Tokyo Metropolitan University.

conversion ratio of this transition, the above value of the branching ratio gives a partial γ-ray half life of 8.7 X 10^4 y, which corresponds to 1.8 Weisskopf estimate of the E4 transition.

(2) Isomeric transition of ^{212m}Po

A high-spin isomer of ^{212}Po was firstly acertained by Perlman et al.[3] Its half life is 45 sec. while its spin and parity is assigned to be (16^+) or (18^+). The partial decay scheme of ^{212}Po is shown in Fig. 3. Only an upper limit (1.5 %) of the branching ratio of γ-decay of ^{212m}Po is known. The ground state of ^{212}Po has a half life of 0.3 μs and emits an α-particle of 8.784 MeV. Therefore, it is possible to determine the branching ratio by comparing yields of the 11.65 MeV α-particles from the isomeric state with those of the 8.784 MeV α-particles from the ground state, if we measure an α-spectrum after a certain cooling time. We used the reaction ^{209}Bi (α, p)^{212m}Po at $E_\alpha = 30 - 40$ MeV for the production of ^{212m}Po. In this case, however, ^{221m}Po produced from the ^{209}Bi(α, pn) reaction emits 8.885 MeV α-particle which corresponds to the α-decay of ^{211m}Po to the ground state of ^{207}Pb. As this α-particle energy is close to that from ^{212g}Po, we applied α – γ coincidence measurement to eliminate the disturbing 8.885 MeV α-decay. The results are shown in Fig. 4, where the 8.784 MeV peak is seen in the delayed spectrum.

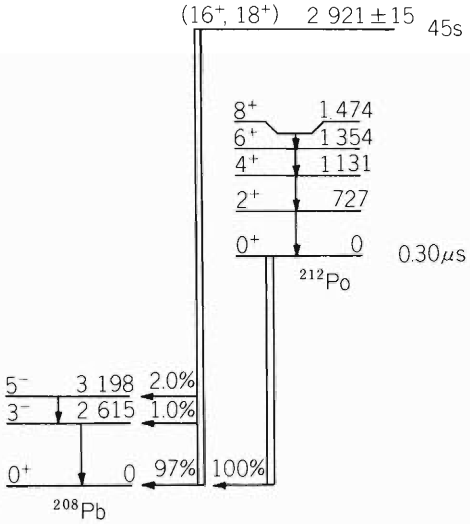

Fig. 3. Partial decay scheme of ^{212m}Po and ^{212g}Po.

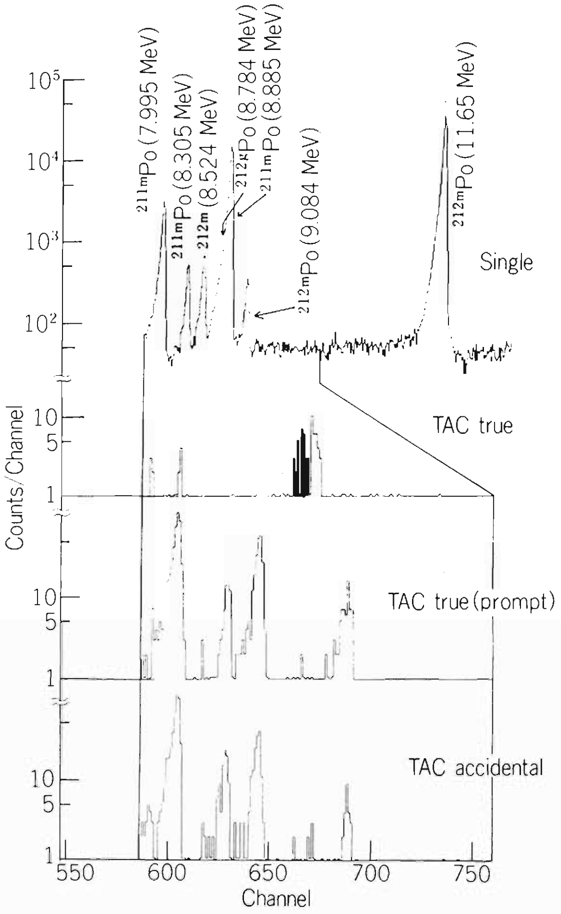

Fig. 4. A part of α-spectra obtained in α – γ coincidence experiment on ^{212m}Po. The delayed spectrum is indicated as TAC true.

It is necessary to know a γ-ray multiplicity of the isomeric transition to deduce the branching ratio of interest from the present measurement. A preliminary result in the α – γ coincidence measurement yields two new γ-rays besides the known transitions below the 8^+ state, which yields the branching ratio of the isomeric transition to be 0.081 ± 0.023 %.

References

1) B. Fant, T. Lonnroth, and V. Rahkonen: Nucl. Phys., A355, 171(1981).

2) H. Kudo. T. Nomura, and J. Fujita: p. 127 in this report.

3) I Perlman, F. Asaro, A. Ghiorso, A. Larsh, and R. Latimer: Phys. Rev., 127, 917 (1962); A. R. Barnett and J. S. Lilley: Phys. Rev., C9, 2010 (1974).

III-1-15. In-Beam γ-Ray Study of ^{212}Po

Y. Gono, Y. Itoh,* M. Sugawara, and I. Fujiwara**

NUCLEAR REACTION ^{210}Pb (α,2n), E = 29 MeV measured $\gamma\gamma$-coin deduced levels.

The nucleus ^{212}Po has been studied by many groups$^{1)}$ since the observation of the 11.65 MeV α-decay from the excited state at 2.91 MeV with a half-life of 45 s. Some experimental works were made by measuring the α- and γ-rays following the β-decays of ^{212}Bi. Others utilized in-beam spectroscopic techniques using the ^{209}Bi (α,p) ^{212}Po and ^{208}Pb (^{7}Li,t) ^{212}Po reactions.

Recently we prepared ^{210}Pb target for the in-beam studies of nuclei in the light actinide region. The target was prepared by the electro-deposition on a 100 μg/cm^2 Ni-foil. The target thickness was about 300 μg/cm^2 which corresponds roughly to 5 mCi.

We have made a test experiment on ^{212}Po by using the ^{210}Pb (α,2n) ^{212}Po reaction (E=29MeV). Resulted singles γ-ray spectrum is shown in Fig. 1. The γ-rays such as 728, 405, and 223 keV in ^{212}Po were easily identified. Some γ-rays which belong to ^{208}Po were also seen in the spectrum since ^{206}Pb was contained in the target as a decay product of ^{210}Pb. Two new γ-rays with the energies of 356 and 578 keV were found to be in cascade with the above mentioned γ-rays and also with each other (see Fig.2). The extensive $\gamma\gamma$-coincidence experiment was performed recently with better statistics. The data analysis is in progress.

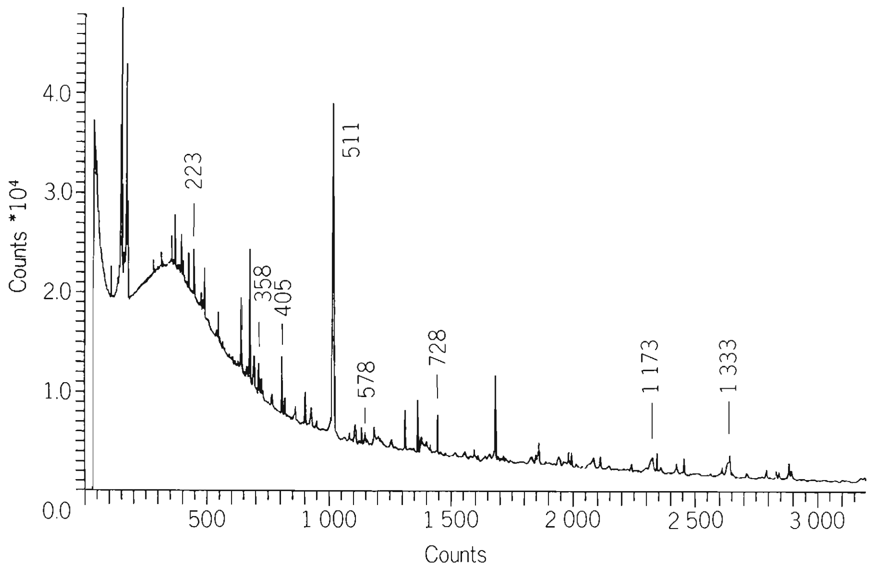

Fig. 1. Singles γ-ray spectrum resulted from the ^{210}Pb + α reaction at 29 MeV. Numbers in the figure are given in keV.

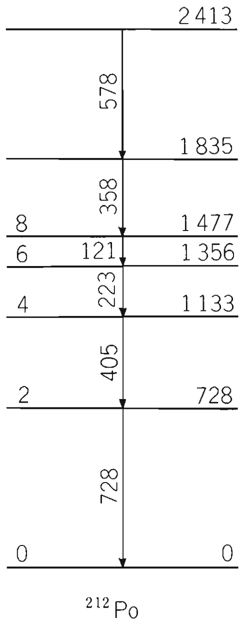

Fig. 2. Level scheme of ^{212}Po.

Reference

1) D. Strottman: Phys. Rev., 20, 1150 (1979), and references therein.

---

* Present address: Hitachi Service Engineering Co.

** Permanent address: Kyoto University.

III-1-16. Delayed γ-Ray Study of ^{217}Ac

Y. Gono, Y. Itoh, K. Huruno,* T. Aoki,* Y. Nagashima,*
Y. Fukuchi,* and T. Komatsubara*

NUCLEAR REACTION ^{209}Bi(^{12}C, 4n) E = 77 MeV, measured $\gamma\gamma$-coin, pulsed-beam

We reported previously a level scheme of ^{217}AC (Ref. 1). However there was still ambiguity on the location of an isomer. Since an isomer with a half-life of $t_{1/2}$ = 810 ns was known to exist, a new experiment was performed with a pulsed-beam of 77 MeV ^{12}C at Tandem Laboratory of Tsukuba University. The beam pulses were given every 1.5 μs width. A $\gamma\gamma$-coincidence experiment was made with a 15 cm^3 LEPS and a 70 cm^3 Ge(Li) in between the beam-burst. A γ-ray coincidence spectrum which was obtained by setting gates on the previously known γ-rays such as 660, 486, 382, 352, and 154 keV is shown in Fig. 1.

Recently a level scheme of ^{217}Ac has also been reported by Maier et al.[2] Our present result is consistent with theirs on the γ-ray coincidence relations up to the $29/2^+$ state at 2013 keV. However the additional γ-rays such as 327, 372, 380, and 501 keV, which were known from our previous report[1] to populate an isomer above the 1682 keV state, appear also in Fig. 1. This is understood only if another long-lived isomer exists at higher energy than 2013 keV. A delayed coincidence analysis shows that there are some low-energy γ-rays such as 75, 122, 156, and 200 keV in addition to the above mentioned γ-rays (as can be seen in Fig. 2) between the two isomers. The present experiment resulted in too low statistics to get information on the coincidence relations among them. It is necessary to make further experiments to clarify the level structure between the isomers.

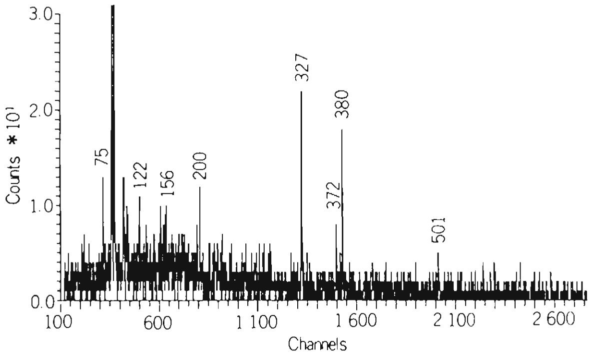

Fig. 1. A delayed γ-ray spectrum obtained from the ^{209}Bi (^{12}C, 4n) ^{217}Ac reaction at E = 77 MeV. Gates were set on 660, 486, 382, 352, and 154 keV γ-rays.

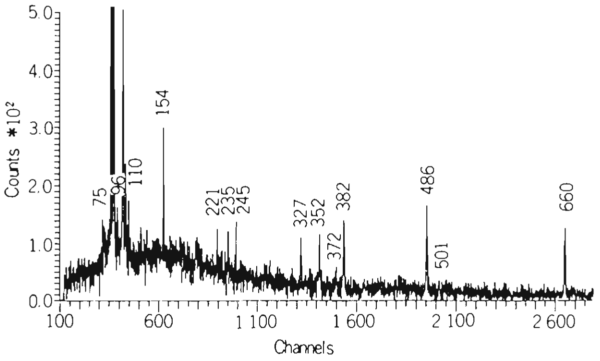

Fig. 2. A delayed coincidence spectrum obtained from the same reaction as Fig. 1. Gates were set on 660 and 486 keV γ-rays. Time gate was also set on the part of off-prompt to see the γ-rays above an isomer.

References

1) Y. Gono, Y. Itoh, S. Sasagase, M. Sugawara, T. Kubo, T. Nomura, S. Hayashibe, and K. Hiruta: Proc. Int. Symp. on Dynamics of Nuclear Collective Motion, Mt. Fuji 1982, p. 283 (1982).
2) K. H. Maier, D. J. Decman, H. Kluge, N. Roy, W. Wiegner, M. Guttormsen, H. Hubel, M. Menningen, and J. Recht: Hahn-Meitner-Institute Progr. Rep., p. 89 (1982).

---

* Permanent address: Tandem Laboratory, Tsukuba University.

III-2. Atomic and Solid-State Physics

1. Theoretical Study of Charge Transfer from H or He to Multicharged Projectile Ions at Impact Energies of keV/amu - MeV/amu

T. Watanabe, N. Toshima, H. Suzuki*
Y. Kajikawa,** and H. Ryufuku***

In the continuation of theoretical work on charge transfer prcesses, we have made a series of works on electron capture from H or He by multicharged projectile ions in the above-mentioned energy region.[1) This energy region corresponds to the impact velocity which is comparable to the orbital electron velocity, i.e., from about one tenth of to about ten times the orbital velocity. One of the main difficulties in the theoretical treatment of electron capture by multiply charged ions from H and He lies in the fact that so many electronic levels are involved in these processes. In a coupled channel calculation of $A^{q+} + H \rightarrow A^{(q-1)+} + H^+$, for example, a large number of electronic states for $A^{(q-1)+}$ should be taken into account. However, the number is necessarily limited in practical calculations. Then, the choice of channels becomes somewhat ambiguous. On the other hand, in UDWA (unitarized distorted wave approximation) we can take into account all states relevant to the process, though in the approximation only two successive states are coupled. The basic idea of UDWA lies in the fact that the electron capture processes at low and intermediate energies are dominated by the contribution from large impact parameters. At higher energies the two state coupling approximation gives reasonable results.

In UDWA three approximations have been made; (1) to drop the chronological ordering operator in the S matrix representation, (2) to retain only first order overlap integrals between two atomic orbitals in the coupled equations, and (3) to neglect all the matrix elements except those involving the initial state in the expansion series of S matrix (neglect of final state interactions). We have investigated the validity of these approximations by the following procedure: (a) to compare the UDWA results directly with calculations using an atomic base close-coupling (ABCC) method[2) in the cases of H^{++} + H and $H^+ + H$, (b) to compare with the calculation in EDWA (exponential distorted wave approximation) in the cases of $He^{++} + H$, $Li^{3+} + H$, $Be^{4+} + H$, $B^{5+} + H$, and $C^{6+} + H$, and (c) to compare the energy levels appearing in UDWA with the exact molecular orbital energy levels.

EDWA[3) takes into account all interactions between final states and is considered to be exact except for the omissions of the chronological time ordering operation T and of higher (≧ the second) order terms in overlap integrals in the atomic base treatment. We write the cross section for electron capture σ_{n0} in terms of the n-0 (0 being the initial state and n the n-th final state) component of the S matrix using impact parameter scheme as

$$\sigma_{n0} = 2\pi \int |S_{n0}|^2 \, b \, db.$$

The S matrix can be written as

$$S = \exp(-iA),$$

where

$$A = \int_{\infty}^{\infty} s^{-1} H(t) \, dt$$

(s: overlap matrix, H(t): the total electronic Hamiltonian matrix). Suppose that A is diagonalized by a unitary matrix U as

$$U^{-1} A U = D = \begin{bmatrix} \lambda_1 & & & 0 \\ & \lambda_2 & & \\ & & \ddots & \\ 0 & & & \end{bmatrix}$$

where λ_k is an eigenvalue of A. The S matrix can be

---

* Department of Applied Physics, University of Tokyo, Present address: Atsugi Laboratory, Fujitsu Laboratory Ltd.

** Department of Applied Physics, University of Tokyo, Present address: Central Research Laboratory, Mitsubishi Electric Corporation.

*** Visible Information Center Ltd.

written as

$$S = U \begin{bmatrix} \exp(-i\lambda_1) & & & \\ & \exp(-i\lambda_2) & & \\ & & \ddots & \\ & & & \cdot \end{bmatrix} U^{-1}$$

We take into account a limited number of atomic base channels, i.e., 1s of H and 1s, 2s, 2p, ..., 5g of $A^{(q-1)+}$. One of the results in illustrated in Fig. 1.

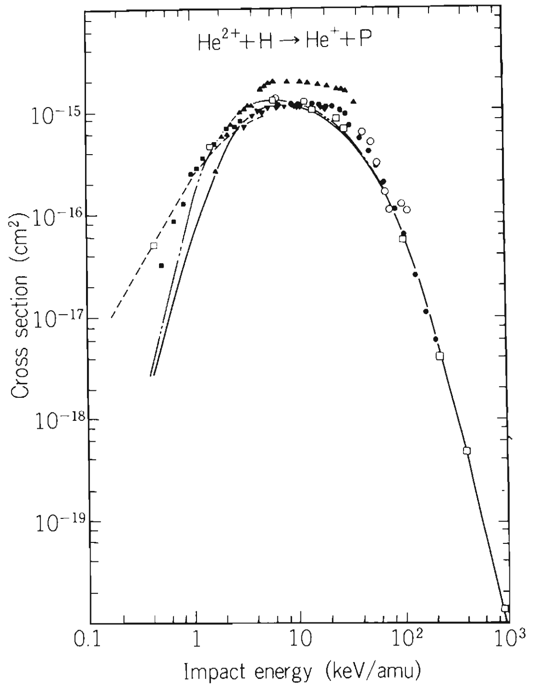

Fig. 1. Electron capture cross sections as functions of impact energy per nucleon in the case of $He^{++} + H \rightarrow He^{+} + H^{+}$. Theories: —— EDWA[3], - - - - Molecular base close-coupling by Winter Lane[4],— - - —UDWA[1], ○ Classical Monte Carlo by Olson[5], □ Atomic base close-coupling by Fujiwara and Toshima[2]. Experiments: ■ Nutte et al[6], ▲ Bayfield et al[7], ● Olson et al[8].

In high velocity impact ($v > 1$ a.u.) the cross section for charge transfer decreases very rapidly. This is predicted by many kinds of theories (Oppenheimer-Brinkman-Kramers (OBK), Born, second Born, continuum distorted wave (CDW), eikonal, distorted wave Born approximation (DWBA), etc.) and has been verified by experimental results. This feature implies that, except for the case of second order Born terms, the dominant interaction is confined within a very small region mainly because of the electron translation factor. Therefore, the distortion effect is important in the atomic base treatment. Indeed it is taken into account in UDWA.

The second Born term predominates over the first Born term in charge transfer processes at high energies. This is due to the importance of the contribution from continuum states. We have compared experimental results with the calculations in UDWA, EDWA and in ABCC in the case of $He^{++} + H$ and $H^{+} + H$. We have found that all these results agree with one another in the velocity region where experimental data are available.

For intermediate and low velocity impact ($0.1 < v < 1$ a.u.) the final state interaction will not be negligible. In order to study this point we have also compared the experimental data with the calculations in UDWA, EDWA and in ABCC in the case of $He^{++} + H$ and with those in EDWA in the cases of $Li^{3+} + H$ through $C^{6+} + H$. We have found that the omission of T leads to an error of less than 30% in the capture cross sections in the velocity region of $v > 0.3$ a.u. In addition we have studied the correspondence between atomic base and molecular base treatments by comparing the diagonal matrix elements in the distorted wave approximation with the exact molecular base eigenenergies.

References

1) H. Ryufuku and T. Watanabe: Phys. Rev., A18, 2005 (1979),; ibid., A19, 1538 (1979), ibid., A20, 1828 (1979).
2) K. Fujiwara: J. Phys. B: At. Mol. Phys., 14, 3977 (1981); N. Toshima: unpublished work.
3) H. Suzuki, N. Toshima, T. Watanabe, and H. Ryufuku: Phys. Rev., A29, 429 (1984).
4) T. G. Winter and N. F. Lane: Phys. Rev. A17, 66 (1978).
5) R. E. Olson and A. Salop: ibid., A13, 1312 (1976).
6) W. L. Nutt, R. W. McCullough, K. Brady, M. B. Shah, and H. B. Gilbody: J. Phys., B 11, 1457 (1978).
7) M. B. Shah and H. B. Gilbody: J. Phys. B: At. Mol. Phys., N7, 630 (1974).
8) R. E. Olson, A. Salop, R. A. Phaneuf, and F. W. Meyer: Phys. Rev., A16, 1867 (1977).

III-2-2 Critical Angle Scattering in High-Velocity Three-Body Coulomb Rearrangement Collisions

J. S. Briggs

In the process of electron transfer from a positive ion to a neutral atom such as

$$P + (T, e) \rightarrow (P, e) + T$$

(P: projectile ion, T: target core or nucleus and e: electron), there exists a problem that the scattering amplitude in the second order perturbation approximation dominates over that in the first order approximation owing to the contribution from electronic continuum intermediate states in the high impact velocity limit of collision. Theoretically this effect is expected to be significant above the impact velocity of ~10 q a.u., where q is the charge of the projectile ion. Even at lower impact velocities the second order term is predicted to appear (and to be discriminated from the first order term) in the form of a peak, called Thomas peak, in the measured differential cross section (angular dependence). Recently the peak has been observed experimentally for the first time. Here we treat generally the problem of rearrangement from the system of a projectile particle 1 (=P) and target (2,3) (=(T,e)), which consists of particles 2 and 3, into the system of a bound complex (1,3) (=(P,e)) and a target particle 2 (= T).

The occurrence of such enhanced probabilities for particle capture at certain angles of scattering of the projectile particle 1 has been analysed by Dettmann and Leibfried.[1)] These critical angles occur when the kinematics of the collision is such that the incident particle 1 and the caputured particle 3 emerge with equal velocity after the collision. Since only kinematic conditions must be satisfied, these processes have a classical counterpart. Indeed the first example of such a critical angle capture was described classically by Thomas[2)] in the case of electron transfer between two nuclei.

Quantum-mechanically the occurence of a critical angle and concomitant enhancement of the capture amplitude are signified by a pole in the free-particle Green function appearing in an expansion of the T-matrix element for rearrangement to second order. This second-order approximation is

$$T = \langle \Phi_f | V_{23} + V_{12} | \Phi_i \rangle + \langle \Phi_f | (V_{23} + V_{12}) G_0^+ (V_{13} + V_{12}) | \Phi_i \rangle , \qquad (1)$$

where V_{ij} denotes the Coulomb interaction between particles i and j and G_0^+ is the Green function for free propagation of all three particles. Expansion of the second (double-scattering) term gives four contributions denoted by T(23,13), T(12,13), T(23,12), and T(12,12).

It is easily seen that the V_{12} interaction plays a special role as the only second-order term to contain the same interaction twice. This term describes the (repulsive) scattering of particles 1 and 2 whilst the captured particle 3 is a spectator. Then capture occurs only through the recoil of target particle 2 and does not lead to critical angles due to two correlated two-body events, as do the other three terms in the second-order T-matrix element.

Dettmann and Leibfried have shown that in the high-velocity limit $\frac{1}{2}v^2 > \epsilon_i$, ϵ_f(where v is the initial relative velocity and ϵ_i, ϵ_f the binding energies of particles 2 and 3 and particles 1 and 3 respectively), critical angles occur as follows:

T(23,13) ; when

$$\cos\theta = \frac{1}{2}(\xi\xi')^{-3/2}(3\xi\xi' - 1), \qquad (2)$$

T(12,13) ; when

$$\cos\theta = \frac{1}{2}(\xi\xi')^{-1/2} \times \left\{ 1 + \xi\xi' - (\xi'/\xi)(1 - \xi\xi')^2 (1 - \xi')^{-2} \right\}, \qquad (3)$$

and T(23,12) ; when

$$\cos\theta = \frac{1}{2}(\xi\xi')^{-1/2} \times \left\{ 1 + \xi\xi' - (\xi/\xi')(1 - \xi\xi')^2 (1 - \xi)^{-2} \right\}, \qquad (4)$$

where θ is the centre-of-mass angle of scattering and $\xi = m_2/(m_2 + m_3)$ and $\xi' = m_1/(m_1 + m_3)$. That the critical angles depend only upon mass ratios emphasises their kinematical origin.

The critical angles occur when the mass ratios are such that the modulus of the right hand sides of Eqns. (2)-(4) is less than or equal to unity. This is illustrated by the consideration of three cases of same importance. The first is the much-studied transfer of an electron from a target nucleus to an incident proton where

$$\xi = \left(1+\frac{m}{M_T}\right)^{-1} \quad ; \quad \xi' = \left(1+\frac{m}{M_P}\right)^{-1}$$

where m, M_T, and M_P are masses of electron, target nucleus and projectile proton respectively. To order (m/M_P), one finds from Eqn. (2) that a critical angle occurs for T(23,13) scattering at

$$\theta \simeq \frac{\sqrt{3}}{2}\frac{m}{M_P}$$

in the laboratory frame.

This correlated scattering is depicted in Fig. 1(a) where, to order m/M_T, the recoil of the target nucleus is neglected. It is the classic case considered by Thomas$^{2)}$ and observed recently by Horsdal-Pedersen et al.$^{3)}$

In the case of electron capture the term T(12,13) also shows a critical angle when

$$\cos\theta \simeq 1 - \frac{1}{2}(1 + M_P/M_T)^2 .$$

This angle varies from π when $M_P = M_T$ to $\pi/3$ in the limit $M_P/M_T \to 0$. This latter case, where no target recoil occurs, is illustrated in Fig. 1(b). Here the incident proton with speed v first scatters the electron through an angle 60° (whereby it acquires a speed v) and then the proton scatters elastically off the target nucleus to emerge, still with velocity v, also at an angle 60°.

Finally, one sees that for electron caputre the term T(23,12) shows a critical angle at

$$\cos\theta \simeq 1 - \frac{1}{2}(1 + M_T/M_P)^2 .$$

For $M_T > M_P$ no critical angle is possible. The explanation is simple. In the first collision the incident proton scatters off the target nucleus which then recoils and scatters the electron. For $M_T > M_P$ the recoil velocity is never high enough that the recoiling nucleus can impact sufficient velocity to the struck electron for it to move with the velocity of the proton.

The case of proton impact is to be contrasted with that of positron impact, leading to positronium formation. Here one has

$$\xi = \left(1+\frac{m}{M_T}\right)^{-1} ; \ \xi' = \frac{1}{2} .$$

For T(23,13) the critical angle is obtained from Eqn. (2) as $\cos\theta = 1/\sqrt{2}$ to order m/M_T.

This mechanism is depicted in Fig. 2(a). The incident positron scatters the electron through 45° and both particles then have speed $v/\sqrt{2}$. The electron then scatters elastically through 90° off the massive target nucleus. The T(12,13) matrix element also shows a critical angle at $\cos\theta = 1/\sqrt{2}$ as may be shown from Eqn.(3). In this mechanism, depicted in Fig. 2(b), the positron first scatters the electron but is then itself scattered through 90° off the target nucleus. Clearly, in the case of positron impact, the two T-matrix elements T(23,13) and T(12,13) differ only in the sign of the

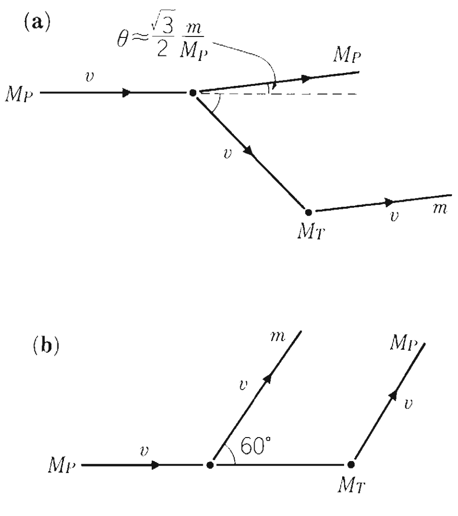

Fig. 1. Schematic figure of critical angle scattering in the electron transfer process. (a) critical angle ($\theta << 1$) for T(23,13) scattering, (b) critical angle ($\theta = \pi/3$) for T(12, 13) scattering in the limit $M_P/M_T \to 0$.

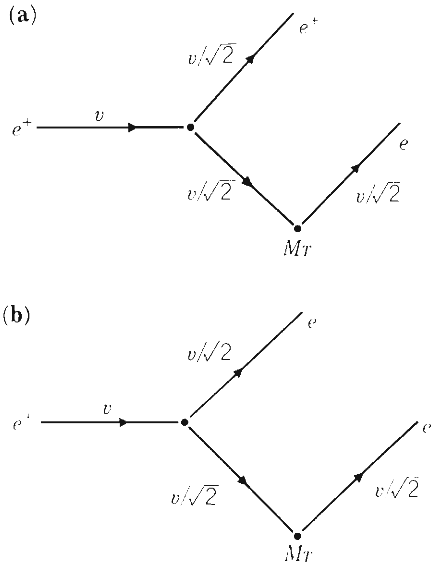

Fig. 2. Schematic figure of critical angle scattering in the collision of a positron with a target atom to form a positronium.
(a) critical angle for T(23,13) scattering,
(b) critical angle for T(12,13) scattering.

second interaction, electron-nucleus or positron-nucleus respectively. This leads to the result obtained by Shakeshaft and Wadehra[4)] that positronium can only be formed in odd-parity states as a result of critical angle scattering. Finally, since $m \ll M_T$ one sees that T(23,12) has no critical angles corresponding to the physical situation that the massive nucleus hardly recoils after being struck by the light position.

References

1) K. Dettmann and G. Leibfried: Z. Physik, 218, 1 (1969).
2) L. H. Thomas: Proc. Roy. Soc., A114, 561 (1927).
3) E. Horsdal-Pedersen, C.L. Cocke, and M. Stöckli: Phys. Rev. Lett., 50, 1910 (1983).
4) R. Shakeshaft and J. M. Wadehra: Phys., Rev., A22, 968 (1980).

III-2-3. Charge Equilibrium of Energetic Heavy Ions and Its Effect on the Stopping Power of Gaseous Media

S. Karashima and T. Watanabe

The problem of charge state distributions[1)] of heavy ions passing through solid target as well as gaseous target is generally of great theoretical interest and of decisive importance for many practical purposes.[2),3)]

When energetic heavy ions traverse through dielectric media, the amount of energy deposited by ions closely relates to their effective charges. Then the LET (Linear Energy Transfer) and the range of the ion beam are fundamental physical quantities in the mechanism of energy deposition.

The fractions of ions in the beam in different charge states can be obtained from the rate equations for the electron loss and capture processes using their cross sections. In a series of works,[4)] we have developed a simple model to describe these charge-exchange processes of energetic heavy ions passing through gaseous atomic hydrogen. The basic rate equations for the charge-state fractions of incident ions are obtained under a condition of local balance (the charges are locally in equilibrium between electron loss and capture processes). The average equilibrium charges of various incident heavy ions in atomic hydrogen gas, their range and the stopping powers of atomic hydrogen for them are obtained.

When an ion of charge q collides with target atoms, the ion may lose or capture one or more electrons in the ion-atom collisions. Let $\phi_q(v_i)$ denote the charge-state fraction of ions with charge q and velocity v_i. It is normalized as $\sum_q \phi_q = 1$ and the average equilibrium charge is given by

$$\bar{q}(v_i) = \sum_{q=1}^{Z} q \cdot \phi_q(v_i) \tag{1}$$

We consider the case where the ion moves by a length dx along its trajectory in a material containing N atoms per unit volume. If we ignore the contribution of excited states of the ion, the change in the fraction $d\phi_q$ can be written in terms of the charge-exchange cross sections $\sigma_{q,p}$ from charge state q to p as

$$\frac{d\phi_q(v_i)}{Ndx} = \sum_{p=0}^{Z} \left[\phi_p(v_i)\,\sigma_{p,q}(v_i) - \phi_q(v_i)\,\sigma_{q,p}(v_i) \right]$$

$$+ \text{(contributions from Auger and autoionizing processes).} \tag{2}$$

Ignoring the multiple-charge-exchange processes, we can obtain the following rate equations:

$$\frac{d\phi_q(v_i)}{Ndx} = \sum_{p=0}^{Z} \left[\phi_p(v_i)\,\sigma_{p,q}(v_i) - \phi_q(v_i)\,\sigma_{q,p}(v_i) \right] \tag{3}$$

with $p = q \pm 1$ and $0 \leqq p \leqq Z$.

If we assume that $d\phi_q(v_i)/dx = 0$ (local balance approximation) for all q, and introduce p_q defined by $P_q = \phi_q/\phi_{q-1}$, we can obtain equations

$$\frac{\sigma_{q-1,q}}{\sigma_{q,q-1}} = p_q \tag{4}$$

and

$$\phi_q(v_i) = \prod_{j=1}^{q} p_j \Big/ \left[1 + \sum_{q=1}^{Z} \prod_{j=1}^{q} p_j \right] \tag{5}$$

We need the information on $\sigma_{q,\,q\pm1}\,(v_i)$ for electron loss and capture processes to obtain the values of $\phi_q(v_i)$. We estimate the cross sections for the processes

$$X^{(q-1)+} + H \rightarrow X^{q+} + e + H(\text{all states}) \tag{6}$$

and

$$X^{q+} + H \rightarrow X^{(q-1)+} + H^{+} \tag{7}$$

For the electron loss process (6) we made an assumption that $\sigma_{q-1,\,q}$ may be approximated by that for the collision of a hydrogen-like ion with an atomic hydrogen $\sigma_{Z-1,\,Z}$. For the process (6) we scaled cross sections calculated by Shirai et al.[5)] based on the binary encounter approximation (BEA). The cross sections for electron capture process (7) were obtained from the scaled results[6)] based on the calculation by the unitarized-distorted-wave (Born) approximation (UDWA).[7)] If the momentum distribution of the outermost electrons in the incident ion is similar to that of the 1s-wave function of a hydrogen-like ion, $\phi_q(v_i)$ can be scaled in terms of v_i.

In Fig. 1 we show the calculated $\phi_q(v_i)$ for Ne ions in H and experimental values for Ne ions in H_2.[8)] The average equilibrium charges $\bar{q}(v_i)$ are displayed in Fig. 2 in the energy range $1.5 \times 10^3 \sim 9.5 \times 10^7$ eV/amu, and are compared with those in Ref. 8 . We also obtained the LET and ranges using the Bethe formula with empirical effective charges based on the numerical results of our calculations. Figure 3 shows the calculated deposi-

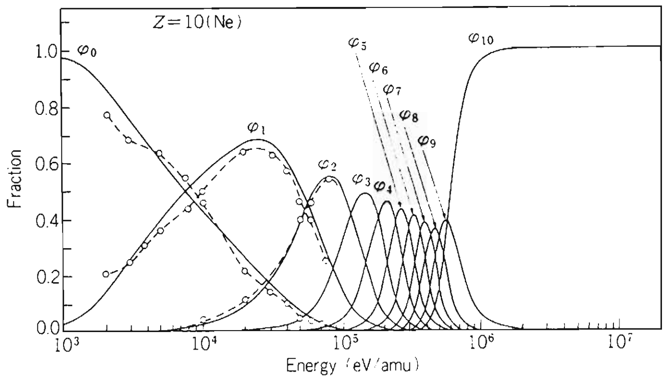

Fig. 1. Charge-state fractions $\phi_q(v_i)$ for Ne ions in H gas, calculated as a function of projectile energy per nucleon. Dashed curve indicates experimental values for ϕ_1 , and ϕ_2 in H_2 [8]

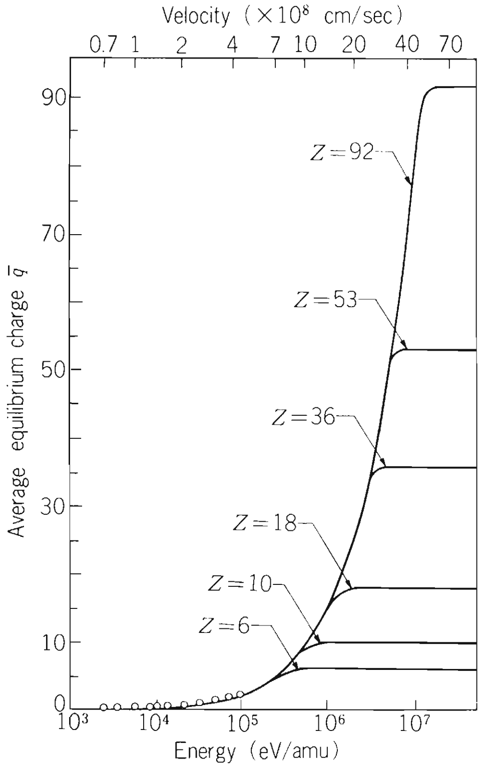

Fig. 2. Average equilibrium charges $\bar{q}$ of C , Ne, Ar, Kr, I, and U ions passing through H gas, calculated as a function of incident beam velocity (upper scale) or of energy per nucleon (lower scale). Open circles show experimental results for $Ne^{q+} + H_2$ [8]

tion profile for the Ne ion. The calculated Bragg curve can be compared with experimental data.[9]

As one of our research work series we are now carrying out the following two calculations. The first one is the calculation of the loss cross sections for arbitrary q by a BEA formula using Thomas-Fermi statistical model for the momentum distribution of electrons in the projectile. This will give information on the efffects of the momentum-distribution difference between hydrogen(1s)-like and Thomas-Fermi density functions. The second one is the calculation of $\phi_q(v_i)$ without the local balance assumption. When projectiles enter a target with a charge far from the average equilibrium value, they will travel a considerable distance before charge-state equilibrium is attained. We are obtaining $\phi_i(q)$'s and $q_i(v)$'s as functions of the distance x the ions have traveled in the medium.

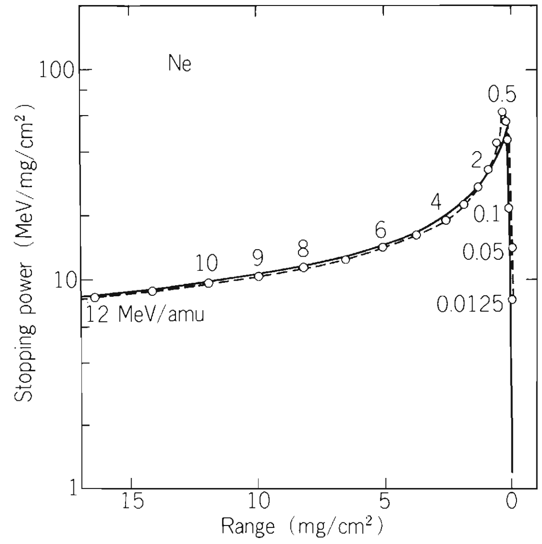

Fig. 3. Relation between stopping power and range for Ne ions in H gas (solid line). Open circles indicate experimental values[9], plotted against the incident energy per nucleon (connected by broken line).

References

1) H. D. Betz: Rev. Mod. Phys., 44, 465 (1972).
2) T. A. Mehlhorn: J. Appl. Phys., 52, 6522 (1981).
3) J. Meyer-ter-Vehn and N. Metzler: Target Design for Heavy Ion Beam Fusion (Max-Planck-Institut für Quantenoptik, Garching bei München, July 1981), p. 15.
4) S. Karashima and T. Watanabe: Jpn. J. Appl. Phys., 22, 895 (1983).
5) T. Shirai, K. Iguchi, and T. Watanabe: J. Phys. Soc. Jpn., 42, 238 (1977).
6) Y. Kaneko et al.: Cross Sections for Charge Transfer Collisions Involving Hydrogen Atoms (Institute of Plasma Physics, Nagoya University, Nagoya, IPPJ-AM-15, 1980).
7) H. Ryufuku and T. Watanabe: Phys. Rev., A18, 2005 (1978); ibid., 20, 1828 (1979).
8) A. B. Wittkower and H. D. Betz: Atom. Data, 5, 113 (1973).
9) L. C. Northcliffe and R. F. Schilling: Nuclear Data Sec. A, 7, 234 (1970).

III-2-4. Transitions of Molecules between High-Angular-Momentum States

I. Shimamura and A. C. Roy

High-energy charged particles and ionizing radiation penetrating matter normally produce secondary electrons of tens of electron volts and even higher in energy. These electrons give up their energy to the matter in collisions with the constituent atoms or molecules, and are eventually thermalized. The energy distribution of the secondary electrons in matter is of crucial importance in the study of radiation physics and chemistry. For molecular matter the energy distribution is determined by the cross sections for electronic, vibrational, and rotational excitations of molecules by electrons. Among these processes rotational transitions play a decisive role in determining the low-energy portion of the energy distribution of secondary electrons.

The cross sections for state-to-state rotational transitions, rather than the averaged cross section, are extremely difficult to measure directly, because the energy resolution of electron spectrometers is too low to resolve rotational lines, which are closely spaced, in the energy-loss spectra. Reliable theoretical calculations are too cumbersome to carry out for many different initial and final rotational states; molecules are normally distributed among many different rotational states. One of the present authors, however, has noted that most molecules occupy high-lying rotational states J, and has derived simple formulas for the cross sections for transitions of linear and spherical-top rotators from high rotational states J to high rotational states $J' = J \pm \Delta J$.$^{1)}$ The main virtue of these formulas is that they give the cross sections for the transitions $J \rightarrow J \pm \Delta J$ for any high J in terms of a single unknown parameter independent of J. The present work is a generalization of these formulas for transitions of symmetric-top rotators.

Main results for the transitions of linear rigid rotators are first summarized. Assume that the collision time is much shorter than the rotational period, which is of the order of $\sim 10^{-12}$s. This assumption is equivalent to the assumption that the electron temperature be higher than the rotational temperature. Without any further approximations it follows for $J \gg |\Delta J|$ that$^{1)}$

$$d\sigma(J \rightarrow J \pm \Delta J)/d\omega = C(|\Delta J|) \times \{1 \pm (\Delta J/2)J^{-1} + O(J^{-2})\}. \tag{1}$$

The two cross sections $d\sigma(J \rightarrow J \pm \Delta J)/d\omega$ plotted versus J approach a value $C(|\Delta J|)$ common to both as $J \rightarrow \infty$, one from above and the other from below in a manner nearly symmetric with respect to the horizontal line that aims at the limiting value. The sum

$$\sum_{J'=J\pm\Delta J} d\sigma(J \rightarrow J')/d\omega = 2C(|\Delta J|)\{1 + O(J^{-2})\} \tag{2}$$

of the two cross sections is nearly independent of J for high J. This 'partial-sum' rule is to be compared with Drozdov's sum rule$^{2)}$

$$\sum_{\text{all } J'} d\sigma(J \rightarrow J')/d\omega = (\text{constant independent of J}). \tag{3}$$

Because the rotational energy $E_r(J)$ is $BJ(J+1)$, B being the rotational constant, the transition energies $\Delta E(J \rightarrow J \pm \Delta J)$ for a fixed value of ΔJ are linear in J. Therefore, the cross sections $\Delta E(J \rightarrow J \pm \Delta J) d\sigma(J \rightarrow J \pm \Delta J)/d\omega$ for energy loss by the electron increase with J as $\underset{\sim}{\propto} J$. The sum

$$\sum_{J'=J\pm\Delta J} \Delta E(J \rightarrow J') d\sigma(J \rightarrow J')/d\omega = 4B(\Delta J)^2 C(|\Delta J|)\{1 + O(J^{-2})\} \tag{4}$$

of the two energy-loss cross sections, however, is nearly constant for high J.$^{1)}$ This is to be compared with the recently proven sum rule$^{3),4)}$

$$\sum_{\text{all } J'} \Delta E(J \rightarrow J') d\sigma(J \rightarrow J')/d\omega = (\text{constant independent of J}) \tag{5}$$

for the mean energy-loss cross section.

Equations (1) through (5) are, in fact, applicable not only to electron scattering but also to atom scattering, ion scattering, photoabsorption, and photoionization in the sudden approximation..

We are generalizing these results for rigid symmetric-top rotators. They have a well-defined quantum number K ($-J \leq K \leq J$) for the projection of the rotational angular momentum onto the body-fixed symmetry axis. Some of the formulas we have proved are

$$d\sigma(JK \rightarrow JK')/d\omega = C(|\Delta J| = 0, |\Delta K|)\{1 + O(J^{-2})\} \tag{6}$$

for transitions with $\Delta J = 0$,

$$d\sigma(JK \rightarrow J \pm \Delta J, K)/d\omega = C(|\Delta J|, \Delta K = 0) \times \{1 \pm (\Delta J/2)J^{-1} + O(J^{-2})\} \tag{7}$$

for transitions with $\Delta K = K' - K = 0$, and

$$d\sigma(JK\rightarrow J \pm \Delta J, K+1)/d\omega = C(|\Delta J|, \Delta K = 1)$$
$$\times [1 \mp \Delta J(2K+\tfrac{1}{2}) J^{-1} \pm C'(|\Delta J|)$$
$$\times \{(2K+1)/\Delta J\} J^{-1} + O(J^{-2})] \qquad (8)$$

for transitions with ΔK = 1.

In all of these cases the partial-sum rules

$$\sum_{J'=J\pm\Delta J} d\sigma(JK\rightarrow J'K')/d\omega$$
$$= 2C(|\Delta J|, \Delta K)\{1 + O(J^{-2})\} \qquad (9)$$

and

$$\lim_{J\rightarrow\infty} \sum_{J'=J\pm\Delta J} \Delta E(JK\rightarrow J'K')\, d\sigma$$
$$\times (JK\rightarrow J'K')/d\omega = (\text{constant}) \qquad (10)$$

immediately follow.

Equations (1) and (6) – (8) are useful also in analyzing rotationally unresolved energy-loss spectra of electrons to extract state-to-state rotational transition cross sections.[4],[5]

References

1) I. Shimamura: Phys. Rev., A28, 1357 (1983).
2) S. I. Drozdov: Sov. Phys. JETP, 1, 591 (1955); ibid., 3, 759 (1956).
3) I. Shimamura: Phys. Rev., A23, 3350 (1981).
4) I. Shimamura: Chap. II in Electron-Molecule Collisions, (eds. I. Shimamura and K. Takayanagi), Plenum, New York p. 89 (1984).
5) I. Shimamura: in Wavefunctions and Mechanisms from Electron Scattering Processes, (ed. F. A. Gianturco), Plenum, New York (1984) in press.

III-2-5. Beam-Foil Spectroscopy

K. Sato, S. Tsurubuchi, K. Ando, H. Kumagai,
S. Kohmoto, T. Tonuma, and Y. Awaya

One of the unique features of beam-foil experiments lies in the point that we can make directly time resolved studies of decay processes of excited species after leaving a foil target. The time t of a decay process of the excited state directly corresponds to the distance from the foil.

We have started a beam-foil experiment by using of the linear accelerator (RILAC) in order to carry out, firstly, a systematic measurement of mean life time of the excited states of highly ionized projectiles which will play an important role in, for example, high temperature fusion plasmas, high density laser plasmas, astrophysics and so forth. We have also much interest in some dynamic feature characteristic of beam-foil interactions.

As a first step, we have tried to determine the relative sensitivity of our detection system including a grazing incidence monochromator and a channel electron multiplier (Ceratron) with a secondary electron covertor. Some preliminary results are reported in this paper.

A detail of our experimental set up is described elsewhere.$^{1),2)}$ Briefly it consists of a vacuum chamber and a grazing incidence monochromator. The chamber contains a disk on which 17 carbon foils are mounted. A broken foil can be changed to a new one without breaking vacuum condition. The carbon foil disk itself can be driven along the ion beam axis as long as 50 cm, and the accuracy of setting the disk position is within ± 25 μm. The monochromator used is a grazing incidence type of Nikon-McPherson (model 247) which has the radius of the Rowland circle of 2 m and an incidence angle of 86 degrees. Its entrance slit specially designed can approach the ion beam as close as 5 mm to have enough spacial resolution of beam length in life time measurements. Figure 1 shows, as an example, line spectra of nitrogen ion excited by a carbon foil of 10 μg/cm^2 with incident energy of 14.8 MeV.

The output signal for the i → j transition I_{ij}^{s} from the detection system is given by

$$I_{ij}^{s} = I_{ij} \cdot S(\lambda_{ij}), \qquad (1)$$

where I_{ij} is the intensity of the light due to the j → j transition entering into the monochromator, $S(\lambda_{ij})$ is the overall sensitivity of the detection system. The $I_{ij}(\lambda)$ is related to the branching ratio by

$$I_{ij} = N_i \frac{A_{ij}}{\sum\limits_{k<i} A_{ik}} \qquad (2)$$

where N_i is the population of the level i of the projectile after foil excitation, $\sum\limits_{k<i} A_{ik}$ is the inverse of

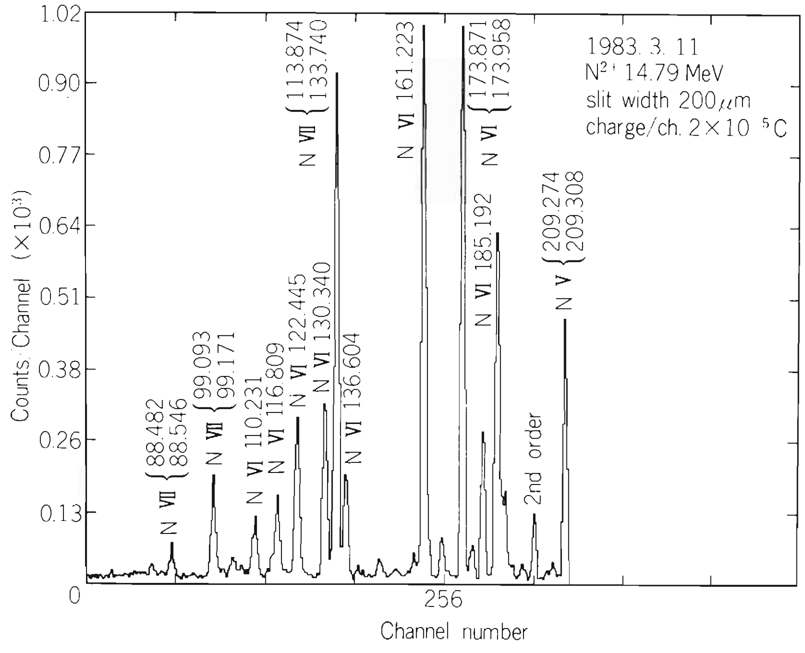

Fig. 1. Line spectra of nitrogen ion excited by a carbon foil of 10 μg/cm^2 with the energy of 14.8 MeV.

the mean life time of the level i, and A_{ij} is the spontaneous transition probability for the i → j transition. Therefore, if we choose two lines originating from the level i, the ratio of their intensities is given by

$$\frac{I_{ij}}{I_{ik}} = \frac{A_{ij}}{A_{ik}} \tag{3}$$

Accordingly, we have

$$\frac{S(\lambda_{ij})}{S(\lambda_{ik})} = \frac{I^{s}_{ij}}{I^{s}_{ik}} \cdot \frac{A_{ik}}{A_{ij}} \tag{4}$$

In the present work, the intensity measurements were made for the following transitions of N V which are listed in Table 1.

Table 1. Observed transitions of N V.

Transition	Wavelength (Å)	A_{ki}*
3p $^2P^o$ – 4s ^2S	777.712, 778.172	2.41
2p $^2P^o$ – 4s ^2S	190.155, 190.249	3.42
3p $^2P^o$ – 4d ^2D	713.518, 713.860	4.30
2p $^2P^o$ – 4d ^2D	186.063, 186.149	14.3
3s ^2S – 4p ^2P	628.874, 628.744	1.55
2s ^2S – 4p $^2P^o$	162.564, 162.556	5.86

* A_{ki} is given in units of 10^9 sec^{-1}.

The values of A_{ki} are calculated from the relation

$$A_{ki} = 6.670 \times 10^{15} / \lambda^2 \cdot g_i / g_k \cdot f_{ik} \quad (\lambda \text{ in Å}) \tag{5}$$

using the multiplet f-values given by Martin and Wiese.[3)]

In Table 2 we show the obtained relative sensitivities of the detection system including the grazing incidence monochromator as well as the Celatron with a secondary convertor coated with cesium iodine.

It should be noted here that the accuracy of S(λ) in Table 2 depends only on the accuracy of the values of A_{ki} as seen from Eqn. (4). The value of $\sum_{j<i} A_{ij}$ for the 4s → np transitions of N V is, as is calculated from Table 1, equal to 5.83×10^9 s^{-1}, which shows nice agreement with the measured value of 5.8×10^9 s^{-1} of Buchet and Buchet-Poulizac.[4)] On the other hand, as for the 4d → np transitions, the calculated value of $\sum_{j<i} A_{ij}$ is 1.86×10^{10} s^{-1} from the table of Martin and Wiese, while different experiments give 1.58×10^{10} s^{-1}, 1.54×10^{10} s^{-1}, and 8.33×10^9 s^{-1} for the corresponding value.[4)-6)] As shown in Table 2, the S(λ) at 713 Å(4d → 3p) is roughly 15 % too low from the averaged value between S(629 Å) (4p → 3s) and S(777 Å) (4s → 3p). This may be attributed to an inaccuracy in the theoretical values of ΣA_{ij}; notice that the experimental $\sum_{j<i} A_{ij}$ value of 1.58×10^{10} s^{-1} for the 4d level of N V is just 15 % lower than the corresponding theoretical values of 1.86×10^{10} s^{-1}.

Table 2. Observed relative sensitivities.

Wavelength (in Å)	S(λ)*
162	1.05
186	1.02
190	1.00
629	0.079
713	0.068
777	0.084

* The relative sensitivity at 190 Å is normalized to unity.

References

1) K. Ando and K. Mori: RIKEN Accel. Progr. Rep., 15, 85 (1981).
2) K. Ando, T. Tonuma, S. Kohmoto, S. Tsurubuchi, and K. Sato; Atomic Coll. Res. in Japan, 9, 94 (1983).
3) G. A. Martin and W. L. Wiese: J. Phys. Chem. Ref. Data, 5, 537 (1976).
4) J. P. Buchet and M. C. Buchet-Poulizac: J. O. S. A., 64, 1011 (1974).
5) L. Heroux: Phys. Rev., 153, 156 (1967).
6) J. P. Buchet, M. C. Poulizac, and M. Carré: J. O. S. A., 62, 623 (1972).

III-2-6. Optical Detection of Atomic Spin Polarization Produced by Beam-Foil Interaction

S. Kohmoto, M. Ishihara, T. Nomura,
and Y. Gono

For an automatic measurement of polarization of light in tilted foil experiment,$^{1),2)}$ we have constructed an apparatus which permits with the aid of a step-motor drive to rotate one of the optical elements (λ/4 plate or linear polarizer). This apparatus is controlled by a micro-computer and the pulse counts from the photomultiplier are accumulated in the PERKIN ELMER computer in MCS(multi-channel scaler) mode.

Using this system, the relative Stokes parameter S/I for the N V (494 nm) line was measured for a single tilted foil with the tilt angle$^{2)}$ $\phi = 45°$ as a function of the incident energy of the N-ions. The ^{14}N ion beam was produced by the Linac. By rotating the λ/4 plate every 2 or 5 seconds, a pair of measurements of light intensity at $\beta = +45°$ and $-45°^{2)}$ were performed so that a S/I value was obtained every 4 or 10 seconds. After the whole measurements, these values were averaged over to deduce a final S/I value. Thus it was possible to minimize an additional error due to the beam path fluctuation during the measurement.

Figure 1 shows our results as well as those obtained by Randolph et at.$^{3)}$ (tilted foil method; TFM) with $\phi = 60°$ and by Winter et al.$^{4)}$ (grazing incidence method; GIM). It seems that the S/I of this line decreases at high energy region when a constant tilt angle is used. Talk et al$^{5)}$ contend that the generation mechanism of the atomic polarization is same for the two methods: the GIM is the extreme case of the TFM with $\phi \simeq 90°$. Thus it will be interesting to measure the ϕ dependence of S/I at $E_N \simeq 5$ MeV where two methods give a same S/I value as well as at higher energy region for the purpose of clarifying the generation mechanism.

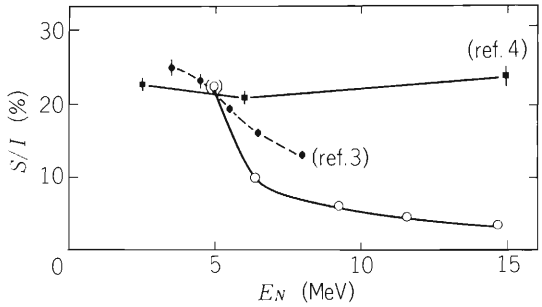

Fig. 1. Relative Stokes parameter S/I obtained by us (open circles; tilted foil method) as well as by Randolph et al.$^{3)}$ (full circles; tilted foil method) and by Winter et al.$^{4)}$ (full squares; grazing incidence method). Our result at $E_N = 5$ MeV was obtained with a slightly different arrangement of apparatus.

References
1) S. Kohmoto, M. Ishihara, T. Nomura, Y. Gono, and M. Sasagase: RIKEN Accel. Progr. Rep., 15, 86 (1981).
2) S. Kohmoto, M. Ishihara, T. Nomura, Y. Gono, and Y. Itoh: ibid., 16, 94(1982).
3) W. L. Randolph et al.: Hyper. Int., 7, 279 (1979).
4) H. Winter et al.: ibid., 8, 261(1980).
5) N. H. Talk et al.: Phys. Rev. Lett., 47, 487 (1981).

III-2-7. K X-Rays from Ar-Ions Passing through Foils (I)

Y. Awaya, T. Kambara, M. Kase, H. Kumagai, J. Urakawa,
H. Shibata, T. Matsuo, J. Takahashi, and M. Namiki

We have studied the dependence of multiple inner-shell ionization of Ar ions passing through various target foils on the atomic number of target element and we had previously reported preliminary results.$^{1)}$ We report here the results obtained thereafter.

The experimental conditions were the same as in the previous work,$^{1)}$: the energy of incident Ar^{4+} ions was 33.6 MeV and K X-rays were measured by using a broad range X-ray crystal spectrometer.$^{2)}$ In the present work, Ar K X-rays from the target of Nb, Cd, Nd, Ho, Tb, and W were measured in addition to the sixteen elements ranging from C to Au reported previously. The thickness of the foils used in the present work was between about 0.9 mg/cm^2 and 2.6 mg/cm^2 except for Nd and W whose thicknesses were 25 μm and 50 μm, respectively. As discussed previously,$^{1)}$ most of Ar K X-rays detected can be regarded to be emitted within first 1 mg/cm^2 of the target.

We obtained the X-ray spectrum of energy higher than about 3.3 keV (Cf. Fig. 1 in Ref. 1) and found that the peaks observed between about 3.17 keV and 3.3 keV, which we had assigned to Kβ satellites and Kα hypersatellites in the previous report, should all be attributed to Kα hypersatellites. The Kβ satellites were observed at energy higher than 3.3 keV and this will be described elsewhere in this volume.$^{3)}$

The values of the ionization probability of L-shell electrons, P_L, are obtained from the spectra of Kα satellites by assuming that the cross section of simultaneous single K-shell and multiple(n) L-shell ionization is given by a binomial distribution of Eqn. (1) in Ref. 1. The P_L values thus obtained inclding previous data are shown as functions of the atomic number of target elements, Z_2 in Fig. 1(a). The P_L values show an oscillatory behaviour against Z_2 as was pointed out previously.$^{1)}$

The charge of Ar ions are estimated to be between 10 and 12 according to the work by Baudient-Robinet.$^{4)}$ In Fig. 1(b), binding energies of orbital electrons of the target element and those of 2p electron of Ar^{10+} and Ar^{12+} are plotted against Z_2. Comparing (a) and (b) of Fig. 1, we find that minima of P_L correspond to the atomic number Z_2 where the binding energy of orbital electons of target atom matches to that of 2p electron of Ar ions. This implies that when the level matching occurs, the electron transfer cross section from the target to the 2p hole of Ar ions becomes large.

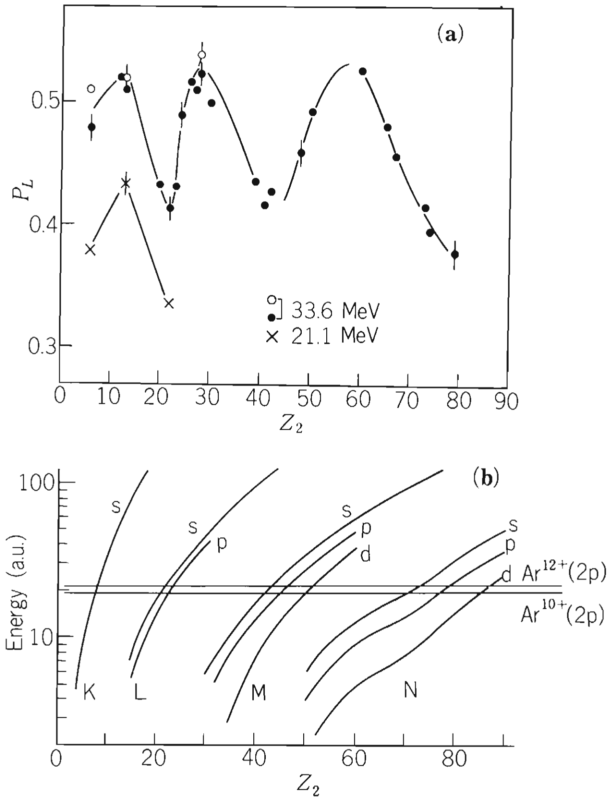

Fig. 1. (a) The plot of ionization probability of L-shell electron P_L vs. the atomic number of target Z_2. The open and closed circles show the values of P_L for 33.6 MeV Ar ions and the former corresponds to the value for thinner target foil (Ref. 1). The crosses show those for 21.1 MeV Ar ions. (b) The binding energy of each orbital electrons of the target element. The binding energies of the 2p electron of Ar^{10+} and Ar^{12+} are also shown.

We also obtained preliminary values of the intensity ratio of Kα hypersatellite X-rays and satellite X-rays, $I(K\alpha^h)/I(K\alpha)$, for each target element and plotted the results as a function of Z_2 in Fig. 2. The value of $I(K\alpha^h)/I(K\alpha)$ oscillates against Z_2 and the oscillation is out of phase with that of P_L. When we estimate the values of $I(K\alpha^h)/I(K\alpha)$, we should take into account the change of detection efficiency due to the change in X-ray energy, because the K absorption edge of argon gas, which is the main component of counter gas (90% Ar and 10% CH_4), is 3.203 keV. As to the Kα satellites, the change of the detection efficiency from peak to peak is so small that it does not give rise to large errors even if we assume that the efficiency is constant for all of them whereas the detection efficiency changes suddenly at the absorption edge for Kα hypersatellites. We show, however, the result without any correction in Fig. 2, since it is difficult to make the correction at the present stage.

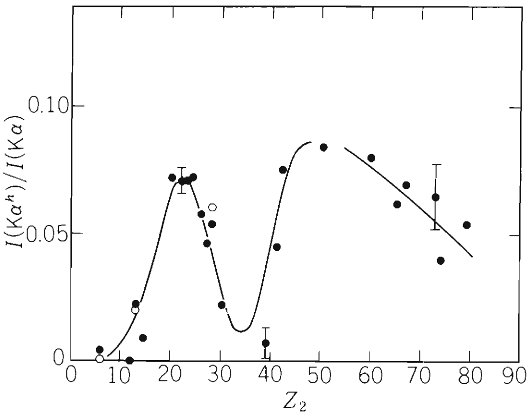

Fig. 2. The values of intensity ratio of Kα hypersatellites and satellites $I(K\alpha^h)/I(K\alpha)$ vs. the atomic number of target Z_2.

We consider that the errors, especially the systematic ones, may be large but the tendency of the oscillatory behaviour will not change much because the main part of the Kα hypersatellites is distributed at energy higher than the K absorption dege of Ar.

This oscillation of $I(K\alpha^h)/I(K\alpha)$ will be explained by the rotaional coupling between molecular orbitals formed by a projectile and a target atom during collision. In Fig. 3, some of the energy level correlation diagrams for different collisional partners and Ar ions are shown in the case where the charge of Ar is assumed to be 10+. When the Ar ions collide with C target, there is no possibility to transfer the 1s electron of Ar ion to its 2p holes, whereas for the Ca target this transition (electron promotion via a quasi-molecule) is possible through 2pπ – 2pσ coupling and the intensity of hypersatellites relative to that of satellites increases. The same discussion can be given to the target element Zn and Sn. For Sn target, the rotaional coupling between 3dπ – 3dσ plays some role.

The electron promotion from 1s to 2p in Ar ions too has effects on the P_L values. This makes the P_L values to be reduced and $I(K\alpha^h)/I(K\alpha)$ value to be increased. The observed behaviour of P_L vs. Z_2, therefore, is considered to originate mainly in the level matching and partly in the rotational coupling between molecular orbitals.

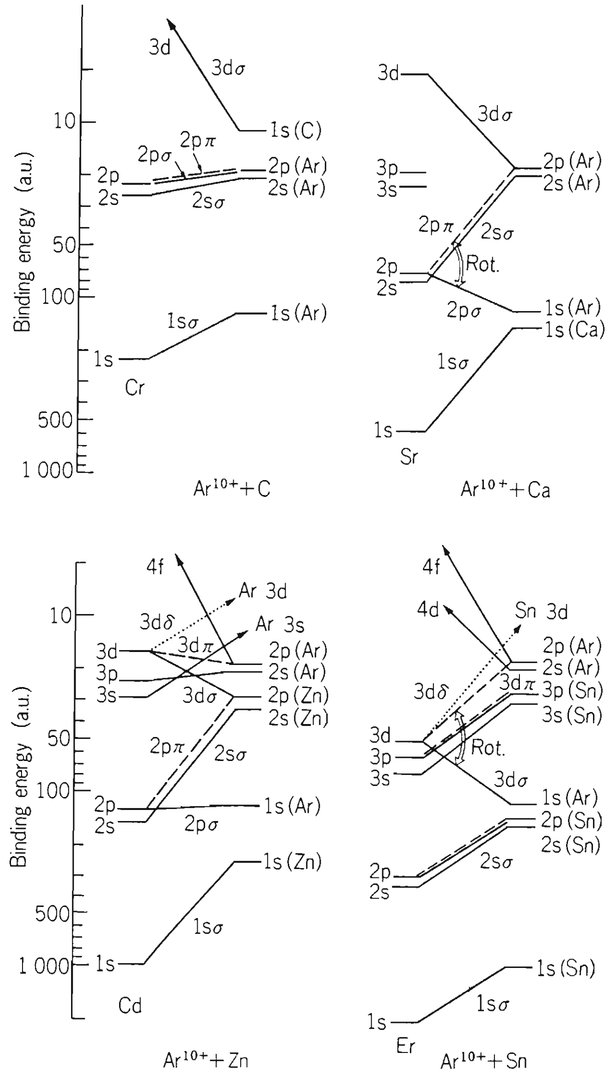

Fig. 3. The energy level correlation diagrams between an Ar^{10+} ion and target atoms (C, Ca, Zn, and Sn).

References

1) Y. Awaya, T. Kambara, M. Kase, H. Kumagai, J. Takahashi, J. Urakawa, T. Matsuo, and M. Namiki: RIKEN Accel. Progr. Rep., 16, 72 (1982).
2) A. Hitachi, H. Kumagai, and Y. Awaya: Nucl. Instr. Meth., 195, 631 (1982).
3) T. Kambara, Y. Awaya, M. Kase, H. Kumagai, S. Shafroth, H. Shibata, and T. Tonuma: p.51 in this report.
4) Y. Baudinet-Robinet: Phys. Rev. A, 26, 62 (1982).

III-2-8. K X-Rays from Ar-Ions Passing through Foils (II)

T. Kambara, Y. Awaya, M. Kase, H. Kumagai,
S. M. Shafroth, H. Shibata, and T. Tonuma

We report on the measurements of the K_β X-rays from Ar-ions passing through various foil targets with energy of 33.6 MeV. The K_β X-rays are emitted by electronic transitions from shells outer than the L-shell to the K-shell of Ar-ions. The equilibrium charge state of Ar ions in target is about 10+ – 12+ and there should be no M-shell electrons if the ions are not excited. However the ions can be highly excited by collisions with the target atoms. The measurement of the K_β X-rays gives us information about the population of outer shell electrons in the ions which have a hole in the K-shell and multiple holes in the L-shell.

The experimental apparatus with a broad range crystal spectrometer was the same as that reported elsewhere$^{1)}$ except that the Bragg angle of the diffraction crystal Ge(111) was changed from 75° to 67° in order to look at higher energy X-rays. The targets were C, Al, Ti, V, Cr, Ni, Mo, Ta and Au. The X-ray energy was calibrated by the L X-rays of indium excited by photons.

Some examples of the X-ray spectra are shown in Fig. 1. The K_β satellite X-rays are seen in the center of the spectra and the high energy part of the K_α hypersatellite X-rays are seen at their left hand side. These X-rays are well separated, in contrast to the case of Ar-target bombarded by 6 MeV/amu N-ions where the K_β X-rays and the K_α hypersatellite X-rays are mixed up in the spectrum.$^{2)}$ The K_β X-rays are resolved into each satellites in the cases of Al and Ti targets, but not in the case of Ni target.

The energy of each K_β satellite is estimated by extrapolating those of the K_β satellites with L-hole number smaller than 4, which was measured by Awaya et al.$^{3)}$ By comparing the present X-ray spectra with these energies, the number of L-shell holes for the maximum X-ray yield among the K_β satellites is estimated to be between 4 and 6. This is larger than the number of average L-shell holes of the K_α satellites which is between 3 and 4.$^{1),4)}$ Therefore the K_β X-rays are supposed to be emitted from higher ionized ions than the K_α X-rays. The X-ray energy for the peak with the maximum X-ray yield among the K_β satellites changes with the target atomic number in the same way as that of the K_α satellites. Therefore the effect of the level matching on the L-shell ionization probability $P_L$$^{4)}$ is also seen in the K_β X-ray spectra.

The intensity ratio between K_β satellite X-rays and K_α hypersatellite X-rays depends significantly on the atomic number of the target. For example, the K_β satellite X-rays are stronger than the K_α hypersatellite X-rays for the Al target, but this situation is inverted for the Ti target. The intensity ratio between K_α satellite X-rays and K_α hypersatellite X-rays is reported to be also dependent on the target species.$^{4)}$ We are planning to make further measurement with wider energy range for the ratio of the K_α satellite, K_α hypersatellite and K_β satellite X-rays.

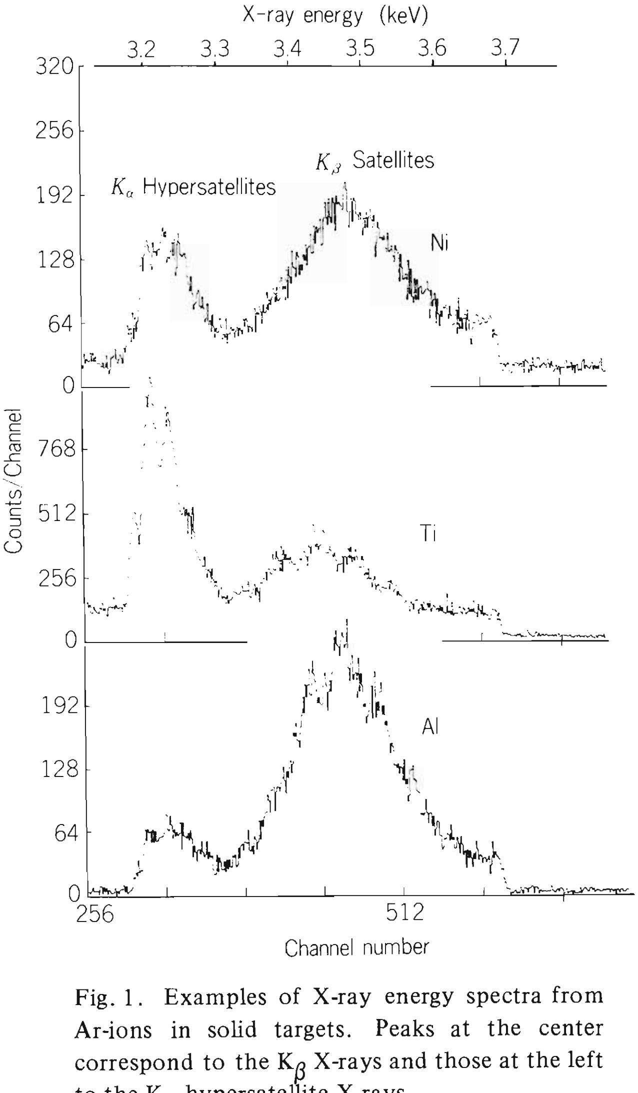

Fig. 1. Examples of X-ray energy spectra from Ar-ions in solid targets. Peaks at the center correspond to the K_β X-rays and those at the left to the K_α hypersatellite X-rays.

References

1) Y. Awaya, T. Kambara, M. Kase, H. Kumagai, J. Takahashi, J. Urakawa, T. Matsuo, and M. Namiki: RIKEN Accel. Progr. Rep., 16, 72 (1982).
2) T. Tonuma, Y. Awaya, T. Kambara, H. Kumagai, I. Kohno, and S. Özkök: Phys. Rev. A, 20, 989 (1980).
3) Y. Awaya, M. Akiba, T. Katou, H. Kumagai, Y. Tendow, K. Izumo, T. Takahashi, A. Hashizume, M. Okano, and T. Hamada: IPCR Cyclotron Progr. Rep., 10, 78 (1976).
4) Y. Awaya, T. Kambara, M. Kase, H. Kumagai, J. Urakawa, H. Shibata, T. Matsuo, J. Takahashi, and M. Namiki: p. 49 in this report.

III-2-9. Au L_3-Subshell Alignment Induced by Heavy-Ion Impact

J. Takahashi, M. Namiki, J. Urakawa, H. Shibata, T. Matsuo,
H. Kumagai, M. Kase, T. Kambara, and Y. Awaya

We have measured the angular distribution of Au L_ℓ X-rays ($M_1 - L_3$ transition) produced by heavy-ion impact to study the projectile atomic number dependence of L_3-subshell alignment.

The projectiles N^{2+}, Ar^{4+}, Kr^{8+}, and Xe^{9+} were accelerated by the linear accelerator, and were momentum analyzed. The energies of the N, Ar, and Kr-ions were 0.87 MeV/amu and that of the Xe-ions was 0.84 MeV/amu. The dimension of the beam spot on the target was 1 mm in width and 3 mm in height. The target Au was evaporated on a 4 μm thick Mylar foil. The thickness of the Au was about 0.2 mg/cm^2. The emitted X-rays were detected at angles (θ) of 25°, 45°, 70°, 90°, 110°, 135°, and 155° by a Si(Li) detector, the energy resolution of which was 230 eV FWHM at 6.4 keV. The distance between the beam spot and the Be window of the Si(Li) detector was about 20 cm and the diameter of the Si(Li) detector was 6 mm, so that the angular resolution was 1.8°. The angle between the target surface and the beam was 147.5° for forward angle measurements and 32.5° for backward ones. Spectra of X-rays were monitored by another Si(Li) detector placed at a fixed angle of $\theta = -90°$.

Spectra of Au L X-rays obtained at $\theta = 90°$ are shown in Fig. 1, where the projectile K X-rays are also seen in the case of Kr impact.

It is expected that the radiation originating from the electronic transitions to the L_3-subshell is anisotropic. This anisotropy reflects the alignment of the L_3 subshell

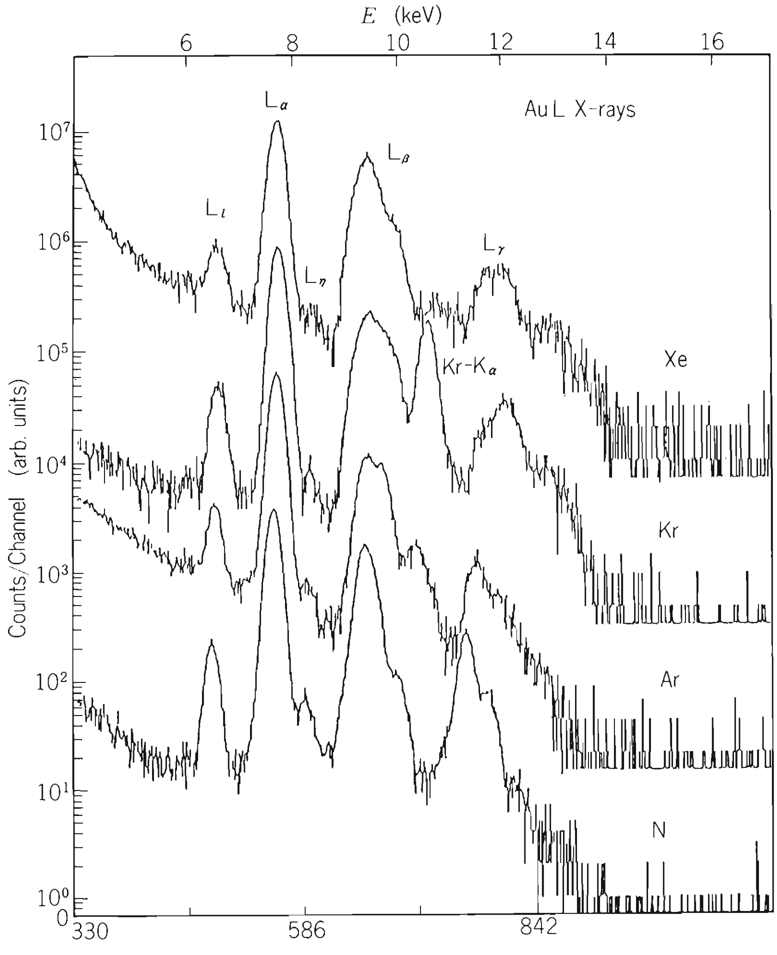

Fig. 1. Au L X-ray spectra induced by N, Ar, Kr, and Xe-ions with the same velocity.

which is caused by different population of vacancies among magnetic substates with $|m_j| = 3/2$ and $1/2$. The anisotropic angular distribution of the L_ℓ line ($M_1 - L_3$ transition) has been observed by Jitschin et al.[1] The angular dependence of the emitted dipole radiation $I(\theta)$ is expressed as

$$I(\theta) = (I_0/4\pi)\{1 + bP_2(\cos\theta)\} \qquad (1)$$

when the outgoing projectiles are not detected, where I_0 is the total intensity, $P_2(\cos\theta)$ the Legendre polynomial of the second degree and b the anisotropy parameter. The parameter b is related to the L_3-subshell alignment coefficient A_{20} by a formula $b = \kappa\alpha A_{20}$. The value of the coefficient α is assumed to be 0.5 according to Berezhko and Kabachnik[2] and that of the dealignment factor κ to be unity. The A_{20} is given by

$$A_{20} = \left(\sigma_{L3}(3/2) - \sigma_{L3}(1/2)\right) / \left(\sigma_{L3}(3/2) + \sigma_{L3}(1/2)\right), \qquad (2)$$

where $\sigma_{L3}(3/2)$ and $\sigma_{L3}(1/2)$ denote the ionization cross sections corresponding to the magnetic substates of $|m_j| = 3/2$ and $1/2$, respectively. In Fig. 2 the intensities of the L_ℓ and L_α X-rays induced by N and Kr-ion impact are shown as a function of $\cos^2\theta$. The intensity of the L_ℓ X-rays depends on θ, whereas that of the L_α X-rays is almost independent of it. The anisotropy of the L_ℓ X-rays induced by the N-ion impact is greater than that induced by the Kr-ion impact. From these angular distribution data, the values of A_{20} are deduced by using the formula (1). They are plotted in Fig. 3 as a function of the projectile atomic number Z_1. For comparison the data obtained by Jitschin et al.[1] for various projectiles with incident energy ranging from 0.74 MeV/amu to 1 MeV/amu are also plotted in Fig. 3. The alignment coefficient decreases monotonically with increasing Z_1.

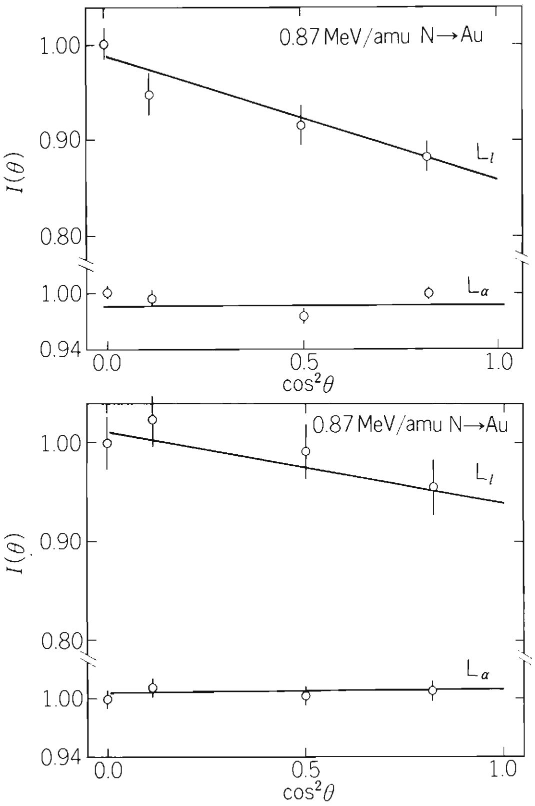

Fig. 2. Intensities of L_ℓ and L_α X-rays as a function of $\cos^2\theta$.

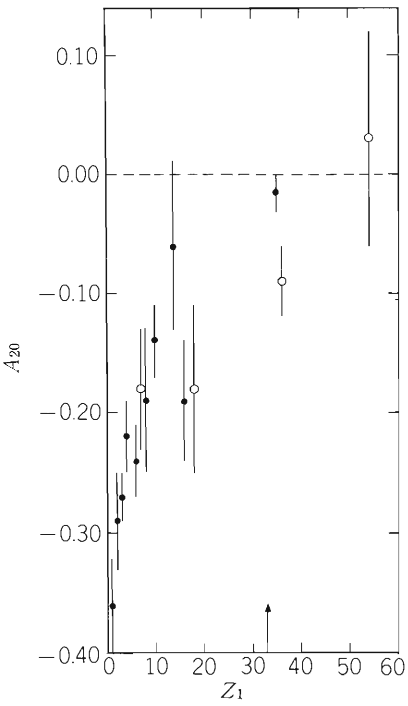

Fig. 3. The alignment coefficient vs Z_1 for Au L_3-subshell vacancies. Open circles are obtained in the present work and closed circles are referred from Jitschin et al.[1]

References

1) W. Jitschin, R. Hippler, R. Shanker, H. Kleinpoppen, R. Schuch, and H. O. Lutz: J. Phys. B: At. Mol. Phys., 16, 1417 (1983).

2) E. G. Berezhko and N. M. Kabachnik: ibid., 10, 2467 (1977).

III-2-10. Angular Distribution of REC for Ar^{4+} on C at 1 MeV/u

S. M. Shafroth, Y. Awaya, M. Kase, T. Kambara,
H. Kumagai, M. Nishida, H. Shibata, and H. Tawara

We have measured the angular distribution of X-rays arising from radiative electron capture (REC) for 45.7 MeV and 51.9 MeV Ar^{4+} ions incident on thin C targets. In the REC process which we studied, a loosely bound target electron is captured into the K-shell of the projectile, and a photon is emitted. Carbon was selected as a target material, since the data of Awaya et al.[1)] shows that there is almost no double vacancy production in the projectile at 33.6 MeV, whereas other target atomic numbers, such as 22 (Ti) give rise to much greater double K to single K vacancies. Furthermore target thickness studies of REC by Shafroth et al.[2)] showed that K vacancy production in the projectile is reached at thicknesses considerably smaller than 80 μg/cm^2 Finally, there are no higher energy characteristic X-rays arising from the target which might disturb the measurement.

The experimental arrangement consisted of a Si(Li) detector whose resolution was 200 eV at 6.4 keV, with an active area of 28 mm^2 and a 7.5 μm beryllium window. It could be rotated to angles of 25°, 45°, 70°, 90°, 110°, 135°, and 155°. At these angles 50 μm Be windows viewed the target. Air path between the detector and target chamber was smaller than 10 mm

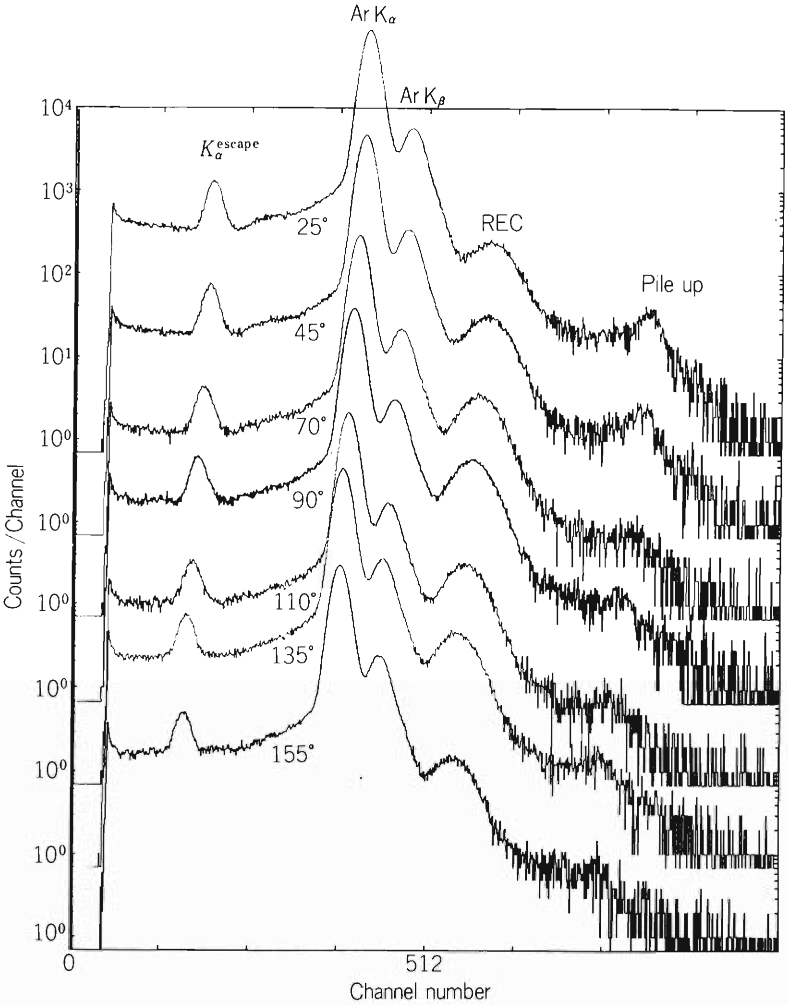

Fig. 1. X-ray spectra for all angles where measurements were made at projectile energy of 51.9 MeV. The X-rays passed through Be-windows with total thickness of 57.5 μm and an Al absorber with a thickness of 8 μm. The absorption correction was not applied.

and it little contributed to the absorption of the REC X-rays. 8 μm and 15 μm Al absorbers were placed between the target chamber exit windows and the Si(Li) detector, in order to attenuate the Ar K-X rays relative to REC. In the first run at 45.7 MeV Ar^{4+}, two absorber thicknesses were chosen in order to see how important the absorption correction was. In the second run at 51.9 MeV, only an 8 μm absorber was used.

A surface barrier detector was placed at 40° with respect to the incident beam. It served as a monitor counter by counting the recoiled carbon atoms from the Rutherford scattering and permits absolute cross section to be determined, without knowing the mean charge state of the Ar^{q+} ions exciting the foil.

A second Si(Li) detector was also used as a monitor. It was placed at 270° relative to the beam direction and had an 8 μm absorber between its Be window and the target chamber. It had the additional advantage that all runs could be summed and the resulting spectrum with good statistics could be used to compare with calculated shapes of REC spectra using Slater wave functions as was done by Kambara et al.$^{3)}$ or more sophisticated wave functions, and the impulse approximation, Bethe-Salpeter radiative capture cross section for free electrons on bare nuclei.$^{4)}$

In the second run the target was oriented at 45° and

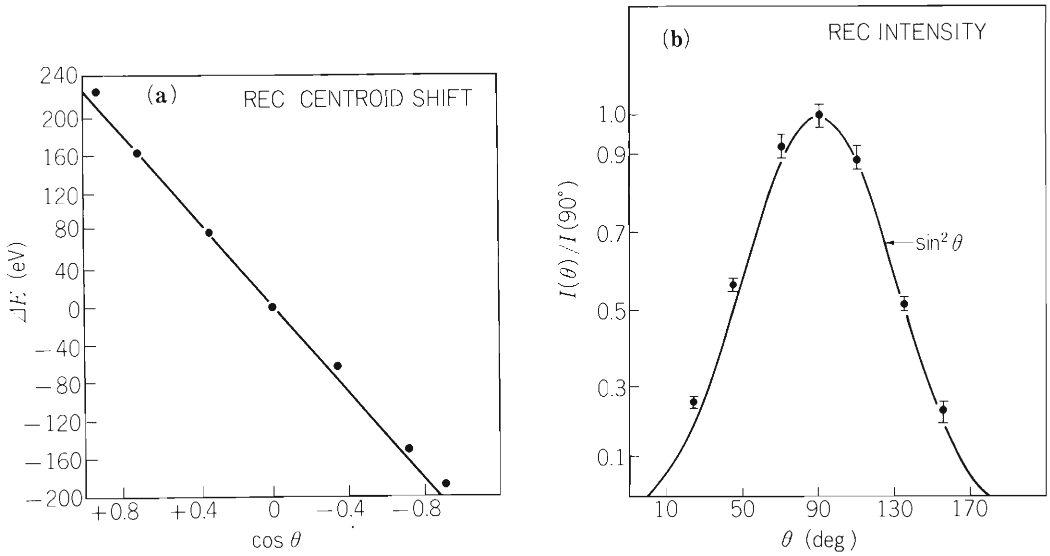

Fig. 2. (a) Angular dependence of shift of the centroid energy of REC peak relative to that at 90°. Solid line shows the prediction from the Doppler shift, (b) Intensity of the REC X-rays relative to that at 90°. Solid curve shows $\sin^2\theta$. The projectile energy is 51.9 MeV. A linear background is assumed.

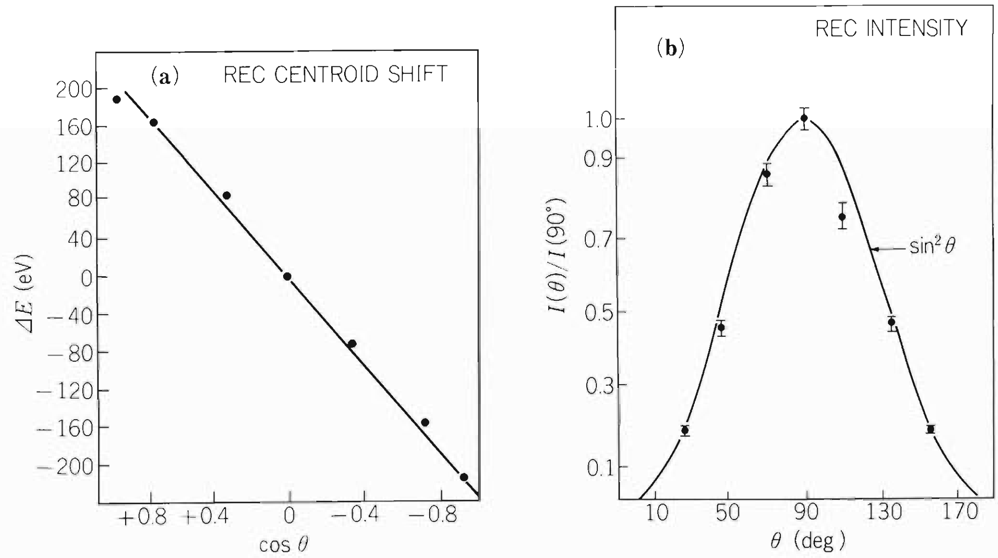

Fig. 3. Same as Fig. 2 except that an exponential background is assumed.

135° to the beam, and in the first run, it was located at 45° and 90° relative to the beam. The target angle had no appreciable effect. The beam spot on the target (1 mm × 3 mm) was defined by a slit, which was located 10 cm in front of the target. Figure 1 shows X-ray spectra at all angles where measurements were made at incident energy of 51.9 MeV.

X-ray absorption corrections were applied to the entire spectrum, channel by channel, approximating the energy dependence of X-ray absorption by a function of the form $N/N_0 = \exp(-Ae^{-B})$, where $A = 33.46$ and 7.27 and $B = 2.7401$ and 3.2571 for Al and Be respectively. These values were calculated using the X-ray absorption cross sections of Veigele.5) The corrected spectra were then fit with Gaussian functions. The centroid energy then shifted with angle as expected due to the Doppler effect. Figure 2(a) illustrates this for the case where a linear background is assumed. Figure 2(b) shows the angular distribution of REC X-rays normalized to 1.0 at 90°. At the forward angles it appear to be high compared to the expected $\sin^2\theta$ distribution4) and at the backward angles the data lies on the expected curve, thus a $(1-\beta\cos\theta)^{-4}$ correction would not describe the data either.

On the other hand, if an exponential background is assumed, as was done by Betz et al.,6) the data agree with $\sin^2\theta$ fairly well as can be seen from Fig. 3. The choice of background makes about 25 % difference in absolute cross section. The absolute cross sections are not yet determined. Further analysis is in progress.

References

1) Y. Awaya, T. Kambara, M. Kase, H. Kumagai, J. Urakawa, H. Shibata, T. Matsuo, J. Takahashi, and M. Namiki: p. 49 in this report.
2) S. M. Shafroth, K. Shima, T. Ishihara, et al.: IEEE Trans. Nucl. Sci., NS-30, 1055 (1983).
3) T. Kambara, Y. Awaya, A. Hitachi, M. Kase, I. Kohno, and T. Tonuma: J. Phys. B: At. Mol. Phys., 15, 3759 (1982).
4) H. A. Bethe and E. E. Salpeter: "Quantum Mechanics of One- and Two-Electron Atoms", Plenum, New York (1977).
5) Wm. J. Veigele: Atomic Data Tables, 5, 51 (1973).
6) E. Spindler, H. D. Betz, and F. Bell: Phys. Rev. Lett., 42, 832 (1979).

III-2-11. Krypton Recoil Ions Produced by 42 MeV Ar^{4+} Ion Bombardment

S. Özkök,* T. Tonuma, J. Urakawa, H. Kumagai, M. Kase,
H. Shibata, T. Kambara, J. Takahashi, T. Matsuo,
S. H. Be, and I. Kohno

We have bombarded Kr gas target with 42 MeV Ar^{4+} ion beam from the heavy-ion linac for various extraction voltages of recoil ions. The present work is a continuation of those reported previously.$^{1),2)}$ The apparatus is evacuated by a 5000 l/s cryo pump (condensation pump) and a 220 l/s turbo molecular pump. The background pressure and operating Kr pressure were 7.4×10^{-8} Torr and 9.2×10^{-7} Torr, respectively. Introduction rate of Kr gas was about 0.1 cc/min.

The block diagram of the electronic system to obtain Kr charge-state spectrum is shown in Fig. 1. Recoil ions were detected by a channeltron (Channel Electron Multiplier). Bias voltage of minus 2.4 kV was applied to the channeltron. The output signals were amplified and accumulated by multichannel scalar through a Timing Filter Amplifier circuit. The channel stepped up with integrated beam charge of 3nC on the Faraday cup. Step-up signals came from a current integrator. The charge-state spectrum of Kr ions was obtained by scanning the magnetic field by a step scanning controller and the number of counts in each channel was recorded on the on-line computer (PE-3220).

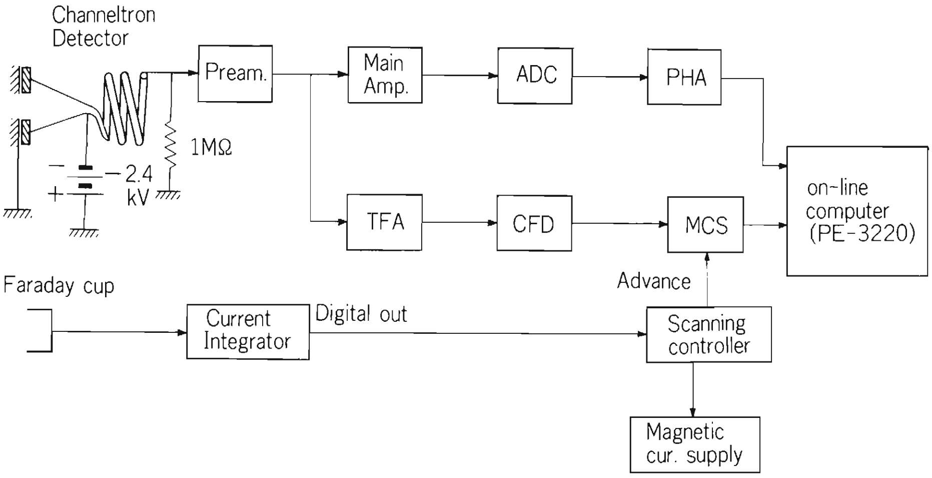

Fig. 1. The block diagram of the electronic system.
PHA : Pulse Height Analyzer
ADC: Analog to Digital Converter
TFA : Timing Filter Amplifier
CFD : Constant Fraction Discriminator
MCS : Multichannel Scalar.

Figure 2 shows the charge-state spectra of recoil Kr ions produced by 42 MeV Ar^{4+} ion bombardment. The Ar^{4+} ion beams have been used preferably because of their high beam intensity and long term stability. A Kr charge-state spectrum for extraction voltage of 4 kV was obtained by subtracting the background as shown in Fig. 2(c).

The recoil Kr ion fraction F_j is obtained as the ratio of each peak count to the sum of all the peak counts. These fractions F_j are plotted as a function of the extraction voltages in Fig. 3. It can be seen that the recoil Kr ion fractions have not so much dependence on the extraction voltage.

---

* Permanent address: University of Istanbul, Nuclear Physics Dept., Istanbul, Turkey.

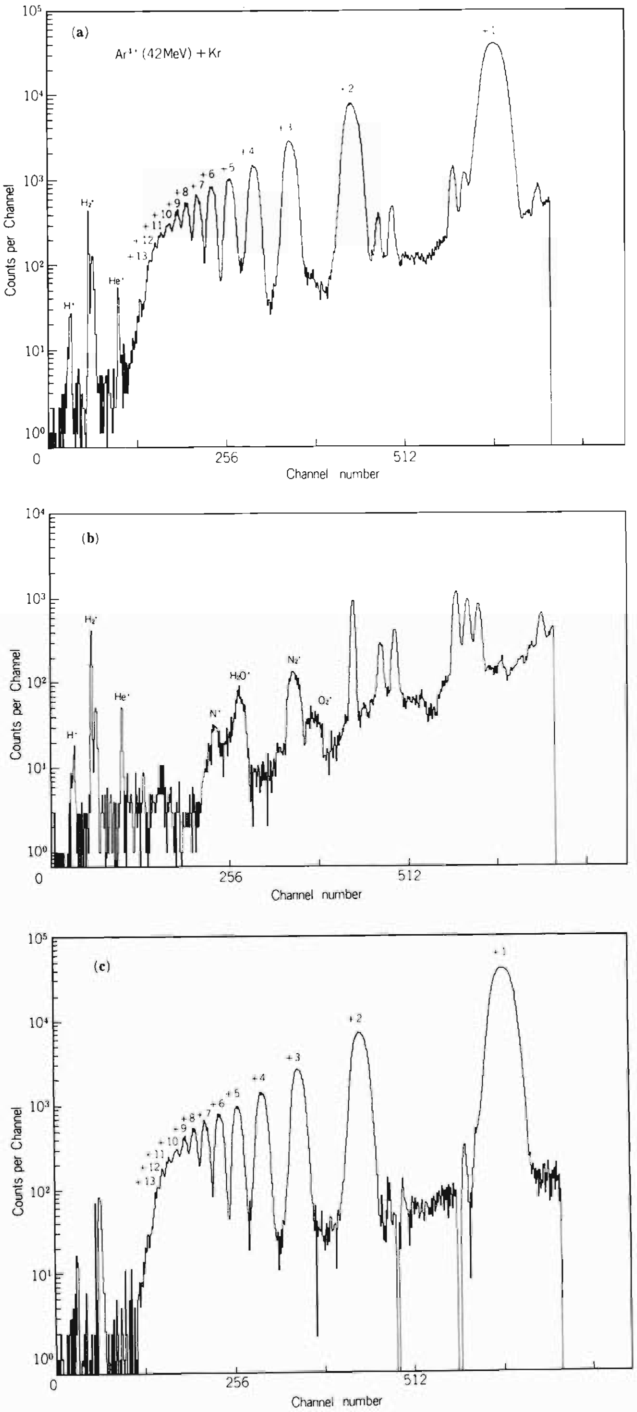

Fig. 2. Charge-state spectra of recoil Kr ions produced by 42 MeV Ar^{4+} ion bombardment. (a) Charge-state spectrum for extraction voltage of 4 kV, (b) Background spectrum, (c) Spectrum obtained by subtracting the background.

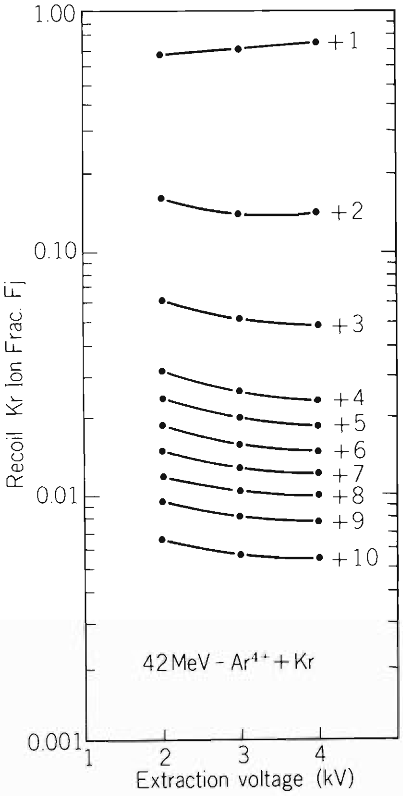

Fig. 3. Recoil Kr ion fraction F_j versus extraction voltage from 2 to 4 kV.

References

1) T. Tonuma, A. Yagishita, M. Kase, T, Kambara, Y. Aways, H. Kumagai, and I. Kohno: RIKEN Accel. Progr. Rep., 15, 72 (1981)

2) T. Tonuma, M. Kase, T, Matsuo, J. Urakawa, J. Takahashi, H. Kumagai, T. Kambara, I. Kohno, S. Özkök, and Suck Hee Be: ibid., 16, 85 (1982).

III-2-12. Projectile Charge-State Dependence of the Fractional Yields of Recoil Ions in Different Charge States

T. Tonuma, M. Kase, J. Urakawa, T. Matsuo, H. Kumagai,
T. Kambara, H. Shibata, J. Takahashi, S. Özkök,
S.H. Be, and I. Kohno

We present results of measurement of charge-state spectra of recoil ions produced in single collisions of 42 MeV Ar^{q+}(q = 4, 10 – 14) with Ar. Ar^{q+}(q = 10 – 14) beam was produced by passing Ar^{4+} beam from the linac through a carbon foil and selected by magnetic analysis. A typical charge-state spectrum of recoil ions produced by 42 MeV Ar^{12+} ion bombardment on Ar target is shown in Fig. 1. Charge states up to Ar^{12+} of the recoil ions were observed.

The fractional yield F_i of the recoil ion in a charge state i is plotted in Fig. 2 against i for 42 MeV projectile Ar^{q+} of different charges q = 4, 10 – 14. The solid and dash-dot-dashed lines are drawn to guide the eye. The fractions of recoil ions in charge states lower than i = 8 do not depend so much on the projectile charge state for $10 \leq q \leq 14$, but those of recoil ions with $i \geq 9$ increase with the projectile charge state.

The fractional yields of Ar with the atomic number of 18 satisfy the normalization condition

$$\sum_{i=1}^{18} F_i = \sum_{i=1}^{8} F_i + \sum_{i=9}^{16} F_i + \sum_{i=17}^{18} F_i = 1, \qquad (1)$$

where the partial sums refer to M-, L-, and K-shell ionization. The contribution from the K-shell ionization is negligible in the present experiment.

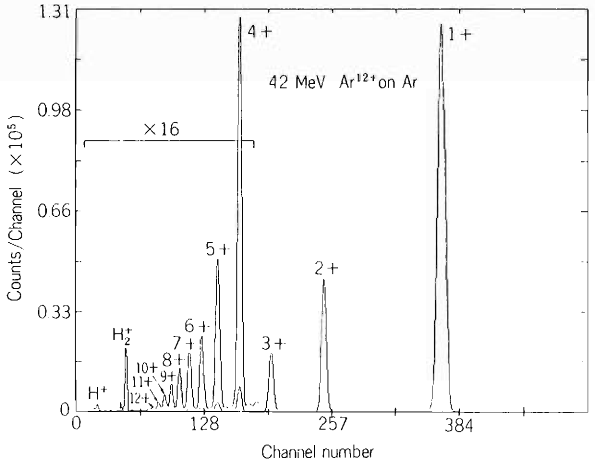

Fig. 1. Charge-state spectrum of recoil Ar ions produced by 42 MeV Ar^{12+} ion bombardment of Ar target.

(1) M-shell ionization

The eight M-shell electrons in the Ar target are bound loosely by the nucleus and are dominantly ejected in distant collisions. Olson[1)] calculated the cross section σ_i for ejecting i electrons in the M shell using an independent-electron-ejection model. We define a fractional yield

$$F_i^M = F_i / \sum_{i=1}^{8} F_i = \sigma_i / \sum_{i=1}^{8} \sigma_i \qquad (2)$$

of M-shell ionized recoil ions. It satisfies the normalization relation $\sum_{i=1}^{8} F_i^M = 1$. Experimental and theoretical fractional yields F_i^M are plotted in Fig. 3. The experimental values are for the 42 MeV Ar^{14+} projectile and the theoretical ones are for the projectile with energy of 1 MeV/amu and charge of 14. The theoretical F_i^M

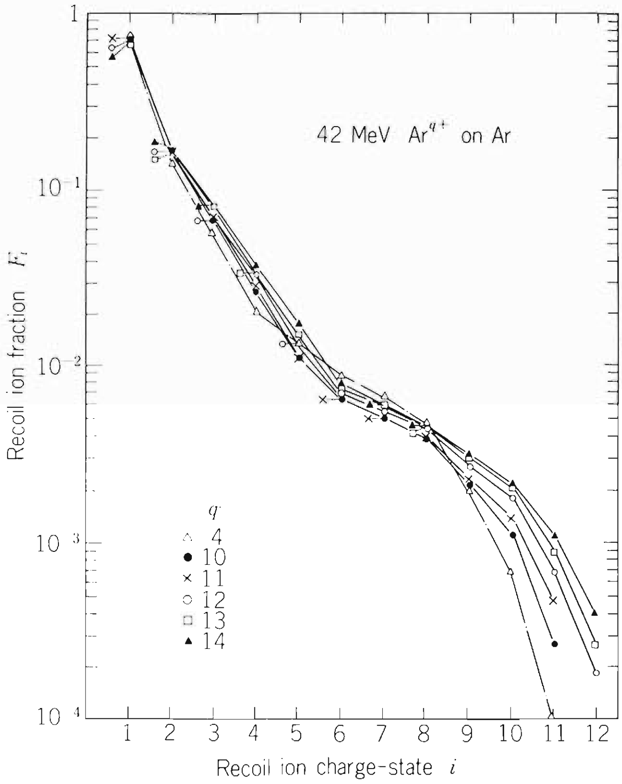

Fig. 2. Recoil ion charge-state fractions F_i for 42 MeV Ar^{q+} in Ar. Projectile charge state q is 4 and 10 ~ 14.

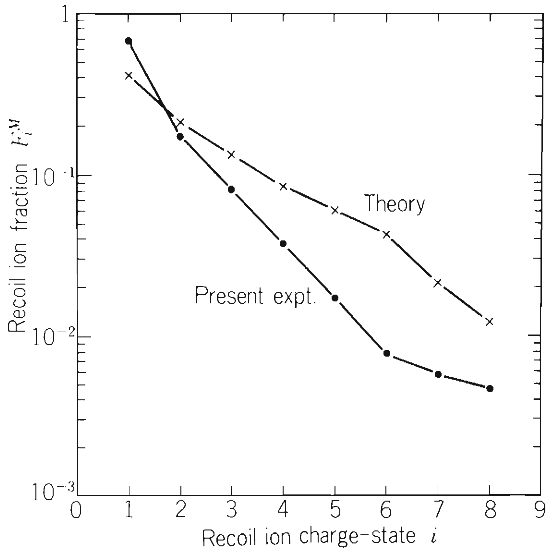

Fig. 3. Recoil Ar ion fraction F_i^M in M-shell ionization versus recoil ion charge state i. The theoretical line is for the calculation for the projectile energy of 1 MeV/amu and the projectile charge of 14 carried out by Olson. Experimental line is for 42 MeV (1.05 MeV/amu) Ar^{14+} in Ar.

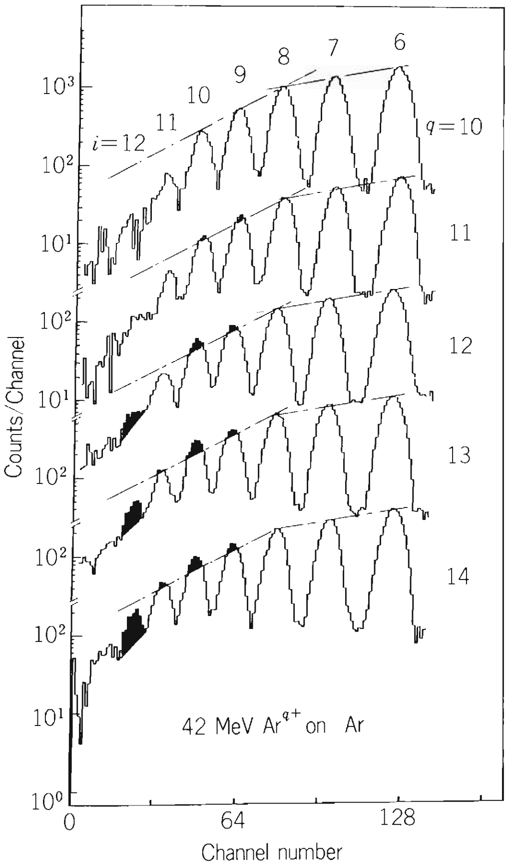

Fig. 4. Charge-state spectra of recoil Ar ions of charge state higher than 6 for 42 MeV Ar^{q+} in Ar.

is underestimated for small i and overestimated for large i. This trend is similar to that found in Ref. 2.

(2) L-shell ionization

Figure 4 shows charge-state spectra of the recoil Ar ions with $i \geq 6$ that are produced in collisions of 42 MeV Ar^{q+} ($q = 10 - 14$) with Ar. The background spectra due to residual gas were subtracted from the observed spectra. The relative yields of recoil ions with i = 6, 7, and 8 are almost independent of q. Those of the ions with $i \geq 9$ increase with an increase of q. Recoil ions Ar^{12+} were observed when $q \geq 12$ and increase with q. A fractional yield F_i^L of L-shell ionized recoil ions is defined by $F_i^L = F_i / \sum_{i=9}^{16} F_i$ and is normalized to unity ($\sum_{i=9}^{16} F_i^L = 1$). Experimental fractions F_i^L are plotted against q with solid points in Fig. 5.

The multiple-ionization probabilities $p_n(b)$ of ejection of n electrons from the L shell containing eight electrons in a collision with an impact parameter b are given by

$$P_n(b) = \binom{8}{n} P(b)^n [1 - P(b)]^{8-n}, \qquad n = 1, 2, \cdots\cdots, 8, \tag{3}$$

provided that all the electrons are ejected independently. Here, $\binom{8}{n}$ is a binomial coefficient and P(b) is the ionization probability for ejecting a single electron. In the simplest form P(b) is a constant probability[3)] within a defined distance of collision, namely,

$$\begin{aligned} P(b) &= P \qquad b \leq R \\ &= 0 \qquad b > R \end{aligned} \tag{4}$$

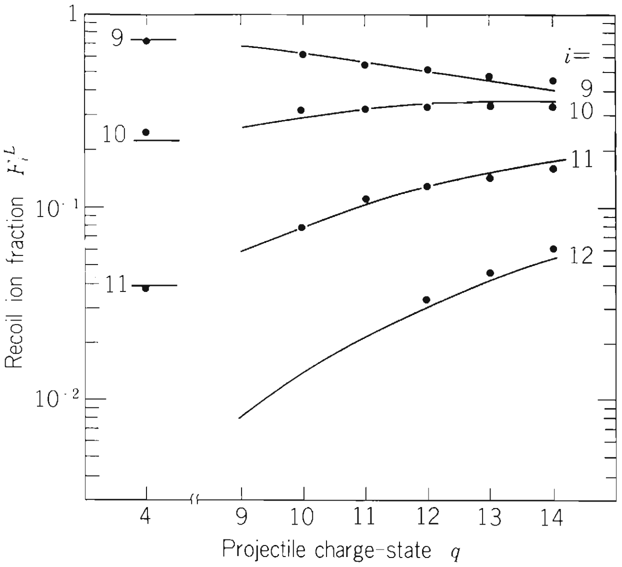

Fig. 5. Recoil Ar ion fraction F_i^L in L-shell ionization versus projectile charge state q. Solid points are the experimental values. Solid lines show the calculated values by the use of the estimated ionization probability P.

where R is given by $R = \sqrt{2}a$, a being the mean shell radius of the target atom. The fraction F_n of recoil ions of the n-th charge state may be expressed as

$$F_n = P_n / \sum_{n=1}^{8} P_n \, . \qquad (5)$$

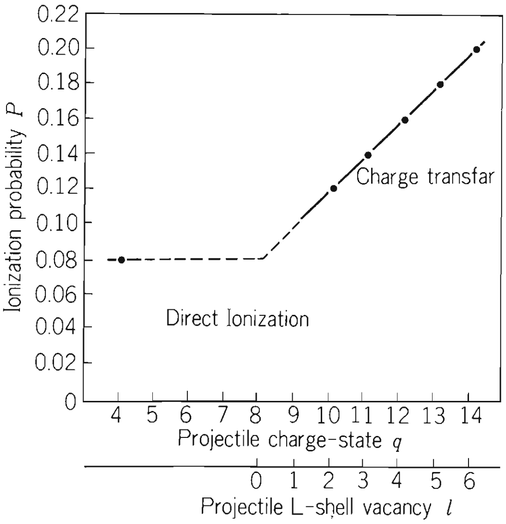

Fig. 6. Probability P of ionization of a single L-shell electron versus projectile charge state q and the number of projectile L-shell vacancies.

In the present case F_n denotes the fraction F_i^L (i = 9, 10, ..., 16). The fraction F_n depends only on one parameter P, which can be estimated by a least squares fitting to the experimental fractions. The fractions calculated using the estimated probability P are shown with solid lines in Fig. 5. Figure 6 displays plots of the probability P versus the projectile charge state q. The probability P increases linearly for q = 10 through 14 which corresponds to the projectile with 2 through 6 L-shell vacancies as shown in the figure. By interpolating these results and the value for q = 4, it is found that the ionization is strongly enhanced once the projectile L-shell vacancies are brought into collisions. This means that the direct transfer of the target L-shell electrons into the projectile L-shell vacancies contributes significantly to the production of highly ionized recoil ions.

References

1) R. E. Olson: J. Phys. B, 12, 1843 (1979).
2) A. S. Schlachter, W. Groh, A. Müller, H. F. Beyer, R. Mann, and R. E. Olson: Phys. Rev. A, 26, 1373 (1982).
3) Q. C. Kessel and E. Everhart: Phys. Rev., 146, 16 (1966).

III-2-13. Measurement of Total Ionization Cross Section for Production of Recoil Ions by Heavy Ion Impact on Gas Target

S. H. Be, T. Tonuma, H. Kumagai, M. Kase, H. Shibata,
T. Kambra, H. Tawara, and I. Kohno

With the purpose of obtaining an absolute ionization cross section of recoil ions, experiments for measuring a relative intensity of recoil ions have been carried out as a first step. Details of experimental results will be presented in another report of this volume.$^{1)}$

Following these experiments a measuring apparatus of the total ionization cross section for production of recoil ions was designed and constructed. The apparatus is shown in Fig. 1. This apparatus is similar to that of the well-known condenser plate method$^{2)}$ but the geometry of the parallel-plate electrodes is different from the conventional one. In the conventional apparatus three pairs of electrodes are employed, whereas in our case only one pair is employed; thus it is hoped to have more uniform electric field since the disturbance of the electric field in the space between the electrodes is avoided.

The condenser plate system including circuits for measuring is shown schematically in Fig. 2. The projectile ion beam enters the gas target via the beam defining aperture A and passes symmetrically between parallel-plate electrodes P_1, P_2 before entering a Faraday cup where its current is recorded. A voltage is applied between the parallel-plate electrodes of strength sufficient to ensure that all recoil ions and electrons emmited in collisions are collected by collector plates C_e and C_i, respectively. The potentials applied to P_1 and P_2 are arranged to be symmetrical with respect to the center line of the system, which is at earth potential. In general, V_{p1} and V_{p2} are at the same potential but the collector plate C_e can be made positive with respect to the grid G, as the case may be. A uniform electric field is maintained at least between high transparency grids, and the recoil ion collector plate C_i is biased a few ten volts positive with respect to the grid to prevent the escape of secondary electrons. Preliminary experimental results showed that when the collector plate C_i is about 20 V positive with respect to G. secondary electron suppression is complete. The grid G of 92 % transparency consists of 40 μm-diameter tungsten wire strung 1 mm apart, and perpendicular and parallel to the beam axis. The distance between each parallel plate and each

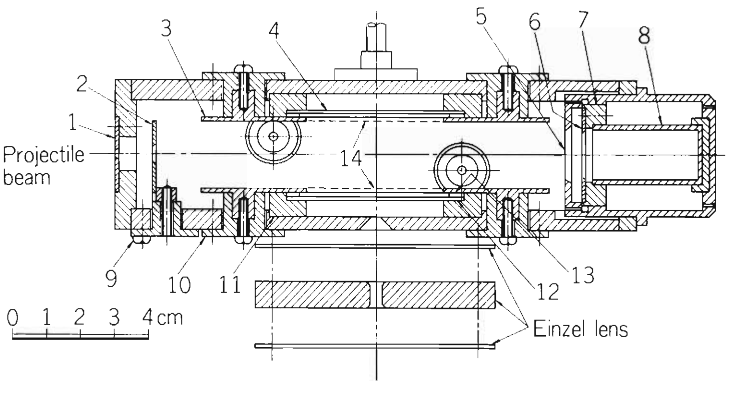

Fig. 1. Drawing of the parallel-plate condenser set-up. 1 : Beam defining aperture, 2 : Electrode for applying the suppressing voltage of secondary electrons produced at the edge of the beam defining aperture, 3 : parallel electrode for applying the accelerating voltage of electrons or ions produced by ionization, 4 : Electron collector plate, 5 : Earth potential electrode, 6 : Electrode for applying the suppressing voltage of secondary electrons produced at the Faraday cup by the impact of the projectile ions, 7 : Insulator (Teflon), 8 : Faraday cup, 9 ~ 11 : Insulator (Teflon), 12 : Recoil ion collector plate, 13 : Insulator (Teflon), 14 : Grid with a high transparency.

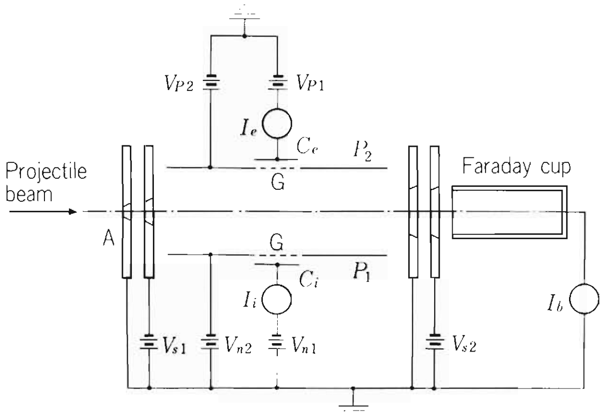

Fig. 2. Condenser plate system including simple circuits for measuring.

V_{n1}, V_{p1} : Applied voltages at ion and electron collector plates, V_{n2}, V_{p2} : Applied voltages for producing the uniform electric field between parallel-plate electrodes P_1 and P_2, V_{s1} : Suppressing voltage of secondary electrons produced at the edge of the beam defining aperture, V_{s2} : Voltage to prevent the escape of secondary electrons from the Faraday cup, I_e, I_i : Electrometer for measuring electron and ion current.

collector one is 2 mm in either case. The distance between parallel-plate electrodes in 20 mm.

The gas target cell is set up in the high vacuum chamber whose ultimate pressure is 7×10^{-8} Torr and evacuated via two apertures of 2 mm in diameter by a pressure difference between the cell and the chamber. The ultimate pressure of the cell is 3×10^{-6} Torr, and the working pressure for actual experiments is above an order 10^{-4} Torr much higher than 3×10^{-6} Torr.

In studies of this type, there occur such processes as ionization of target atom, electron capture of projectile ion and stripping of projectile one, i.e., as those in the following reaction

$$X^{q+} + Y \rightarrow X^{m+} + Y^{n+} + (m + n - q). \qquad (1)$$

A total ionization cross section Q_+ is defined by

$$Q_+ = \sum_{m,n} n \, {}_{q0}Q_{mn}, \qquad (2)$$

where ${}_{q0}Q_{mn}$ is the cross section for the charge state n of recoil ions. q is charge state of projectile ion, 0 is charge state of target atom, m is charge state of projectile particle after collision and n is charge state of target particle after collision. Q_+ can be determined by measuring the current I_i due to all recoil ions of all charge states n. At pressure low enough to ensure single collisions we have

$$Q_+ = 2.81 \times 10^{-17} I_i/(I_b \, l \, P) \text{ cm}^2, \qquad (3)$$

where l(cm) is a definite length of the projectile beam path, P(Torr) target pressure and I_b(A) the projectile ion beam current. A schematic diagram of the electronics for measuring I_i, P, and I_b, which are necessary for the determination of Q_+, is shown in Fig. 3.

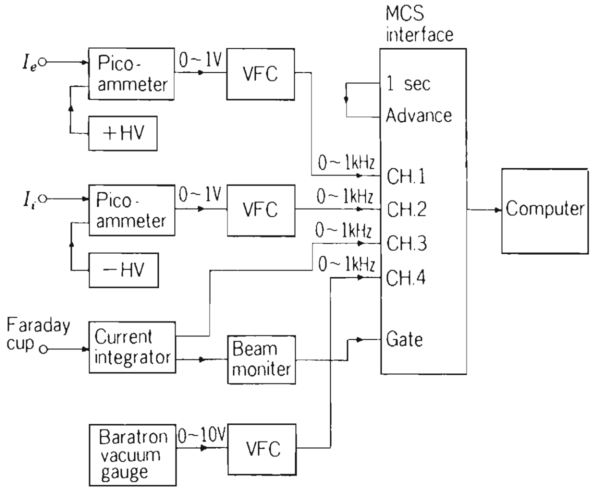

Fig. 3. Schematic diagram of the electronics.

Using constructed apparatus and the instrument described above preliminary experiments were made over two times so far. The Q_+ calculated from Eqn.(3) using the experimental results is 3.5×10^{-15} cm^2 for 1.14 MeV/amu A_r^{4+} projectiles and 2.4×10^{-15} cm^2 for C^{5+} of the same energy, both on the same gaseous A_r target. The measured value of the latter is in good agreement with Schlacter's result$^{3)}$ of 2.6×10^{-15} cm^2. The detailed experiments are in progress.

References

1) T. Tonuma, M. Kase, J. Urakawa, T. Matsuo, H. Kumagai, T. Kambara, H. Shibata, J. Takahashi, S. Özkök, S. H. Be, and I. Kohno: p. 60 in this report.
2) Hooper McDaniel Martin, and Harmer: Phys. Rev., 121, 1123 (1961).
3) A. S. Schlachter, K. H. Berkenr, W. G. Graham, R. V. Pyle, P. J. Schneider, K. R. Stalder, J. W. Steans, J. A. Tanis, and R. E. Olson: Phys. Rev. A, 23, 2331 (1981).

III-2-14. Ar L-MM Auger Spectra in Ar^{4+} + Ar Collisions

T. Matsuo, H. Shibata, J. Urakawa, A. Yagishita, Y. Awaya,
T. Kambara, M. Kase, H. Kumagai, and J. Takahashi

In order to investigate the ionization mechanism in heavy-ion atom collisons, we have measured the energy spectra of ejected electrons in Ar^{4+} + Ar collisions. In this report, we present the line-identifications for the L-MM Auger electron spectrum. The experimental apparatus used in this experiment has been described in Ref. 1. The gaseous Ar target of pressure 10^{-3} Torr was bombarded with Ar^{4+} beams of energy 6.6 – 45.7 MeV from the RILAC. The energies of electrons ejected at an angle of 132° with respect to the incident beam direction were measured with an electrostatic analyzer. The measured energy range of electrons was from 80 to 330 eV. The L-MM Auger lines from projectile ions shifted to low energy, out of the present measurement range, due to the Doppler energy shift, so that the peaks which appeared in the spectrum were attributed to the electrons from the target.

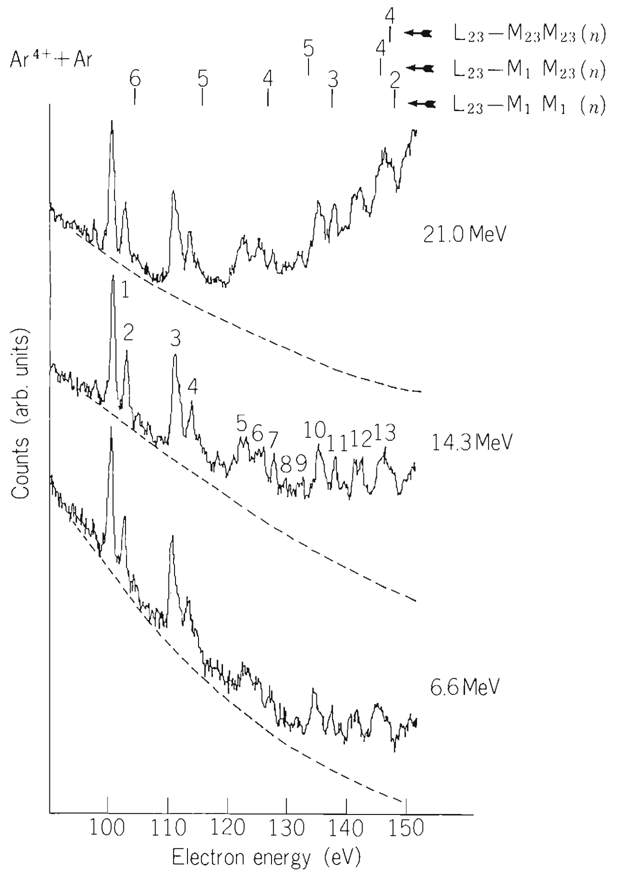

Fig. 1. Electron energy spectra by Ar^{4+} impact on Ar, measured at an angle of 132° with respect to the incident beam direction. The energy resolution is 0.6 eV FWHM. The lines above the spectra indicate the L_{23}-MM(n) transition energies calculated by Larkins, where the number of M_{23}– shell vacancies is indicated in the parenthesis. The prominent peaks are numbered. The broken line shows the estimated background.

In a previous paper,$^{2)}$ we have reported that the electron spectrum consists of sharp peaks at about 101 and 112 eV, and a broad-peaked structure extending from 120 to 260 eV, and interpreted them as arising from the transitions in the initial vacancy states, $Ar^{m+}(1s^2 2s^2 2p^5 3s^2 3p^n)$, by referring to the theoretical result by Larkins.$^{3)}$ Figure 1 shows the electron energy spectra for projectile energies of 6.6, 14.3, and 21.0 MeV. The prominent peaks are labeled by integers, 1,2, ... 11. The line energies calculated by Larkins are also indicated above the spectra. The broken lines show continuum background, which was evaluated assuming the form ae^{-bE}. Here, E is electron energy, and a and b are parameters which were obtained by extrapolation from the regions above and below the Auger structure, though the spectrum of full energy range is not shown. It is noted that the positions and shapes of the peaks did not change with the projectile energy. On the other hand, relative intensities among them changed considerably depending on the projectile energy. Relative intensities of each peak to peak 1 are shown in Fig. 2. It is considered that peaks (1 and 2), (3 and 4), and (5,6 and 7) are produced respectively from the same initial configuration states, because the intensity ratio of the

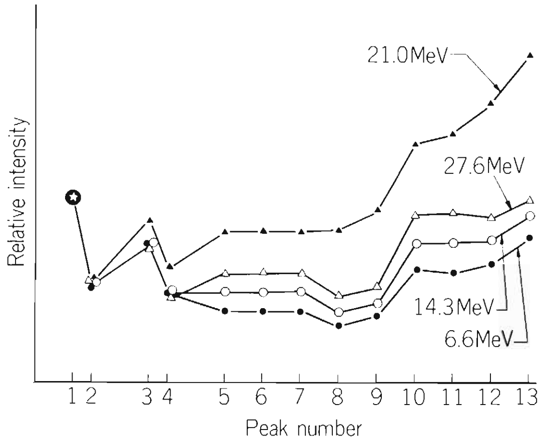

Fig. 2. Variation of the relative peak intensity with the projectile energy. The intensities of the peaks are normalized to that of peak 1. Peak number indicated is the same as in Fig. 1.

constituent peaks in each peak group is independent of the projectile energy.

For peaks 1 and 2, we have already interpreted them as arising from the $L_{23}-M_1M_1(6)$ transistions; $Ar^{7+}(2s^2 2p^5 3s^2) \rightarrow Ar^{8+}(2s^2 2p^6)$, where the number in the parenthesis in the L–MM expression indicates the number of M_{23}–shell vacancies. Peaks 3 and 4, at about 110 and 113 eV, are considered to be due to the L_{23}–$M_1M_1(5)$ transitions; $Ar^{6+}(2s^2 2p^5 3s^2 3p) \rightarrow Ar^{7+}(2s^2 2p^6 3p)$. The energy splitting between the final states, $Ar^{7+}({}^2P_{1/2}$ and ${}^2P_{3/2})$, has been reported to be 0.3 eV by spectroscopic study[4] and less than the present resolution of 0.6 eV FWHM. The peak structure is, therefore, considered to reflect the energy difference among the initial states $Ar^{6+}({}^1D, {}^1P, {}^1S, {}^3D, {}^3P$, and ${}^3S)$ in the L-S coupling scheme. Unfortunately, the energy levels of these states are not known. Peaks 5,6, and 7 are ascribed to the L_{23}–$M_1M_1(4)$ transitions; $Ar^{5+}(2s^2 2p^5 3s^2 3p^2) \rightarrow Ar^{6+}(2s^2 2p^6 3p^2)$. The energy difference among final states, $Ar^{6+}({}^3P, {}^1D$, and ${}^1S)$, is smaller than 0.3 eV. Again, the peak structure is ascribed to the energy difference in the initial states of Auger transition, but the energy levels of the $Ar^{5+}(2s^2 2p^5 3s^2 3p^2)$ are not known.

A high resolution measurement (0.35 eV FWHM) has been made for 45.7 MeV Ar^{4+} impact, and the spectrum is shown in Fig. 3. Peaks between 110 and 115 eV, corresponding to peaks 3 and 4 in Fig. 1, are well resolved into several sharp peaks, which originate from various combinations of the initial and final states for the transitions. The peaks distributed from 120 to 128 eV correspond to peaks 5,6, and 7 in Fig. 1. For the further discussion of the identifications of the measured peaks, it is highly required to make a more rigorous theoretical calculation for the energy levels of the multiply-ionized states.

So far, we restricted ourselves to discussion of the most intense peaks. But one can find some small peaks around the $L_{23}-M_1M_1(6)$ peaks in every spectrum. From the result by Larkins, peaks which appear on the lower energy side of peak 1 are considered to be produced by the $L_{23}-M_1M_1$ Auger transitions from the L – shell double vacancy state, $Ar^{8+}(2s^1 2p^5 3s^2)$, and those on the higher energy side from the $Ar^{8+}(2s^2 2p^4 3s^2)$. Thus the spectra indicate that the inner-shell double vacancy states are produced apparently by heavy-ion atom collisions in MeV energy region.

To study the ionization mechanism, more detailed analysis of the data is in progress.

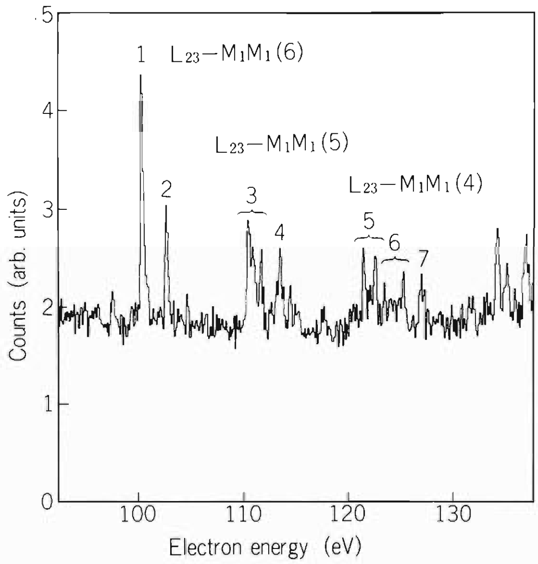

Fig. 3. A high resolution (0.35 eV FWHM) electron spectrum obtained by 45.7 MeV Ar^{4+} impact.

References

1) A. Yagishita and T. Nakamura: IPCR Cyclotron Progr. Rep., 14, 143 (1980).
2) T. Matsuo, J. Urakawa, A. Yagishita, Y. Awaya, T. Kambara, M. Kase, and H. Kumagai: J. Phys. B, 16, L239 (1983).
3) F. P. Larkins: ibid., 4, 1 (1971).
4) S. Bashkin and J. O. Storner Jr.: "Atomic Energy-Levels and Grotrian Diagrams II", North-Holland Publishing Co., Amsterdam (1978).

III-2-15. Krypton M-Shell Auger Spectra Produced in Collisions with about 0.2 MeV/amu Heavy Ions

J. Urakawa, T. Matsuo, H. Shibata, Y. Awaya, T. Kambara,
M. Kase, H. Kumagai, J. Takahashi, and A. Yagishita

In order to obtain detailed information on both energy levels of highly ionized atoms and their production processes, energy distributions of Kr M-shell Auger electrons produced by 0.83 MeV He^+, 2.9 MeV N^{2+}, 4.14 MeV Ne^{3+}, and 8.3 MeV Ar^{4+} ion bombardment on krypton have been measured at an emission angle of 132° with respect to the ion beam direction. The projectile ions were accelerated by the RILAC. The experimental apparatus, procedure and conditions were described previously.$^{1)}$ The energy scale of the ejected electrons was calibrated by Kr M-NN and Ar L-MM Auger peaks induced by 1.2 keV electron impact. The energy values of each M-NN and L-MM Auger peak were referred to the results by Werme et al.$^{2)}$

The ejected electron spectra obtained are shown in Fig. 1. These spectra are characterized by a continuous background and complicated Auger structure, which is superimposed upon the continuous background resulting from the direct ionization process. The pattern of continuous background is assumed to be expressed by a function $f(E) = Ae^{-BE}$, since this function reproduces the feature of the lower and higher energy wings of the measured spectra well, where A and B are fitting parameters and E the ejected electron energy. In order to compare the Auger structures obtained for different projectiles, the continuous background estimated by the function f(E) was subtracted from each ejected electron spectrum. Figure 2 shows such a comparison of the Auger spectra. For an investigation of the structure, we have compared the spectra with the theoretical results by Larkins,$^{3)}$ who showed that the Auger lines shift to lower energies as the degree of ionization increases. The lines above spectra in Fig. 2 indicate the energies calculated by Larkins using the adiabatic model. The number on each line shows the number of 4p holes in the initial state of Auger transition. The following results can be derived from Fig. 2:

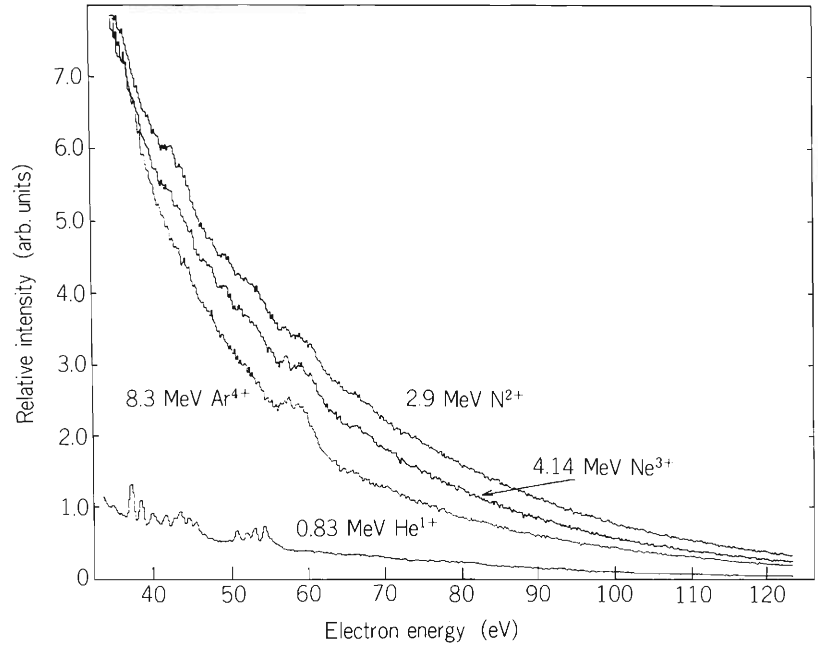

Fig. 1. Kr M-Auger spectra produced at 132° from the beam direction by He^+, N^{2+}, Ne^{3+}, and Ar^{4+} impacts with equal-velocity (0.215 MeV/amu).

1) The intensity of normal Auger lines indicated by number 1 and 2 in the figure weakens as the atomic number Z of projectile increases and become negligibly small for Ar^{4+}.

2) Auger lines from about 40 eV to 50 eV are

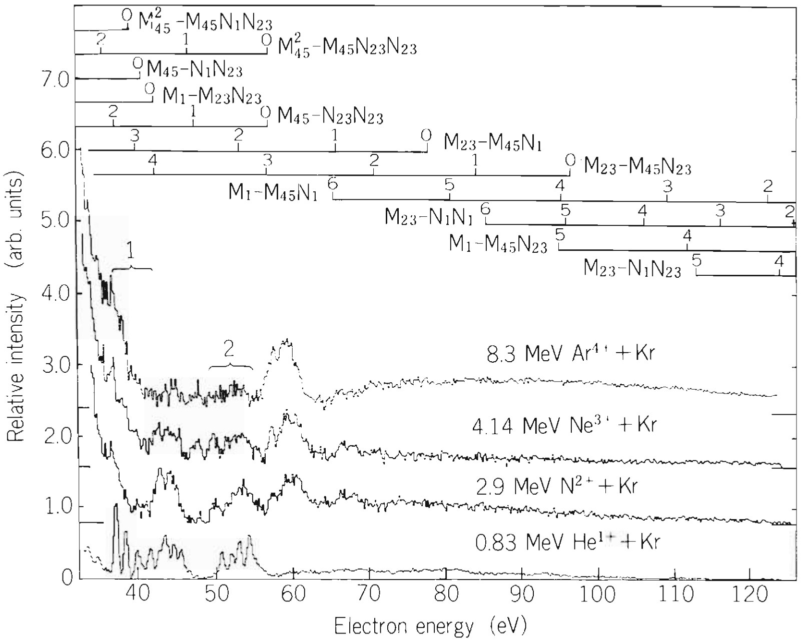

Fig. 2. Kr M-shell Auger spectra produced at 132° by 0.83 MeV He^+, 2.9 MeV N^{2+}, 4.14 MeV Ne^{3+}, and 8.3 MeV Ar^{4+}. The continuous background estimated by the function Ae^{-BE} is subtracted. The lines shown above the spectrum indicate the calculated energies for the corresponding transitions, which are denoted on their right or left. The number on each line shows the number of 4p holes in the initial state of Auger transition.

mainly ascribed to the transition M^n_{45} $N_{23}N_{23}(1)$, where n is the number of 3d holes and the number in the parenthesis indicates the number of 4p holes, because the lines due to the transition M^n_{45}-$N_{23}N_{23}(1)$ shift to lower energies as the number n of 3d holes in the initial state increases, according to the theoreitical results of Larkins. The experimental result that the mean energy of these Auger lines for 0.83 MeV He^+ impact is higher than that for 2.9 MeV N^{2+} impact supports the identification mentioned above, since the probability of multiple ionization increases for heavier ion impact.

3) The intensity of Auger peaks from about 55 eV to 65 eV enhances as the atomic number Z of projectile increases. The strong Krypton M-vacancy production is expected to be induced by the projectile with the same velocity as the orbital velocity of the M-shell bound electrons. The corresponding velocity of the projectile is about 0.2 MeV/amu for the Kr M_{45} – shell. Futhermore, the strong electron stripping of the outer shell is expected to be produced by a sufficiently heavy projectile. These facts might imply that the Auger peaks from about 55 eV to 65 eV are ascribed to the transition M_{23}-$M_{45}N$ or M_{23}-NN with many 3d and N-shell holes in the initial states, namely, with the number of 3d holes and N-shell holes of about 9 and 6, respectively.[4] In order to identify the line structure from about 55 eV to 65 eV, the theoretical calculations involving electron excitation with many 3d holes are highly desired.

References

1) T. Matsuo, J. Urakawa, A. Yagishita, Y. Awaya, T. Kambara, M. Kase, and H. Kumagai: J. Phys. B, 16, L239 (1983).
2) L. O. Werme, T. Bergmark, and K. Siegbahn: Phys. Scr., 6, 161 (1972); ibid., 8, 146 (1973).
3) F. P. Larkins: J. Phys. B, 6, 2450 (1973).
4) D. Schneider, B. M. Johnson, B. Hodge, and C. F. Moore: Phys. Lett., 59A, 25 (1976).

III-2-16. Secondary Electrons Induced by N^{2+} Ion Bombardment

A. Koyama, Y. Sasa, and M. Uda

It is of great importance to carry out experiments with clean surfaces and to obtain the reproducibility of data in the study of secondary electron emission phenomena. Therefore the aforesaid$^{1)}$ ultra high vacuum apparatus was examined from this standpoint.

It takes about 20 minutes to obtain the spectra of secondary electrons by using the apparatus in the case of ion bombardment, and the surface of the target should be kept clean enough during the measurement after target preparation.

The surface of an Al target was examined by Auger electron analysis using 1 keV exciting electrons. The target was in-situ vacuum deposited in the target preparation chamber. The target was transferred into the target chamber, and then the Auger analysis was made. Within 20 minutes after target preparation no contamination was detected on the surface. When the target was left in the target chamber for 25 h, however, carbon impurities were detected as shown in Fig. 1. The thickness of the adsorbed carbon compound was estimated to be 2 ~ 3 A, from the comparison between Al and C peaks. Then the amount of surface impurities would be less than the equivalent of 1% of a monolayer after a measurement taking 20 minutes, and are considered to be of no significance in this study of electron spectroscopy.

Further the reproducibility of the data was examined for spectra of secondary and Auger electrons induced by ion irradiations. Projectiles were N^{2+} ions with energy of 1.1 MeV/amu, and the target was also a clean Al target. Figure 2 shows the scattering of the data to be about ± 10 % in the spectra of secondary electrons with energies lower than 2 eV. Figure 3 shows a similar amount of data scattering in the spectra of L–VV Auger electrons. Hereafter an effort will be made to find out the origin of the scattering of the data and to improve the performance of the apparatus.

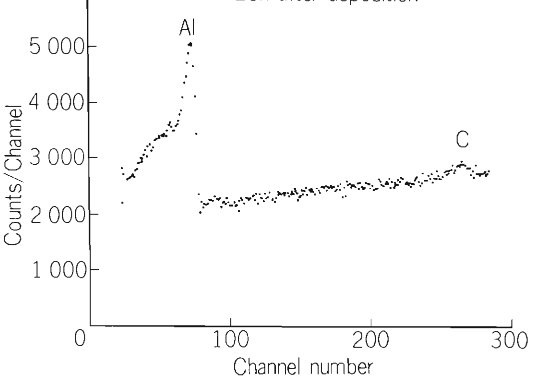

Fig. 1. Auger peaks of Al and C from the Al target which was left in the target chamber for 25 h after in-situ vacuum-deposition. The energy of exciting electrons is 1 keV.

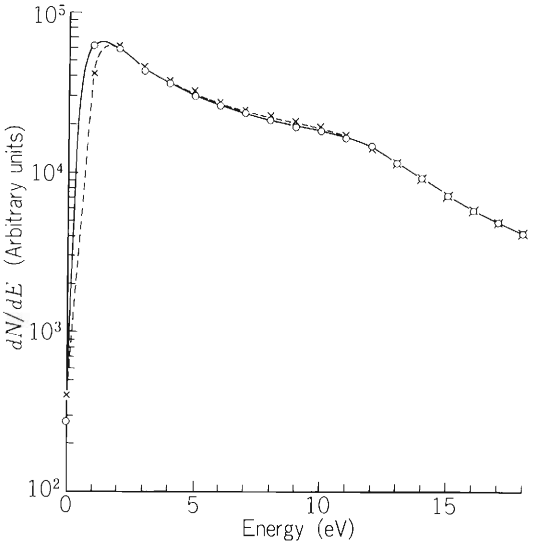

Fig. 2. Energy spectra of secondary electrons from a clean Al target. Projectiles are N^{2+} ions with energy of 1.1 MeV/amu. Different marks correspond to different measurement runs.

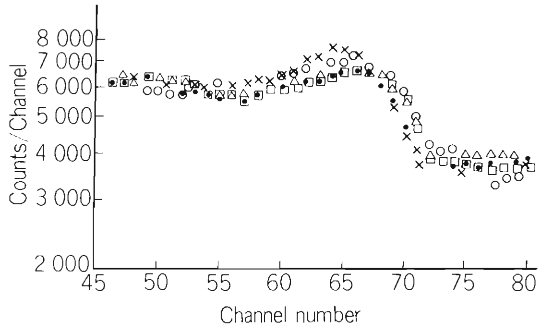

Fig. 3. Energy spectra of L-VV Auger electrons from a clean Al target. Projectiles are N^{2+} ions with energy of 1.1 MeV/amu. Different marks correspond to different measurement runs.

Reference

1) A. Koyama, Y. Sasa, Y. Ishibe, A. Shiraishi, T. Shiga, H. Omori, K. Nishi, M. Fuse, and M. Uda: p. 122 in this report.

III-2-17. Stopping Power of Al, Ni, Ag, Au, and Pb for 5 – 7 MeV/nucleon α Particles and Carbon Ions: Z_1^3 Deviation from the Bethe Formula

T. Takahashi, Y. Awaya, T. Tonuma, H. Kumagai, K. Izumo, M. Nishida,
A. Hashizume, S. Uchiyama, K. Masuda, and T. Doke

The stopping power of Ni, Ag, Au, and Pb for 7 MeV/nucleon C ions and α particles have been measured by using the cyclotron and the results are shown in Table 1. In order to analyze our results we use a semi-empirical expression

$$-\frac{dE}{dx}=\frac{4\pi N_0 e^4 Z_2}{mv^2 A_2} Z_1^2 (L_0 + Z_1 L_1 + \Phi) \qquad (1)$$

for the stopping power of a target with atomic number Z_2 and mass number A_2, and a projectile of velocity v and charge Z_1e. Here, N_0 is the Avogadro number, m and e are the electronic mass and charge, respectively, L_0 is the Bethe stopping number per target electron, L_1 expresses the Z_1^3 deviation from the bethe formula, and Φ is the Bloch term which is calculated as described in Ref. 1.

From Eqn. (1), $L_0 + Z_1 L_1$ is given by

$$L_0 + Z_1 L_1 = L = \left[-\frac{dE}{dx}\right] \frac{mv^2 A_2}{4\pi N_0 e^4 Z_2 Z_1^2} - \Phi. \qquad (2)$$

For the cases of both α particles and carbon ions, L_0 holds a common value if the same target is used and the velocities of the projectiles are equal, and moreover if the carbon ions are regarded as point charges. In such a case, L_1 is given by the following formula:

$$L_1 = (L_c - L_\alpha)/(Z_c^* - Z_\alpha), \qquad (3)$$

where L_c and L_α are L values for carbon ions and α particles, respectively, Z_c^* is the effective charge of carbon ions, and Z_α is the nuclear charge of α particles. Since L can be determined from the experimental stopping power, we can obtain L_1 from formula (3) if the stopping powers of the same material for carbon ions and α particles of the same velocity are measured. Table 1 shows the stopping powers of Ni, Ag, Au, and Pb (without the effective-charge correction) for carbon ions and α particles with the same velocity as well as the values of L_1 for both projectiles obtained with the use of three different charge-correction formulas. The stopping powers in the table are also shown in Fig. 1

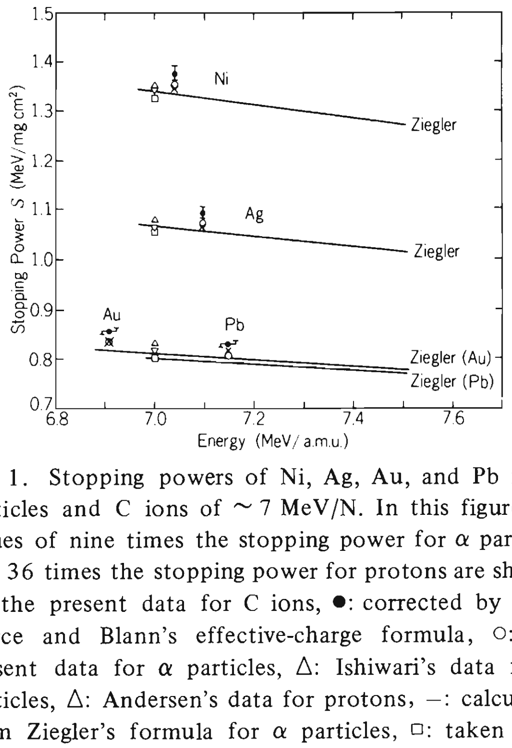

Fig. 1. Stopping powers of Ni, Ag, Au, and Pb for α particles and C ions of ~ 7 MeV/N. In this figure the values of nine times the stopping power for α particles and 36 times the stopping power for protons are shown. ×: the present data for C ions, ●: corrected by using Pierce and Blann's effective-charge formula, ○: the present data for α particles, △: Ishiwari's data for α particles, △: Andersen's data for protons, —: calculated from Ziegler's formula for α particles, □: taken from Northcliffe and Schilling's table for α particles.

Table 1. Stopping-power values for ~7 MeV/N α particles and C ions and their Z_1^3 deviation term L_1.

Stopping material	Energy (MeV/N)	Stopping power for C ion (MeV/mg cm²)	Stopping power for α particle (MeV/mg cm²)	L_1 values (1)[a]	(2)[b]	(3)[c]	(4)[d]
Ni	7.039	1.347 ± 0.016	0.1502 ± 0.0011	0.0270	0.0427 ± 0.014	0.0464	0.0400
Ag	7.097	1.069 ± 0.010	0.1190 ± 0.0008	0.0286	0.0424 ± 0.012	0.0458	0.0450
Au	6.908	0.839 ± 0.006	0.0928 ± 0.0007	0.0339	0.0453 ± 0.010	0.0479	0.0537
Pb	7.148	0.814 ± 0.006	0.0895 ± 0.0008	0.0374	0.0491 ± 0.012	0.0519	0.0558

a: No effective-change correction,
b: Corrected by Pierce and Blann's effective-charge formula,
c: Corrected by Ziegler's effective-charge formula,
d: Corrected by Anthony and Lanford's effective-charge formula.
References are cited in Ref. 1.

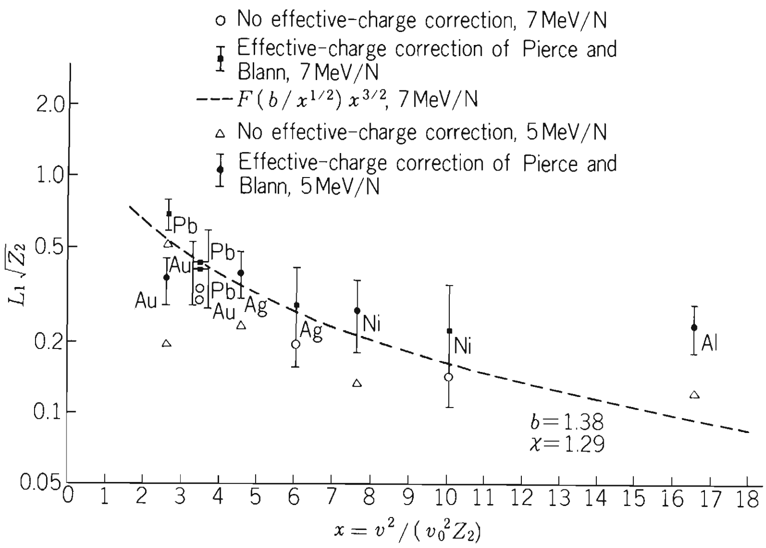

Fig. 2. Experimental values of $Z_2^{1/2}$ L_1 as a function of $(v/v_0)^2 Z_2^{-1}$. The broken curve was obtained by fitting to the ~ 7 MeV/nucleon data.

Table 2. Stopping-power values for ~5 MeV/N α particles and C ions and their Z_1^3 deviation term L_1.

Stopping material	Energy (MeV/N)	Stopping power for C ion (MeV/mg cm^2)	Stopping power for α particle (MeV/mg cm^2)	L_1 values (1)^a	(2)^b	(3)^c	(4)^d
Al	5.368	1.970 ± 0.014	0.2198 ± 0.0015	0.0340	0.0662 ± 0.015	0.0742	0.0533
Ni	5.339	1.612 ± 0.019	0.1819 ± 0.0013	0.0252	0.0517 ± 0.017	0.0580	0.0482
Ag	5.354	1.272 ± 0.012	0.1421 ± 0.0010	0.0343	0.0572 ± 0.013	0.0628	0.0624
Au	5.149	0.961 ± 0.007	0.1100 ± 0.0008	0.0222	0.0415 ± 0.009	0.0442	0.0528
Pb	5.412	0.982 ± 0.007	0.1060 ± 0.0010	0.0570	0.0767 ± 0.011	0.0820	0.0884

a: No effective-change correction,
b: Corrected by Pierce and Blann's effective-charge formula,
c: Corrected by Ziegler's effective-charge formula,
d: Corrected by Anthony and Lanford's effective-charge formula.
References are cited in Ref. 1.

as well as the stopping power for α particles obtained by Ishiwari et al. with their values multiplied by nine, and those for protons by Andersen et al. with the values multiplied by 36. The solid lines in the figure are obtained from Ziegler's stopping-power formula. Our values for α particles are in better agreement than with those of Ishiwari et al., rather than those obtained from Ziegler's formula.

According to Ritchie and Brandt, $L_1 Z_2^{1/2}$ is expressed by a function $F(b/x^{1/2})/x^{3/2}$, where $x = (v/v_0)^2/Z_2$ (v_0 is the Bohr velocity) and $b = \eta\chi Z_2^{1/6}$. Here, χ is a constant describing correlations between electrons in an atom in a way that $\omega\rho(r)$ should be written as $\chi\left\{4\pi Z_2 e^2\rho(r)/m\right\}^{1/2}$, where $\rho(r)$ is the number density of electrons. If each electron acts independently, χ should be unity. The contribution from distant collision to the stopping power is calculated by integration over the impact parameter from a minimum value a_ω to infinity. The parameter η in the definition of b relates the minimum impact parameter to the radius r of the shell, associated with the plasma frequency $\omega\rho(r)$, by $a_\omega = \eta r$. Thus, the theoretical value of $L_1 Z_1$ increases as b decreases and, in addition, it depends on the effective charge of the projectile. On the other hand, Bloch's value of Φ is opposite in sign to $L_1 Z_1$ and depends only on the effective charge. In Fig. 2 are shown experimental values of $Z_2^{1/2}$ L_1 as a function of $(v/v_0)^2 Z_2^{-1}$ and theoretical values for the values of b found with the use of Pierce and Blann's effective charge for Z_C^* in Eqn. (3). Pierce and Blann's effective-charge correction gives a reasonable value (1.38) of b for ~7 MeV/nucleon which appears in the Ritchie-Brandt theory, if a χ value of 1.29 in their theory is assumed.$^{1)}$ Stopping power of Al, Ni, Ag, Au, and Pb have been measured for ~5 MeV/nucleon α particles and carbon ions. The results are presented in Table 2 and in Fig. 2. Analyses are now in progress.

Reference

1) T. Takahashi, Y. Awaya, T. Tomuma, H. Kumagai, K. Izumo, M. Nishida, A. Hitachi, A. Hashizume, S. Uchiyama, and T. Doke: Phys. Rev., A27, 1360 (1983).

III-2-18. Reactions Induced by High Energy Ions at the Pd-Si Interface

Y. Horino,* N. Matsunami,* N. Itoh,* and K. Kimura

It has been demonstrated that silicide phase is formed at the Si-metal interface under irradiation with heavy ions, e.g. 300 keV Xe ions. In order to investigate the mechanism of the ion-induced silicide formation, we have measured the Pd-silicide formation induced by H, He, and Ar ion bombardment with energies ranging from 1 keV/amu to 1 MeV/amu, using the Rutherford backscattering (RBS) of 1 MeV He ions. We have also investigated the ion-induced reactions at an Si-Pd interface with intervening SiO_2 layer. The interfaces were prepared by evaporation of Pd on a cleaned surface of Si substrate and on native SiO_2-Si substrate. The thickness of the Pd layer was determined as 200 – 400 Å and that of the SiO_2 layer was estimated to be ~10Å.

The results are summarized in Table 1, which also includes the results obtained by Mayer et al.[1] In the case of the Pd-Si interface, uniform Pd_2Si and/or PdSi layers were formed at room temperature. It was found that the formation yields of Pd_2Si per ion scale with the elastic energy deposition rates of ions at the interface. This result contradicts the prediction by the current theory, i.e. the collision mixing mechanism.

In the case of the Pd-SiO_2-Si interface, the presence of the SiO_2 layer impeded thermal growth of silicides and no reaction took place at temperatures below 200 °C. The ion-induced reaction was observed, as shown in Fig. 1, for irradiation with 40-MeV Ar ions to a dose of $5 \times 10^{15}/cm^2$ at 180 °C. The Pd spectrum shows a long tail and the Si spectrum indicates an Si-rich phase ($PdSi_4$). This result contrasts with the Pd_2Si formation by 1-MeV He and 5-keV He ion irradiation. This Si-rich phase formation can be due to high energy deposition rate into inelastic collisions (high-density excitation effect).

The ion-induced formation of Pd_2Si was observed for irradiation of 1 MeV He ions at 200 °C. The RBS spectrum for Pd shows a long tail, indicating that Pd penetrates deeply into Si, in contrast to the uniform Pd_2Si layer. Island structure was observed at the surface of this sample by a scanning electron microscope. A probable explanation for the non-uniform silicide formation is as follows: paradium passes through ion-induced damage spots which are distributed non-uniformly in the SiO_2 layer and reacts with silicon to form columnar Pd_2Si.

Table 1. Thermal and ion-induced Pd-silicide formation.

		Si-Pd		Si-SiO_2-Pd	
Thermal growth		Pd_2Si PdSi	≤ 700 °C > 700 °C	N.R.	≤ 200 °C
Ion-induced reaction	5 KeV He	Pd_2Si	R.T.	N.R. Pd_2Si	R.T. 200 °C
	300 KeV Xe	Pd_2Si PdSi	R.T.		
	1 MeV He	Pd_2Si	R.T.	N.R. Columnar Pd_2Si	R.T. 200 °C
	40 MeV Ar			Si-rich phase ($PdSi_4$)	180 °C

N.R. = no reaction,
R.T. = room temperature

---

* Department of Crystalline Materials Science, Faculty of Engineering, Nagoya University.

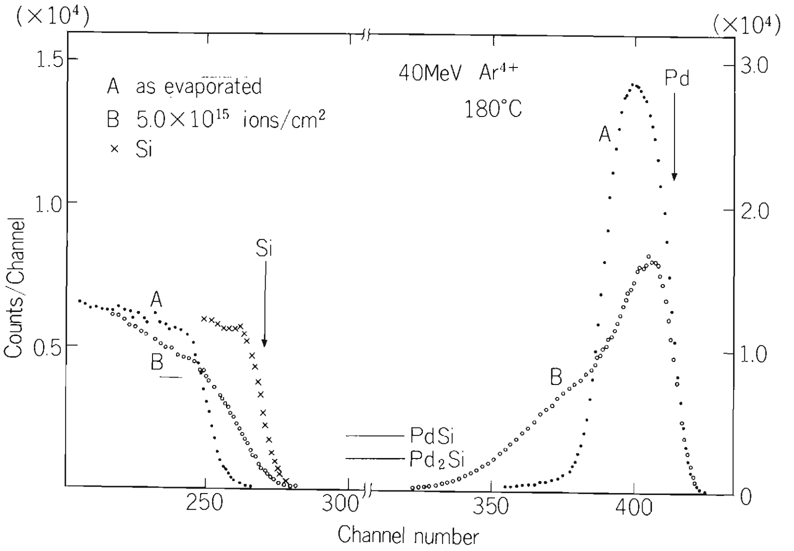

Fig. 1. RBS spectra of 1 MeV He$^+$ on Si-SiO$_2$-Pd irradiated with 40 MeV Ar$^+$ to a dose of 5 x 10^{-5} cm^{-2} at 180 °C.

Reference

1) J. W. Mayer, B. Y. Tsaur, S.S. Lau, and L. S. Hung: Nucl. Instr. Methods, 182/183, 1 (1983).

III-2-19. Emission Mössbauer Studies of Dilute ^{119}Sb Ions Adsorbed on Ferrimagnetic Cobalt Ferrite Surfaces

T. Okada, S. Ambe, F. Ambe, and H. Sekizawa

Previously, we reported results of emission Mössbauer measurement of ^{119}Sn arising from carrier free pentavalent ^{119}Sb ions hydrolytically adsorbed on surfaces of antiferromagnetic and ferrimagnetic oxides.[1),2)] The present work aims to clarify the chemical states of dilute pentavalent antimony ions hydrolytically adsorbed on the surfaces of cobalt ferrite, and also the diffusion and coagulation of the ^{119}Sb ions by heat treatments.

Mössbauer analysis was made on the 23.8 keV γ-rays emitted by the first excited states of ^{119}Sn (^{119}Sn*, half life: 17.8 ns) arising from ^{119}Sb (half life: 30.8 h) by the EC decay. Experimental procedures have already been reported in the previous reports.[1),2)] Carrier-free ^{119}Sb ions were adsorbed on the surfaces of the ferrimagnetic oxide powders of cobalt ferrite($CoFe_2O_4$), the Néel temperature of which was about 520 °C. The obtained emission spectra suffered apparent broadening compared with those of non-magnetic substrates. From analysis of the broadening of the emission spectra, the diamagnetic nuclei of $^{119}Sn^{4+}$ arising from the adsorbed $^{119}Sb^{5+}$ were shown to be under the influence of the supertransferred hyperfine fields from the magnetic ions in the ferrite. This finding indicates that the $^{119}Sb^{5+}$ ions predominantly from $Sb^{5+} - O^{2-} - M^{n+}$ bonds with the metal ions (M) of the ferrite.

Some of the observed spectra are shown in Fig. 1. These spectra were analyzed by means of Hesse-Rübartsch procedure to obtain the distributions of the hyperfine magnetic field shown in Fig. 2. Our experimental findings are summarized as follows:

(1) In "as adsorbed" state, the distribution function P(H) has large values in larger field range compared with other magnetic oxides.

(2) After 400 °C heat treatment, there appears a peak of P(H) at around 100 kOe.

(3) After 600 °C treatment, there appears a peak at around 0 kOe, which can be attributed to clustering of ^{119}Sb ions.

(4) By higher temperature treatment up to 1000 °C,

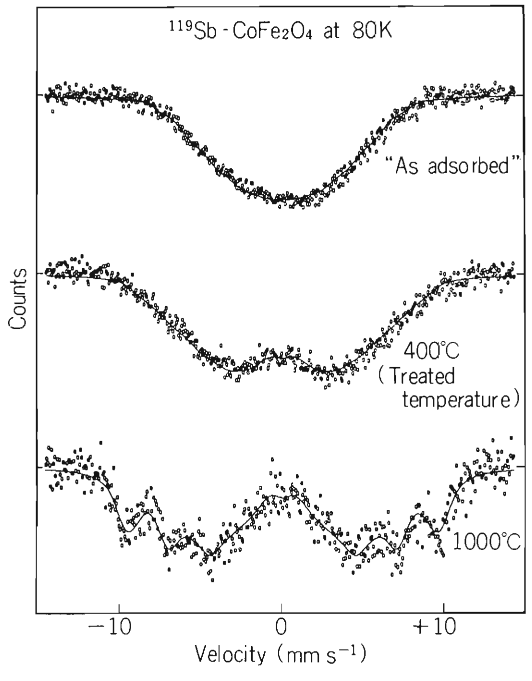

Fig. 1. Emission Mössbauer spectra of the $CoFe_2O_4 - {}^{119}Sb^{5+}$ specimens taken at liquid-nitrogen temperature.

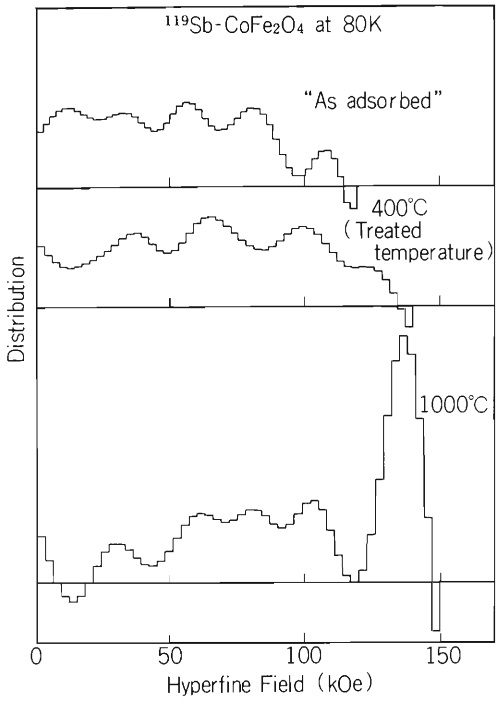

Fig. 2. Distribution of the supertransferred hyperfine (STHF) magnetic fields on $^{119}Sn^{4+}$ arising from $^{119}Sb^{5+}$ of the $CoFe_2O_4$ specimens derived from the spectra of Fig. 1.

diffusion of ^{119}Sb ions becomes remarkable, and a fairly sharp peak appears in the higher field region accompanied by a rapid decrease of distribution in lower field region below 50 kOe.

(5) The observed isomer shift is rather large compared with other magnetic oxides.

The detailed investigation, as well as similar studies on various other ferrites, is in progress.

References

1) T. Okada, F. Ambe, S. Ambe, and H. Sekizawa: J. Phys. Chem., 86, 4726 (1982).
2) T. Okada, F. Ambe, S. Ambe, and H. Sekizawa: RIKEN Accel. Progr. Rep., 16, 101 (1982).

III-2-20. Perturbed Angular Correlation of γ-Rays Emitted from ^{111}Cd($\leftarrow$ ^{111}In) in α-Fe_2O_3

K. Asai, F. Ambe, S. Ambe, and H. Sekizawa

Perturbed Angular Correlation (PAC) or γ-rays is a valuable tool not only in the field of nuclear physics but also in the field of solid state physics, because it provides useful information on the electronic states in solids through the hyperfine interactions. ^{111}Cd ($\leftarrow$ ^{111}In) is one of the most popular nuclide emitting suitable cascade γ-rays for this type of measurement and many investigations using this nuclide have been done. In these previous investigations, it has been found that well-defined hyperfine frequencies are observed for ^{111}Cd embedded in metals such as Fe$^{1)}$, Ni$^{1),2)}$, and In,$^{3),4)}$ while hyperfine frequencies are widely distributed in insulators such as In_2O_3,$^{4)}$ $In(OH)_3$$^{4)}$ and $InPO_4$.$^{3)}$ Such distribution has been ascribed to the after-effects of the preceding electron capture (EC) decay of ^{111}In; in insulators, the lifetime of the electronic holes produced by the Auger process following the EC decay is rather long and the unstable perturbed state heavily contributes to the perturbation factor.

When we apply PAC measurement to studies of magnetic oxides, above mentioned situation is very important, because their electrical conductivities are widely distributed depending on their compositions and temperatures. From this point of view, we have been measuring PAC of γ-rays emitted from ^{111}Cd in a typical antiferromagnetic oxide α-Fe_2O_3 at various temperatures. In this report, we present the data obtained at 400 °C and also preliminary results of analysis.

The sample was prepared by firing the coprecipitate from Fe^{3+} and $^{111}In^{3+}$ solution. The firing was done at 800 °C for 2 h. For a polycrystalline specimen, the perturbation factor $A_{22}(t)$ is obtained by the normalization of the time spectra N(180° , t) and N(90°, t) in the form

$$A_{22}(t) = \frac{4}{3}\{N(180°,t) - N(90°,t)\} / \{N(180°,t) + N(90°,t)\}. \qquad (1)$$

For a unique but randomly oriented static interaction, A_{22} is expressed in the form$^{5)}$

$$A_{22}(t)_{\mathrm{uniq.}} = \sum_{N,m_1,m_2,n_1,n_2} (-1)^{21+m_1+m_2} \times \begin{pmatrix} I & I & 2 \\ m_1' & -m_1 & N \end{pmatrix} \begin{pmatrix} I & I & 2 \\ m_2' & -m_2 & N \end{pmatrix} \exp\left[(-i/\hbar)(E_{n_1} - E_{n_2})_t\right] \times \langle n_1|m_2\rangle^* \langle n_1|m_1\rangle \langle n_2|m_2\rangle \langle n_2|m_1\rangle^*, \qquad (2)$$

where ( ) denotes the Wigner 3−j symbol, I the spin quantum number of the intermediate state of the ^{111}Cd, $|m_i>$ the state assigned by its z component m_i, $|n_i>$ the eigenstate of the interaction Hamiltonian $\mathcal{H}$ and E_{n_i} its energy eigenvalue. In general, $A_{22}(t)_{\mathrm{uniq.}}$ has I × (2I+1) discrete Fourier components.

The perturbation factor $A_{22}(t)$ in α-Fe_2O_3 at 400 °C was obtained by Eqn.(1). (Fig. 1(a)) We assume that A_{22} (t) is composed of two parts. One part A_{22}' (t), which is described well by Eqn.(2) ($= C_1 \times A_{22}(t)_{\mathrm{uniq.}}$), has well-defined interaction frequencies. The other part $A_{22}''(t)$ has a widely distributed frequency spectrum so that its value is constant ($= C_2$) in the region where t is sufficiently large. We obtained the values of C_1, C_2 and the parameters in the Hamiltonian $\mathcal{H}$ by least-squares fitting with the equation $A_{22}(t) = C_1 \times A_{22}(t)_{\mathrm{uniq.}} + C_2$ in the regin $t \geqq 50$ ns. It is assumed that the asymmetry of the electric field gradient (EFG) is equal to zero and that the angle between the directions of EFG and the hyperfine magnetic field, H_{hf}, is equal to 90° from consideration of the crystal symmetry of α-Fe_2O_3. The best fitted values of C_1, C_2, ω_L (the Larmor angular frequency) and ω_Q (the quadrupole angular frequency) are 0.06,

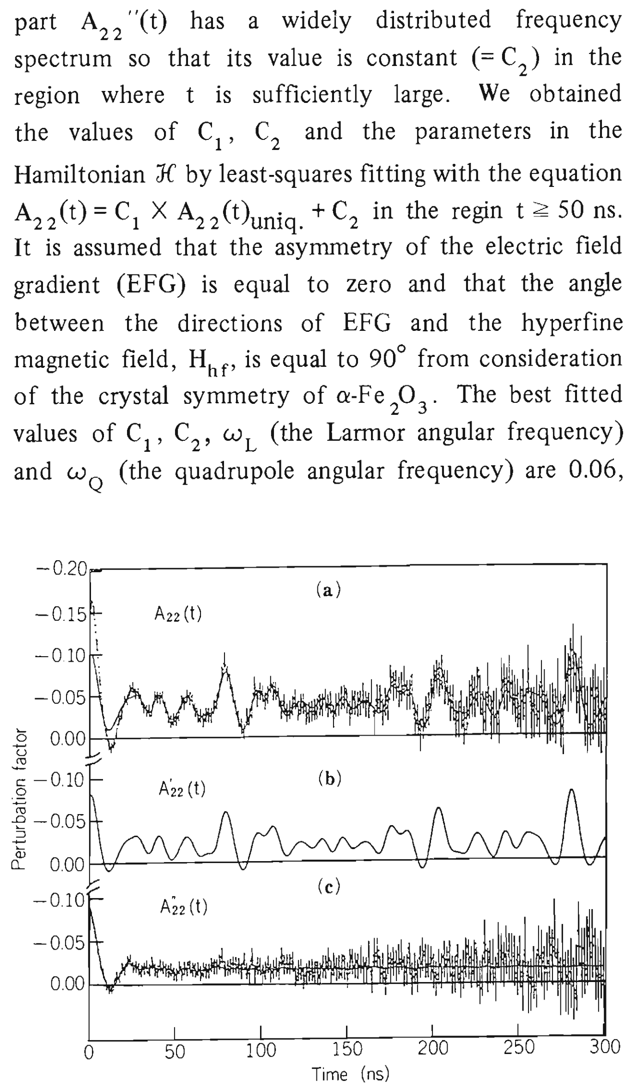

Fig. 1. (a) Perturbation factor $A_{22}(t)$ of the ^{111}Cd γ−γ correlation in α-Fe_2O_3 at 400 °C. The solid curve represents the value of $C_1 \times A_{22}(t)_{\mathrm{uniq.}} + C_2$, (b) Perturbation factor $A_{22}'(t)$. (c) Perturbation factor $A_{22}''(t)$. The solid curve represents the value calculated from the frequency spectrum in Fig. 2(b).

0.015, 8.27×10^7 rad/s and 2.52×10^7 rad/s, respectively. The hyperfine magnetic field calculated from ω_L is 54.7 kOe. $A_{22}'(t)$ and $A_{22}''(t)$ are shown in Fig. 2(a) and (b), respectively. The latter is obtained by subtracting $A_{22}'(t)$ from $A_{22}(t)$. Ratio of the former to the latter is about 0.9. Figure 2 shows the frequency spectra of $A_{22}'(t)$ and $A_{22}''(t)$. As can be seen, the spectrum of $A_{22}''(t)$ is very broad without any salient features.

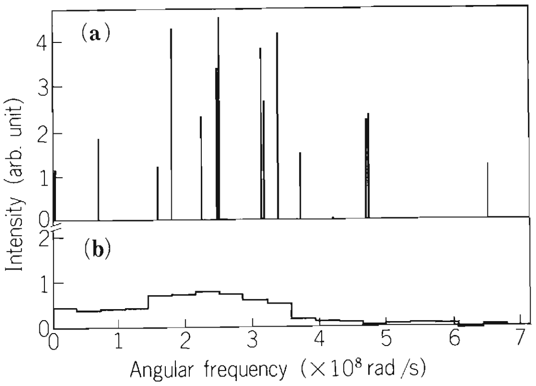

Fig. 2. Frequency spectra of (a): $A_{22}'(t)$, and (b): $A_{22}''(t)$.

It is considered that ^{111}Cd ions which contribute to $A_{22}'(t)$ retain little effect of the preceding EC decay and those which contribute to $A_{22}''(t)$ feel hyperfine interactions due to the after-effect of the EC decay. The present study shows that ^{111}Cd ions in α-Fe_2O_3 are rather clearly classified into the above two groups at 400 °C. For further discussion measurements at other temperatures are necessary which are now in progress.

References

1) R. S. Raghavan and P. Raghavan: Nucl. Instr. & Methods, 92, 435 (1971).
2) D. A. Shirley, S. S. Rosenblume, and E. Mathias: Phys. Rev., 170, 363 (1968).
3) H. Haas and D. A. Shirley: J. Chem. Phys., 58, 3339 (1973).
4) P. P. Lehmann and J. Miller: J. de Phys., 17, 526 (1956).
5) H. Frauenfelder and R. M. Steffen: $\alpha-$, $\beta-$, and $\gamma-$Ray Spectroscopy, Vol. 2, (ed. by K. Siegbahn), North-Holland, Amsterdam (1964).

III-2-21. Perturbed Angular Correlation of γ-Rays Emitted from ^{111}Cd($\leftarrow$^{111}In) in MFe_2O_4 (M=Fe, Mn, Co, and Mg)

K. Asai, T. Okada, and H. Sekizawa

It is well known that large hyperfine magnetic fields are observed at the nuclei of diamagnetic cations in magnetic materials below its magnetic transition temperature. Since the origin of these hyperfine magnetic fields H_{hf} at the nuclei is the electron-spin polarization induced by the surrounding magnetic cations, the investigation of these fields supplies important information on the exchange interactions between magnetic cations. As for ferrimagnetic oxides with the spinel structure, H_{hf} at Sn[1] and Sb[2], both occupying the B site (octahedral), have been investigated. Similar investigation of H_{hf} at the nuclei of diamagnetic ions on the A site (tetrahedral) is also desirable, because it supplies information complementary to that obtained in the previous investigations. From this point of view, we have been investigating H_{hf} at ^{111}Cd($\leftarrow$ ^{111}In) in various ferrimagnetic oxides with the spinel structure.[3],[4] In this report, we present experimental data of perturbed angular correlation of γ-rays emitted from ^{111}Cd in $M^{2+}Fe^{3+}{}_2O_4$ with M = Fe, Mn, Co and Mg.

Samples were prepared by diffusing ^{111}In into the oxides at 1250 °C for $MnFe_2O_4$ and 1150 °C for others. Specimens about 150 μCi in activity were submitted to measurement with an external magnetic field of 10 kOe applied perpendicularly to the counter plane. We measured the time spectra at $\theta = 90^\circ$ and 180°, and then obtained the normalized anisotropy R(t) defined as follows:

$$R(t) = \left\{N(90^\circ, t) - N(180^\circ, t)\right\} \Big/ \left\{N(90^\circ, t) + N(180^\circ, t)\right\},$$

where, $N(\theta,t)$ denotes the time spectrum, θ the angle between the two cascade γ-rays, t the time interval between them. For a unique and static H_{hf} oriented perpendicularly to the counter plane, R(t) is expressed in the form $R(t) = (-3/4)A_{22}\cos(2\omega_L t)$, where ω_L is the Larmor frequency.[5]

Figure 1 shows R(t) for MFe_2O_4 (M = Fe, Mn, Co, and Mg) at room temperature and Fig. 2 shows their

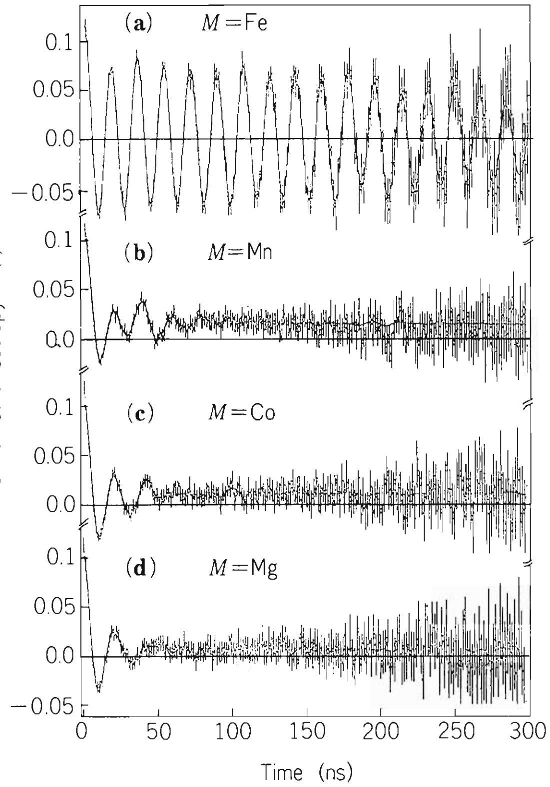

Fig. 1. Normalized anisotropy R(t) of the time spectra of $\gamma-\gamma$ cascade emitted from ^{111}Cd in MFe_2O_4. The solid curve represents the value reproduced from the frequency spectra in Fig. 2: M = (a)Fe, (b)Mn, (c)Co, and (d)Mg.

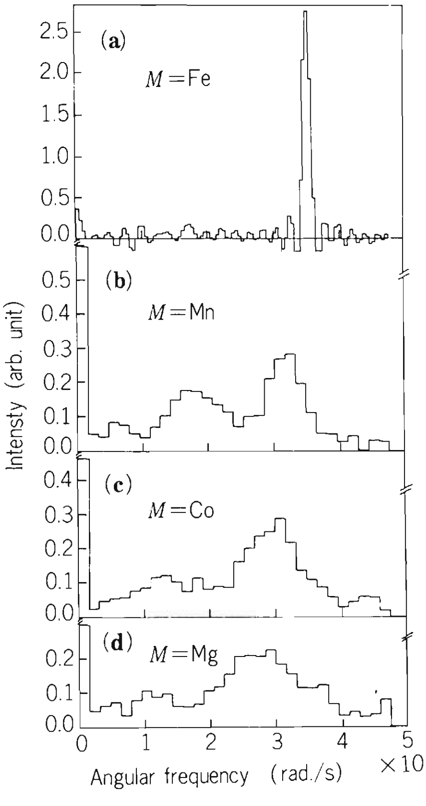

Fig. 2. Frequency spectra of R(t) for MFe_2O_4: M = (a)Fe, (b)Mn, (c)Co, and (d)Mg.

frequency spectra. For M = Fe, R(t) has a very sharp single frequency compoent at $\omega = 3.6 \times 10^8$ rad/s and the derived value of H_{hf} is equal to 118 kOe. On the other hand, for M = Mn, Co, and Mg, R(t) have very broad frequency spectra in non-zero regions and further have large and sharp components at $\omega = 0$. The latter feature can be explained by the fact that the axes of the hyperfine interactions are not parallel to the applied magnetic field at some nuclei. Since the abundance of these nuclei is estimated to be the order of a half of the total ^{111}Cd nuclei, the contribution of these nuclei to R(t) in non-zero region is not negligible. At present, it is considered that the broad peak in the higher frequency region in each spectrum is attributed to ^{111}Cd which feel H_{hf} parallel to the applied magnetic field, and the very broad plateau in the lower frequency region is attributed to that which feel some other hyperfine interactions. The values of H_{hf} corresponding to the tops of the peaks are 110 kOe, 105 kOe, and 100 kOe for M = Mn, Co, and Mg, respectively. The average of H_{hf} decreases and the width of its distribution increases in the above order of the ions M. This tendency is qualitatively explained by the magnitude of the magnetization of the ions in the B site. More detailed consideration will be given later.

References

1) G. V. Novikov, B. A. Trukhtanov, L. Cher, S. I. Yuschuk, and V. I. Goldanskii: Zhur. eksp. teor. Fiz., 56, 743 (1969).
2) B. J. Evans and L. J. Swarzendruber: Phys. Rev., B6, 223 (1972).
3) H. Sekizawa, K. Asai, T. Okada, N. Shiotani, E. Yagi, and S. Ambe: IPCR Cyclotron Progr. Rep., 10, 99 (1976).
4) H. Sekizawa, K. Asai, T. Okada, N. Sakai, N. Shiotani, and E. Yagi: ibid., 11, 106 (1977).
5) H. Frauenfelder and R. M. Steffen: α–, β– and γ – Ray Spectroscopy, Vol. 2, (ed. by K. Siegbahn), North-Holland, Amsterdam (1964).

III-2-22. Plasma Wall Interaction

Y. Sakamoto, Y. Ishibe, K. Yano, K. Okazaki,
S. Ishii, and H. Oyama

The report deals with following three works in the study of plasma wall interaction: 1) Discharge cleaning of the Tokamak first wall for the reduction of light impurities in Tokamak plasma, 2) Formation of nitride on the titanium surface as one of candidate materials for the first wall and 3) Neutral particle measurement by laser induced resonance fluorescence spectroscopy for the observation of the behavior of impurity particles.

Those works are complementarily related each other and will help in understanding the surface changes and the processes concerned with physical and chemical reactions on the surface caused by plasma irradiation.

(1) Fundamental Study of Electron Cyclotron Resonance-Discharge Cleaning (ECR-DC).

The ECR-DC method for torus devices has been developed by our group and we have also done experiments with the following apparatuses: JFT-2 (Tokai),[1] JIPP-TII (Nagoya),[2] and TEXTOR (Jülich, Fed. Rep. of Germany).[3] The purpose of obtaining clean surface wall and pure hydrogen tokamak plasma which has $z_{eff}=1$, has been achieved.

In the cleaning discharge, however, there still remain some unresolved problems. Among them we have studied the following problems; the reaction of oxygen and carbon on the surfaces with incoming H_2^+ and H^+ ions, the behaviors of organic substances on the surface, and the depth profile of light elements near the surface.

i) Investigation of the reaction of carbon with hydrogen molecular and atomic ions.

The carbon peak was observed by Auger electron spectroscopy before and after irradiating a stainless steel surface with hydrogen ion beam of energy 100 eV. In the case of H^+ ion irradiation with dose $10^{18}/cm^2$, the carbon peak height was reduced drastically, but in the case of H_2^+ ion irradiation it did not change at all with the same dose. It is shown that H_2^+ ions in a plasma with low energy (< 100 eV) have no chemical cleaning effect on carbon.

ii) Study on the behaviors of organic substances

The surface exposed to atmosphere is usually contaminated by organic substances. We studied how these organic substances on the surface of JIPP-TII tokamak are removed by ECR-DC, using a quadrupole mass analyzer (QMA). The mass spectra of the gases desorbed by the cleaning discharge were examined by comparing with standard cracking patterns of QMA. These were identified as methane, water and carbon monoxide. The others were presumed as ethylene, propylene and carbon dioxide. The origin of these hydrocarbons is explained as follows: Organic substances on the surface are initially long chain hydrocarbons. Being bombarded by energetic particles from the plasma, they are cut short into fragments and desorbed. The bonding energy of single bond of the carbon chain is 3.44 eV and the energy of incident particles is about 5 eV, which is high enough to cut the bond.

iii) Depth profiles of light elements near the surface.

We studied wall samples to see whether there remained some effects of discharge cleaning after the samples had once been exposed to the atmosphere by measuring the depth profiles of light elements near the surface using the Rutherford scattering method with RILAC.

For CuO, the depth profiles of oxygen of the wall samples differed from those of the reference samples. In Fig. 1 examples of measured depth profiles are shown. The difference in the profiles is due to the effect of ECR-DC. For the stainless steel samples, there was no difference in the depth profiles from those of the wall reference samples. In this case the effect of ECR-DC is obscured after the samples are once exposed to atmosphere. It is supposed that exposure to air resulted in reoxidization of the surface cleaned by ECR-DC to have the oxide layer with the same thickness as before.

(2) Preparation of TiN samples

TiN samples were prepared by following two method.

i) In one method samples of titanium nitride were prepared by nitriding titanium plates by chemical reaction with nitrogen ions produced by arc plasma. The schematic diagram of the apparatus for the reaction is shown in Fig. 2. Working gases were N_2 and H_2. Their mixing ratio was 6 : 1, and the total pressure was 80 Pa. The typical discharge voltage and current density were 600 volts and $10 mA \cdot cm^{-2}$, respectively. The sample temperature rose up to about 800 °C by discharge and this was appropriate for nitriding. XPS and Rutherford scattering observation show formation of a very thick nitride layer on the sample. Determination of the thickness is being carried out.

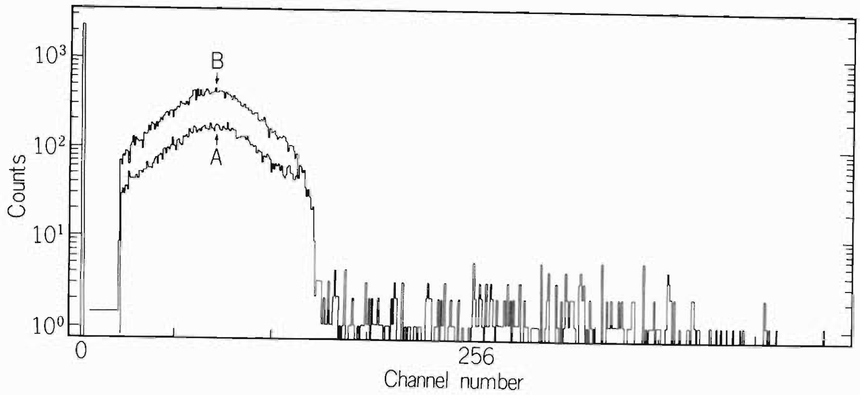

Fig. 1. The oxygen depth profiles of CuO samples measured by the Rutherford scattering method. Curves are obtained (A) with discharge cleaning and (B) without discharge cleaning reference samples. The scale of pulse counts is normalized to incident ion doses.

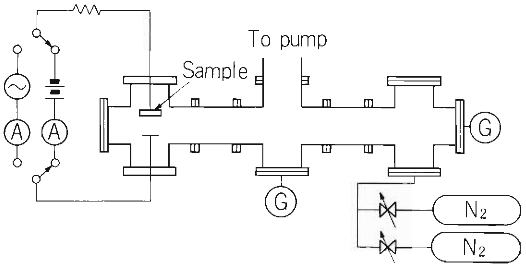

Fig. 2. The schematic diagram of the apparatus for making the TiN by PCVD.

ii) In the second method, nitrides were produced by cluster ion bombardment. Surface treatment by the interaction of energetic cluster ions with solid surfaces recently arise interest in its application to surface coating. The mean cluster size used was about 3×10^4 molecules/cluster. Nitriding conditions were as follows: The cluster ion current was 0.6 μA. This means that the particle current was 1.1×10^{17} molecules/sec. The accelerating voltage of ions was 27.5 kV. The temperature of the titanium was about 400 °C.

After 2 hr's bombardment, the surface was examined by ESCA (electron spectroscopy for chemical analysis). It was found from this analysis that a part of the surface was nitrided, and the ratio of N to Ti was less than 0.5. The preliminary result suggests that nitrides can be effectively produced by bombarding with intense cluster ion beams.

(3) Neutral particle measurement in the gas phase

For the purpose of understanding how materials interact with plasmas or how they react under the irradiation with accelerated heavy ion beams, the study of the behavior of atoms in the gas phase released from the material surfaces gives very useful information. For this purpose, we have adopted laser induced resonance fluorescence spectroscopy (LFS) to measure neutral atom densities and velocity distributions close to the material walls. This method has extremely high sensitivity and moreover it is not affected by ambient plasma parameters. So far an LFS measurement system has been constructed which is composed of a dye laser and a fluorescence detection part. In 1984 this LFS system is to be applied to measure the iron neutral atom density near a stainless steel sample which is irradiated by a plasma with energy around the sputtering threshold. The result will be compared with the sputtering yield data of monochromatic energy.

References

1) Y. Sakamoto, Y. Ishibe, K. Yano, and H. Oyama et al.: J. Nucl. Mater., 93 & 94, 333 (1980).
2) Y. Sakamoto, Y. Ishibe, S. Ishii, K. Okazaki, H. Oyama, and K. Yano et al.: ibid., 111 & 112, 485 (1980).
3) S. Ishii, K. Okazaki, Y. Sakamoto, and K. Yano: Jpn. J. Appl. Phys., 22, L403 (1983).

III-2-23. Studies of a-Si : H Growth Mechanism by Rutherford Recoil Measurement of H and D in Films Prepared from SiH_4-D_2 and SiD_4-H_2

Y. Yatsurugi,* O. Kuboi,* M. Hashimoto,* H. Nagai,
M. Aratani, M. Yanokura, I. Kohno, and T. Nozaki

Hydrogenated amorphous silicon (a-Si : H) prepared by glow discharge$^{1)}$ in a gas mixture of SiH_4 and H_2 has been studied extensively as a new semiconductor material. For the improvement and control of the characteristics of this substance, it is essential to elucidate its growth mechanism.$^{2)-4)}$ We used deuterium as a tracer to study the growth mechanism, determining H and D contents of the product a-Si : H film by Rutherford forward recoil measurement.$^{5)-6)}$ Using samples prepared from SiH_4-D_2 mixtures and from SiD_4-H_2 mixtures, we clearly determined the origin of the hydrogen in the film.

The same glow discharge system as in the literature$^{7)}$ was used. The substrate for the a-Si : H deposition was a high-purity silicon wafer, and its temperature was set at 250 °C. The Rutherford recoil was measured in a scattering chamber. The experimental arrangement is described in detail in a preceding report$^{8)}$ of this volume.

An example of H and D spectra is shown in Fig. 1. Standard error in the total counts taken for hydrogen in our experiment corresponded to ± 0.1 atomic percent. Since the energies of detected H and D are dependent on the depth in the sample where they were recoiled, the shapes of the recoil spectrum give information about their depth profiles.

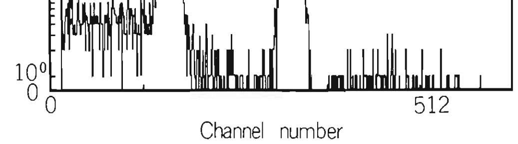

Fig. 1. A Rutherford forward recoil spectrum for H and D. Reactant gas for a-Si samples: SiH_4 (1 vol) + D_2 (4 vol)

The technique of coincidence detection of recoiled and scattered particles was employed, in order to ascertain the reliability of the quantity of H obtained as above. A-Si : H films of 2250 Å in thickness prepared on several thin aluminium backings were bombarded with a 45 MeV ^{3}He particle beam, and recoiled H particles were detected in coincidence with the correspondingly scattered ^{3}He particles. A polyethylene film of 0.90 mg/cm^2 in thickness was used as the reference substance. The argon beam method and the ^{3}He coincidence method gave results of 14.7 atomic percent and 14.4 atomic percent respectively, which can be regarded as a good agreement.

The relation between the RF power for glow discharge and H and D concentrations in a-Si : H is shown in Figs. 2 and 3 for the discharge in a SiH_4(1 vol)–D_2(4 vol) mixture. It is clear that more H atoms than D atoms were incorporated in the amorphous silicon in low RF power region. With increase in the RF power, isotopic fraction of H decreases, while the fraction of D increases. The correlation between the isotopic composition of the reactant gas and that of the product amorphous silicon is shown in Fig. 4 for the RF power relatively high in the present study but usual in practical a-Si : H production. The isotopic compositions of the reactants and the products in such a RF power range are shown to be almost equal regardless of both isotopic ratio and initial chemical forms of H and D in the reactant gas.

From these results, we can infer the following mechanisms for the growth of a-Si : H under the RF glow discharge in a $SiH_4 - H_2$ mixture. In low RF power region, the SiH_4 is not decomposed completely into Si and H but SiH_n (n = 1 ~ 3) are also formed. The SiH_n arriving at the surface of the growing a-Si : H reacts with it, and is then incorporated in the product. This is regarded as the principal growth mechanism for low RF power.

With the increase in the power, the decomposition of SiH_4 and H_2 proceeds more completely into atoms

---

* Komatsu Electronic Metal Co.

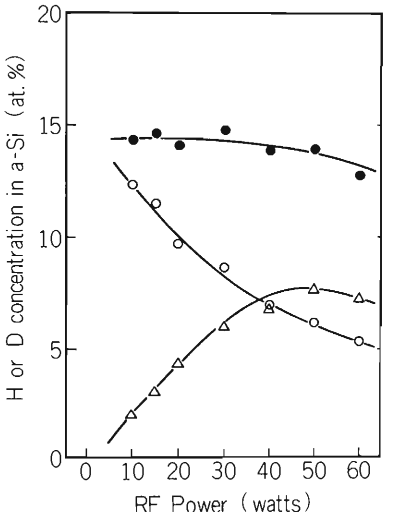

Fig. 2. Concentrations of H and D in a-Si vs RF power. Reactant gas for a-Si samples:

SiH_4 (1 vol) + D_2 (4 vol)

●: H + D, ○: H, △: D

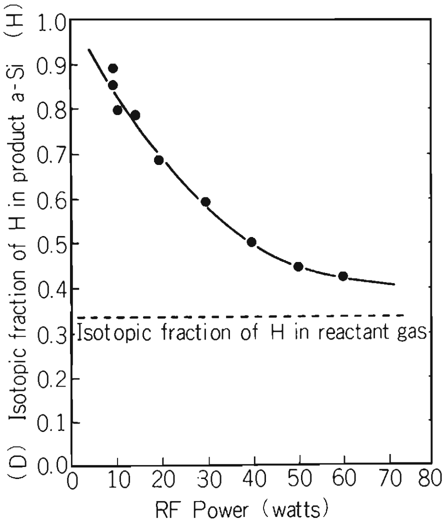

Fig. 3. Isotopic fraction of H in a-Si vs RF power. Reactant gas for a-Si samples:

SiH_4 (1 vol) + D_2 (4 vol)

Isotopic fraction of H in reactant gas

$$: \frac{[H]}{[H] + [D]}$$

and ions of Si and H. The Si is deposited and H is chemisorbed on the growing a-Si : H surface, and a part of the hydrogen atoms are incorporated in the product. In such a RF power region which gives the results of Fig. 4 the decomposition is so complete that the reactive H can behave independently of its origin.

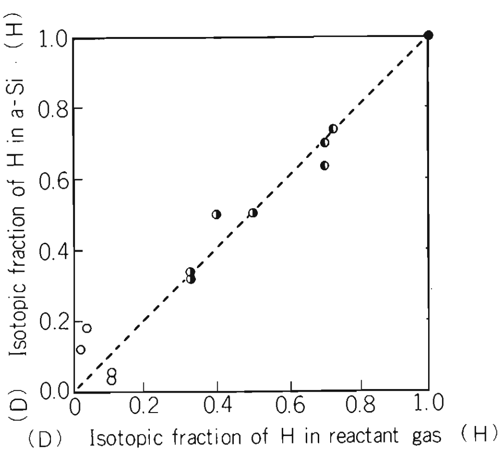

Fig. 4. Isotopic fraction of hydrogen in reactant gas and product a-Si in the region of high RF power.

○: SiD_4 + (D_2), ◐: $SiD_4 + H_2$, ◑: $SiH_4 + D_2$, ●: SiH_4 + (H_2).

It is seen in Fig. 2 that the concentration of total hydrogen (H + D) in the a-Si : H was almost independent of the RF power. This concentration seems to be determined by some other factors, for example, substrate temperature. Deuterium can be used effectively for further study of a-Si : H growth. No serious attention needs to be paid to kinetic isotope effect, as is understood from Fig. 4, but marked and predictable change is caused in the IR absorption band by H-to-D replacement.

References

1) W. E. Spear and P. G. LeComber: Philos. Mag., 33, 935 (1976).
2) F. J. Kampas: J. Appl. Phys., 53, 6408 (1982).
3) A. Matsuda, K. Nakagawa, K. Tanaka, M. Matsumura, S. Yamasaki, H. Okushi, and S. Iizima: J. Non-Cryst. Solids, 35-36, 183 (1983).
4) G. Turban, Y. Catherine, and B. Grolleau: Thin Solid Films, 77, 287 (1981).
5) J. L'Ecuyer, C. Brassard, C. Cardinal, J. Chabbal, L Deschenes, and J. P. Labrie: J. Appl. Phys., 47, 381 (1976).
6) H. Nagai, M. Aratani, T. Nozaki, M. Yanokura, I. Kohno, O. Kubori, and Y. Yatsurugi: RIKEN Accel. Progr. Rep., 16, 125 (1982).
7) O. Kuboi: J. Electrochem. Soc., 130, 1749 (1983).
8) H. Nagai, M. Aratani, S. Hayashi, T. Nozaki, M. Yanokura, I. Kohno, O. Kuboi, and Y. Tatsurugi: p. 102 in this report.

III-2-24. Depth Profiling of Hydrogen in Solids by Using Nuclear Reaction $^{1}H(^{11}B, \alpha)\alpha\alpha$

E. Yagi, T. Kobayashi, and S. Nakamura

In the present study the depth distribution of hydrogen in amorphous Si was measured by using nuclear reaction $^{1}H(^{11}B, \alpha)\alpha\alpha$. Hydrogen in amorphous Si plays an important role in reducing the density of dangling bonds. Then the p-n control by impurity doping becomes possible. The nuclear reaction mentioned above exhibits a narrow resonance at the energy 1.793 MeV of ^{11}B beam. The resonance width is about 66 keV, which corresponds to the thickness of about 640 Å in Si. Hydrogen can be detected by measuring emitted α-particles, energy of which extends up to about 5 MeV. From the yields of emitted **α**-particles measured by changing the incident energy of ^{11}B beam, the depth distribution of hydrogen can be deduced.

A specimen was mounted at an angle of 45° with respect to the incident beam. The emitted α-particles were measured by a solid state detector placed at an angle of 90° with respect to the incident beam. In front of the detector a Mylar foil of 4 μm in thickness was placed to detect only α-particles. The amorphous Si specimens were prepared by growing the amorphous layer on the Si crystals in SiH_4 atmosphere by glow discharge method. They were supplied by Komatsu Electronic Metals Co., Ltd. On four specimens prepared under different conditions the dependence of the α-particle yield on the incident energy of ^{11}B beam was measured. The results are shown in Fig. 1. Although the energy scale on the abscissa is not transformed into the depth scale, 1.793 MeV corresponds to the specimen surface. The four specimens are devided into two groups with respect to the flow rate of SiH_4 gas in preparation of specimens, which were 5 cm^3/min and 2 cm^3/min (Fig. 1 (a) and 1 (b)). To each group belong two specimens. One of them was prepared without hydrogen gas and the other by flowing hydrogen gas at a flow rate of 45 – 48 cm^3/min. Figure 1 seems to indicate that the difference in flow rate of SiH_4 gas has no strong effect on the hydrogen concentration, but the hydrogen gas flow rate has rather strong effect to the resultant hydrogen concentration, although measurement was not made on many specimens. The detailed investigation is in progress.

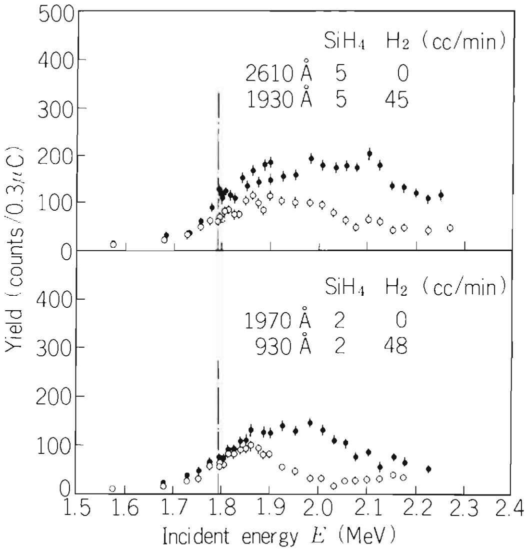

Fig. 1. α-particle yield as a function of the incident energy of ^{11}B beam. The conditions for preparation of the amorphous Si layer, i.e. the flow rates of SiH_4 and H_2 gases and the thickness of the layer, are indicated in the figure.

III-2-25. Lattice Location of Hydrogen in Tantalum as Observed by Channeling Method Using Nuclear Reaction $^{1}H(^{11}B, \alpha)\alpha\alpha$

E. Yagi, T. Kobayashi, S. Nakamura,
Y. Fukai,* and K. Watanabe*

Direct determination of the lattice location of hydrogen in metals has been made for the first time. Hydrogen diffusion in solids is an important problem because of the great theoretical and technological interest, e.g. tritium permeation in fusion reactor materials, hydrogen embrittlement of metals, etc. The lattice location of hydrogen is closely related to its diffusion behavior. Therefore the detailed knowledge on the location is required. There have been several experiments on the location of deuterium in metals by means of neutron scattering or channeling methods, while no experiments have hitherto been made on hydrogen because of experimental difficulties in detecting hydrogen. But, it became possible to locate hydrogen by using high energy heavy ion beam. In the present investigation the nuclear reaction $^{1}H(^{11}B, \alpha)\alpha\alpha$ was applied to detect hydrogen. This nuclear reaction exhibits a narrow resonance at the energy 1.793 MeV of ^{11}B beam. The hydrogen can be detected by measuring the emitted α-particles. In order to locate hydrogen this nuclear reaction was combined with channeling effect of incident ^{11}B beam. The lattice location of hydrogen can be determined from the measurement of angular dependence of the backscattering yield of ^{11}B beam and the yield of emitted α-particles. In the present investigation the lattice location of hydrogen dissolved in a tantalum crystal $TaH_{0.08}$ was determined. For channeling analysis 2.08 MeV $^{11}B^{2+}$ beam was used. A $TaH_{0.08}$ single crystal mounted on a three-axis goniometer was set so that the specimen surface makes an angle of about 45° with respect to the incident beam direction. The backscattered ^{11}B beam was measured by a solid state detector (SSD) placed at a scattering angle of 150°. The emitted α-particles, the energy of which extends up to about 5 MeV, were measured by another SSD placed at an angle of 90° with respect to the incident beam. In front of the latter SSD a Mylar foil of 4 μm in thickness was placed to stop the scattered ^{11}B beam and for only the emitted α-particles to be detected. The angular scan was made for < 100 > and < 110 > axial channels, and {100} and {111} planar channels. The results are shown in Fig. 1, where projections of octahedral (O) and tetrahedral (T) interstitial sites on the plane perpendicular to each channel are also shown. Hydrogen in a bcc crystal is expected to be located at a T-site or an O-site. The different angular profiles of emitted α-particles are expected for the O-site occupancy and the T-site occupancy. The detailed dis-

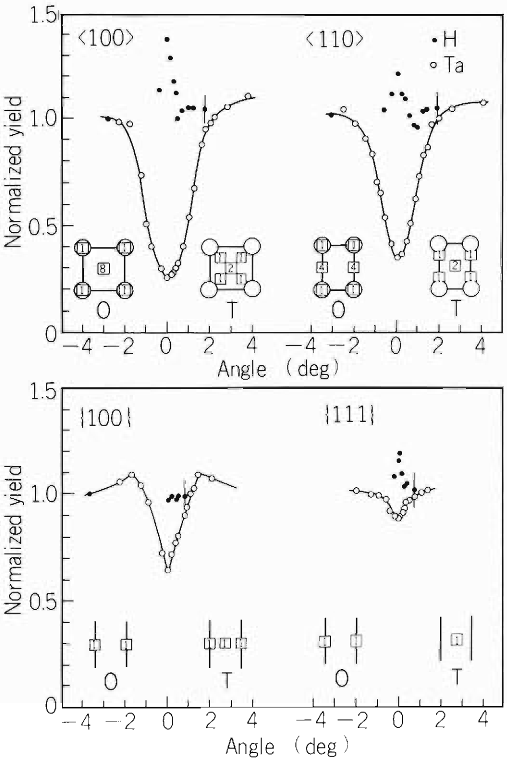

Fig. 1. Angular scans of backscattered ^{11}B and emitted α-particles across <100> and <110> axes, and {100} and {111} planes in a $TaH_{0.08}$ crystal. The incident energy of ^{11}B beam is 2.08 MeV. The insets in the figure indicate the projection of the octahedral (O) or tetrahedral (T) interstitial sites on the plane perpendicular to the related axes or planes. The circles and the lines represent the projections of atomic rows, and those of atomic planes, respectively. The squares represent the projected positions of the interstitials with their relative weights which are indicated by numbers in the squares.

---

* Faculty of Science and Engineering, Chuo University.

cussion is given Ref. 1. An unambiguous result was obtained for the {111} planar channel. All of O-sites are shadowed by the {111} planes, while all of T-sites are located at the center of the {111} planar channel. Therefore a dip is expected for the O-site occupancy, while a central peak for the T-site occupancy. The observed result clearly shows a central peak. The result is definitely in favor of the T-site occupancy. The results of angular profiles for other channels are also in favor of the T-site occupancy.

Reference

1) E. Yagi, T. Kobayashi, S. Nakamura, Y. Fukai, and K. Watanabe: J. Phys. Soc. Japan, 52, 3441 (1983).

III-2-26. Annealing of Cd-Implanted GaP

K. Aono, M. Iwaki, and S. Namba

In our previous report, radiation damage and Cd-depth profiles in Cd-implanted GaP have been investigated by means of 1.0 MeV and 1.5 MeV ^{4}He channeling technique, using the TANDETRON.[1]

Substrates used were a number of < 111 >, < 110 >, and < 100 > orientated n-type GaP. Cadmium-implantations were performed with the dose range from 1×10^{13} to 1×10^{16} cm^{-2} at the energy of 150keV. The ion beam was sent in a direction deviating by a few degrees from each crystal axis in order to reduce the deep penetration of implanted-Cd by channeling. The target during implantation was held at room temperature (as-implanted specimens) in some cases and at about 350 °C (hot-implanted specimens) in others.

The Cd depth profiles in the random spectra of as-implanted and hot-implanted specimens are similar and are Gaussian. No difference is exhibited between the random and the aligned spectra of the as-implanted specimens for < 111 >, < 110 >, and < 100 > substrates. However, in the scattering yield from the hot-implanted specimen, the aligned spectra of the specimens show a strong reduction. The result shows that most of Cd atoms occupy substitutional lattice sites in the case of hot implantation.

Radiation damages in Cd-implanted GaP were investigated from the spectra obtained from Ga in GaP. No difference is exhibited between random yields of 10^{16} Cd cm^{-2} implanted and un-implanted < 110 > substrates, as shown in Fig. 1 (a). The random yields of < 111 > and < 100 > substrates implanted with 10^{16} Cd cm^{-2} are comparatively lower than those of un-implanted specimens near the surface layer, as shown in Fig. 1 (b).

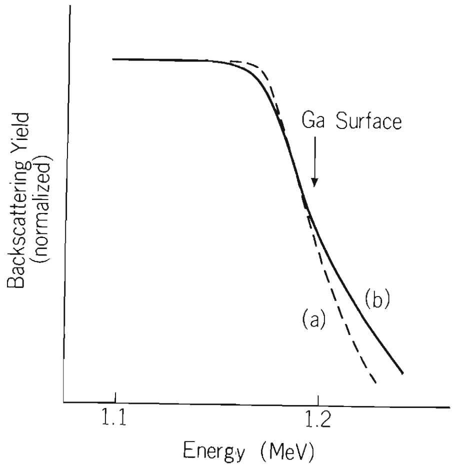

Fig. 1(a). Random spectra of Ga atoms in Cd-implanted <110> GaP.
(a) the un-implanted specimen.
(b) the 10^{16} cm^{-2} Cd-implanted specimen.

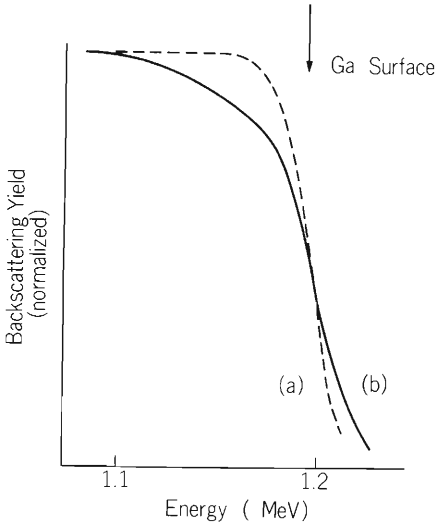

Fig. 1(b). Random spectra of Ga atoms in Cd-implanted <111> GaP.
(a) the un-implanted specimen.
(b) the 10^{16} cm^{-2} Cd-implanted specimen.

We can conclude that radiation damage in as-implanted specimens depends on the orientation of substrates. Analytical treatment for this is in progress.

Reference

1) K. Aono, M. Iwaki, and S. Namba: RIKEN Accel. Progr. Rep., 16, 111 (1982).

III-2-27. Defect-Impurity Interaction in Sn-Implanted Al

E. Yagi and S. Nakamura

The ion implantation method is a well-developed technique for modifying the surface layer of materials. Ion implantation introduces impurities and simultaneously lattice defects. The implanted atoms would be associated with implantation-introduced defects through the interaction between them. The defect-impurity interaction plays an important role in determining the lattice location of implanted atoms. Therefore, from the study on the lattice location of implanted atoms we can obtain information on the defect-impurity interaction in metals implanted with impurities.

In the present study the lattice location of Sn atoms implanted into Al crystals was investigated by means of channeling method and the microstructures of implanted region was observed by a transmission electron microscope. The implantation of Sn^+ was made at 150 kV with dose of $1 \times 10^{14}/cm^2$, $4 \times 10^{14}/cm^2$ or $1 \times 10^{15}/cm^2$ at room temperature. Backscattering-channeling angulur scan was made with respect to < 100 >, < 110 >, and < 111 > axial channels with 1 MeV He^+ ion beam. The typical angular profiles for the < 110 > axial channel for three different implantation doeses are shown in Fig. 1. In the case of implantation with $1 \times 10^{14} Sn/cm^2$, angular scan of backscattering yield from Sn atoms exhibits dips with minimum yield $\chi_{min}^{Sn} = 0.5 - 0.6$ and with smaller half-width than the Al-dips in three axial cases. In the case of implantation with $4 \times 10^{14} Sn/cm^2$, χ_{min}^{Sn} increases to 0.75 – 0.87 and is different with channel. A < 110 > angular profile of backscattering yield from Sn atoms shows a small central peak. For implantation with $1 \times 10^{15} Sn/cm^2$, angular scan of backscattering yield from Sn atoms gives a dip with $\chi_{min}^{Sn} \cong 0.87$ and with the same half-width as that of the Al-dip in each of three axial channeling cases. Electron micrographs are shown in Fig. 2. In the case of implantation with $5 \times 10^{14} Sn/cm^2$ and $1 \times 10^{15} Sn/cm^2$, small precipitates of diameter several tens Å are observed. In the latter case the precipitates are a little larger and voids are also observed.

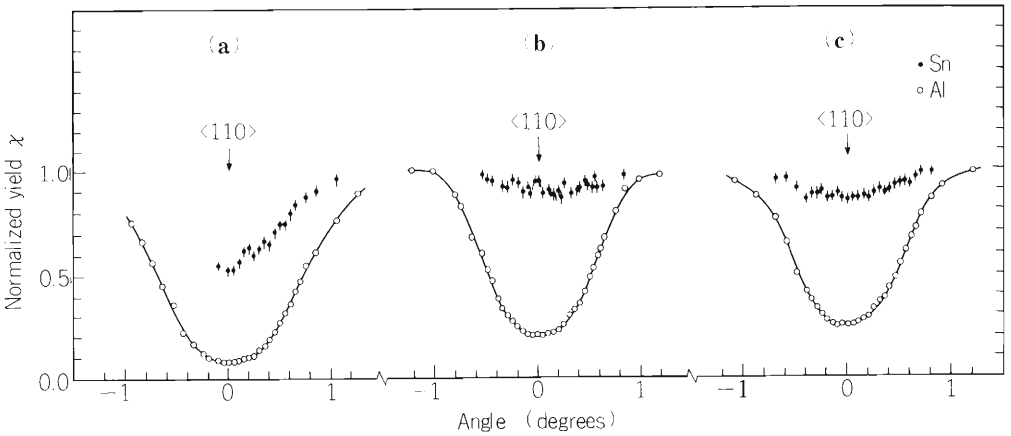

Fig. 1. <110> angular profiles of backscattering yield from Al and Sn atoms in the Sn-implanted specimens with dose of (a) 1×10^{14} Sn/cm^2, (b) $4 \times 10^{14} Sn/cm^2$ and (c) $1 \times 10^{15} Sn/cm^2$.

From the analysis of angular profiles of Sn-dips, the lattice location of Sn atoms are determined as follows: in the case of $1 \times 10^{14} Sn/cm^2$ implantation, about 35 % of Sn atoms are at substitutional sites, 50 % at random sites, i.e. in the form of precipitates, and remaining 15 % at interstitial positions displaced in the < 112 > or < 114 > direction by about 0.68 Å from a lattice point. In the case of $4 \times 10^{14} Sn/cm^2$ implantation, a certain fraction of Sn atoms are at both tetrahedral and octahedral interstitial sites, and the others are at the interstitial positions mentioned above, substitutional sites and random sites. In the case of $1 \times 10^{15} Sn/cm^2$ implantation, 19 % of Sn atoms are at substitutional sites and 81 % at random sites. To

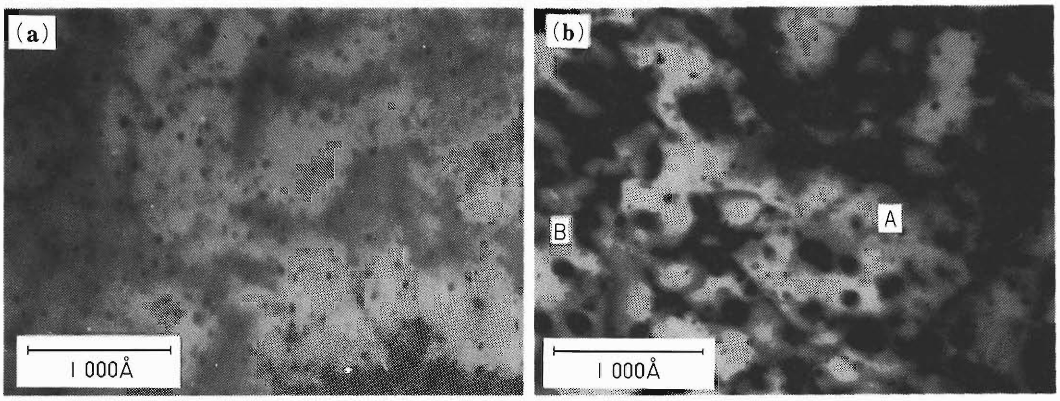

Fig. 2. Electron micrographs of Sn-implanted Al crystals. Implantation dose is 5×10^{14}Sn/cm^2 in (a) and 1×10^{15}Sn/cm^2 in (b). In the latter case precipitates (A) and voids (B) are observed.

sum up, most of Sn atoms are located at random sites and substitutional sites in any case of three different implantation doses. In the case of high dose only such two kinds of sites are occupied, while in the case of low dose the interstitial positions displaced in the $<112>$ or $<114>$ direction are also occupied in addition. In the case of medium dose, tetrahedral and octahedral sites are occupied in addition to the three kinds of sites described above. Sn atoms are known to interact strongly with vacancies. The lattice locations of Sn atoms at interstitial positions are interpreted as follows from the point of view of defect–impurity interaction.

In the case of 1×10^{14}Sn/cm^2 implantation the displacement of Sn atoms into interstitial positions in the $<112>$ or $<114>$ direction is induced by trapping a divacancy. In the case of 4×10^{14}Sn/cm^2 implantation, a certain fraction of Sn atoms are displaced into T- or O-sites by trapping more than two vacancies to form a trivacancy or pentavacancy configuration.

III-2-28. Wear Properties of Nitrogen-Implanted Steels

M. Iwaki

The principal industrial use of small accelerators at the present time is restricted to implanting impurities in the Si-wafers for making semiconductor devices. However, this ion implantation technique has a high potentiality for introducing desired atomic species into near-surface layers of a material without a thermal equilibrium process. For these ten years, therefore, modifications of metals by ion implantation have been carried out in the fields of basic researches on aqueous corrosion, oxidation, catalysis, adhesion etc. without economic benefits. Some technological areas, where such a process can be applied with commercial justification, have been selected and recently one of them is considered to be tribology. This report introduces the improvement of the wear resistance in various steels by nitrogen molecule ion implantation.

Steels used as substrates were SKD61 (Fe-5%Cr – 15%Mo), maraging steels (M1, M2: Fe – 18%Ni – 5%Mo – 8%Co) and preharden steels (P1: Fe – 3%Ni – 1%Al, P2: Fe – 5%Cr – 1%Mo), which were mechanically mirror-polished by a buffing wheel with 0.3 μm diamond paste. Ion implantation was carried out with a dose of 1.5×10^{17} N_2/cm^2 at an energy of 150 keV, whose condition corresponds to a dose of 3×10^{17} N/cm^2 at an energy of 75 keV. The target temperature during ion implantation gradually rose from room temperature and reached about a hundred degrees of centigrade by the heating effect of the ion beam itself.

Wear tests were carried out under unlubricated conditions at atmospheric room temperature by using a pin-on-disk configuration test equipment as illustrated at the upper and left part in Fig. 1. One of two contacting materials was always an un-implanted pin, which was made of a high carbon steel (S45C) with a half sphere of diameter 5 mm. The test pin was kept in contact with the surface of a disk, which was rotated continuously at a constant velocity of 105 mm/s. The amount of wear was measured by loss in weight before and after wear tests.

Figure 1 shows the wear amounts of un-implanted and N_2-implanted tool steels. The normal applied load was 0.71 kgf and the sliding distance was 69 m. The results show that nitrogen ion implantation reduced the wear amounts for all of the specimens although their reduction rates were different among specimens. These implanted specimens indicated the decrease in the friction coefficient during wear testing and the essential increase in Knoop hardness. The improvement of wear resistance, decrease in friction coefficients and increase in hardness can be explained by formation of iron-nitride caused by nitrogen implantations.

These results suggest the possibility of practical applications of ion implantation to engineering tools.

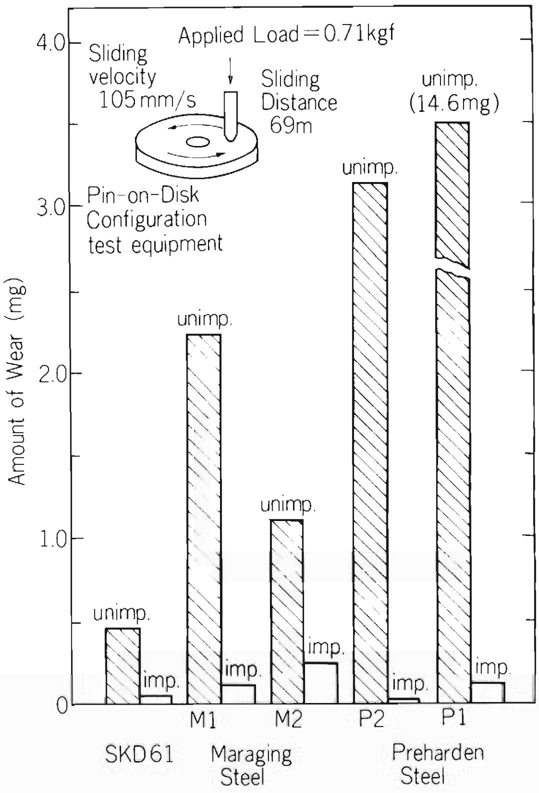

Fig. 1. Amount of wear loss on nitrogen implanted SKD61, maraging steels and preharden steels. Nitrogen molecule ion implantation was carried out with a dose of $1.5 \times 10^{17} N_2/cm^2$ at an energy of 150 keV. Wear conditions are indicated in the figure.

III-2-29. Irradiation Creep Experiments under 16 MeV Proton Bombardment in a Torsional Creep Apparatus

J. Nagakawa, H. Shiraishi, I. Uchiyama,* H. Kamitsubo,
I. Kohno, and T. Shikata

Materials undergo a slow plastic deformation even with a small load when the temperature is rather high. This phenomenon is known as "creep". Creep of a material is one of the essential data imperatively needed for designing a machine to be used at high temperatures with that material. This creep deformation is known to be significantly enhanced when the material is irradiated with energetic particles. When irradiated, atoms are displaced from their lattice sites and absorbed by dislocations, resulting in an enhanced deformation if stress is applied. This phenomenon is called "irradiation creep" and is particularly important for the structural materials of the fusion reactors because those materials will be under both stress and irradiation at a rather high temperature.

Since it is impossible to evaluate the irradiation creep using the present fusion devices because of their very short operation time, a simulation study by a light-ion bombardment is desired. For this purpose, a sensitive creep testing apparatus is newly constructed and connected to the cyclotron. The mechanism of the apparatus is schematically shown in Fig. 1. Controlled torque is applied on a thin wire sample (~130 μm dia.) utilizing the mechanism of a movable-coil DC current meter. Rotation of the sample is continuously monitored by an optical transducer attached to a turntable which follows the small mirror connected to the torque coil. An on-line computer in the instruments room controls the coil current and also processes the rotation data as well as the beam current. Temperature of the sample is controlled by a high temperature helium jet (~100 m/s) and, if necessary, an additional direct joule heating. The general features of the torsional irradiation creep facility are listed in Table 1.

Irradiation creep experiments were carried out for a 20 % cold-worked 316 stainless steel which has been used in some experimental fusion devices. The chemical composition of the sample is shown in Table 2. Bom-

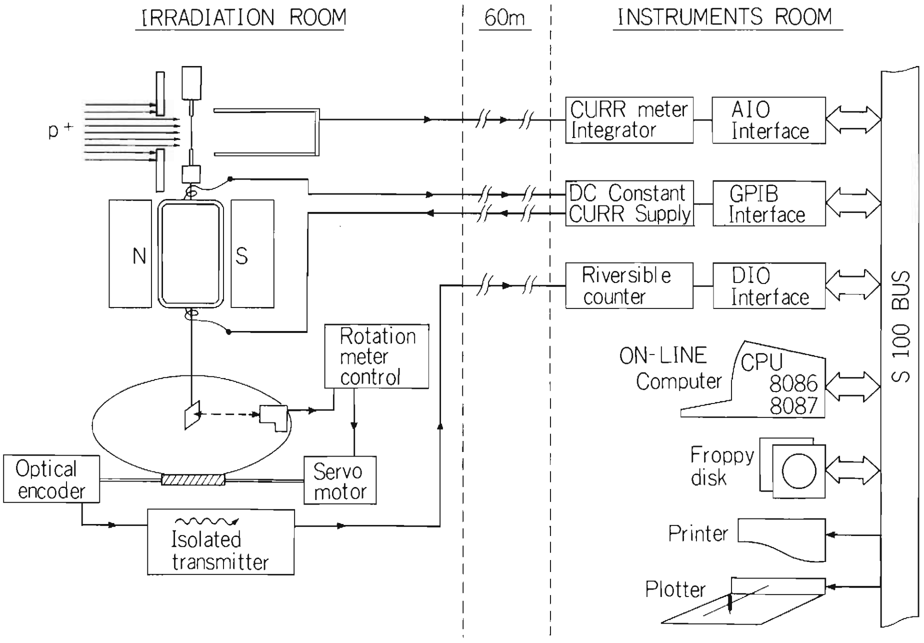

Fig. 1. Schematic figure of the loading and measuring components of the torsional irradiation creep facility. Other components not shown here include chamber, helium gas loop, beam monitors and so on.

---

* National Research Institute for Metals.

barding particles were 16 MeV protons which are the best to simulate the irradiation by 14 MeV neutrons produced by the deuterium-tritium fusion reaction. Figure 2 shows the temperature dependence of the irradiation creep rate at three stress levels. The temperature dependence is quite different from that in the unirradiated, thermal creep case. Besides, the irradiation creep rate itself is extremely high compared with the thermal creep rate. Stress dependence is plotted in Fig. 3 for three different temperatures. The slope in the log-log plot is about one, which means that the irradiation creep rate is approximately proportional to the applied stress. This stress dependence also differs very much from that of the thermal creep which gives stress-exponent of around five. These results on the 316 stainless steel clearly indicate that the mechanism of creep deformation is altered by the irradiation under the present experimental condition.

Table 1. General features of the TICF.

Strain sensitivity : ~1 X 10^{-7} (1 X 10^{-3} deg)
Strain rate sensitivity : ~2 X 10^{-10} s^{-1}
(in 100 min)
Stress range : ± 600 MPa (± 3 g.cm torque)
Stress cycling : 1 Hz maximum
Temperature range : 200 ~ 800 °C
30 ~ 500 °C
(gas heating only)
Temperature control : ± 1 °C
On-line computer : digital smoothing
real-time graphic display
stress control

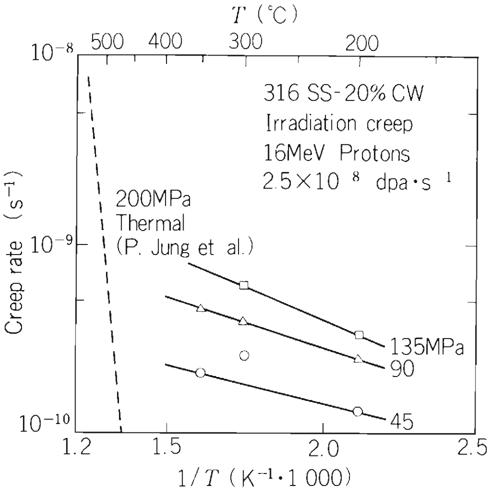

Fig. 2. Temperature dependence of the irradiation creep rate. Dependence is much weaker than the unirradiated, thermal case (dashed line). The creep rate is extremely higher than the thermal creep rate in the temperature range examined.

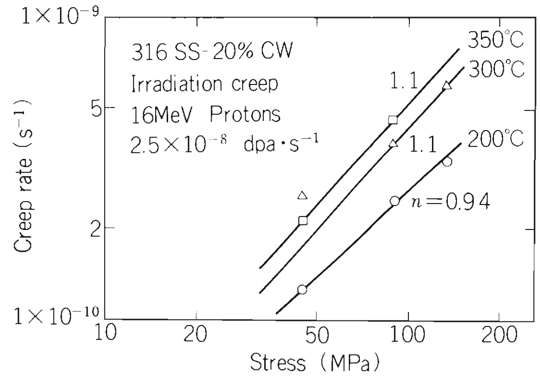

Fig. 3. Stress dependence of the irradiation creep rate. The creep rate is approximately proportional to the applied stress. The stress exponent, i.e. n, of the thermal creep is around five, much higher than the one for this case.

Table 2. Chemical composition of the type 316 stainless steel sample (wt. %).

C	Cr	Ni	Mn	Si	Mo	B	O	N	P	S	Fe
0.043	16.09	13.92	1.42	0.44	2.50	0.0006	0.0058	0.0035	0.005	0.010	Balance

III-2-30. Effect of Injected Helium on the Mechanical Properties of Ti-6.5 Al Alloy

Y. Higashiguchi,* E. Yagi, Y. Suzuki,* and H. Kayano*

As a fusion reactor material, titanium alloys have several attractive properties such as high strength-to-weight ratio, high resistance to void swelling and compatibility with coolants such as lithium, helium and water. But, when it is used as a first wall material in a fusion reactor, it faces a serious problem. The material will be subject to high fluence of high energy neutrons (14 MeV). Gaseous products such as helium and hydrogen are introduced into the first wall itself due to the transmutation reactions (n, α) and (n, p). Effect of helium produced by such reactions may lead the material to significant embrittlement due to the accumulation of helium atoms at grain boundaries. Although there are a few methods to introduce helium into specimens, the most convenient way is to use an accelerator because helium implantation is achieved in a short time, the resultant radioactivity is relatively low etc. For the study of the effect of helium on the mechanical properties, a cyclotron which has capability to inject high energy helium ions is suitable because tensile test usually requires specimens thicker than 0.2 mm to obtain the data reflecting the bulk properties. In the present study helium was injected into Ti-6.5 Al alloys of 0.3 mm in thickness as α-particles accelerated to 36 MeV by the cyclotron.

Ti-6.5 Al alloys were prepared by arc-melting the mixture of Ti and Al metals. Sheets of 0.3 mm in thickness were prepared through hot forging, hot and cold roll processes. Specimens for tensile test of 5 mm in width and with 15 mm gauge length were cut from the sheets and annealed at 850 °C for 3 h in vacuum below 5×10^{-5} Torr. Helium injection was carried out at room temperature in such a way that helium distribution will be uniform in the direction of thickness using a wedge-shaped graphite degrader.

Tensile test was made at 600 °C in vacuum below 5×10^{-5} Torr at a strain rate of 1.85×10^{-4} s^{-1} for uninjected, 5, 18, and 30 appm He-injected specimens. The dependence of the strength and the elongation on the helium concentration is presented in Fig. 1. Helium had only small effect on the yield stress σ_y and no effect on the ultimate strength σ_u. On the other hand, the total elongation ϵ_f considerably decreased with increase in the helium concentration up to 18 appm, and for higher concentration the elongation slightly increased again to be about 35 % at 30 appm He. The minimum of the elongation appeared at about 18 appm He similarly to that of the yield stress.

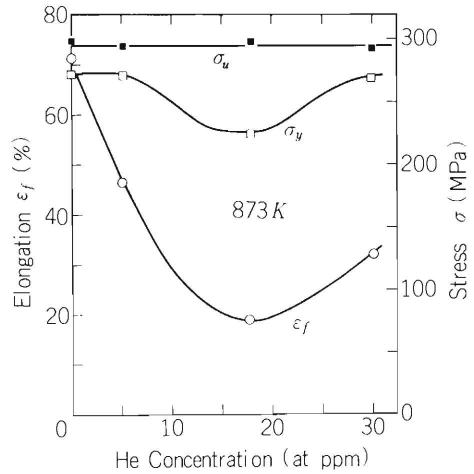

Fig. 1. Dependence of the yield stress σ_y, the ultimate strength σ_u and the total elongation ϵ_f on the helium concentration in Ti-6.5 Al alloys tensile-tested at 600 °C and at a strain rate of 1.85×10^{-4} s^{-1}

In order to investigate in more detail, fractured surfaces were observed by a scanning electronmicroscope (SEM). It is indicated that there is apparent difference among the micrographs of uninjected, and 18 and 30 appm He-injected specimens (Fig. 2). The microscopic fracture mode in the uninjected specimen was that of ductile rupture with dimple as shown in Fig. 2(a). The mode in the 18 appm He-injected specimen was that of mixed fracture which consists of fine dimple and integranular fracture as shown in Fig. 2(b). The fracture mode became simple again with increase in the helium concentration up to 30 appm. Although the fracture was of integranular type, numerous deformations observed within all the grains.

Microstructures around fractured area were observed by a transmission electronmicroscope (TEM) and the

---

* The Oarai Branch, The Research Institute for Iron, Steel and Other Metals, Tohoku University.

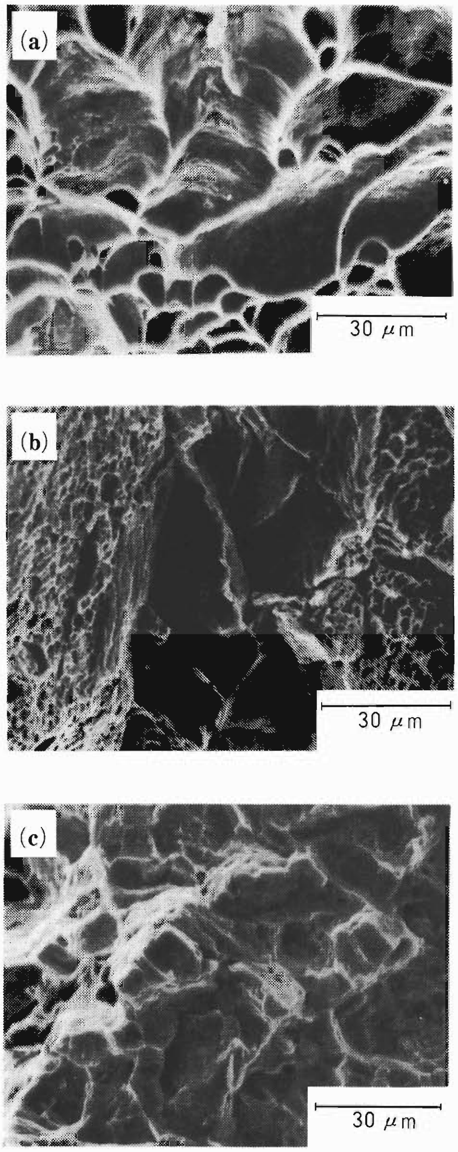

Fig. 2. Electron fractographs of the fractured surface of tensile-tested Ti-6.5 Al specimens containing various amounts of helium: (a) uninjected, (b) 18 appm, and (c) 30 appm.

results for uninjected, 18 and 30 appm He-injected specimens are shown in Fig. 3(a), (b), and (c), respectively The change in the deformation mode was observed with increase in helium concentration. The twinning deformation was found both in uninjected and 18 appm He-injected specimens, but not in 30 appm He-injected one, in which the homogeneous dislocation cell structure was observed instead of twins. As a result of detailed investigation, the deformation modes were elucidated and they are listed in Table 1 together with the fracture modes. The small concentration of helium up to 30 appm changed significantly the deformation and fracture modes in Ti-6.5 Al alloys at 600 °C.

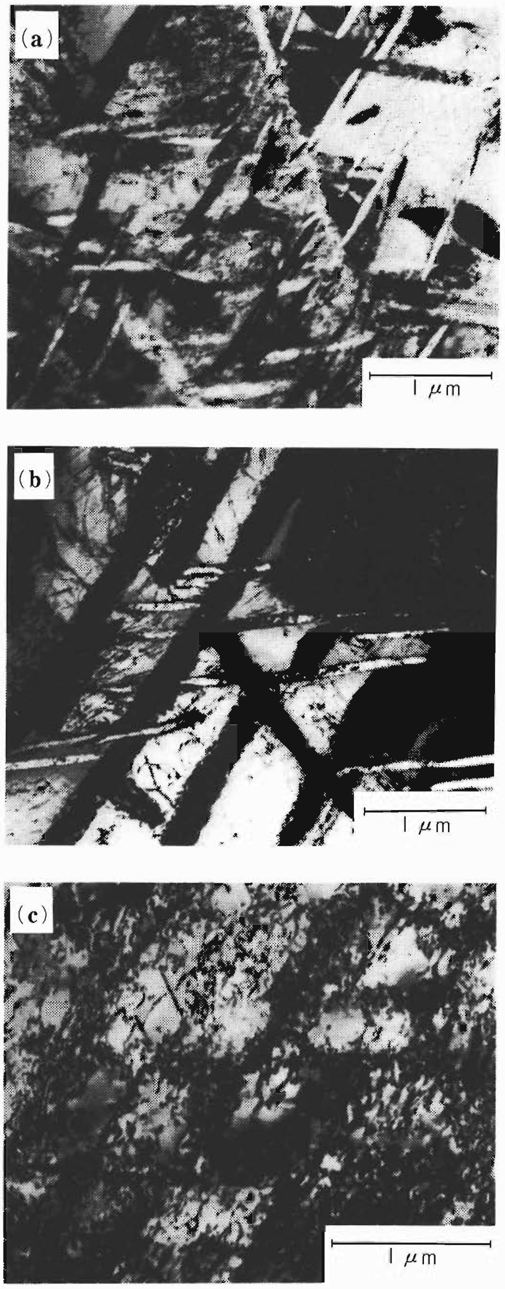

Fig. 3. Transmission electron micrographs of Ti-6.5 Al alloys tensile-tested to fracture. Specimens contain various amounts of helium: (a) uninjected, (b) 18 appm, and (c) 30 appm.

Table 1. Effect of helium concentration on the deformation and fracture modes of Ti–6.5 Al alloys.

He concentration appm	Deformation mode			Fracture mode
0	Slip			
	Twin	$\{10\bar{1}2\}$	$<10\bar{1}\bar{1}>$	Transgranular
		$\{11\bar{2}1\}$	$<11\bar{2}6>$	
18	Slip			
	Twin	$\{11\bar{2}1\}$	$<11\bar{2}6>$	Mixed
30	Slip			
	No twin			Intergranular

III-3. Radiochemistry and Nuclear Chemistry

1. Radioisotope Production and Labelled Compound Synthesis

T. Nozaki, S. Ambe, M. Iwamoto, and Y. Minai

The study of production and use of ^{29}Al has been continued, and its distribution in rat body was measured. Aluminium-29 formed by the ^{26}Mg(α,p)^{29}Al reaction in target magnesium was separated by acetylacetone extraction followed by sublimation.[1] The sublimate was dissolved in dilute hydrochloric acid, and the pH of the solution was adjusted with a $NaHCO_3$ solution. The ^{29}Al solution was injected into rats (about 0.1 ml for each) through a millipore filter, and the organ distribution was measured. The result is shown in Table 1. There remains some uncertainty in this result, because the chemical form and physical state of the ^{29}Al were not quite clear. We intend to repeat the experiment.

Recently, the acetylacetone extraction of ^{29}Al has been found to be very slow under ice cooling but fast over 30 °C. From the organic phase, the ^{29}Al has proved to be extracted back into hot dilute hydrochloric acid. Xylene is a suitable solvent for these extractions. The separation by extraction and back-extraction is thus now preferred to that by extraction and sublimation.

Radiobromines, ^{77}Br and ^{75}Br, were produced by the ^{75}As(α, 2n)^{77}Br and ^{75}As(He, 3n)^{75}Br reactions in GaAs target, and separated by sublimation.[1] The radiobromines were dissolved in dimethylformamide or water, and used for the labelling of 6-bromo-9-benzylpurine by isotopic exchange[1] or for the synthesis of aryl bromides by the Sandmeyer reaction. The time course of the brain concentration of ^{77}Br was measured after injection of 6-bromo-9-benzylpurine-^{77}Br into mice, and compared with that of ^{18}F and ^{125}I after injection of the corresponding fluoro- and iodo-purine. The results will be reported soon.

No-carrier-added bromobenzene-^{77}Br was synthesized with a good yield by the usual process of the Sandmeyer reaction. The product was found to be highly volatile. Its distribution in mouse body was measured. High concentrations of ^{77}Br were observed in the liver and kidney, together with its rapid clearance from the blood. The brain concentration of ^{77}Br was found to be low. We intend to label a variety of organic bromides including bromoperidol with the radiobromines by the Sandmeyer reaction.

Table 1. Organ distribution of ^{29}Al in rats.

pH of ^{29}Al Sol.	2.5 – 3.5			about 8
Time after Inject.	1 m	5 m	15 m	5 m
Blood	7.69 ± 0.75	6.38 ± 0.67	2.55 ± 0.23	1.43 ± 0.19
Liver	1.66 ± 0.32	2.41 ± 0.10	0.97 ± 0.25	9.91 ± 0.28
Kidney	2.87 ± 0.43	2.52 ± 0.06	3.18 ± 1.16	0.78 ± 0.15
Spleen	1.45 ± 0.06	2.65 ± 0.66	0.97 ± 0.26	4.79 ± 0.60
Lung	2.26 ± 0.40	6.47 ± 0.50	1.37 ± 0.20	2.08 ± 0.45
Heart	1.10 ± 0.19	2.34 ± 0.08	0.52 ± 0.04	1.85 ± 0.08
Muscle	0.36 ± 0.00	0.30 ± 0.02	0.25 ± 0.02	0.35 ± 0.08
Bone	0.64 ± 0.06	0.33 ± 0.12	0.68 ± 0.32	0.61 ± 0.33
Brain	0.19 ± 0.06	0.20 ± 0.04	0.07 ± 0.03	0.05 ± 0.01

The concentration is shown by [Count rate for the organ (after decay correction)]·[Animal body weight]/[Organ weight]·[Total ^{29}Al count rate].

Reference

1) Y. Minai, T. Nozaki, S. Ambe, and M. Iwamoto: RIKEN Accel. Progr. Rep., 16, 120 (1982).

III-3-2. Charged Particle Activation Analysis

T. Nozaki, Y. Itoh, M. Iwamoto, H. Shinyashiki,
K. Nomura, T. Kimura,* and H. Fukushima*

The utilization of charged particle activation analysis has been continued mainly in collaboration with semiconductor industries. The need for the determination of oxygen in various semiconductor materials is still increasing. Previously we developed a highly useful method for the separation of ^{18}F formed by the $^{16}O(^{3}He, p)^{18}F$ reaction in any matrix.1) We predicted at that time that the detection limit of oxygen could be lowered down to 1 ppb or still less by the coincidence measurement of the positron annihilation radiation with a pair of BGO (bismuth germanium oxide) scintillators. We obtained recently two BGO crystals (2" x 2"), and have succeeded in realizing reliable determination of such low concentrations of oxygen. The positron counting efficiency of our counter usually is about 20 % with a background of about 1.2 cpm. Silicon specially prepared for use as a radiation detector was found to contain 2.3 ± 0.8 ppb of oxygen by this analysis.

Oxygen in many matrices and carbon and nitrogen in a limited number of matrices can now be determined reliably and routinely. In order to contribute widely to various fields of science and technology through these routine analyses, we have contracted with the Japan Chemical Analysis Center. The Center, thus, performs the analysis on semi-commercial base by the use of the IPCR Cyclotron and of techniques we developed. The samples shown in Table 1 can now be analyzed according to the demand of any organization or personnel. Efforts will be continued to make analyzable more variety of samples in this trust analysis system.

Table 1. Samples analyzable on semi-commercial base.

Element determined	Matrix	Lower limit of determination	
C	Al	1 %	(wt)
	Semiconductor Si	20 ppb	(wt)
N	Semiconductor Si	10 ppb	(wt)
O	Al	1 ppm	(wt)
	Semiconductor Si	5 ppb	(wt)
	Semiconductor GaAs	5 ppb	(wt)
	Almost any matrix†	5 ppb	(wt)

† Stable in the bombardment and dissolvable.

In 1983, the following works have been undertaken: (1) determination of ultra-trace amounts of oxygen in GaAs produced under various conditions; (2) determination of oxygen in Sb-doped silicon, to show the escape of oxygen as antimony oxide; (3) analysis of surface oxygen under various atmospheric conditions; (4) studies on the relationship between IR absorption and composition of evaporated silicon oxide films; and (5) improvement in the separation method of ^{11}C from silicon and some other matrices. Work 2 and Work 4 are reported separately in this volume. Work 3 will further be continued;2) its details will be reported next year.

Oxygen in GaAs has been guessed to form a deep level in the forbidden band and to play an important role in the formation of semi-insulating GaAs. However, oxygen concentrations in GaAs single crystals are so low as to be determined reliably only by charged particle activation analysis.3) Some difficulties are encountered even in this method, because this matrix cannot withstand the heat evolution in high-flux bombardment and because the matrix itself is highly activated. By our technique written above, we can now determine as low as 1 ppb of oxygen in GaAs. A decay curve of ^{18}F separated from GaAs is shown in Fig. 1. The sample in this example was bombarded for 40 min, but the saturation factor for ^{18}F (110 m half-life) can be doubled

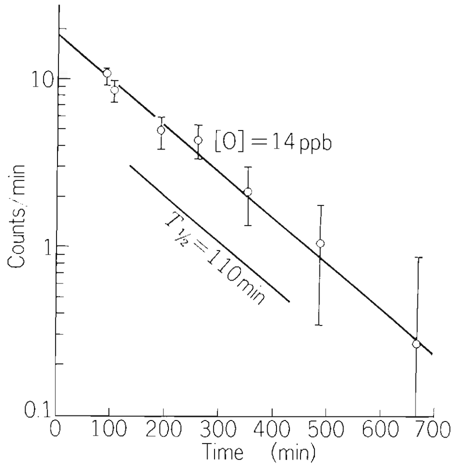

Fig. 1. Decay Curve of ^{18}F Separated from GaAs.

---

* Japan Chemical Analysis Center.

with ease. For silicon matrix, the detection limit of oxygen is guessed to be about 300 ppt. GaAs samples prepared by two different methods from six-nine purity Ga and As were analyzed, together with those after further purification. The results are shown in Table 2.

In the analysis of carbon and nitrogen in silicon by the $^{12}C(^3He,\alpha)^{11}C$ and $^{14}N(p,\alpha)^{11}C$ reactions, respectively, we converted the ^{11}C into Li_2CO_3 precipitate by dissolution of the silicon matrix in $HF\text{-}HNO_3\text{-}KIO_4$. Some fraction of the ^{11}C, however, was found not to be oxidized into $^{11}CO_2$ by this treatment, and a conventional factor was applied to the final result. This correction factor was obtained by the use of ^{11}C-containing silicon prepared by proton bombardment of boron-doped silicon. We looked for some other method in order to convert the ^{11}C quantitatively and easily into $^{11}CO_2$, and found that the dissolution of the sample in a NaOH solution and its heating close to dryness after addition of $KMnO_4$ can provide a much better process for the ^{11}C separation. A routine procedure will be established soon. With slight modifications, the procedure will be applicable to some other matrices.

Table 2. Oxygen content of GaAs.

Crystal growth	Seed	H_2O in B_2O_3 (wt ppm)	Crucible	Oxygen (wt ppb)	Content (at/cm^3)
HB method	–	–	SiO_2 Boat	55	1.1×10^{16}
				7.5	1.5×10^{15}
Direct synthesis	–	200	SiO_2	180	3.6×10^{16}
				70	1.4×10^{16}
LEC method	< 100 >	100	PBN	8.0	1.6×10^{15}
LEC method	< 100 >	1000	PBN	16	3.1×10^{15}

References

1) T. Nozaki: J. Radioanal. Chem., 72, 527 (1982).
2) H. Emori, M. Umehara, T. Takeya, K. Nomura, Y. Terai, and T. Nozaki: "Gallium Arsenide and Related Compounds 1981", Inst. Phys., London, p. 47 (1982).
3) T. Nozaki and M. Iwamoto: RIKEN Accel. Progr. Rep., 15, 105 (1982).

III-3-3. Oxygen Concentration in Antimony-Doped Silicon

T. Nozaki, Y. Itoh, T. Masui,
and T. Abe

Oxygen in silicon wafers heavily doped with an electrically active impurity cannot be determined by infrared absorption, because of the strong free-carrier absorption. The precipitation of oxygen in Czochralski-grown silicon is known not to take place by heat treatment of a sample heavily doped with antimony, without which the precipitation should surely take place.[1] It has not been made clear as yet whether this phenomenon is due to an effect of antimony in the crystal or to the reduction of oxygen concentration by evaporation as antimony oxide in the crystal formation. We measured oxygen concentration in silicon crystals with various amounts of antimony dopant crystallized in vacuum or under atmospheric pressure, using charged particle activation analysis with the $^{16}O(^{3}He, p)^{18}F$ reaction.

The samples used were Czochralski-grown silicon crystal <111> <100> oriented and antimony-doped n-type with resistivities of 0.007 ~ 82 Ω·cm. The sample was bombarded with a ^{3}He beam of 18 MeV incident energy through a 30 μm thick aluminium foil for the activation of oxygen. A specially designed apparatus was used for the successive bombardment of four samples in the cyclotron vacuum. The method of the oxygen measurement was described previously.[2] Boron- and phosphorus-doped silicon crystals were also analyzed for oxygen.

Oxygen and antimony distributions along the growth direction in silicon crystals are shown in Fig. 1. Oxygen concentrations normalized to the concentration at the head of the ingot are shown in Fig. 2, where the solid lines are the theoretical curves of the oxygen distribution for the given distribution coefficients after normal freezing. As is clear from Fig. 1 and 2, (1) silicon crystals heavily doped with antimony show a remarkable decrease of oxygen concentration with an apparent distribution coefficient lower for antimony but higher for oxygen and (2) crystals of medium or low antimony content or high boron or phosphorus content show no remarkable decrease in oxygen concentration.

It is now highly probable that (1) antimony and oxygen partly evaporate in the crystal formation of silicon, with its rate depending on the antimony con-

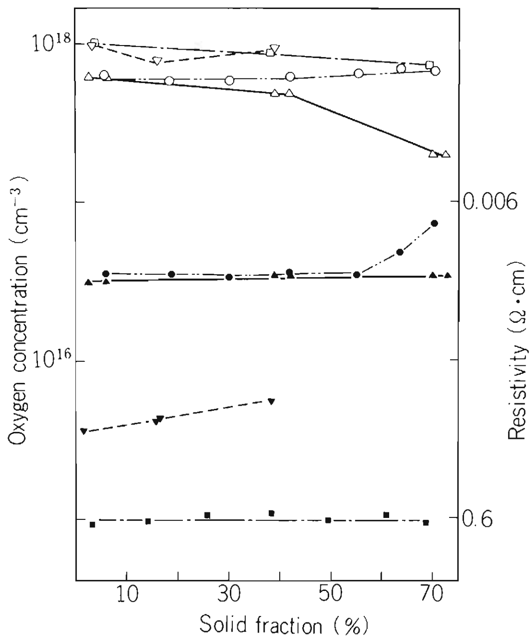

Fig. 1. Oxygen and antimony distribution in a CZ silicon. Crystallization atmosphere: △▲ and □■, vacuum; ○● and ▽▼, 1 atm.

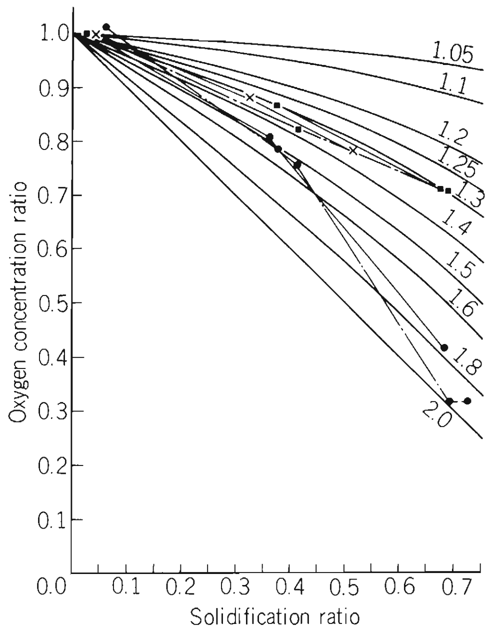

Fig. 2. Normalized oxygen distribution. Solid lines show theoretical distribution curves for given distribution coefficients. ●: high antimony concentration in vacuum, ■: low antimony concentration in vacuum, ×: phosphorous concentration in 1 atm.

centration and ambient atmosphere and (2) the difficulty in the formation of oxygen precipitate in silicon heavily doped with antimony is due to the decrease of oxygen concentration itself rather than to some effects of antimony.

References

1) A. J. R. de Kock, W. T. Stacy, and W. M. Van de Wijert: Appl. Phys. Lett., 34, 611 (1979).
2) T. Nozaki, Y. Itoh, and M. Iwamoto: RIKEN Accel. Progr. Rep., 16, 122 (1982).

III-3-4. Infrared Absorption and Composition of Evaporated Silicon Oxide Films

T. Nozaki, Y. Itoh, Y. Mochizuki,
M. Nakamura, and K. Usami

Oxygen-containing polycrystalline silicon films, often called SIPOS(semi-insulating polycrystalline silicon), have been extensively studied because of their practical importance as a passivation layer of silicon devices.$^{1)}$ SIPOS films prepared by chemical vapor deposition (CVD) have macroscopic chemical compositions expressed as SiO_x $(0<x<2)$.$^{2)}$ It is well known that silicon oxides show a characteristic infrared absorption peaks in the 9 – 10 μm region with the wave number increasing with oxygen content. However, the relationship between x and the peak wavenumber has scarecely been studied systematically. Using charged particle activation analysis with the $^{16}O(^3He,p)^{18}F$ reaction for the determination of the film oxygen content, we undertook this study and obtained meaningful results.

Detailed techniques of activation analysis in the present study were quite similar to those used earlier for the analysis of oxygen in silicon nitride films.$^{3)}$ A silicon dioxide film with 1.05 μm thickness and 2.10 ± 0.02 g cm^{-3} density was prepared by steam oxidation for use as the activation standard. This film can be regarded as of the stoichiometrical SiO_2. High purity FZ silicon plates (O content: 10^{16} at.cm^{-3}) with thicknesses of 300 μm and 1 mm were used as film substrates for activation analysis and IR measurement. The weight and deposition rate of the evaporated film were monitored in situ by a quartz microbalance calibrated with an evaporated gold film. The thickness of the silicon dioxide film was measured with a thickness meter after partly removing the film on the substrate by etching in 1 : 1 hydrofruoric acid under a suitable masking. The density of the film was calculated from the measured weight and thickness. Then, x in SiO_x was obtained from the results of the above measurements. The infrared spectrum was measured from 4000 to 400 cm^{-1} by a Hitachi spectrometer(EPI G3) with reference to the same silicon plate. Films of SiO_x with various values of x were prepared by the following method. Powder of SiO (Osaka Titanium Co., <200 mesh) was heated under various residual gas pressures to give evaporated films with various growth rates. The films were then heated in air at appropriate temperatures for appropriate times.

The change in IR spectrum on the heat treatment in air is shown in Fig. 1 for a film evaporated in a high vacuum (0.67 mPa) at a high deposition rate (6.2 nm s^{-1}). The relation between x in SiO_x and νM (Wavenumber for the maximum absorption) is shown in Fig. 2, in which x increases monotonously but not

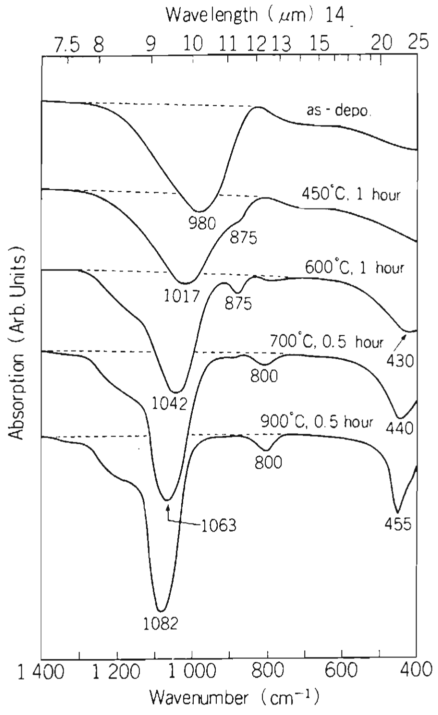

Fig. 1. Infrared absorption spectra for as-deposited and heat-treated SiO_x films.

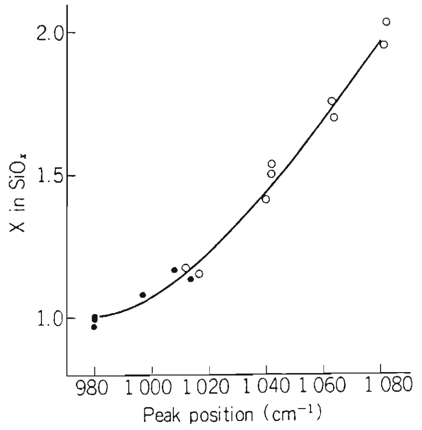

Fig. 2. Relation between IR absorption peak position and x in SiO_x. Closed circles, as-deposited films; open circles, heat-treated films.

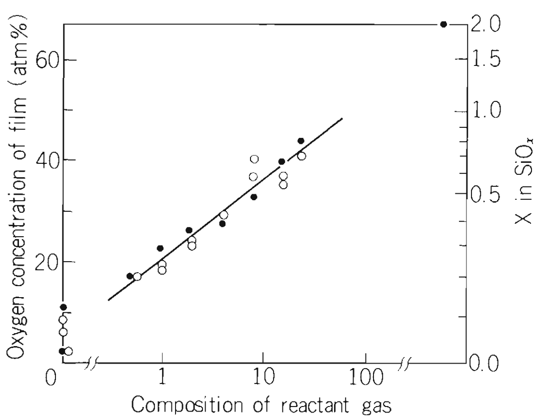

Fig. 3. Composition of the reactant gas vs. oxygen concentration in CVD films. Film preparation: CVD method from SiH_4, N_2O. Closed circles, IR; open circle, charged particle activation analysis.

linearly. As for the absorption coefficient, its maximum value exists at around x = 1.5. This can be explained from the random bonding model. Oxygen concentration in SIPOS films is controlled by the logarithm of oxygen pressure in the reactant gas, as is shown in Fig. 3. Detailed results will be published soon in a journal.

References

1) T. Matsushita, T. Aoki, T. Otsu, H. Yamato, H. Hayashi, M. Okayama, and Y. Kawana: Jpn. J. Appl. Phys., Suppl., 15, 35 (1975).
2) M. Hamasaki, T. Adachi, S. Wakayama, and M. Kikuchi: J. Appl. Phys., 49, 3987 (1978).
3) T. Nozaki. Y. Iwamoto, K. Usami, K. Mukai, and A. Hiraiwa: J. Radioanal. Chem., 52, 449 (1979).

III-3-5. Rutherford Recoil Detection Method

H. Nagai, M. Aratani, S. Hayashi, T. Nozaki, M. Yanokura,
I. Kohno, O. Kuboi, and Y. Yatsurugi

We have already reported the usefulness of the Rutherford forward recoil detection method for the study of hydrogen analysis in near surface regions of solids.[1] We have further improved this method and have obtained fairly good results.

The experimental procedures were almost the same as described previously.[1] Some modifications were made in the detection system for recoiled and scattered atoms. Two silicon surface barrier detectors (SSD) were used as shown in Fig. 1. The one at forward angle (SSD-1) was used for the detection or recoiled hydrogen ions, which can be detected after passing through an aluminium absorber. The other (SSD-2) was placed at 10° backward from the forward SSD for the monitoring of the incident beam current by counting recoiled silicon ions. The energy spectra of SSD-1, shown in Fig. 2, indicate that recoiled silicon ions and scattered argon ions, which cause the continuous background spectrum to hydrogen peak, were stopped in the aluminium absorber. By the use of the absorber of suitable thickness, a recoil spectrum without continuous background spectrum is obtained. These modifications brought several advantages:

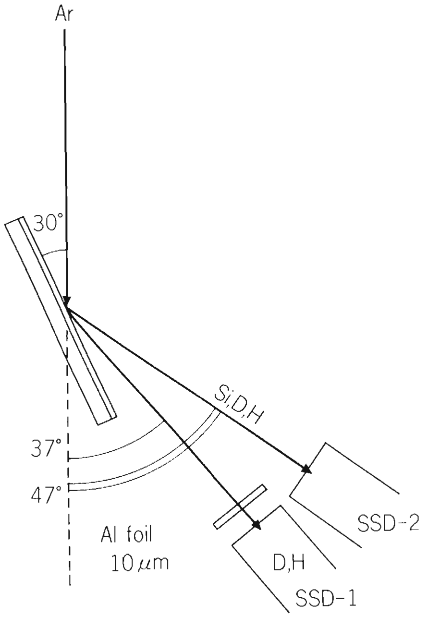

Fig. 1. Experimental arrangement.

(1) High sensitivity and precision are achieved, since the statistical errors are reduced.

(2) Simultaneous detection of light elements (C, N, O) and hydrogen becomes feasible. The spectra of these elements are shown in Fig. 3. By the present counting method, we can discriminate C, N, and O peaks in the same sample of less than 200 Å thickness.

(3) Deuterium can be used as tracer, since the detection of deuterium becomes easy. The spectra of amorphous silicon (a-Si : H) samples prepared from deuterated monosilane are shown in Fig. 4. Application of this technique to the study on the reaction mechanism for the formation of a-Si : H resulted in good results.[2]

(4) Precise depth profiling of hydrogen and other light elements is possible. The depth profiles of H and

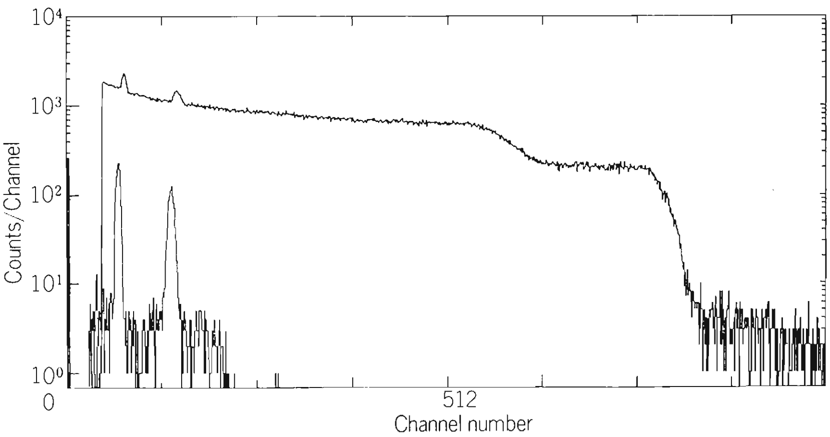

Fig. 2. Energy spectra of recoiled and scattered particles from a-Si : H : D film for 42 MeV Ar incident particle.
Lower: with 10 μm Al absorber, Upper: without Al absorber.

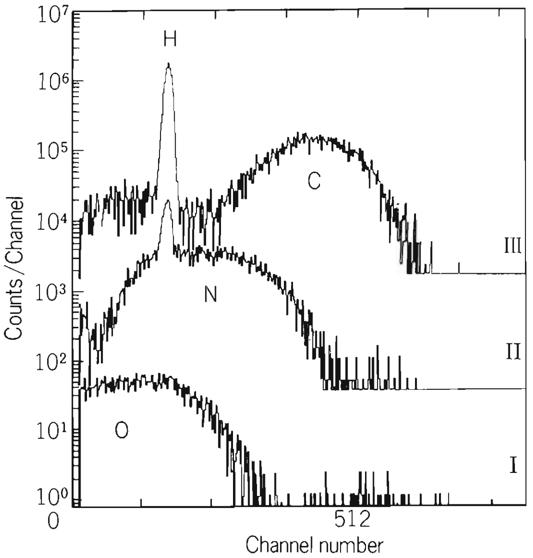

Fig. 3. Spectra of light element forward recoils seen as continua with narrow peaks of H.
I : oxygen from quartz, II : nitrogen from SiN_x,
III : carbon from PIQ (polyiminoquinone).

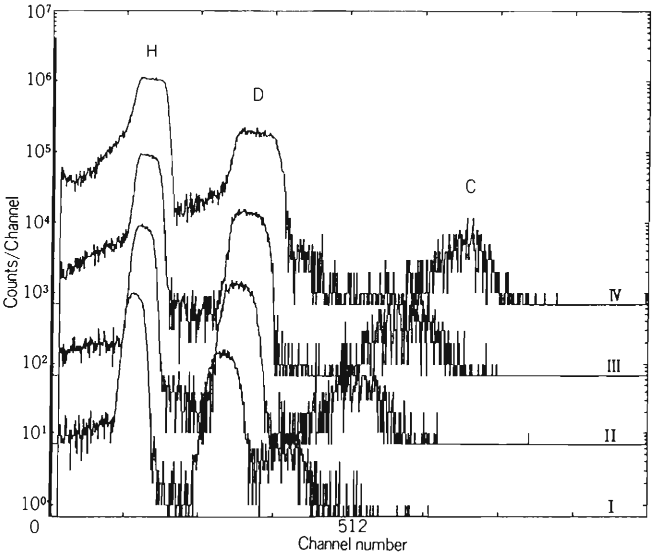

Fig. 4. Spectra for a-Si : H : D film observed at various detector angles (sample thickness: 6520 Å).
I: 40°, II: 37°, III: 35°, IV: 33°.

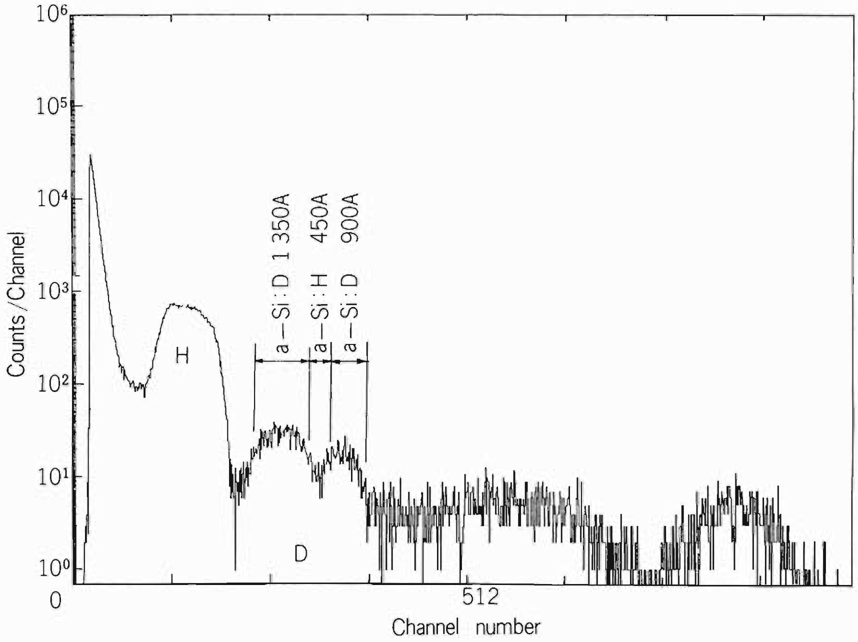

Fig. 5. Depth profiles of H and D in three-layer a-Si film deposited in the sequence of 1350 Å a-Si : D, 450Å a-Si : H, and 900 Å a-Si : D on Si substrate.

D are shown in Fig. 4 (IV). In the spectrum, peak width indicates the thickness of a-Si : H, and curve shape of the peak indicates the distribution of hydrogen concentration along the depth of the a-Si : H film. The depth profile of deuterium in a-Si film is shown in Fig. 5. The split peak is due to two a-Si : D layers of 900 and 1350 Å thickness, respectively. The valley is due to the a-Si : H layer of 450 Å thickness. From this spectrum, the depth resolution of hydrogen was estimated to be about 500 Å.

References

1) H. Nagai, M. Aratani, T. Nozaki, M. Yanokura, I. Kohno, O. Kuboi, and Y. Yatsurugi: RIKEN Accel. Progr. Rep., 16, 125 (1982).
2) Y. Yatsurugi, O. Kuboi, M. Hashimoto, H. Nagai, M. Aratani, M. Yanokura, I. Kohno, and T. Nozaki: p. 82 in this report.

III-3-6. Characterization of Surface Hydrogen by the Rutherford Forward Recoil Measurement

M. Aratani, H. Nagai, S. Hayashi, M. Yanokura, O. Kuboi,
Y. Yatsurugi, I. Kohno, and T. Nozaki

Surface hydrogen on various materials for electronic devices has been characterized by the Rutherford forward recoil measurement using 45 MeV argon beam from the Riken Linear Accelerator. The following samples were examined: high-purity crystalline silicon (c-Si), c-Si plasma-annealed in hydrogen gas for various times, c-Si treated chemically with acids and alkalies, and c-Si ion-implanted with hydrogen beam. The majority of them were produced by Komatsu Electronic Metal Co., and the other by Toshiba Corporation and Hitachi Ltd.

Experimental arrangement and procedures were reported previously.[1)] Marked improvement has been made by the use of two silicon surface-barrier detectors; one was shielded from scattered argon and recoiled silicon ions with a 10 μm aluminium-foil for the detection of hydrogen ions, and the other was used for the detection of recoiled silicon ions for beam monitoring. The improved arrangement is described in detail[2)] in a preceding report of this volume.

The Rutherford forward recoil spectra of c-Si plasma-annealed in hydrogen gas measured by the detector without the aluminium absorber are shown in Fig. 1. In a continuum due to scattered argon and recoiled silicon, a hydrogen peak is observed in every spectrum, although it is not so prominent in c-Si without plasma-annealing. Hydrogen peak height rapidly increase with the plasma-annealing time. The hydrogen plasma-annealing was performed as a pretreatment of the surface of c-Si substrate for hydrogenated amorphous silicon (a-Si : H) film just before its growth. The narrow widths of the hydrogen peaks observed suggest that hydrogen atoms are situated in the surface layer not deeper than 20 nm; those peaks are referred to as surface hydrogen peaks. These peak heights are estimated to correspond to hydrogen atoms of the order of 10^{15} per cm^2.

The spectra obtained by the use of the aluminium absorber are shown in Fig. 2. In addition to a hydrogen peak, an oxygen peak is clearly observed. This is an example of the marked improvement of the spectra owing to the new experimental arrangement. These spectra exhibit another aspect of the hydrogen plasma-annealing procedure, in which, oxygen, one of the ordinary residual elements in the annealing chamber under the vacuum pumping, is incorporated in the c-Si surface, accompanied with hydrogen.

The spectra for c-Si after chemical treatment with a mixture of HF-HNO$_3$ or with a NaOH solution are shown in Fig. 3. No distinguishable features are found between the two spectra. Hydrogen and oxygen peaks

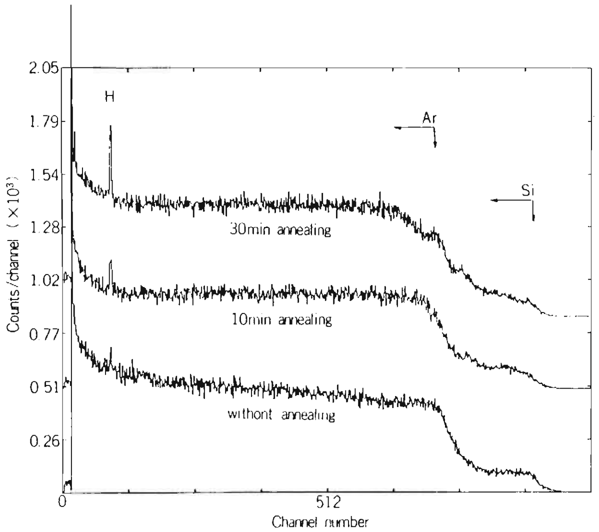

Fig. 1. Rutherford forward recoil (energy-dispersed) spectra of the hydrogen plasma-annealed c-Si by the use of the unsheltered detector.

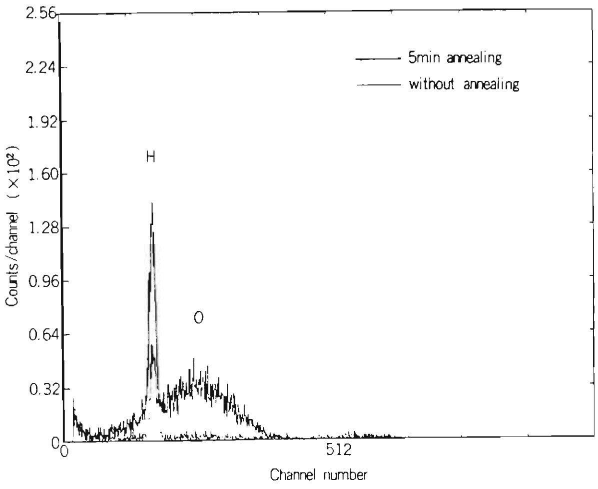

Fig. 2. Rutherford forward recoil (energy-dispersed) spectra of the hydrogen plasma-annealed c-Si by the use of the detector sheltered with the 10 μm aluminium absorber.

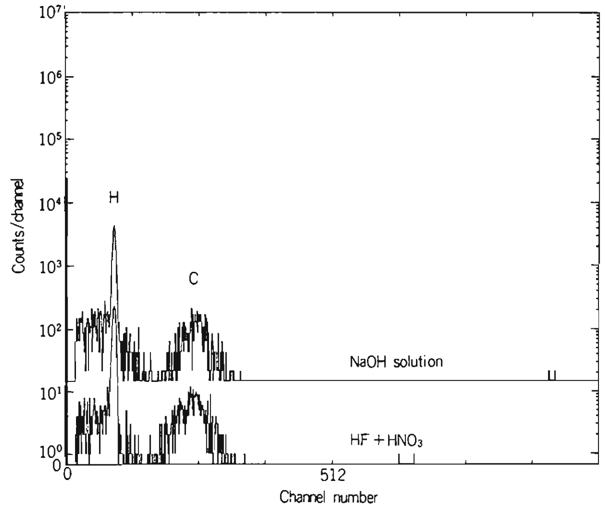

Fig. 3. Rutherford forward recoil (energy-dispersed) spectra of the chemically treated c-Si.

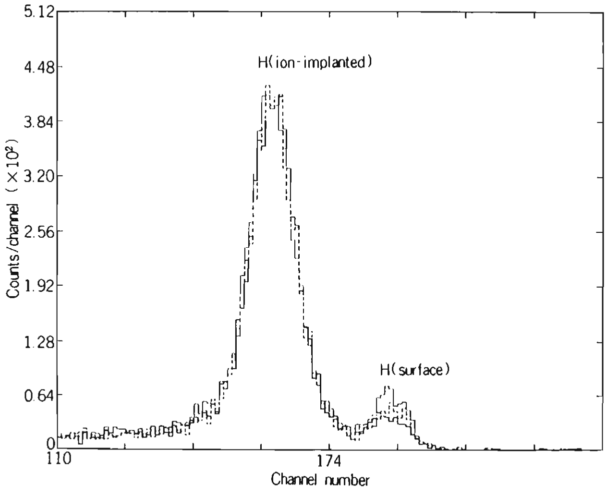

Fig. 4. Rutherford forward recoil (energy-dispersed) spectra of the ion-implanted c-Si.

attributable to the surface atoms are observed for them. Carbon peaks are also seen. Appearance of the carbon peak, however, cannot be attributed directly to the initial surface carbon, because we have observed an increase of carbon peak height with irradiation time in another experiment.

A change of spectra of hydrogen ion-implanted c-Si at the same time-intervals under the measurement is shown in Fig. 4. Two hydrogen peaks are observed in every spectrum. They are attributed to the ion-implanted hydrogen and surface hydrogen. During the measurement, the ion-implanted hydrogen peak remains constant. The surface hydrogen peak, on the other hand, slightly increases with irradiation time in general, but sometimes decreases. The amount of surface hydrogen, therefore, is not simply estimated in this case.

In spite of some problems left to be elucidated, the Rutherford forward recoil measurement using heavy ions indicates a promising approach to surface and interface studies intimately relating to the presence of light elements.

References

1) H. Nagai, M. Aratani, T. Nozaki, M. Yanokura, I. Kohno, O. Kuboi, and Y. Yatsurugi: RIKEN Accel. Progr. Rep., 16, 125 (1982).
2) H. Nagai, M. Aratani, S. Hayashi, T. Nozaki, M. Yanokura, I. Kohno, O. Kuboi, and Y. Yatsurugi: p. 102 in this report.

III-3-7. Depth Profiling of Hydrogen and High Sensitivity Analysis of Deuterium with ^{15}N-Induced Nuclear Reactions

S. Hayashi, H. Nagai, M. Aratani, T. Nozaki, M. Yanokura,
I. Kohno, O. Kuboi, and Y. Yatsurugi

It is desired to determine accurately hydrogen depth profiles in solids or thin layers, especially, of metals, semiconductors, and nuclear reactor materials. The quantitative information about microscopic location of light-elements in these materials can be obtained by means of position sensitive analytical techniques. We employed the resonance nuclear reaction, $^1H(^{15}N,\alpha\gamma)^{12}C$ ($E_\gamma = 4.44$ MeV), which has been reported to be of the most accurate method for the depth profiling of hydrogen in solids by now.$^{1)-3)}$ The resonance energy of ^{15}N ions is 6.385 MeV, while the resonance width is 6.4 keV in the laboratory system. Using the characteristics of the isolated narrow resonance width, we can determine the hydrogen concentration in any material with high accuracy. For example, the resonance width corresponds to about 50A for silicon wafers. The resonance cross section was reported to be about 450 mb, and off-resonance one was to be three orders of magnitude smaller than the resonance peak value.

The ^{15}N ions with energy higher than the resonance energy lose their energies in the sample materials, and induce the 4.44 MeV gamma-ray emission at the resonance point. We adopted two ways in determining the depth location of hydrogen in solids. One is varying incident ^{15}N ion energy, and the other is inclining the target with respect to the beam axis. By comparing with the standard materials of known hydrogen contents, absolute hydrogen concentrations in the samples were determined.

Samples of amorphous silicon (a-Si : H) were prepared, in Komatsu Electronic Metals Co., by the glow-discharge decomposition of monosilane as layers deposited on substrate silicon wafers. Several pieces of the samples for targets were settled at the center of 1 m scattering chamber on the A11 course in the RIKEN heavy-ion linear accelerator (RILAC). In order to estimate the beam intensity, a thin carbon foil (about 10 $\mu g/cm^2$) was placed in the upper stream from the targets in the scattering chamber, and scattered and recoil particles were detected with a silicon surface barrier detector (SSD). We employed two BGO ($Bi_4Ge_3O_{12}$) scintillators (2″ ϕ × 2″), located about 2 cm from the target center. The BGO scintillator is well known to have slightly poorer energy resolution, but higher detection efficiency especially at the high energy region than NaI(Tl). Gamma-ray pulses from the two BGO scintillators were summed up by a sum amplifier in order to get higher detection efficiency, and the summed pulses were collected in a pulse-height analyzer (PHA), see Fig. 1.

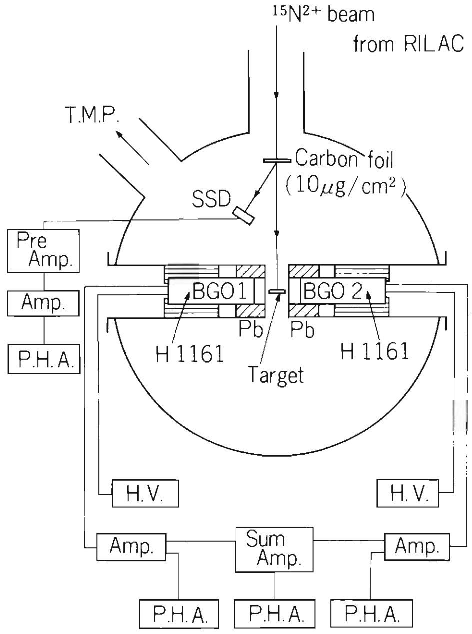

Fig. 1. Experimental arrangement for gamma-ray measurement by ^{15}N-induced nuclear reactions with beam-monitoring counter system.

Typical energy spectra for gamma-rays induced by ^{15}N ions in the a-Si : H are shown in Fig. 2. There appear full energy peaks of 4.44 MeV, and single and double escape peaks. There are few background gamma-ray peaks around the 4.44 MeV region. Using the intensities of these spectra, we can obtain the depth profile of hydrogen in the a-Si : H. An example is shown in Fig. 3, in which the energies of incident ^{15}N ions are given; different experimental points with the same energy correspond to different target angles. The absolute hydrogen concentration in the material is obtained with reference to the standard material of $TiH_{1.8}$.

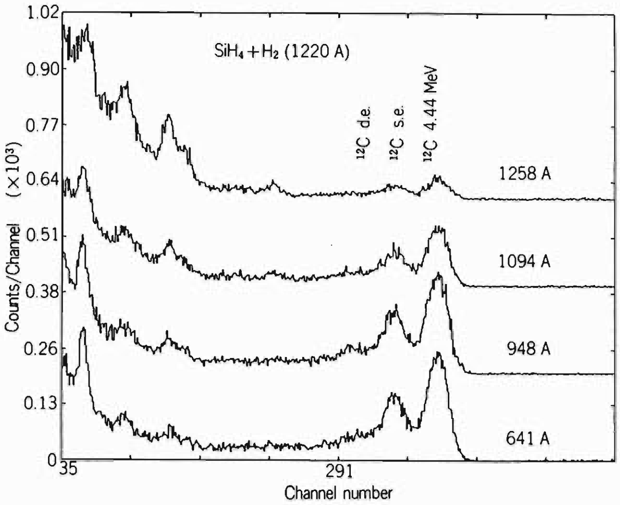

Fig. 2. Typical energy spectra for gamma-rays induced by $^{1}H(^{15}N,\alpha\gamma)^{12}C$ (E_{γ} = 4.44 MeV) in the a-Si : H. ^{12}C 4.44 MeV: full energy peak; ^{12}C s.e. : single escape peak; ^{12}C d.e.: double escape peak. Each value with angstrom unit means the depth from the surface of the a-Si : H.

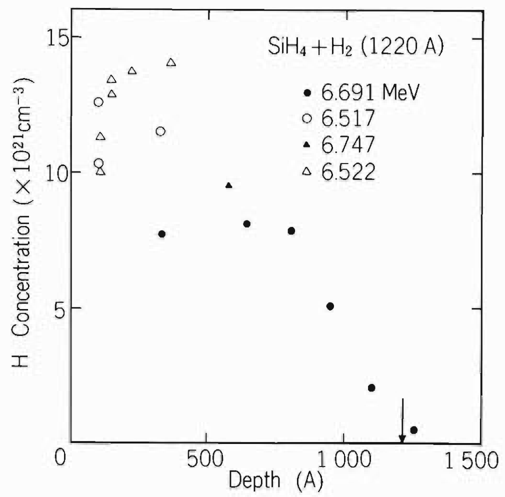

Fig. 3. Depth profiling of hydrogen in the a-Si : H (1220A). Incident energies of ^{15}N ions are shown in the figure.

Figure 3 shows that the thickness of the hydrogen layer thus obtained agrees well with that previously measured with a Talystep for the a-Si : H (1220A).

Besides the hydrogen depth profiling, we have found a method of high sensitivity quantitative analysis of deuterium with ^{15}N-induced nuclear reactions. Figure 4 shows typical spectra of gamma-rays induced by ^{15}N ions in a deuterium-doped a-Si : H (D). As is shown in Fig. 4, several other gamma-ray peaks are observed in addition to 4.44 MeV originating from hydrogen. All these peaks are shown to have originated only from deuterium, but not from contaminants in the sample. The following three nuclear reactions have been considered in order to elucidate the origins of these gamma-

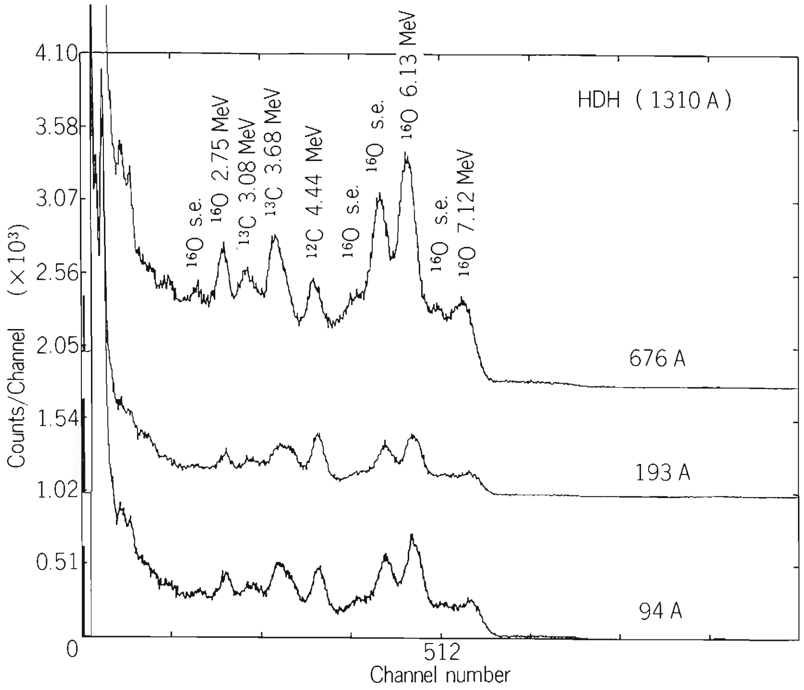

Fig. 4. Typical energy spectra for gamma-rays in deuterium-doped a-Si: H : D induced by $^{1}H(^{15}N,\alpha\gamma)^{12}C$, $^{2}D(^{15}N,p\gamma)^{16}N$ (β^{-} – decay, $T_{1/2}$ = 7.13 sec), $^{2}D(^{15}N,n\gamma)^{16}O$, and $^{2}D(^{15}N,\alpha\gamma)^{13}C$. Notations are the same as in Fig. 2.

ray peaks: a) $^{2}D(^{15}N,p\gamma)^{16}N(\beta^{-}$ – decay, $T_{1/2}$ = 7.13 sec), b) $^{2}D(^{15}N,n\gamma)^{16}O$, and c) $^{2}D(^{15}N,\alpha\gamma)^{13}C$. In the peaks appearing in Fig. 4, 2.75, 6.13, and 7.12 MeV photo-peaks originated from the excited states of ^{16}O, and 3.08 and 3.68 MeV ones from those of ^{13}C. Among these peaks, 6.13 and 7.12 MeV peaks are very useful for deuterium quantitative analysis, because there are no interference peaks in the energy region higher than the hydrogen-originated 4.44 MeV peak. Figure 5 shows the depth profiling of hydrogen in the a-Si : H : (D).

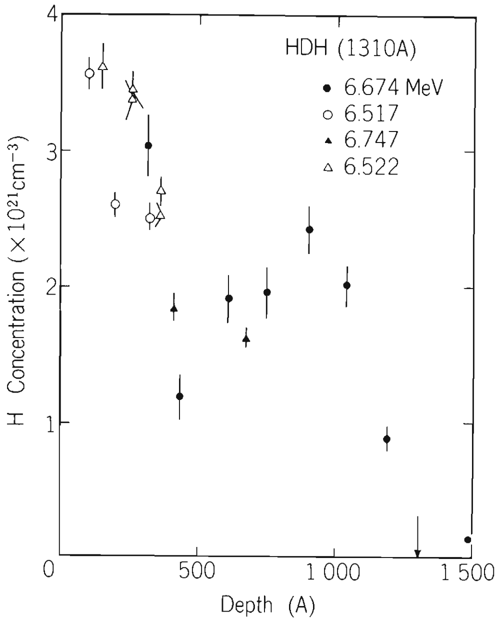

Fig. 5. Depth profiling of hydrogen in deuterium-doped a-Si : H(D) (1310A), which consists of three layers of hydrogen, deuterium, and hydrogen; HDH. Incident energies of ^{15}N ions are shown in the figure.

No precise cross section has been measured for the three nuclear reactions, but unlike $^{1}H(^{15}H,\alpha\gamma)^{12}C$ process, these reactions are considered not to be sharp resonance reactions.[4)–6)] The intensities of these higher-energy gamma-ray peaks (6.13 and 7.12 MeV) are proportional to the total amount of deuterium within the ranges of ^{15}N incident ions in the samples. Therefore, the deuterium-originating peaks can be applied not to the depth profiling, but to the very high sensitivity quantitative analysis of deuterium in solids. Further, two isotopes, H and D, can be measured simultaneously without mutual interference by scintillation counters.

References

1) W. A Lanford: Nucl. Instr. & Methods, 149, 1 (1978).
2) G. L. Clark, C. W. White, D. D. Allred, B. R. Appleton, F. B. Koch, and C. W. Magee: ibid., p. 9.
3) J. F. Ziegler et al.: ibid., p. 19.
4) N. A. Bostron, E. L. Hudspeth, and I. L. Morgan: Phys. Rev., 105, 1545 (1957).
5) J. L. Weil and K. W. Jones: ibid., 112, 1975 (1958).
6) N. A. Mansour, H. K. Saad, Z. A. Saleh, E. M. Sayed, I. I. Zaloubovsky, and V. I. Gontchar: Nucl. Phys., 65, 433 (1965).

III-3-8. Chemical States of Carrier-Free $^{119}Sb^{5+}$ at α-Fe_2O_3-Aqueous Solution Interfaces Studied by *in situ* Emission Mössbauer Spectroscopy

F. Ambe, S. Ambe, T. Okada, and H. Sekizawa

We reported previously that chemical states of cyclotron-produced $^{119}Sb^{5+}$ ions adsorbed on magnetic metal oxides can be studied by emission Mössbauer measurement of supertransferred hyperfine (STHF) magnetic fields on $^{119}Sn^{4+}$ produced by the EC decay of $^{119}Sb^{5+}$.[1] This year, *in situ* measurement was carried out on $^{119}Sb^{5+}$ at the interfaces between α-Fe_2O_3 particles and aqueous solutions of various pH values. Because of insensitiveness of the Mössbauer effect to chemical species in the solution, exclusive information on $^{119}Sb^{5+}$ at the interfaces was obtained. The chemical states of adsorbed $^{119}Sb^{5+}$ ions were found to be dependent on pH of the aqueous phase.

To a 0.25 mol dm^{-3} LiCl solution of carrier-free $^{119}Sb^{5+}$, about 30 mg of α-Fe_2O_3 powder was added. After adjusting pH to an appropriate value, the suspension was shaken at room temperature for 30 min. All the procedures were done in a Teflon vessel equipped with 0.5 mm Teflon window at the bottom. After settling of the α-Fe_2O_3 particles, the emission spectra of $^{119}Sn(\leftarrow ^{119}Sb^{5+})$ were measured at room temperature against a barium stannate absorber with the experimental setup shown in Fig. 1. The absorber was driven with a Ranger 700 series drive-system connected to a Tracor-Northern TN-7200 multi channel analyzer.

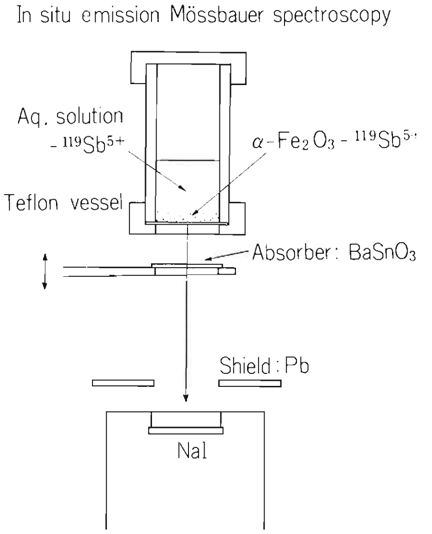

Fig. 1. Experimental setup of *in situ* emission Mössbauer measurement.

Typical spectra obtained are shown in Fig. 2. The ^{119}Sn arising from $^{119}Sb^{5+}$ at the α-Fe_2O_3 – aqueous solution interfaces gave at pH 6.5 a comparatively narrow emission spectrum ascribable to $^{119}Sn^{4+}$ (Fig. 2(a)). With lowering of the pH value, the spectrum broadened gradually and attained a FWHM of about 7.3 mm s^{-1} at pH 2.5 (Fig. 2(b) and (c)).

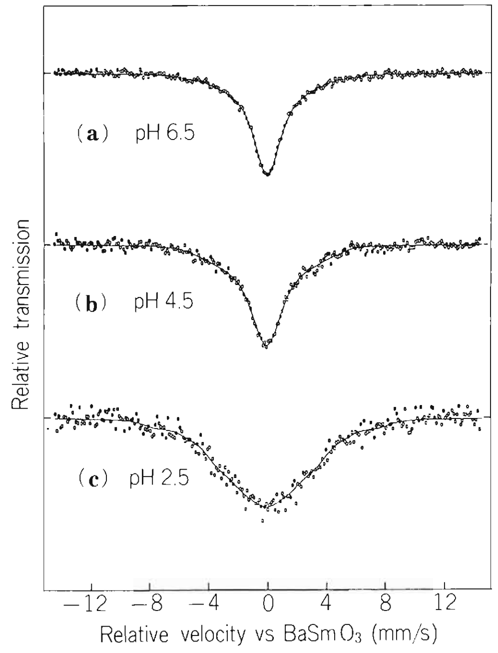

Fig. 2. *in situ* emission Mössbauer spectra of ^{119}Sn arising from $^{119}Sb^{5+}$ at α-Fe_2O_3 – 0.1 mol dm^{-3} NaCl interfaces.

Figure 3 shows the distribution of hyperfine magnetic fields on $^{119}Sn^{4+}$ calculated from the spectra by the method of Hesse and Rübartsch.[2] At pH 6.5 and 4.5, the distribution has a marked peak at zero field, which demonstrates that the majority of $^{119}Sn^{4+}$ arising from $^{119}Sb^{5+}$ ions at the interfaces is not or only weakly interacting with magnetic Fe^{3+} ions of the substrate. The hyperfine fields at pH 2.5 have broad distribution extending from zero field almost up to the value observed for $^{119}Sn^{4+}$ ions in bulk α-Fe_2O_3. This shows that a large part of $^{119}Sb^{5+}$ ions at the interfaces are

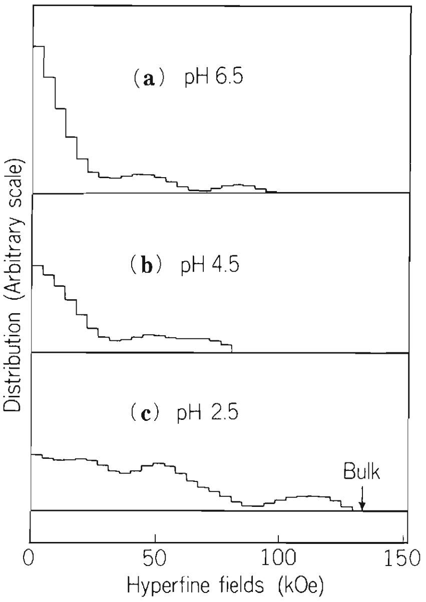

Fig. 3. Distributions of STHF magnetic fields on ^{119}Sn calculated from the spectra of Fig. 2.

interacting with Fe^{3+} ions of the substrate through $^{119}Sb^{5+}$-O^{2-}-Fe^{3+} bonds at the pH.

It can be concluded from these observations that the so-called "hydrolytic adsorption" of metal ions is not simply adsorption of hydrolyzed species formed in the solution onto solid surfaces. Studies on other oxides are in progress.

References

1) T. Okada, S. Ambe, F. Ambe, and H. Sekizawa: J. Phys. Chem., 86, 4726 (1982).
2) J. Hesse and A. Rübartsch: J. Phys. E, 7, 526 (1974).

III-3-9. Mössbauer Emission Study of Defect ^{119}Sn Atoms in p- and α-Irradiated SnS

S. Ambe and F. Ambe

Mössbauer emission spectroscopy of ^{119}Sn using cyclotron-produced ^{119m}Te and ^{119}Sb has been applied in this period to studies on defect structures in solids and on surfaces. Trials to incorporate ^{119}Sb into living matters were also performed. Here, a study on defect ^{119}Sn atoms in p- and α-irradiated SnS is reported. Surface studies on magnetic oxides are described in separate reports.[1),2)]

Previously, we reported the Mössbauer emission spectra of defect ^{119}Sn atoms produced by ^{120}Sn(p,2n)^{119}Sb$\xrightarrow{EC}$ ^{119}Sn and ^{117}Sn(α,2n) ^{119m}Te $\xrightarrow{EC}$ ^{119}Sb $\xrightarrow{EC}$ ^{119}Sn reactions in SnSe and SnTe.[3),4)] The chemical states of ^{119}Sn were found to be different drastically in the two matrices. The study has now been extended to defet ^{119}Sn in SnS.

The conditions of p- and α-irradiations were essentially the same as in the previous cases of SnSe and SnTe. The Mössbauer emission spectra of the irradiated samples were measured against a $BaSnO_3$ absorber at liquid nitrogen temperature.

The ^{120}SnS sample irradiated with protons gave a partly resolved asymmetric doublet as shown in Fig. 1. We attribute it to ^{119}Sn in Sn site of the matrix on the basis of the similarity of its Mössbauer parameters with those of normal tin in SnS obtained by absorption measurement. As the recoil energy of the EC decay of ^{119}Sb is smaller than the displacement energy in solid, it can be concluded from the observation that the energetic ^{119}Sb atoms produced by the proton reaction were exclusively stabilized in Sn site of SnS.

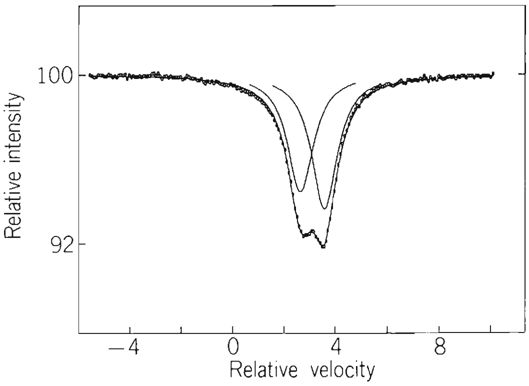

Fig. 1. Emission Mössbauer spectrum of p-irradiated ^{120}SnS at liquid nitrogen temperature.

The α-irradiated ^{117}SnS gave an emission spectrum decomposable into three Lorentzians (Fig. 2(a)). Thermal annealing of the irradiated sample resulted in remarkable change in the spectrum, as shown in Fig. 2(b) – (d). The relative intensity of the first peak (numbered from left to right) decreased by annealing and disappeared at 600 °C. The second and the third peaks shifted closer to each other, giving finally a doublet similar to that observed in p-irradiated ^{120}SnS. The first peak of the as-irradiated sample (Fig. 2(a)) is assigned to an unstable Sn^{4+} species from its isomer shift. The second and third peaks are considered to be a quadrupole doublet due to ^{119}Sn in Sn site of ^{117}SnS accompanied by local distortion of the lattice. Thermal annealing of the sample results in disappearance of the unstable Sn^{4+} and also in restoration of the distortion around the Sn^{2+}.

These observations demonstrate a close similarity of

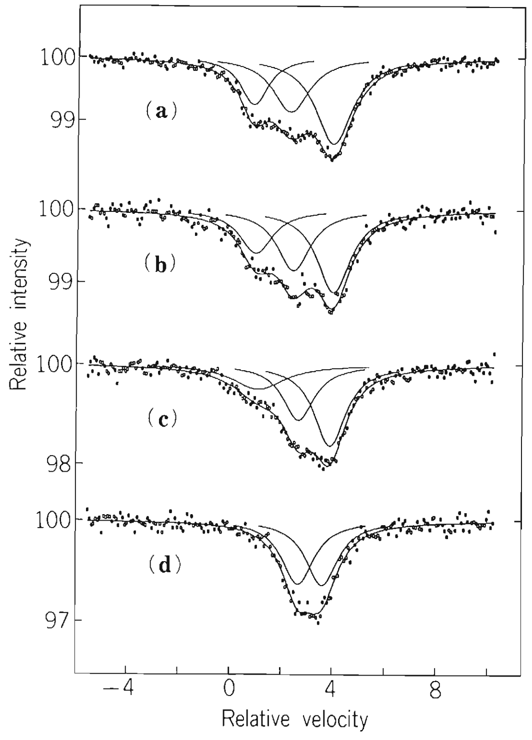

Fig. 2. Emission Mössbauer spectra of α-irradiated ^{117}SnS at liquid nitrogen temperature. (a) As irradiated, (b) after 2h annealing at 100 °C, (c) at 200 °C, and (d) at 600 °C.

the chemical effects of p- and α-reactions in SnS to those in SnSe reported previously.[4]

References

1) F. Ambe, S. Ambe, T. Okada, and H. Sekizawa: p. 109 in this report.
2) T. Okada, F. Ambe, S. Ambe, and H. Sekizawa: p. 74 in this report.
3) F. Ambe and S. Ambe: J. Chem. Phys., 73, 2029 (1980).
4) F. Ambe and S. Ambe: IPCR Cyclotron Progr. Rep., 14, 98 (1980).

III-4. Radiation Chemistry and Radiation Biology

1. Measurements of Photoemission Spectra and their Decay at Different Locations along a 50 MeV N-Ion Trajectory in Helium Gas at 400 Torr and at 5 K

K. Kimura, T. Kato,* N. Yamazaki,* S. Kubota, and M. Imamura

Electronic excitation processes induced in matter irradiated by heavy-ions are dependent on the ion energy and classified into the processes such as optical approximation, δ-rays, charge exchange, multiionization, and multiexcitation. Emission measurements of excited states formed in matter may allow us to know the probabilities of the aforementioned processes and their characteristic excitation. In a last report1) we revealed that N-ion irradiated He gas at several tens of mmHg near critical temperature exhibits characteristic dependence of emission spectra on (1) irradiation temperature and (2) irradiation pressure. No such dependence has been observed for the emission spectrum by microwave discharge and electron irradiation at room temperature or at a liquid phase.

This report presents experimental results on (1) stopping power dependence of the excitation and (2) dynamic properties of excited species along an N-ion trajectory traversing through cooled and high-pressure He gas.

Experimental arrangements are shown in Fig. 1. The beam spur of 90 MeV N-ions injected in He gas at 400 Torr at ca. 5 K was observed as a luminous zone of ca 10 mm in length. The emission spectra were measured at every few mm along the beam spur by sliding a condenser lens; a typical emission spectrum is shown in Fig. 2. Most emission peaks are assignable to those of He excimers, their hot bands, and their rotational side bands by comparing with the known peak positions reported by many workers.2) New bands were observed at 4945, 4598, 4585, 4521, 4289, and 4262 Å, all of which have not been reported in the previous optical studies. In view of our special experimental conditions, i.e. high density excitation with N-ion, low temperature, and high density, clusters of the He excimers(e.g. $He_2^* - He_2^*$) may be regarded as plausible candidates for the origin of these new bands. (Helium forms clusters at similar temperatures and densities according to Gspann.3))

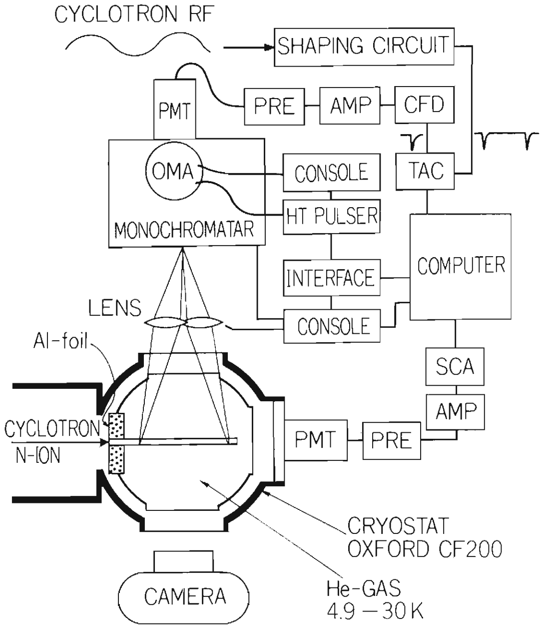

Fig. 1. Experimental layout. OMA, optical multichannel analyzer (Princeton Applied Research Co.)

Intensities of all emission peaks and stopping powers are plotted as a function of the N-ion range in Fig. 3. The lower five curves for peak intensities are seemingly similar to that for stopping power except for slight differences in peak position, rate of increase, and shape of curve; in contrast the upper three ones show different variations with range. These results suggest that excimers are formed through different physical and chemical processes with decreasing N-ion energy. Detailed analysis of these curves will provide information on the dynamic atomic and molecular processes which are dependent on particle energy.

To elucidate the dynamics of the He excimers at different positions along the trajectory, the time decay curves of respective emission peaks were measured along the trajectory. Some of the excimers were found to decay through two steps, the lifetimes of which are tens of nanoseconds and milliseconds. The initial rises of the fast components are plotted as a function of the range in Fig. 4. Figure 4 indicates that the formation of the state d^3 has a broad maximum shifting to the smaller range compared with the curves in Fig. 3 and that the state f^3 increases more sensitively with increasing

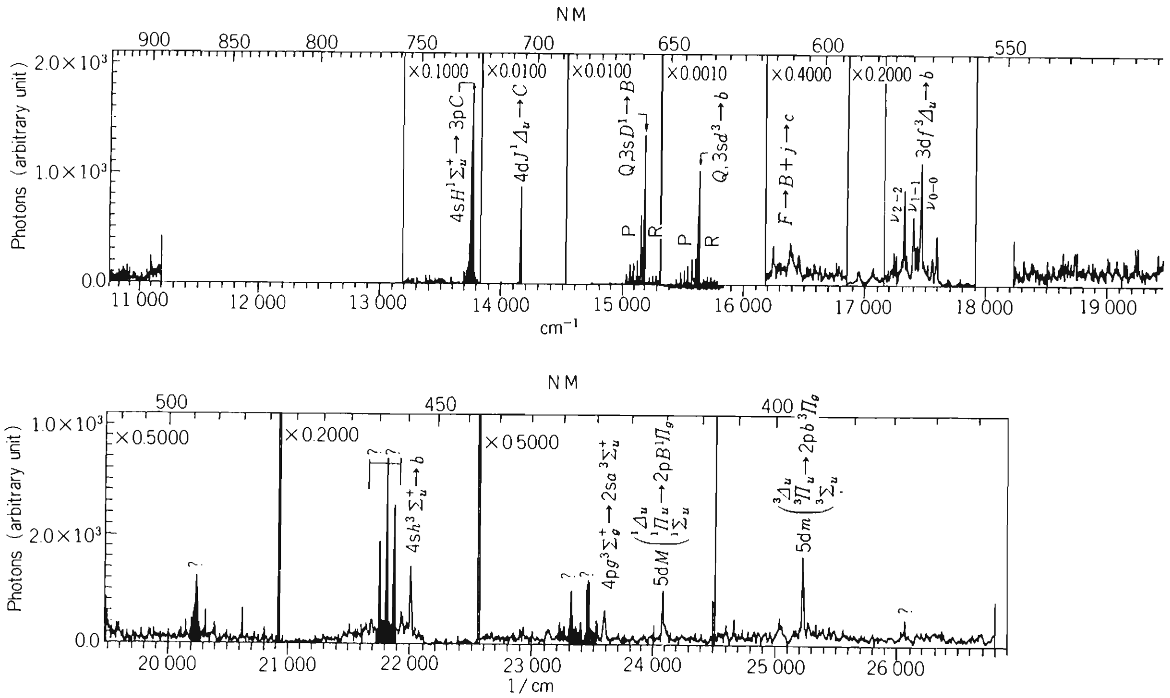

Fig. 2. Emission spectrum of He gas (at 390 Torr) irradiated with 5.33 MeV/amu N ions at 5.2 K. Measured at 10 mm of N-ion range. Assignments of peaks are due to Ref. 1.

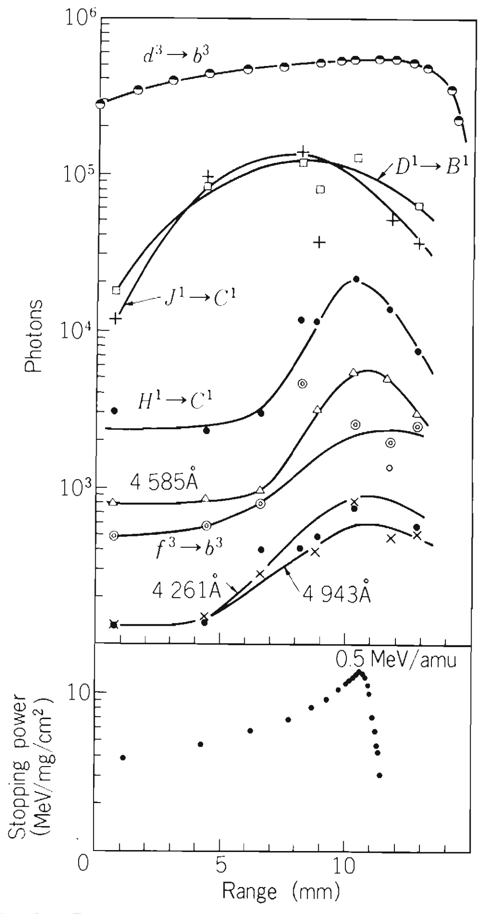

Fig. 3. Peak emission intensities and stopping power as a function of N-ion range. Incident energy of N-ions, 5.33 MeV/amu; He gas 420 Torr and 5.2 K. Stopping powers were calculated from the table by Northcliffe and Schilling.[7]

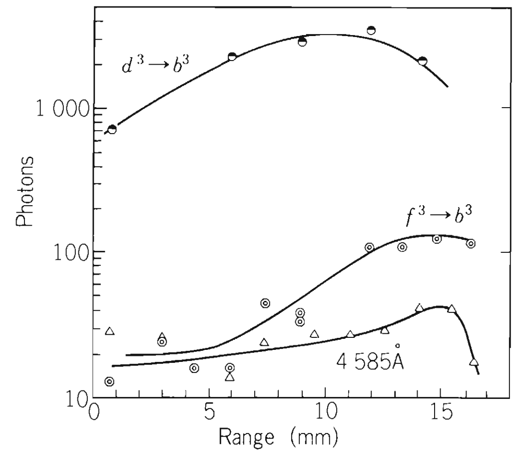

Fig. 4. Initial formation of fast emission components vs. ion range. Helium gas at 420 Torr was irradiated with 6.0 MeV/amu at 6.0 K.

range than the others, being formed rather efficiently near the end of the trajectory where the stopping power begins to fall off.

The slow decay component is explainable in terms of the reformation process of the upper-state excimer through a bilinear reaction of the excimer a^3 which is the lowest state with the longest lifetime as was proposed by Keto et al.:[4]

$$a^3 + a^3 \longrightarrow \text{upper state excimers.} \qquad (1)$$

If the decay of emission includes this reformation process, the inverse square-root of the emission intensity, $I^{-1/2}$, must be proportional to time from the initial excitation, t, as expressed by the following equation:

$$I^{-1/2} = I_0^{-1/2} + mt, \qquad (2)$$

where I_0 stands for the initial emission intensity. Thus, the slower decay processes, which were measured by using a chopped beam and gated OMA methods,5) were checked whether they obey Eqn. (2) or not. The result shows that the state d^3 and an unknown triplet at 4858, 4571, and 4598 Å are reproduced by Reaction 1 but the states D^1, J^1, h^3, and f^3 are not.

For investigation of He density effects, emission measurements of liquid-phase He irradiated by N-ions were undertaken by using a new cryostat. Preliminary experiments provides spectra different from those obtained for the gas-phase He mentioned above; detailed results will be reported shortly.

The fast-decay measurement of the emission using a technique of single-ion hitting and single-photon counting was developed to study the dynamics of the electronic excited states formed by heavy-ion irradiation.6) This year, we constructed a new detector consisting of a thin carbon foil, MCP, and a magnet instead of the system using photomultipliers, which will be used for the measurement of the fast decay and subnanosecond time-dependent spectra.

References

1) K. Kimura, Y. Toda, and M. Imamura: RIKEN Accel. Progr. Rep., 16, 134 (1982).
2) See references in "Constants of Diatomic Molecules", (eds K. P. Huber and G. Herzberg), Van Nostrand Reinthold, New York (1979).
3) J. Gspann: Surface Science, 106, 219 (1981).
4) J. W. Keto, F. J. Soley, M. K. Stockton, and W. A. Fitzsimmons: Phys. Rev., A10, 887 (1974).
5) K. Kimura and M. Imamura: Phys. Lett., 67A, 159 (1978).
6) K. Kimura, K. Mochizuki, T. Fujisawa, and M. Imamura: ibid., 78A, 108 (1980).
7) L. C. Northcliffe and R. F. Schilling: Nuclear Data Tables, 7, 233 (1970).

III-4-2. Inactivation of Bacterial Spores by a Single Heavy Ion

T. Takahashi, F. Yatagai, T. Katayama, Y.H. Kang,
S. Tamada, I. Kaneko, and S. Okada

In a recent paper.$^{1)}$ the inactivation cross sections of *B. subtilis* spores by C, N, and O ions have been shown to be explained fairly well by the track-structure models proposed by Katz and by Chatterjee and Schaefer, if parameters of the target theory are chosen so as to allow them to have proper experimental bases. For very heavy ions, however, experimental inactivation cross sections given by Schäfer et al.$^{2)}$ are somewhat larger than those calculated by our model.$^{1)}$ The discrepancy may be ascribed to a "long range effect" of heavy ions as previously pointed out by Takahashi et al.$^{3)}$

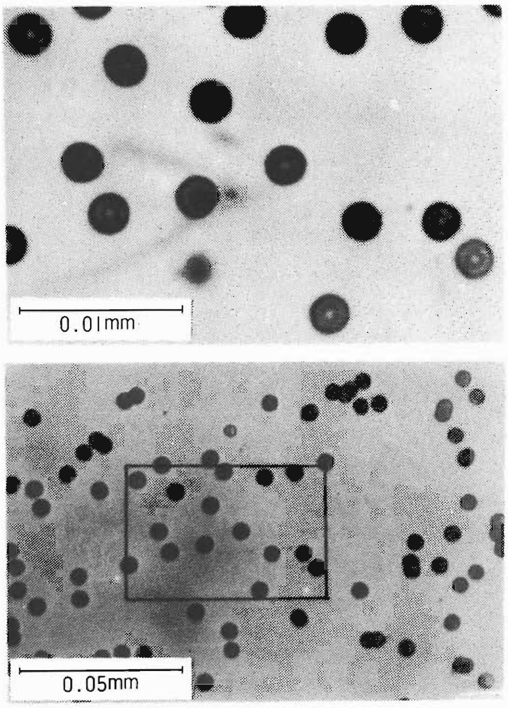

Fig. 1. Ar-ion tracks in CR-39 chemically etched with 70 °C in 7N-NaOH for 75 min.

To get better understanding of the mechanism of inactivation, experiments have been carried out to characterize a microscopic structure of the radiation action around a single heavy ion. This was done by measuring the rate of dead spores as a function of the distance between individual spores and the center of the path of an ion. The spores were fixed with 10 % aqueous polyvinylalcohol solution on a CR – 39 plastic detector, which is necessary for particle detection.

We have succeeded in incubating spores on the plastic detector and observed and photographed the outgrowth for each spore. The plastic detectors were irradiated by Ar ions from the heavy-ion accelerator (RILAC) and immersed in 7N–NaOH solution at 70 °C. Etch pits were found to be sufficiently developed in 60 – 75 minutes with their diameters of about 2.5 μm (Fig. 1). We are also examining a possibility that UV photons are emitted when the ion impinges upon the plastic detecor, because photons may also induce inactivation of the spores. Since very weak UV light seems to be emitted by α-particles, attempts have been made to estimate quantitative light yields.

References

1) T. Takahashi, F. Yatagai, and S. Kitayama: Adv. Space Res., 3, No. 8, 95 (1983); T. Takahashi and F. Yatagai: RIKEN Accel. Progr. Rep., 15, 139 (1982).
2) M. Schäfer, R. Facius, K. Baltschkat, and H. Bücker: 7th Symp. on Microdosimetry (1980).
3) T. Takahashi, F. Yatagai, and A. Matsuyama: Sci. Papers I.P.C.R., 74, 51 (1980); F. Yatagai, T. Takahashi, Y. Kitajima, and A. Matsuyama: J. Radiat. Res., 15, 90 (1974).

III-4-3. Rescue of Mitomycin C Sensitive Mutants of *Deinococcus radiodurans* by Irradiation with UV, γ-Rays, or N-Ions Following Mitomycin C Treatment

S. Kitayama and F. Yatagai

Living organisms have multiple systems to protect themselves against DNA lesions made spontaneously or induced by various physical or chemical treatments. Among the lesions, double-strand scissions and inter-strand cross-links in duplex DNA result in serious damage for cells, i.e. loss of genetic information, if the complementary DNA strands are cut off simultaneously at the lesion.

It is known that *Deinococcus radiodurans,* one of the extremely radio-resistant bacteria, can repair double-strand scissions and cross-links in duplex DNA.[1)-3)] DNA cross-links in the cells were found to be removed through several steps including incision of nicks on one or both strands of duplex DNA.[3)] Mutation was induced in the wild type strain on the removal of cross-links.[4)] Mutants sensitive to mitomycin C or to psoralen-plus-light were isolated and some of them were unable to induce nick at or near the lesion. As can be expected from its repair deficiency, one of such mutants gave no mutant progeny after the treatment which induces DNA cross-links.[4)] In this mutant strain which is unable to induce nick on the removal of cross-links, the defective step will be substituted by other physical or chemical procedures such as irradiation with γ-rays or ultraviolet light, or treatment with chemicals which induce strand breakage in DNA. As shown in Fig. 1, cells of KI696 which is a mitomycin C sensitive mutant were rescued from the lethal effect of mitomycin C by irradiation with ultraviolet light (254 nm), γ-rays from ^{60}Co, or accerelated N-ions (~67 MeV). It was reported previously that incision step was defective and cross-links in DNA were not removed in this sensitive strain.[3)] However, this mutant is resistant to ultraviolet light or γ-rays as well as the wild type strain. Therefore, it can be assumed that DNA strands were incised at pyrimidine dimer, a main photoproduct of uv irradiation. The defective incision step following mitomycin C treatment in this strain could be substituted by endonuclease for the dimer and the cells recovered their colony forming ability. It is also plausible that irradiation with γ-rays or N-ions induced DNA strand breakages which relieved the cells from the lethal effect of cross-links induced by mitomycin C. In order to substantiate these possibilities more detailed experiments must be carried out.

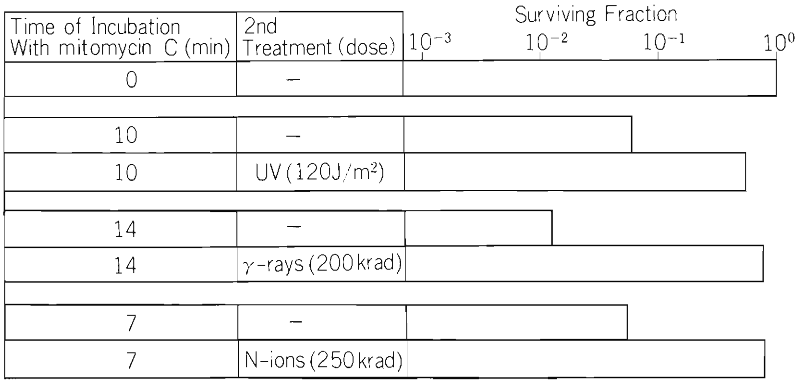

Fig. 1. Rescue of Mitomycin C Treated *D. radiodurans* KI696 (*mtc F*) by Irradiation with UV(254 nm), γ-rays or N-ions. Exponentially growing cells of *D. radiodurans* KI696 were incubated with mitomycin C(1 μg/ml) for various time at 30 °C. The cells were harvested, washed and resuspended with M/15 potassium phosphate buffer (pH 7). The resuspended cells were irradiated with uv(254 nm), γ-rays, or N-ions (~67 MeV).

References
1) S. Kitayama and A. Matsuyama: Biochem. Biophys. Res. Commun., 33, 418 (1968).
2) S. Kitayama: Biochim. Biophys. Acta, 697, 381 (1982).
3) S. Kitayama, S. Asaka, and K. Totsuka: J. Bacteriol., 155, 1200 (1983).
4) F. Yatagai and S. Kitayama: Biochem. Biophys. Res. Commun., 112, 458 (1983).

III-4-4. Effect of 3-Aminobenzamide on Sister Chromatid Exchange Frequency in Chinese Hamster V79 Cells Irradiated with Heavy Ions

I. Kaneko, K. Nakano, and G. Okada

DNA strand breakage is required for the formation of a sister chromatid exchange (SCE).[1)] Ionizing radiation is an efficient DNA strand breaking agent and an inducer of SCE in cultured cells. A majority of radiation-induced DNA breaks are very short lived, and they are resealed before they can elicit an SCE response.

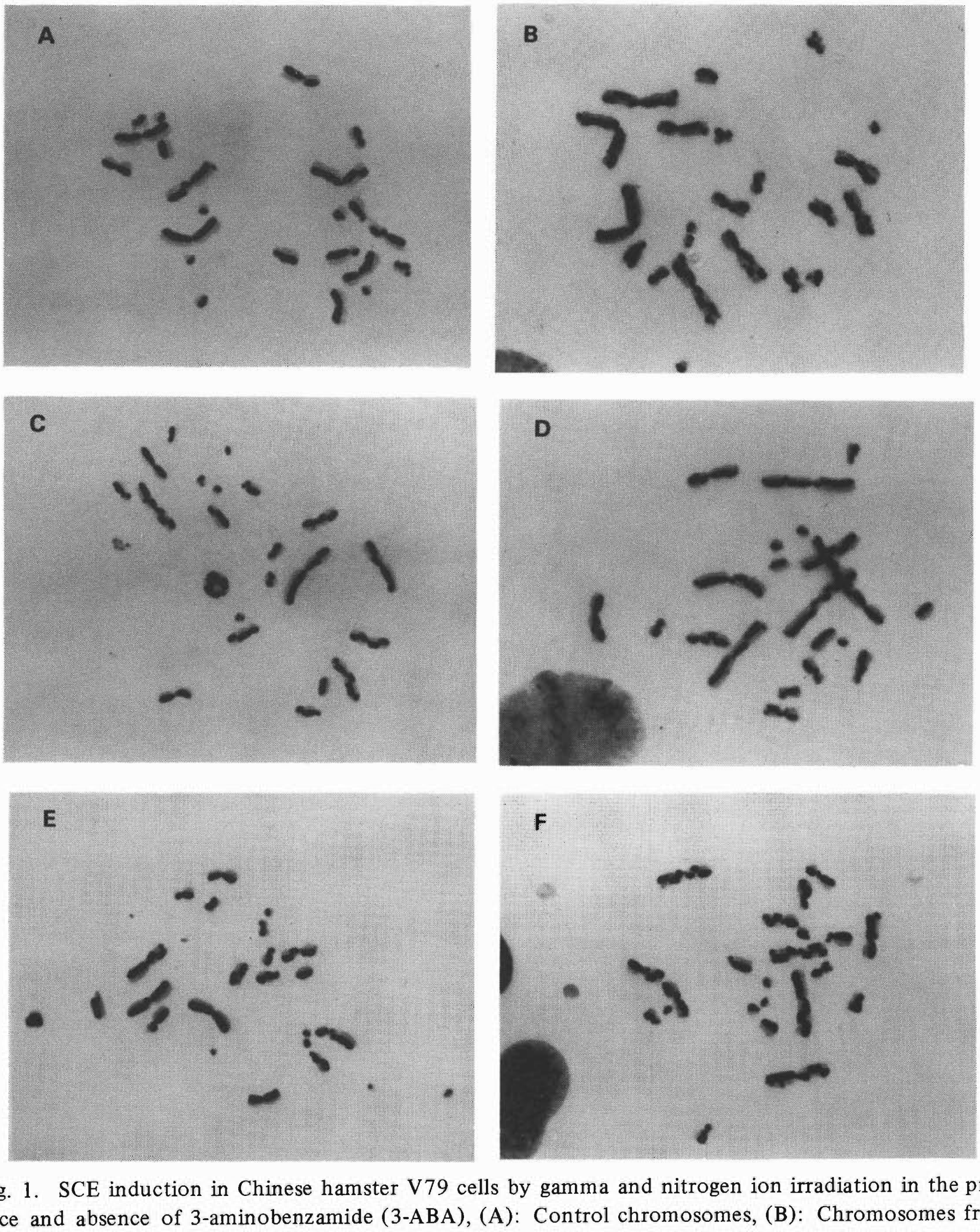

Fig. 1. SCE induction in Chinese hamster V79 cells by gamma and nitrogen ion irradiation in the presence and absence of 3-aminobenzamide (3-ABA), (A): Control chromosomes, (B): Chromosomes from cells exposed to 3-ABA, (C): Chromosomes from cells exposed to gamma-rays (4.5 Gy), (D): Chromosomes from cells exposed to gamma-rays (4.5 Gy) and 3-ABA, (E): Chromosomes from cells exposed to nitrogen ions (3.0 Gy), (F): Chromosomes from cells exposed to nitrogen ions (3.0 Gy) and 3-ABA.

The synthesis of poly adenosine diphosphate-ribose [poly (ADP-ribose)] is stimulated by a variety of DNA-damaging agents, including alkylating agents,[2] ultraviolet light,[3] and ionizing radiations.[4] DNA strand breakage appear to act as a stimulant for activity of the poly (ADP-ribose) polymerase, which can modify both itself and other cellular proteins by ADP ribosylation.[5] Inhibitors of poly (ADP-ribose) polymerase, such as 3-aminobenzamide (3-ABA) and benzamide, significantly increase a baseline of the enzyme activity.[6]

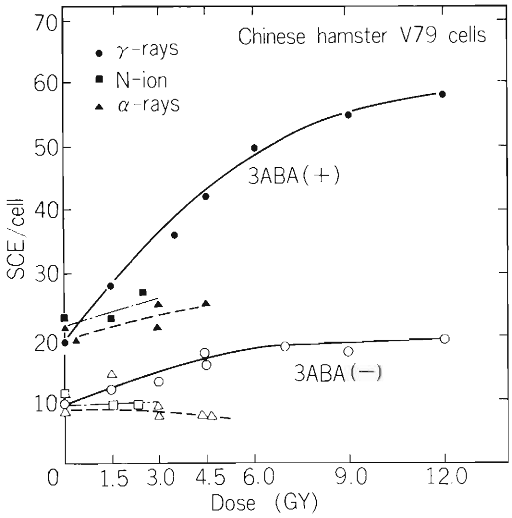

Fig. 2. Effect of 3-aminobenzamide (5 mM) on sister chromatid exchange frequency in Chinese hamster V79 cells exposed to γ-rays and helium- or nitrogen-ions accelerated in the cyclotron.

The purpose of the experiment is to find whether high LET radiations, helium- or nitrogen-ions accerelated in the cyclotron, can induce SCE in mammalian cells in the presence and the absence of 3-ABA. Gamma-rays alone caused a very slight increase in SCE frequency in the dose-dependent manner up to the dose of 5.0 Gy. The presence of 3-ABA before and/or after gamma-irradiation enhanced frequency of SCE in Chinese hamster V79 cells (Fig. 1 and Fig. 2). The presence of 3-ABA itself did rise SCE frequency. However, no sensitization effect on SCE induction was observed after helium- or nitrogen-ion irradiation. This was clearly different from a 3-ABA sensitization effect on gamma-irradiated cells.

References

1) W. F. Morgan and P. E. Crossen: Eviron. Mutagenesis, 2, 149 (1980).
2) R. C. Benjamin and D. M. Gill: J. Biol. Chem., 255, 10502 (1980).
3) B. W. Durkacz, O. Omidji, D. A Gray, and S. Shall: Nature, 283, 593 (1980).
4) W. F. Morgan, J. L. Schwarz, J. P Murane, and S. Wolf: Radiat. Res., 93, 567 (1983).
5) N. Nduka, C. J. Skidmore, and S. Shall: Eur. J. Biochem., 105, 525 (1980).
6) D. Cressen and S. Shall: Nature, 296, 271 (1982).

III-5. Instrumentation

1. Test of MCP and PSD for Electron Spectrograph Using Alpha-Source

J. Urakawa, H. Kumagai, Y. Awaya, T. Kambara, M. Kase,
T. Matsuo, H. Shibata, and A. Yagishita

A parallel-plate electrostatic spectrograph using a tandem microchannel plate (MCP) and a position sensitive detector (PSD) has been designed for the study of Auger electrons produced in ion-atom collisions.[1)] The MCP (Hamamatsu TV Co., Ltd.) is an image intensifier to amplify the extended image produced by an electron energy analyzer. The output electrons produced by the MCP are accelerated and impact upon the surface of the PSD (Hamamatsu TV Co., Ltd. Model S1352). In order to investigate the operating condition of this detection system, we tested the MCP and PSD using alpha-source of ^{241}Am. Figure 1 shows a typical position spectrum obtained by setting two 50 μm slits in front of the PSD. The position resolution of the PSD is estimated to be 360 μm (FWHM), where the shaping time of main amplifiers was 1 μsec. Figure 2 shows the position spectrum obtained by the combination of the MCP and the PSD. The position resolution is estimated to be about 500 μm (FWHM) where each MCP is operated at the voltage of 800 V and electrons from MCP is accelerated by the potential of 500 V between MCP and PSD. It is noted that the MCP is recommended to be operated with saturation mode of the supply voltage of about 1000 V but in this test the MCP was operated with the supply voltage of 800 V in order to optimize the total gain of the system.

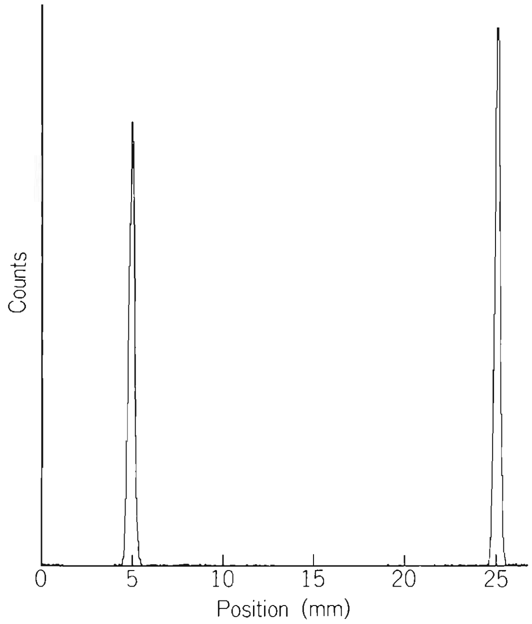

Fig. 1 Position Spectrum of PSD.

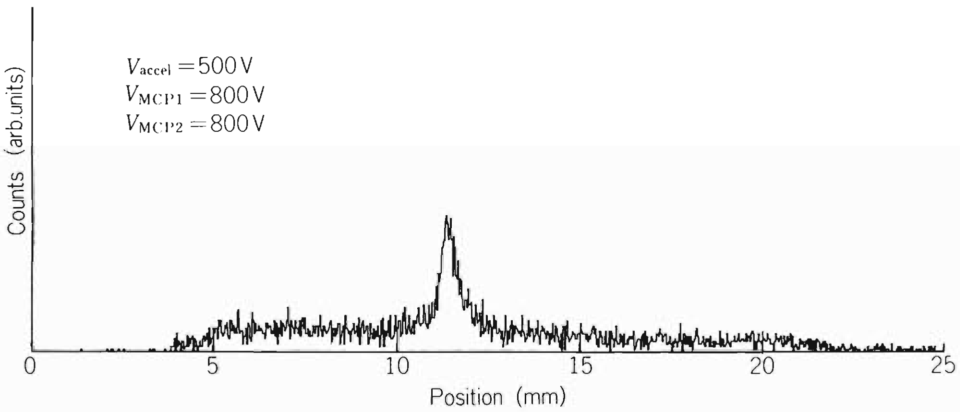

Fig. 2. Position Spectrum measured by the combination of MCP and PSD.

Reference

1) A. Yagishita and K. Agata: RIKEN Accel. Progr. Rep., 15, 83 (1981).

III-5-2. Experimental Setup for Electron Spectroscopy

A. Koyama, Y. Sasa, Y. Ishibe, A. Shiraishi, T. Shiga,
H. Omori, K. Nishi, M. Fuse, and M. Uda

An ultra high vacuum apparatus has been constructed in order to study spectra of electrons emitted from solid surfaces under heavy ion bombardment. Figure 1 is its photograph and Fig. 2 shows its schematic diagram. This apparatus is mainly composed of three parts: the slit box, the target preparation chamber and the target chamber, as illustrated in Fig. 2. Each of these chambers can be independently evacuated into ultra high vacuum.

The slit box contains slits S_1 and S_2, and a collimator. The slits S_1 and S_2 are equipped for differential pumping. They are made of copper pipes with inner diameter of 10 mm. S_1 is 150 mm long and S_2 50 mm. The slit box is connected to the beam transfer duct through S_1. When the pressure of the duct is 1×10^{-6} Torr, the pressure of the slit box can be reduced to 1×10^{-8} Torr. The collimator has an aperture of 1 mm diameter for beam collimation and is movable in the plane perpendicular to the beam direction. By adjusting the position of the aperture, incident beams are easily introduced onto the point where the optical axis of the energy analyser intersects the target surface.

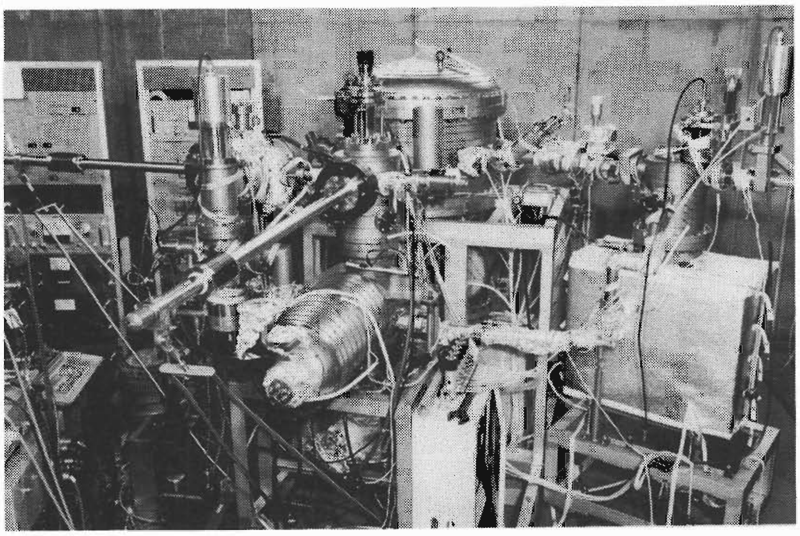

Fig. 1. Photograph of the ultra high vacuum apparatus for the spectroscopy of electrons induced by heavy ion bombardment.

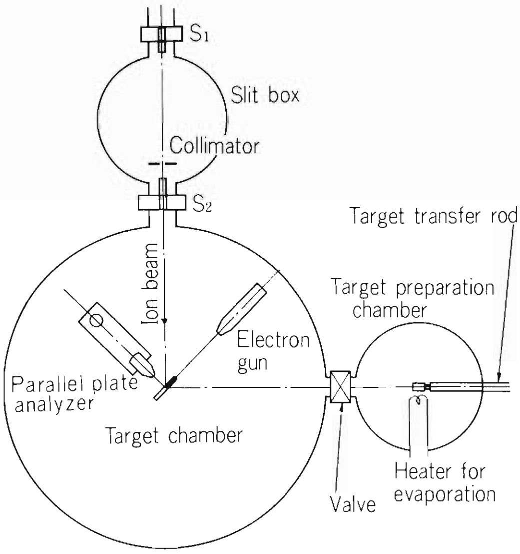

Fig. 2. Schematic diagram of the apparatus shown in Fig. 1.

The target preparation chamber is equipped with a vacuum deposition system and an ion gun for surface cleaning. In-situ vacuum deposition is carried out at pressure lower than 1×10^{-8} Torr. The target prepared can be transferred to the target chamber by sliding the target transport rod within a few minutes after target preparation.

The target chamber contains a parallel plate energy analyser with the energy resolution ($\Delta E/E$) of 1 % on a turntable, a rotatable target holder and an electron gun. The pressure inside the chamber is in the range of 10^{-10} Torr under beam irradiating conditions, and the magnetic field is reduced to about 10 mG by using a mu-metal cage. In order to improve the reproducibility of the data, measurements are being carried out repeatedly and each part of the apparatus is being examined.

III-5-3. Experimental Setup for PIXE

K. Maeda, Y. Sasa, and M. Uda

A scattering chamber for particle induced X-ray emission (PIXE) analysis was constructed and connected to RILAC. A photograph of the chamber is given in Fig. 1. The chamber is evacuated with a turbo-molecular pump and a rotary pump. The pressure in the chamber goes down to 3×10^{-6} mmHg after one hour pumping.

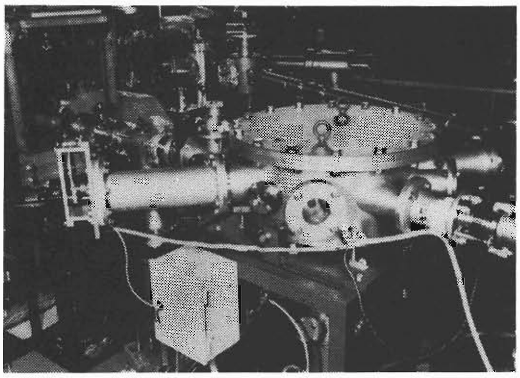

Fig. 1. Photograph of the scattering chamber for PIXE.

The schematic diagram of the experimental setup for PIXE is shown in Fig. 2. A target sample placed on a sample holder is irradiated with ion beams accelerated by RILAC. To analyze many samples rapidly, the sample holder was of a cassette type which can be loaded with 35 samples at once. The target can be changed automatically by remote control. A graphite collimator is placed in front of the target to prevent the target from being irradiated by undesired ions such as scattered ions. Ions transmitted through the target are collected on a Faraday cup and counted with a current integrator. Beam current absorbed by the target can also be measured through a terminal (T).

X-rays emitted from the target are detected by an energy dispersive semiconductor (Si(Li)) detector through a thin Mylar (4 μm in thickness) window. If necessary, X-rays in a particular energy region can be depressed by inserting an X-ray absorber between the target and the window. Six X-ray absorbers are arranged on a disk and can be exchanged by remote control. The detected X-ray signals are amplified by a pre-amplifier and a linear amplifier, and then processed by a multichannel analyzer (MCA). The data obtained are transported to a personal computer (IF800) and recorded on a floppy disk. Simple, on-line data analyses are done by the personal computer. Precise treatments of data, such as peak deconvolutions and estimation of the concentrations of elements from the peak intensities, are carried out with an off-line computer (FACOM M-380).

A Si(Li) detector designed especially for soft X-ray analysis is under construction.

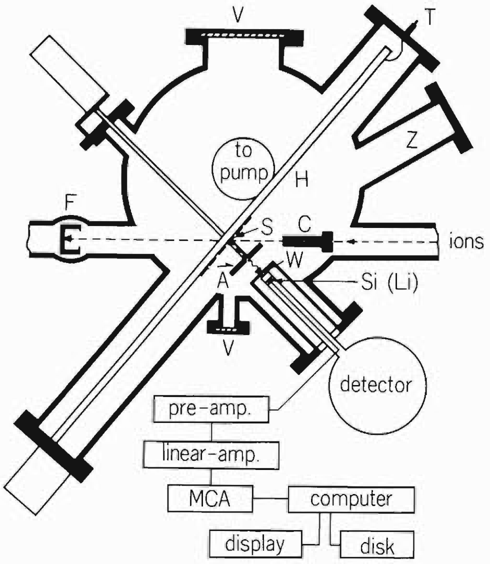

Fig. 2. Schematic diagram of the experimental set-up.
A: X-ray absorber, C: collimator, F: Faraday cup, H: sample holder, S: target sample, T: terminal, V: viewing port, W: window, Z: port for arbitrary use.

III-5-4. Nuclear Data Acquisition System with CAMAC

T. Inamura, T. Murakami, J. Kasagi, H. Kumagai, and Y. Gono

A CAMAC system has been developed to accommodate demands for arbitrary multi-parameter data acquisition.

A computer, Perkin-Elmer 3220, that controles the CAMAC system is in the RILAC laboratory.[1] For the time being the nuclear experimental station will be in the 160 cm cyclotron facility. Because of this, the CAMAC crate is placed in the cyclotron laboratory, and is connected to the computer with optical fiber cables about 150 m long. We have chosen a pair of LeCroy 5210 U-port Adapters. They provide an electrically isolated byte-serial highway, being used with a type L2 Serial Crate Controller (L2SCC) and a built-in serial driver of the computer. The circuit system allows transmission of greater than 4 megabytes/sec.

Needless to say, optical fiber transmission is immune to electromagnetic interference. Taking into account this advantage, we are thinking of adopting optical fiber transmission of data from experimental area to the counting room in the SSC facility. The present experiment would provide a nice feasibility test for this purpose. Figure 1 shows a block diagram in the case of neutron-charged particle-gamma coincidence experiment that is currently underway.[2]

The basic acquisition software supplied has been modified to improve the data acquisition rate. Although we have not yet tested it fully, we hope the acquisition rate will be a few kilo events/sec without changing any hardware. To improve the data acquisition rate further, we will introduce a local intelligence, for instance, a stand-alone microcomputer with a buffer memory at the site of experimental station. The data acquisition rate will then be several tens-kilo events/sec.

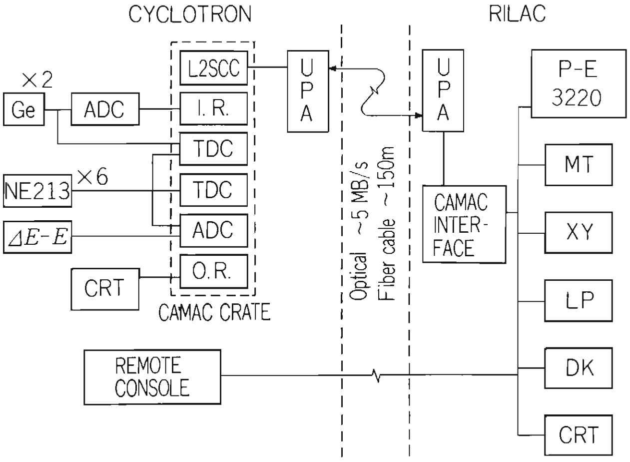

Fig. 1. An example of the CAMAC data acquisition system.

References
1) H. Kumagai and M. Sasagase: RIKEN Accel. Progr. Rep., 15, 123 (1981).
2) T. Murakami, J. Kasagi, H. Harada, and T. Inamura: p. 125 in this report.

III-5-5. Neutron Multiplicity Filter

T. Murakami, J. Kasagi, H. Harada, and T. Inamura

A neutron multiplicity filter and its data acquisition system were constructed to investigate the excited states in neutron deficient nuclei, especially around A = 80 – 100, produced via heavy-ion reactions. The neutron multiplicity filter is used to identify the residual nuclei from which γ-rays are emitted, being coupled with or without a ΔE – E counter telescope.

Figure 1 shows a photograph of the neutron multiplicity filter. Its performance is summarized in Table 1. Neutrons are detected with an array of six NE213 liquid scintillators. A center detector is placed at 0 degree to the beam and surrounded by five detectors. The center piece is a regular pentagon with sides of 78 mm and its thickness is 75 mm. The other five pieces are pentagons with one side of 78 mm and four sides of 98 mm; their thickness is 75 mm. They cover 40 % of the whole solid angle in the laboratory system. Since the detection efficiency of the neutron detector is estimated to be around 30 %, the counting rate in which one or more detectors are fired is about 35 % of the single events in the reaction of neutron multiplicity 4.

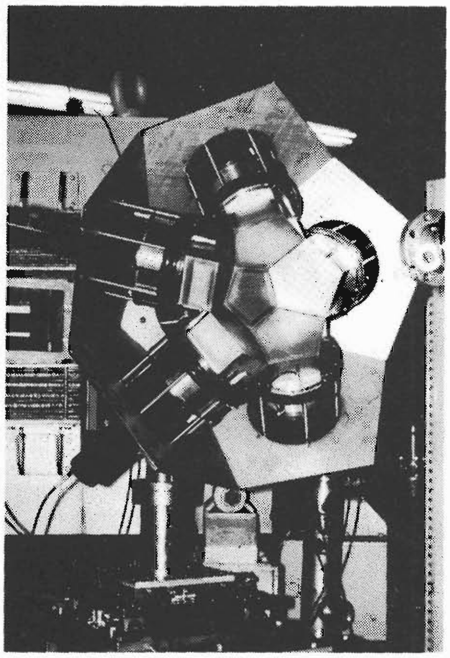

Fig. 1. A photograph of neutron multiplicity filter.

The CAMAC is adopted as the data acquisition system to accept many parameters of the data. The details are described in another report of this volume.[1]

Neutrons and γ-rays from the ^{100}Mo + ^{16}O reaction at 80 MeV were measured using this system. Gamma spectra in coincidence with one or more neutron detectors are shown in Fig. 2. The prominent peaks mainly come from the 4n reaction product ^{112}Sn. Ratio

Table 1. Performance of the neutron detector.

Size	center :	105 cm^2 × 7.5 cm × 1 (regular pentagon)
	surrounding :	154 cm^2 × 7.5 cm × 5 (pentagon)
Scintillators & photomultiplier		NE 213 R 1250 (Hamamatsu, 5″φ)
Solid angles		0.50 sr/the center detector 0.71 sr/the surrounding detector in a typical case. Efficiency including solid angle is estimated to be 1.7 %/each surrounding detector: for the center one 1.2 %.

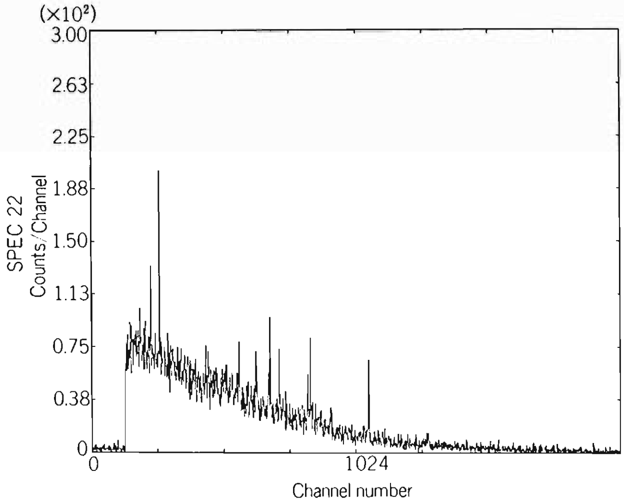

Fig. 2. Gamma spectrum observed in coincidence with the neutron detectors ($N_n \geqq 2$) for the ^{100}Mo + ^{16}O reaction at 80 MeV.

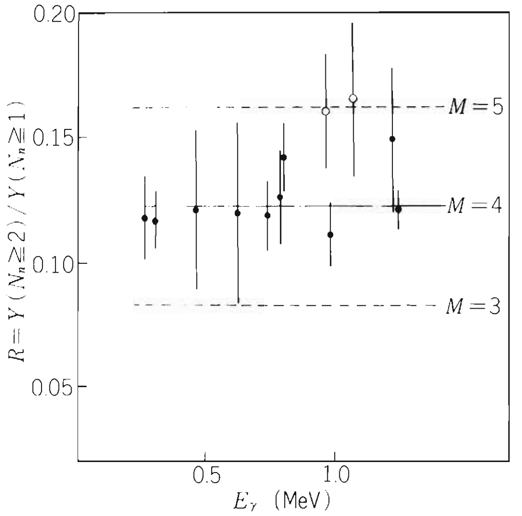

Fig. 3. Ratio of the yield of $N_n \geqq 2$ to the one of $N_n \geqq 1$. The dotted lines are estimated values for multiplicity M.

of the yield of $N_n \geqq 2$ to the one of $N_n \geqq 1$ is plotted in Fig. 3, where N_n is the number of triggered neutron detectors. As can be seen in the figure, the obtained values of the ratio increase as the neutron multiplicity increases and agree well with the estimated ones.

Reference

1) T. Inamura, T. Murakami, J. Kasagi, H. Kumagai, and Y. Gono: p. 124 in this report.

III-5-6. He-Jet Transport System

H. Kudo, T. Nomura, and J. Fujita

A gas-jet transport system is now widely used for the investigation of unstable nuclei with relatively short half lives. Typical lifetimes covered with this transport system ranges from a few tens of ms to a few minutes. The gas-jet transport system can easily be combined with other experimental facilities such as those of a gas phase chemistry, a rapid chemistry, and an isotope separator on line.

We have constructed a helium-jet transport system which consists of an aerosol generator, a reaction chamber, and a collection tape system.

1) Aerosol generator and gas supply system

It has been reported that aerosols in the gas flow passing through a capillary play an important role to realize stable efficiency and good reproducibility of transporting reaction products through the capillary and of collecting them onto a catcher.[1)] Imanishi[2)] obtained almost 100% efficiency for fission products by using aerosols of dioctyl phthalate (often used as a diffusion-pump oil) as a carrier of recoil products. The system they used was stable over a few weeks of running time and reproducible over a period of about 6 months. Therefore, we have made the same kind of aerosol generator and gas supply system.

The aerosol generator system consists of a nebulizer, a nucleater, a reheater, and a condenser, which is schematically drawn in Fig. 1. The diffusion pump oil is vaporized by the nebulizer, and mixed in the reheater with NaCl seeds produced from the nucleater. Then the vapor in helium, passing through the condenser which is cooled with water, comes to condense on NaCl seeds and grows into aerosol particles.

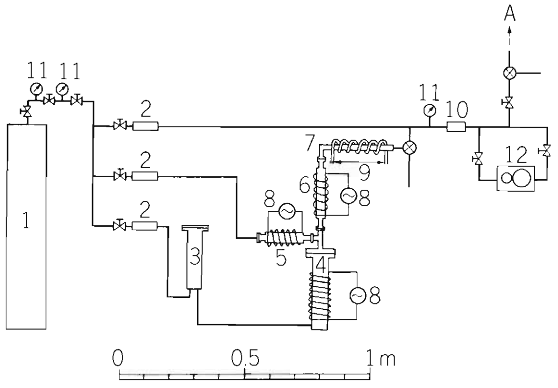

Fig. 1. Aerosol generator and gas supply system
1 : helium gas, 2 : rotameter, 3 : reservoir, 4 : nebulizer, 5 : nucleater, 6 : reheater, 7 : condenser, 8 : temperature-controlled heater, 9 : water cooling, 10 : check valve, 11 : pressure gauge, 12 : compressor.

2) Reaction chamber

The reaction chamber is composed of an energy degradator, a target holder, a thermalizing room, and a Faraday cup with a water cooling jacket as shown in Fig. 2. In the thermalizing room, the pressure of helium is kept at 1 atm, and the vacuum of the cyclotron is maintained by sealing the window of the reaction chamber with a thin metal foil. Reaction products are slowed down, thermalized with helium, and deposited on surfaces of the aerosols. The aerosols are transported through a 1 or 2 mm $\phi \times 10$ m long teflon capillary to the collection chamber.

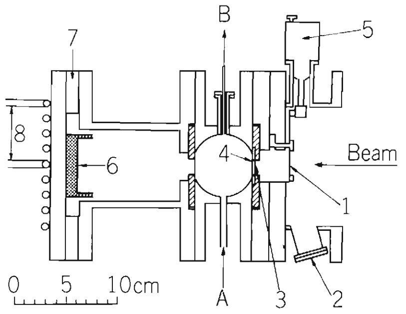

Fig. 2. Reaction chamber
1 : energy degrader, 2 : viewer, 3 : vacuum seal foil, 4 : target, 5 : vacuum sealed rotator, 6 : graphite beam stopper, 7 : insulator, 8 : water cooling.

3) Collection tape system

The collection chamber is evacuated with a mechanical booster pump backed by a rotary pump. The end of the teflon capillary is finely adjustable for changing the collection position. The transported aerosols are deposited on a magnetic tape which serves as a collector and moves to the detector position by menas of a micro-computer controlled stepping-motor and two servo motors. The end of the magnetic tape is monitored by a photo-senser. The system is shown in Fig. 3.

In the collection chamber, a temperature controlled heating apparatus is mounted for the purpose of evaporating the oil which will cause a poor resolution in an α-spectrum. For the differential pumping needed for

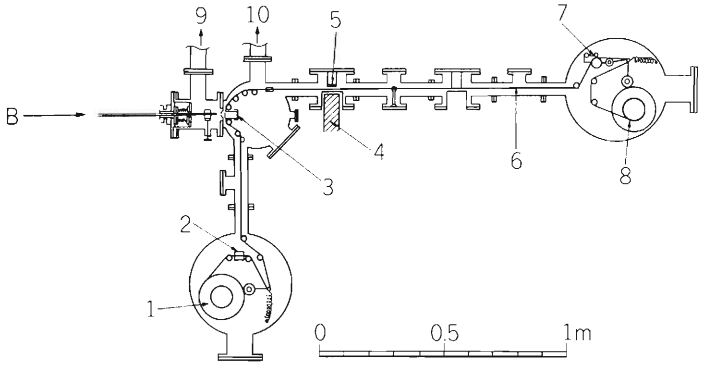

Fig. 3. Collection tape system
1 : feed reel, 2 : photo-senser, 3 : heater, 4 : Ge(Li) detector position, 5 : Si (Au) detector position, 6 : collection tape, 7 : pulse motor, 8 : take-up reel, 9 : to roots pump, 10 : to diffusion pump.

more evacuated condition, for example, in the case of measurement of electrons, a skimmer can be attached between the end of the teflon capillary and the collection tape.

Some preliminary results using this system are given in this Report.

References

1) H. Jungclas, R. D. Macfarlene, and Y. Fares: Phys. Rev. Lett., 27, 556 (1971).

2) N. Imanishi, I Fujiwara, and T. Nishi: J. Nucl. Sci. and Tech., 17, 935 (1980).

III-5-7. A Goniometer for Internal Transient Magnetic Field Study

A. Hashizume, N. Sakai, K. Asai, H. Kumagai,
and Y. Yamada

The measurement of perturbed angular distributions of γ-rays from Coulomb excited states gives us information on magnetic moments or internal magnetic fields if life-times of the excited states are already known. By use of very large transient magnetic field caused by the recoil nucleus travelling through polarized ferromagnetic substance, g-factors of excited states with life-times in pico-second region can be measured.

A goniometer combined with a C type magnet was installed at D1 beam channel[1)] in the RILAC experimental area (Fig. 1). The magnet was designed also for use in the measurement of perturbed angular distributions of γ-rays with external magnetic field. With pole pieces of 70 mm in diameter and of 30 mm pole gap, the maximum magnetic field of 1.25 T was obtained. The instability of current was less than 4×10^{-3} %/3 h. The 350 kg magnet can be easily removed from the normal position to set up a SSD in a target chamber. The target and the chamber are insulated from earth potential and the magnet, and serves as a Faraday cup. The angle of a detector on

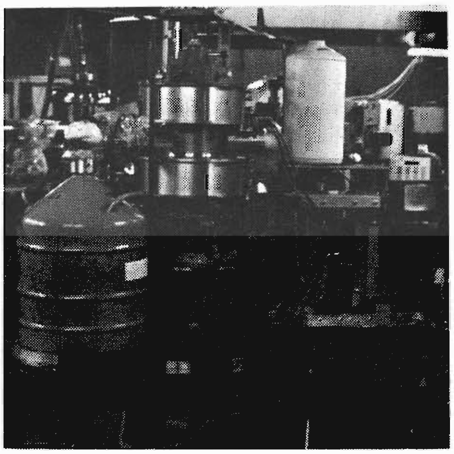

Fig. 1. Photograph of the goniometer for internal transient magnetic field study.

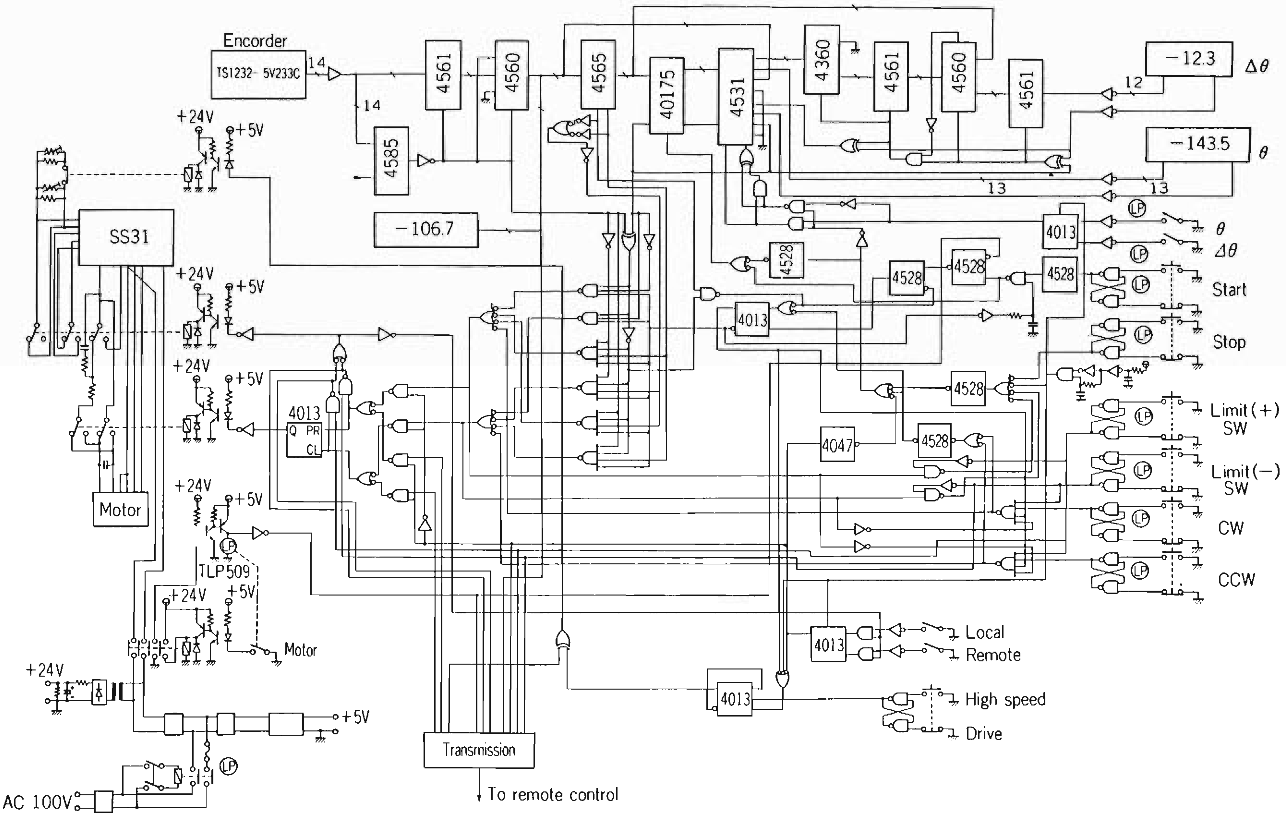

Fig. 2. The circuit for the control of the goniometer.

a rotating arm is detected by an encorder with which digitized readings of the angle can be easily obtained. The control circuit is shown in Fig. 2. The arm can be controlled in an operating room. An interface between the control circuit and an on-line computer was also designed. Angular distributions of γ-rays from natural dysprosium evaporated on a thin Fe backing and excited by 45 MeV $^{40}Ar^{4+}$ were studied in a trial run.$^{2)}$

References

1) M. Hemmi, Y. Miyazawa, and M. Odera: IPCR Cyclotron Progr. Rep., 14, 126(1980).
2) A. Hashizume, N. Sakai, K. Asai: p. 27 in this report.

III-5-8. In-Beam Alpha- and Electron-Measurements with a Superconducting Solenoid

Y. Gono, Y. Itoh, M. Sugawara, and T. Kasuya

A superconducting solenoid was installed at a beamline of the cyclotron to measure the in-beam alpha-particles and electrons.

This magnet was originally constructed for the laser research use by Kasuya et al.[1] The magnetic field strength up to 70 kOe can be obtained with the excitation current of 32 A. The diameter of the working space is 38 mm. These values result in the transmission of alpha-particles with 73 and 36 msr for 10 and 20 MeV, respectively. The detection efficiency depends on the size of the Si detector which is used for the energy analysis. The alpha-particle spectrum taken by a 300 mm^2 Si detector with the solenoid is shown in Fig. 1. This spectrum is taken from the ^{209}Bi + ^{12}C reaction at E = 80 MeV with a Bi target of about 500 μg/cm^2 thick. The energy resolution is about 50 keV at FWHM. The continuum background is substantially suppressed in comparison with a spectrum taken without the solenoid. A propeller shaped baffle was used for this measurement. However this did not work well enough to eliminate the electron background and it was still necessary to use a timing measurement with respect to the beam-bursts. A new baffle has been prepared recently to suppress further the background.

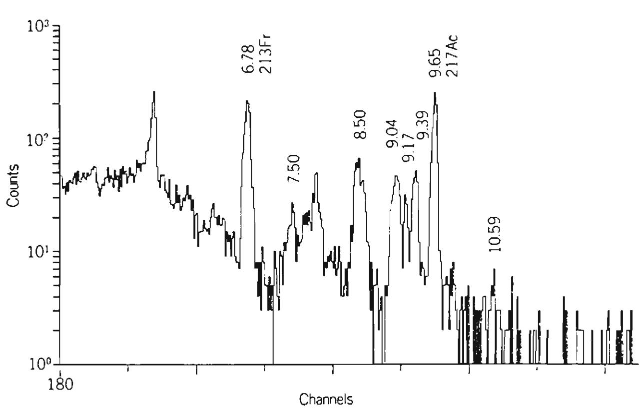

Fig. 1. Delayed alpha-spectrum from the ^{209}Bi(^{12}C, 4n)^{217}Ac reaction at 80 MeV taken by a Si detector with a superconducting solenoid. Numbers given in the figure are in MeV.

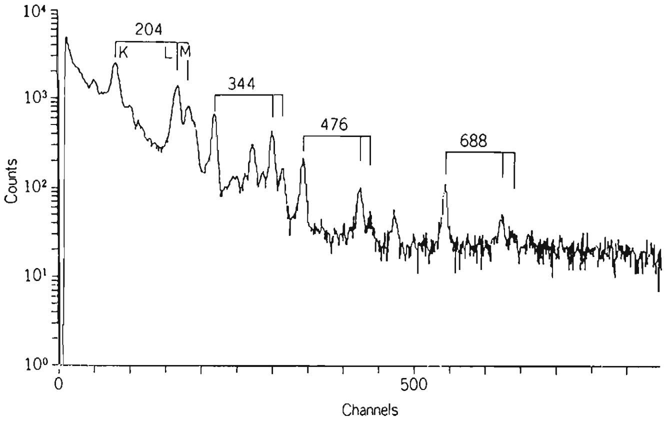

Fig. 2. Delayed electron-spectrum from the ^{208}Pb(^{12}C, 4n)^{216}Ra reaction at 80 MeV taken by a cooled Si detector with a superconducting solenoid. Numbers given in the figure are in keV.

This system could also be applied for the in-beam electron measurement by using a cooled Si detector. For this purpose a 5 mmϕ baffle was placed at the center of working space of the solenoid to avoid a tremendous background due to delta-electrons. One example of the delayed electron spectrum is shown in Fig. 2. This spectrum was obtained from the ^{208}Pb(^{12}C,4n)^{216}Ra reaction at E = 80 MeV. The energy resolution of the peaks is about 8 keV at FWHM which should be easily improved by replacing the Si detector with a better one.

Reference

1) T. Kasuya et al.: Jpn. J. Appl. Phys., 12, 1572 (1973).

III-6. Miscellaneous

1. PIXE Analysis for Environmental Substances

K. Maeda, Y. Sasa, M. Maeda,* M. Kobayashi, and M. Uda

Particle induced X-ray emission (PIXE) spectroscopy was applied to the elementary analysis of environmental substances. In environmental science, a large number of samples collected in various situations should be analyzed in a short time. Sometimes the samples to be analyzed are very small in size or quantity. Relative concentration of each component element is important in evaluating the material balance in the system of interest. The PIXE, which is a rapid, non-destructive, multielemental, trace analysis technique, is therefore most suitable for analysis of environmental substances. We describe here several examples of the application of the PIXE. The details of the experimental procedures and setups are reported elsewhere.[1),2)]

(1) River pollution at an urban area. The composition of suspended particulates in water of the Tama River was determined by the PIXE. The sampling was made in August 1978 at nine locations in the lower reaches extending over 25 km from the river mouth (see Fig. 1). The samples collected on membrane filters served as the targets for the PIXE without any pre-treatment. A half of each sample was used for the induced coupled plasma emission spectrometry (ICP) and the atomic absorption spectrometry (AAS) to get the absolute amount of Si and to check the results of the PIXE.** Figure 2 shows a typical PIXE spectrum obtained from the suspended particulates. Here 15 MeV N^{2+} ions accelerated by RILAC were used for excitation. The elements Al, Si, P, S, Cl, K, Ca, Ti, Mn, and Fe were detected. The concentrations of these elements were evaluated from the spectra by referring to those of the standard samples. Variations in the contents of particulate silicon, potassium and titanium along the river are given in Fig. 3. The high contents of the elements at location 6 must be due to the local perturbation of the river stream. Except the values at location 6, the particulate silicon content did not change significantly. On the other hand, the contents of particulate potassium and titanium showed minimum values at location 7. The distributions of the concentrations of Al, Ca, and Fe were similar to those of K and Ti. These features indicate that the components originated from minerals were deposited at an early stage and then the pollution arising from human actions took place. As can be seen from Fig. 3(b) and Fig. 3(c), the results

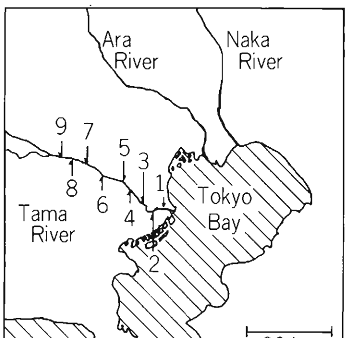

Fig. 1. The sampling locations for the particulate matters.

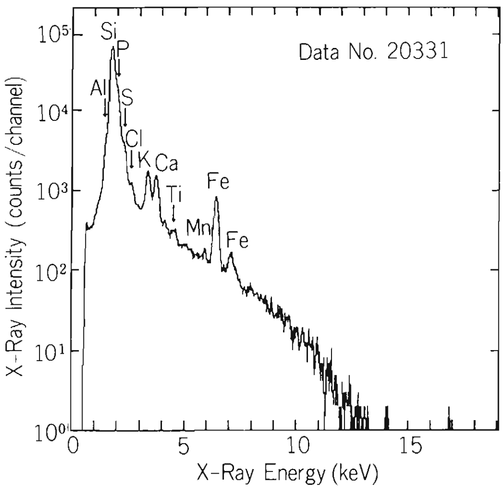

Fig. 2. The PIXE spectrum from the suspended particulates collected from the Tama River water at location 4.

---

* Tokyo University of Fisheries.

** The ICP and the AAS analyses were carried out by Dr. Takahashi at Inorganic Analysis Center.

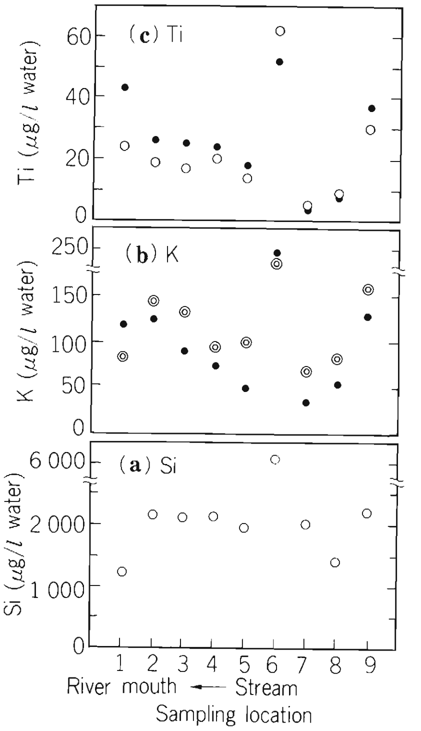

Fig. 3. Variations of the concentrations of the particulate silicon (a), potassium (b) and titanium (c) along the Tama River.

● : by PIXE, ○ : by ICP, ◎ : by AAS.

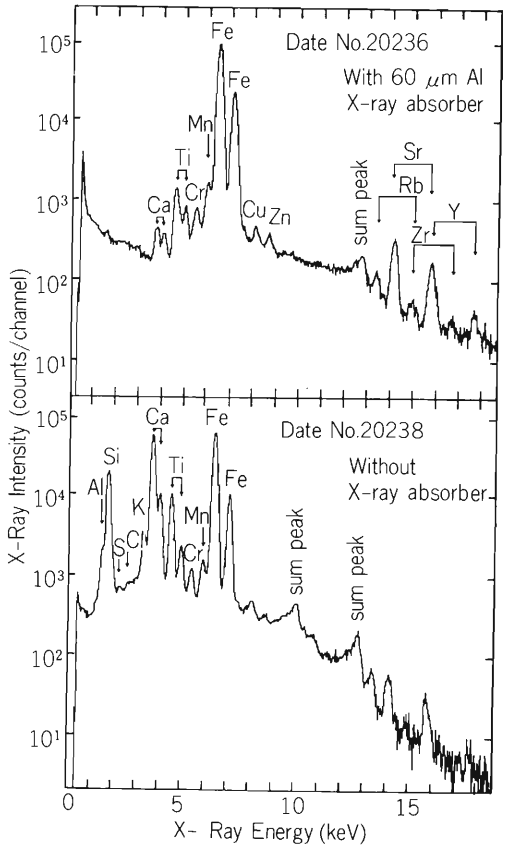

Fig. 4. The PIXE spectra from one of the volcanic locks extravasated from the Kilauea in 1979.

of the ICP and the AAS are consistent with the PIXE data.

(2) Volcanic rocks from the Kilauea. The volcanic rocks extravasated from the Kilauea in 1969, 1974, and 1979 were analyzed with the PIXE and X-ray diffraction technique. Figure 4 shows the PIXE spectra obtained from one of the volcanic rocks excited by 5 MeV H^+ ions. The X-ray diffraction patterns suggest that the main component of the rocks is feldspar.

(3) Volcanic ashes from Mt. Asama. The volcanic ashes from Mt. Asama were collected at Shinagawa, Tokyo in April 1982. The PIXE spectrum obtained from the ashes excited by 5 MeV H^+ ions resembles the spectra of the volcanic rocks from the Kilauea except that the content of the volatile element, S, in the ashes is much higher than that in the rocks.

Detailed analysis of the experimental results for the volcanic rocks and the volcanic ashes is in progress.

References

(1) K. Maeda and M. Uda: Reports I. P. C. R., (in Japanese), 58, 96 (1982).
(2) K. Maeda, Y. Sasa, and M. Uda: p. 123 in this report.

III-6-2. Application of PIXE to Medical Science (I)

M. Uda, K. Maeda, Y. Yokode,* and Y. Sasa

The PIXE (Particle Induced X-ray Emission) method is one of the advanced techniques for elemental analysis without destruction. This method is characterized as follows: (1) applicable to all the elements except Z = 1 ~ 3, (2) simultaneous analysis of all the elements present, (3) high and relatively constant sensitivity to all the elements, and (4) high speed analysis. Thus, the method has wide varieties of applications, especially in trace-elemental analyses of biological and environmental (pollution) materials. The most effective samples for this are those containing small amounts of heavy elements embeded in matrices which are mainly composed of light elements, especially in organic materials.

Chemical compositions in biologic tissues might not be the same as normal ones if the tissues are cut out from the affected part. The PIXE method is now expected to be used for diagnosis. In this report we deal with a few applications of this method to medical science.

Fresh tissue samples were freeze-dried and sectioned with a microtome at 10 μm, and then deposited on Mylar film of 4 μm in thickness. Characteristic X-rays

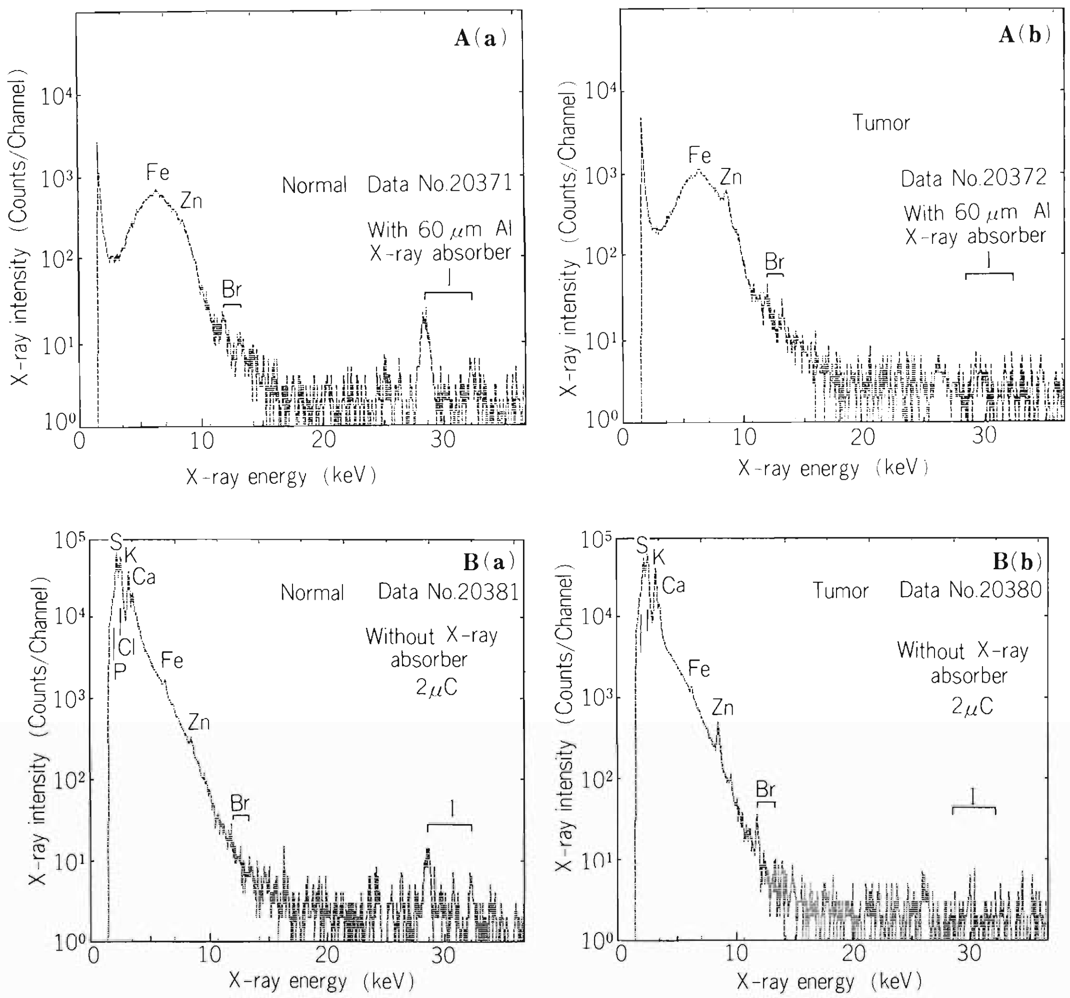

Fig. 1. PIXE spectra obtained from normal (a) and tumor (b) tissues in a thyroid gland taken from a patient of colloid adenoma.

A : with 60 μm Al X-ray absorber, B : without X-ray absorber.

---

* School of Medicine, Nihon University.

were emitted from these samples by irradiation of 5 MeV protons accerelated by the cyclotron, and detected by a Si(Li) detector. Signals from the detector were amplified by pre- and linear- amplifier, and finally analyzed by a multichannel analyzer and a mini-computer. Here spot size and electric current of the proton beam were regulated to be 2×2 mm^2 and $2 \sim 20$ nA, respectively. To get better statistics for the data in a high energy X-ray region an aluminum foil with 60 μm thickness was inserted between the sample and the detector. Energy calibration of X-rays was performed by use of Ag Kα, Ag Kβ and Ag L X-rays emitted from a silver foil of 1 mg/cm^2. The bovine liver from NBS was used as a standard sample for most of the elements analyzed here.

PIXE spectra obtained in this experiment are shown in Fig. 1. Chemical compositions of the tissues used were estimated$^{1)}$ from the individual peak intensities in these figures, and are summarized in Table 1. No traces of iodine were present, but zinc was much enriched in the tumor (Colloid adenoma). Lack of iodine was also observed from the tissue cut out from the thyroid gland with the chronic thyroiditis.

Table 1. PIXE Kα peak intensities and elemental concentrations in human tissues.

Disease	Organ	Kα peak intensity (counts/μC)				Elemental concentrations (μg/cm^3)		
		Fe	Zn	Br	I	Fe	Zn	Br
Colloid adenoma	Thyroid gland normal tissue	19	11	3	7	95	32	15
	Thyroid gland tumor tissue	18	37	3	<0.5	90	110	14
Chronic thyroidites	Thyroid gland	21	38	3	<0.5	105	38	16
Habitual angina	Tonsil	17	17	4	<0.2	85	49	20
Nasal papilloma	Nasal cavity tumor tissue	22	21	4	<0.2	110	61	18

Reference

1) K. Maeda and M. Uda: Reports I.P.C.R., (in Japanese), 58, 96 (1982).

Ⅳ. ACCELERATOR DEVELOPMENT

1. Present Status of the RIKEN SSC Project

H. Kamitsubo

The project for construction of a k = 540 MeV separated sector cyclotron (SSC) at RIKEN has progressed satisfactorily in 1983. The sector magnets with twenty-nine pairs of trim coils fixed on pole faces were made one by one at Niihama Factory of Sumitomo Heavy Industries, Ltd. and the last one was completed in October, 1983. Accuracy of machining and assembling poles, yokes, main and trim coils and base of the magnet was inspected for each magnet, installing it at the factory. Performance of piping for cooling water and of wiring for coils was also inspected. Excitation characteristics and field distributions were measured for the first magnet. Interference effect of fields produced by the sector magnets at the SSC and the field distribution in the valley region between two magnets were preliminarily studied in 1982 by using the first and second magnets. The measurement was performed after carefully installing them in such a way that two sectors were precisely concentric and their center radii were perpendicular to each other. The median planes of two magnets must coincide with each other, too. Results of the measurement were quite satisfactory. The beam dynamical analysis has been pursued taking these results into account. Distribution of the field produced by each trim coil was also measured in 1982 along the center radius of the sector, varying strength of the base field and excitation current of the trim coil. Optimization method of the trim coil currents to realize the isochronous field distribution has been studied. The final data of the field distributions will be taken after four magnets are installed in the cyclotron vault of the SSC building.

Power supplies for the main and trim coils are in fabrication and will be delivered in the middle of 1984. Numbers of the power supplies for the main and trim coils are two and thirty-seven, respectively, and those of parameters to be adjusted are five and fifty-six, respectively. We decided to use SCR (silicon controlled rectifier) in the power supplies of the main coils to reduce their costs. Protection method for SCR noise propagation is under investigation.

Design studies of the RF system have been carried out in this period and we finally decided to adopt a resonator system using a moving box as a frequency changing device. Although this system has merits that total height of the system and current density at the contact fingers of the moving short (or box) are smaller compared with a conventional λ/s or half wave-length type resonator, it has a demerit that shunt impedance is relatively low and it needs more electric power. To improve this situation the frequency range may be reduced to that from 20 to 45 MHz. Then the problem will occur in matching of the SSC and the RILAC in the low frequency range since the frequency range of the latter is 17 to 45 MHz. A possible way is to change a harmonic number of the SSC in the low frequency range. At present, design work of the resonator which covers the frequency range from 20 to 45 MHz is in progress.

Design studies of a high power amplifier for the RF system have been pursued. The maximum output power is 300 kW and stability of the RF voltage as well as its frequency must be very high. A tetrode, RCA 4648, is a candidate for the power tube at the final stage of the amplifier system. Grid tuning circuit for cathode-grounded amplifier has been studied by taking into account neutrization of RF voltage fed back through the interelectrode capacitance.

Final design of the vacuum system and the vacuum chambers is almost finished. The vacuum system is composed of ten cryopumps, four turbomolecular ones and four rough vacuum systems. Total evacuation speed is 12×10^4 ℓ/sec and the final vacuum lower than 10^{-7} Torr is expected inside the chamber. Pneumatic expansion seals will be used as vacuum seals between the RF resonator and the vacuum chamber. Mechanical and vacuum technological tests was continued in this period for one-third scale models. Structure analysis using the finite element method was also performed. Model studies of the ECR (electron cyclotron resonance) discharge cleaning of the magnet chambers were finished.

Basic design of the computer control system was finished and the system was ordered to Mitsubishi Electric Co. It consists of a network of three minicomputers, MELCOM 350-60/500, connected with each other by double optical cable lines and CAMAC systems.

One computer is used for control of the RILAC whereas the other two are used for the SSC control. To save number of CAMAC crates and standard modules, and also to realize efficient control of the accelerators, new CAMAC modules named CIM (Communication Interface Module) and DIM (Device Interface Module) are being developed. Two prototype models were made and are being tested: one is for control of beam diagnostic devices and the other is for control of power supplies of the sector magnets.

Final design of the SSC building as well as the investigation of radiation safety problems for that design was finished last year and construction of the building started this year. It is devided into three phases. The first phase is to build the cyclotron vault, which will be finished in March, 1984. The sector magnets will be transferred from the factory to RIKEN and installed by the end of June. The second phase for construction of the control room, four experimental rooms and a counting room will start in the middle of 1984 and completed in 1985. The remaining part of the building will be constructed after the first beam is obtained.

Design of the beam transport system to the experimental areas was finished and final design of magnets and beam diagnostic devices is in progress. The first operation of the SSC in combination with the RILAC is expected in 1986. Discussions on experiments using the beams started this year by both inside and outside users and workshops on the possible experimental facilities to be built were organized.

Ⅳ-2. Control System of the RIKEN SSC

T. Wada, J. Fujita, K. Shimizu, I. Yokoyama, and T. Kambara

RIKEN separated sector cyclotron (RIKEN SSC) consists of two injectors (linac and AVF cyclotron) and a separated sector cyclotron.1) A large number of devices are distributed around them. There are thousands of parameters. In order to obtain a desired beam (particle and energy) and to transport it to a proper experimental area in a short time, complicated and fast control sequences are necessary. Because of this, computers are introduced.2)

The characteristics of the control system are as follows:

(1) A computer network consisting of distributed mini-computers is adopted;

(2) CAMAC crates are linked by a serial highway with optical fiber cables;

(3) Micro processors are used for the interface between CAMAC and devices;

(4) A simple network is adopted for the local control;

(5) As many analog signals as possible are digitized and sent to the control room;

(6) Application programs are written in FORTRAN 77 language.

Three mini-computers are linked using optical fiber cables. Each computer is of the same type, and is MELCOM 350 – 60/500 (Mitsubishi Electric Corp.). This is a new 32-bit industrial computer. The characteristics of the computer is listed in Table 1, where SHD is a bit-serial highway driver. An intelligent system console includes two flexible disk drives. Many of the system subroutines required for real-time operation have been converted to firmware which allows faster execution of programs. The time critical part of operation system can be made resident on the cache memory. Table 2 lists the configuration of each computer. The network is that of duplex system. Even in the failure of one line or failure/power-off of any one computer, the computer link can be retained. The computer 1 and 2 are installed in the control room of SSC and the computer 3 is in the control room of RILAC.

The computer 1 controlles the SSC through the CAMAC serial loop. The console devices such as touch panels, color displays and shaft encoders are installed in the control desk. These devices are linked to the computer 1 without a CAMAC system. The control desk consists of three parts (center, left and right parts). The

Table 1. Characteristics of MELCOM 350 – 60/500.

CPU	ECL LSI
memory	64 Kbit LSI with ECC
word length	32 bit
max. memory	16 MB
max. address	4 GB
cycle time	250 ns/8 byte
cache memory	160 KB
cache cycle time	95 ns/8 byte
register	24 (32 bit)
instruction	450
pipeline	5 steps
MIPS	3.7
computation time	ADD 0.095 μs
	FADD 0.3 μs
	FMULT 0.5 μs
	SIN (x) 5 μs
interrupt	8 levels
network	15.36 Mbps
CAMAC SHD	5 Mbps
GP – IB	250 kBps

Table 2. Configuration of each computer.

Computer 1 (SSC)	
memory	3 MB
fixed disk	70 MB
CAMAC SHD	1
GP – IB	1
Computer 2 (data base)	
memory	3 MB
fixed disk	70 MB × 2
magnetic tape	2 (1600/800 bpi)
line printer	1 (670 lpm)
TSS terminal	4
plotter	1 (7 pens)
communication port	11
graphic display	1 (7 colors)
hard copy	1
CAMAC SHD	1
Computer 3 (linac)	
memory	2 MB
fixed disk	70 MB
magnetic tape	1 (1600/800 bpi)
line printer	1 (670 lpm)
plotter	1 (7 pens)
graphic display	1 (7 colors)
hard copy	1
character display	1 (7 colors)
GP – IB	2

left and right parts are equivalent. The devices which are linked to the computer 1 are installed in these areas. The minimum time of data refresh on a CRT is 280 msec. This time interval is determined by that of the digital displays in automobiles. The center part is prepared for the devices such as ITV's and scopes which are not linked to the computer.

The computer 2 is used to store the data-base of the control system in large disk files. Most of the data are initial values, logging data and device name/link tables. The current values are stored mainly in the memories of the micro processors mentioned later. The source programs are also stored in the disk file. The machine codes of the control programs are stored in the disk files of control computers. The control computers pick up the necessary data or ask for remote batch jobs to this computer. This computer is also equipped with a CAMAC SHD and can be used as a back-up computer for the control computers. This computer is linked to the central computer of our institute.

The computer 3 controlles the RILAC through the GP – IB.3)

The first computer and a CAMAC system are scheduled to be delivered in summer, 1984 and used for the field measurement of the four sector magnets.4) Because a GP – IB interface is not ready by this time, we will use a personal computer as a makeshift. The other two computers, GP – IB interfaces and an operator console will be installed in October, 1985.

Figure 1 shows the CAMAC system. Seven CAMAC crates are distributed in four power supply rooms. Because the distance between these rooms and the control computer is very long (90 m max.), these CAMAC crates are connected by a serial CAMAC loop using optical fiber cables.

Two types of modules which include micro processors and memory are developed for the interface between controlled devices and the CAMAC system.5) One is a CAMAC module which has 16 pairs of serial I/O ports. The other is an interface module to each controlled device and is installed at a place close to the device. The information are transferred serially between these two modules.

The advantage of using these modules is in that it is possible to decrease the number of crates and electronic components in comparison with a system using conventional CAMAC modules. Consequently the reliability can be enhanced and the mobility of the control computer can be improved.

These modules are named as a communication interface module (CIM) and a device interface module (DIM),

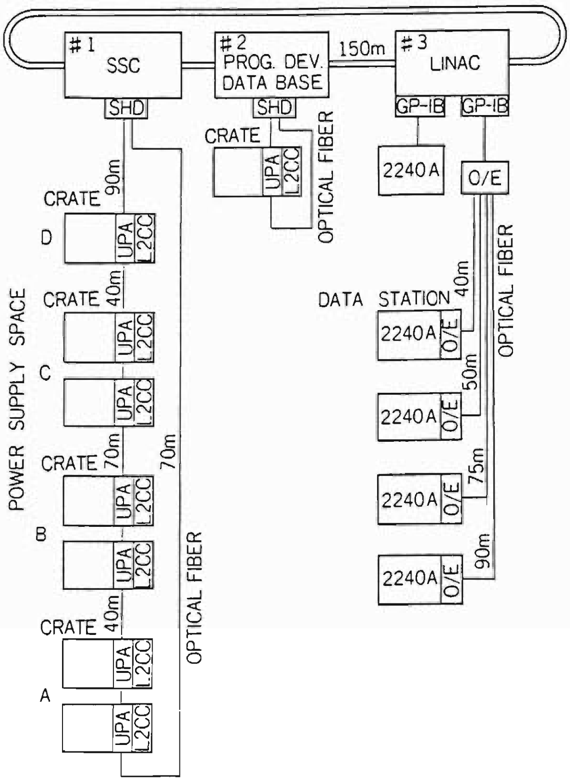

Fig. 1. Configuration of CAMAC system.

respectively. The CIM resembles the ER16VM module6) or LOCT module.7) This includes a micro processor and is linked to each DIM by a pair of plastic optical fiber cables. The information is transmitted with the rate of about 170 kbps and the maximum distance is 30 m. Figure 2 shows the schematic diagram of a CIM, where ROM and RAM are read only memory and random access memory, respectively. Each DIM is addressed by a subaddress (A) of CAMAC instruction. The instruction/data between CIM and DIM are defined by a 24-bit CAMAC word. The DIM consists of a micro processors, memories, parallel and serial I/O ports. It can include ADC, DAC and another micro processor depending on the controlled devices. A small console can be connected temporarily to the DIM for stand alone operation. The DIM can control several devices. It performs necessary control sequences such as start up, monitoring and stop. For example, the sequences of driving pulse motors for slits and detectors, scanning analog data from multi-wares and storing the digital data in memory are performed for a emittance measuring device independently on a control computer. The monitoring is performed at predetermined time intervals and the results are stored onto memory. In case of the failure of devices, the control computer reads out the contents of memory for trouble shooting. The numbers of CIM's and DIM's are about 50 and 150, respectively.

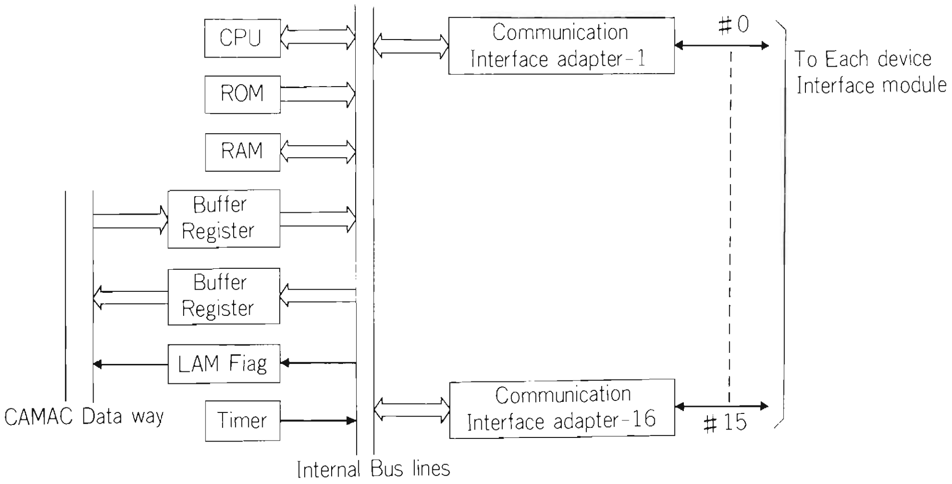

Fig. 2. Schematic diagram of communication interface module (CIM).

The CIM and DIM are made using multilayer boards.

The construction of the prototypes of CIM and DIM (CPU 8031) will be completed this November and functional tests will be done by linking to an emittance measuring device of linac.

For the local diagnosis, it is conveninet to use movable consoles.$^{8)}$ However, we made another decision in order to lower the cost and to have more flexibility. A simple network is adopted and only the ports for CRT display are prepared at necessary places. In making diagnosis, a CRT display is carried and plugged into the nearest port. These ports are also used for the display of machine operations at operator rooms or counting rooms by selecting desired part of the machine from a keyboard.

As many analog signals as possible are digitized and sent to the control room through the CAMAC loop. It is often necessary to observe wave forms of the signals from some beam detectors such as coaxial Faraday cups and phase probes. For these signals a sampling method is adopted and the band width is reduced. The results are sent by coaxial cables (100 MHz) and displayed on the scopes on the control desk. The contents of the display memory are read into the control computer through a GP – IB.

The operating system (OS60) is a real time and multi task system. It is also possible to transfer meassages and the contents of disk files to other computers via a computer network. Another important function is the starting of tasks in other computers by sending or receiving parameter values.

The application programs are written in FORTRAN 77 language which includes real-time functions. A FORTRAN 77 debugger is incorporated for the interactive debugging of the programs. Many software packages for graphic display, network and data-base are prepared. The source program are updated by a screen editor.

References

1) H. Kamitsubo: Proc. 9th Int. Conf. on Cyclotrons and their Applications, p.13 (1981).
2) T. Wada, J. Fujita, K. Shimizu, I. Yokoyama, and T. Kambara: Proc. Japan – China Joint Symp. on Accel. for Nucl. Sci. and their Applications, (to be published) (1983).
3) T. Kambara, M. Kase, and T. Kubo: RIKEN Accel. Progr. Rep., 16, 176 (1982).
4) H. Takebe, I. Takeshita, J. Fujita, I. Yokoyama, T. Wada, S. Motonaga, and T. Sato: ibid., p. 188.
5) K. Shimizu, I. Yokoyama, T. Wada, J. Fujita, and Y. Yano: 6th Symp. on Future Project of RCNP, Osaka, Jan. (1983).
6) R. Baumgarten: Int. Report, GANIL 81R/062/CC/09 (1981).
7) P. Lienard: Int. Report, CERN/PS/LI/82-15 (1982).
8) M. Prome: IEEE Trans. Nucl. Sci., NS – 28, No. 3, (1981).

Ⅳ-3. On the Fundamental Constitution of the SSC Control System

K. Shimizu, J. Fujita, T. Wada, and I. Yokoyama

Many apparatus are used in each section of the RIKEN SSC. In order to control such a large number of apparatus quickly and precisely, it is essential to use a computer as a control element because the hardware of the control system can be standardized partially and the operation flexibility can be increased. When a more effective control system for the SSC is desired, the computer system should satisfy the following conditions.

(1) Several computers are employed to obtain a short turn-around time through their concurrent operation.

(2) All the computers are compatible with each others to allow easy back-up of the remaining ones when one computer fails.

(3) Each computer has high performance and a large directly addressable memory area to process rapidly the information such as beam adjustment and graphical display.

(4) Time delay arising from the transmission of information between computers is as short as possible.

(5) With regard to software supports, the overhead in operating system is as short as possible. Standard language such as FORTRAN and computation libraries accepted widely are utilized to promote programmer's productivity. An interpreter, which makes the program development, testing and debugging fast and easy, is included.

Next we turn to interfacing systems which link the computers and many apparatus. The systems should satisfy the following requirements.

(6) Since the distance from the computer to the controlled apparatus of the SSC is very long, it is desirable to decrease the number of wires between them as much as possible and to enhance the noise immunity of signal wires. It is preferable to standardize the hardware of the interfacing system in view of expandability and preventive maintenance. In order to realize the above requirements, it is necessary to divide one interfacing system into several stories and to facilitate communication between the stories. Additionally, one should consider how to reduce the load of the control computer due to the interfacing systems. Therefore, each story should have the following functions: communication, data format conversion, data storage and monitoring of apparatus status information. Here, an interlock for protection of the controlled apparatus from stress and shock is provided.

Figure 1 shows the fundamental constitution of the SSC control system, where all the above mentioned items, system reliability and trade-offs in performance and cost are taken into consideration.

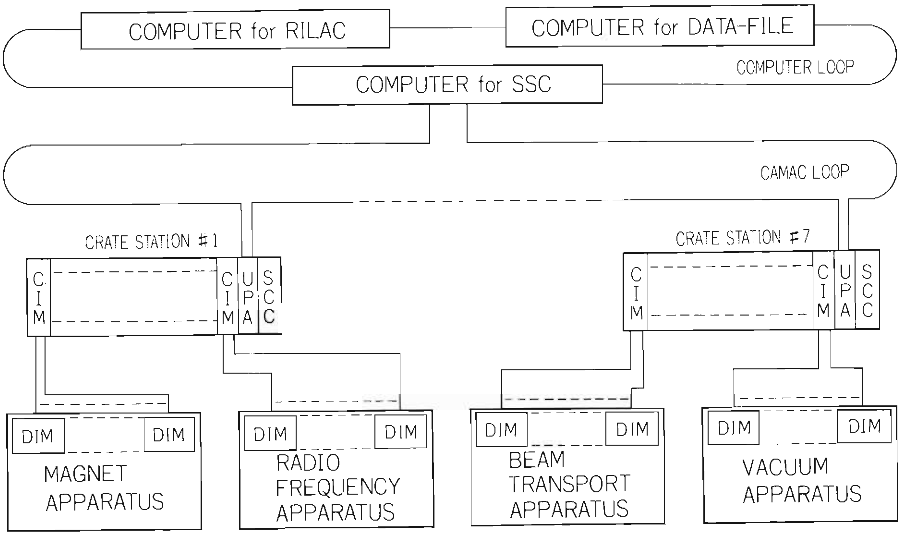

Fig. 1. Fundamental constitution of the SSC control system.

The computer system is a poly-processor system of channel-to-channel coupled type using three computers, each one for the LINAC, the SSC and the data-file. The computer system has a duplex optical loop connecting three computers. All the computers are MELCOM-350-500/60 (32 bits machine) with performance capability of 3.7 MIPS, the maximum memory capacity of 16 M bytes as a physical space and 4 G bytes as a logical space, and transmission rate through the loop is 15 M bps. The computer software includes the supervisory program for a poly-processor system, user's programming language FORTRAN77, computation libraries and a real time debugger like interpreter written by the language.

The RILAC computer is mainly used for the control of the heavy-ion linear accelerator with a magnetic tape handler, a magnetic disk unit and display terminals. The computer can be operated independently of other computers by its console.

The SSC computer is used for the control of all the controlled apparatus of the SSC. It is connected with the interfacing systems mentioned below as well as various peripherals.

The data-file computer is used for the data base file applied to the SSC beam adjustment and for the back-up against the SSC computer failure. In future when an AVF cyclotron is built, the computer will be used for the control of it.

The interfacing system consists of three stories: CAMAC equipments, CIMs (Communication Interface Module) and DIMs (Device Interface Module). The CAMAC equipments are operated mainly in the CAMAC's standard specification and constructed with a serial highway driver and a U-port adapter (UPA) mounted in the SSC computer, seven crate stations including another UPA and a serial crate controller (SSC), and a serial loop linking the first UPA and all the crate stations.

The CIM and the DIM were devised by one of the authors (K.S.)$^{1)}$ to satisfy the requirements mentioned in item 6. They consist mainly of a micro-processor and a memory. A CIM of this type is mounted on each crate station, while a DIM of this type is connected with the controlled apparatus. Two plastic optical cables are used for the connection between CIM and DIMs. The CIM can link sixteen DIMs. The DIM has sixteen input ports and sixteen output ports, each port having parallel eight bits.

It will be understood from the above explanation that the designed SSC control system is a distributed computer control system with three mini-computers and many micro-processors, which has powerful control capability, expandability, flexibility and maintenancability.

Details of the SSC operator console will be described elsewhere.

Reference

1) K. Shimizu, T. Wada, J. Fujita, and I. Yokoyama: Tenth Int. Conf. on Cyclotrons and Their Applications (1984).

IV-4. Extraction of Off-Centered Beam in the RIKEN SSC

N. Nakanishi, A. Goto, and Y. Yano

Possibility of extraction of an off-centered beam in the RIKEN SSC has been examined by computer simulation. It is well known that the off-centered beam shows the oscillatory pattern in the turn separation. The oscillatory pattern is due to the rotation of the averaged orbit center of the accelerated particles around the machine center. Such an orbit of which radius equals to zero is called a well-centered orbit. Thus the well-centered orbit does not show the oscillation in the turn separation. Some examples of the pattern are shown in Fig. 1 on an off-centered and a well-centered orbits of the 9 MeV p beam. The properties of the reference orbit of the off-centered beam can be described in the phase space with respect to the reference orbit of the well-centered beam with the central position phase of zero.

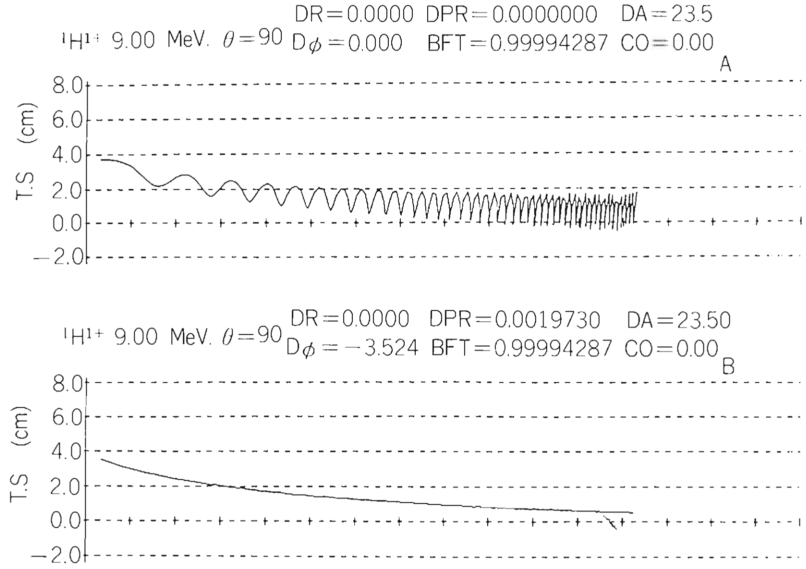

Fig. 1. Turn separation of an off-centered (a) and a well-centered (b) orbits on the 9 MeV p beam. The beams in case a and b are injected under the conditions that $r' = 0.0$ mrad and $\varphi_0 = 0.0°$, and that $r' = 14.21$ mrad and $\varphi_0 = -3.52°$, respectively.

The radial position R_n of the reference orbit of an accelerated particle is given by

$$R_n = R_{cn} + A_0 \cdot \cos \left\{ \varphi_0 - 2\pi \int_n (\nu_r - 1)\, dn \right\},$$

where R_{cn} is the radial position at turn number n of a well-centered orbit, and A_0 and φ_0 are the radial amplitude of deviation and the initial angular phase in phase space with respect to the reference orbit of the well-centered beam, respectively. The indispensable conditions required for the extraction method are as follows: (1) The beam clears obstacles like MIC1 and EIC in our case$^{1)}$; (2) Necessary beam separation is obtained at the extraction point; (3) Quality of the extracted beam is not worse than that of the well-centered beam.

The numerical calculation has been done for a 9 MeV p beam in the RIKEN SSC. The radial focusing frequency ν_r at the injection energy is 1.07. The azimuthal angle at the closest point to an obstacle after injection is 315 °, and the radial position at the point is taken to be 97.5 cm. An example of sets of parameters to satisfy the above conditions is as follows; radial angle r′ and phase deviation φ_0 of the reference orbit at the injection point are 7.68 mrad and −2.18°, respectively. The turn separation and phase slip of the corresponding orbit are

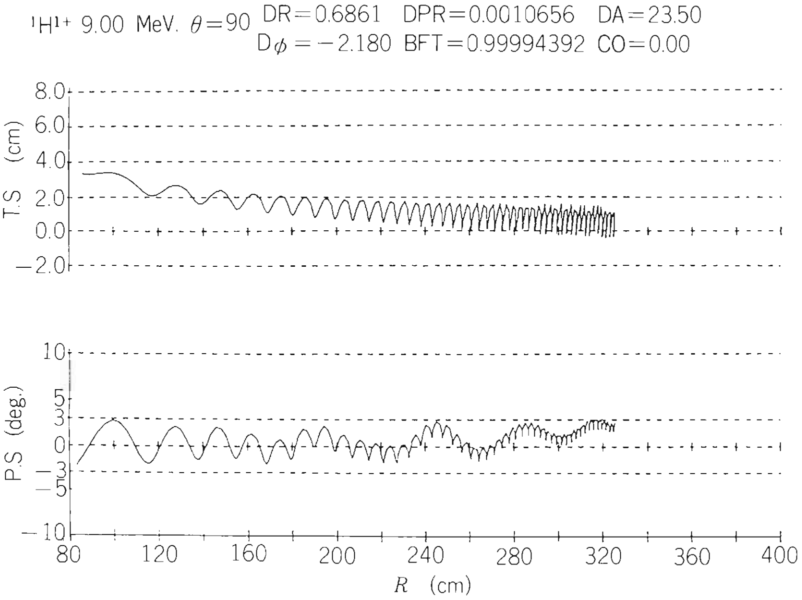

Fig. 2. Turn separation and phase slip of the corresponding off-centered beam. See text for injection parameters.

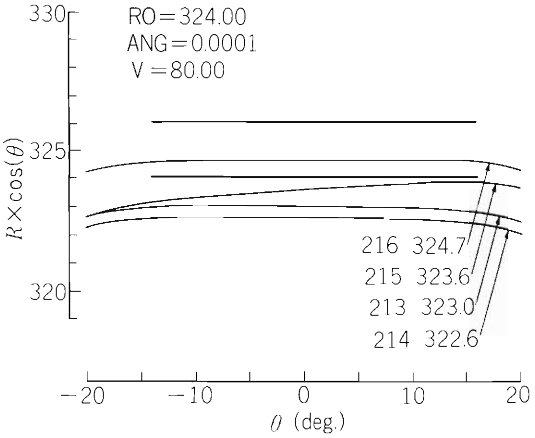

Fig. 3. A last few orbits in the extraction region. Two solid lines means the EDC which is the first device for extraction.$^{2)}$ A 9 MeV p beam is accelerated to the final energy of 184 MeV under conditions of harmonic number of 5 and an accelerating voltage of 250 kV. In this figure R0 and V are the radial position of the center of the EDC, and applied voltage, respectively. Numerals attached to each orbit represent turn number and radial position at the valley center.

shown in Fig. 2. It has been comfirmed that the degradation in energy resolution is negligibly small for this solution. A last few orbits in the extraction region are shown in Fig. 3. Extensive analysis is now in progress.

References

1) A. Goto, Y. Yano, T. Wada, and N. Nakanishi: Sci. Papers I.P.C.R., 74, 124 (1980).
2) N. Kishida, Y. Yano, and A. Goto: ibid., 77, 63 (1983).

Ⅳ-5. Model Study of RF Resonator for the RIKEN SSC

K. Ogiwara, T. Fujisawa, and Y. Oikawa

The RF resonator for the RIKEN SSC is required to work in a frequency range of 17 to 45 MHz at the dee voltage of 250 kV (Maximum). The movable box type resonator[1] has been investigated. On the basis of the result of the 1/5 scale model test[2] and the calculations of transmission line approximation, the 1/4 scale model resonator was constructed to investigate the RF characteristics and the method of fabrication in detail. Figure 1 shows a photograph of the 1/4 scale model resonator. Resonant frequency is changed coarsely by a pair of movable boxes and finely by a trimmer capacitor which is opposite to the dee. The RF power is fed through a coaxial feeder of 50 ohm characteristic impedance. The impedance of the resonator is matched with that of the feeder by a movable capacitive coupler which is attached to the top of the feeder and opposite to the dee. The movable boxes, the feeder with the coupler, and the trimmer capacitor are driven by each driving mechanism.

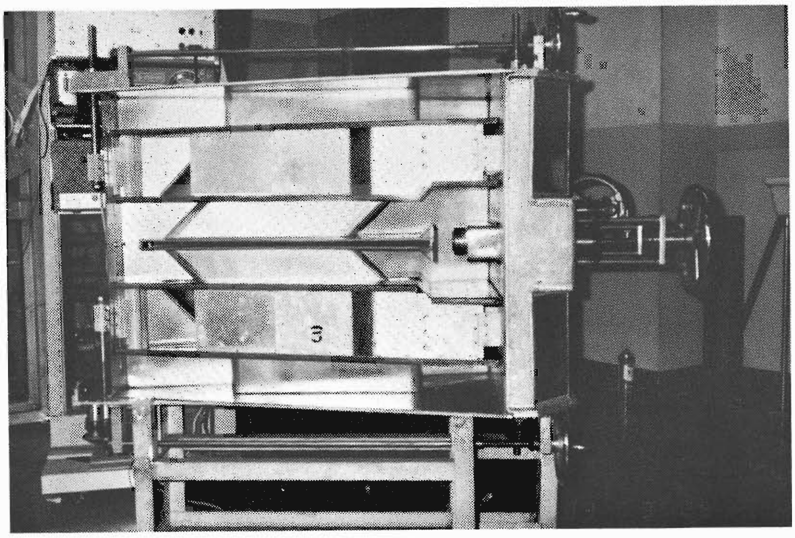

Fig. 1. A photograph of the 1/4 scale model resonator.

The resonant frequencies, Q-values, shunt impedances and the radial distributions of RF electric field along the dee gap were measured and the impedance matching conditions between the resonator and the feeder line were studied. Q-values of the actual resonator are estimated by multiplying the measured Q-values by the scale factor of $\sqrt{4}$ and resonant frequencies by 1/4. In Fig. 2, Q-values and positions of the movable box deduced from the experimental results are shown against the resonant frequency together with the values calculated by the transmission line approximation.

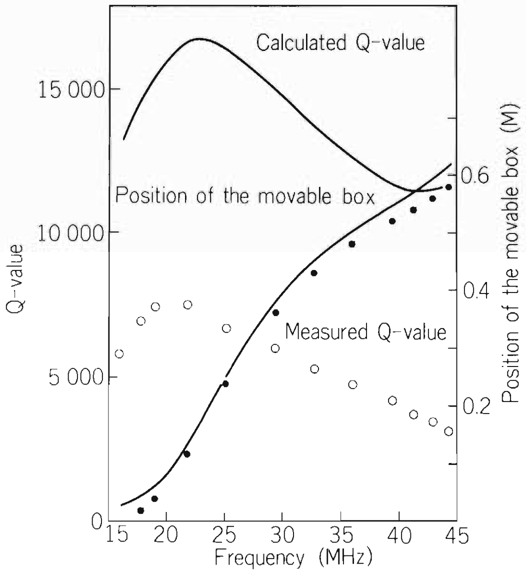

Fig. 2. Q-values and positions of the movable boxes for the actual resonator estimated by the experimental results. Solid lines show the calculated values by transmission line approximation.

The resonant frequencies measured are fairly well reproduced by the calculation. However, the measured Q-values are about 1/3 of the calculated one. One reason of poor agreement is attributed to poor contact between the movable box and the outer wall in the model. Another reason considered is that the resonator is too complex to be calculated in terms of one-dimensional transmission line.

Relative distributions of RF electric field along the dee gap were measured by perturbation method.[3] The results are shown in Fig. 3, where the dee voltages are normalized at beam injection radius.

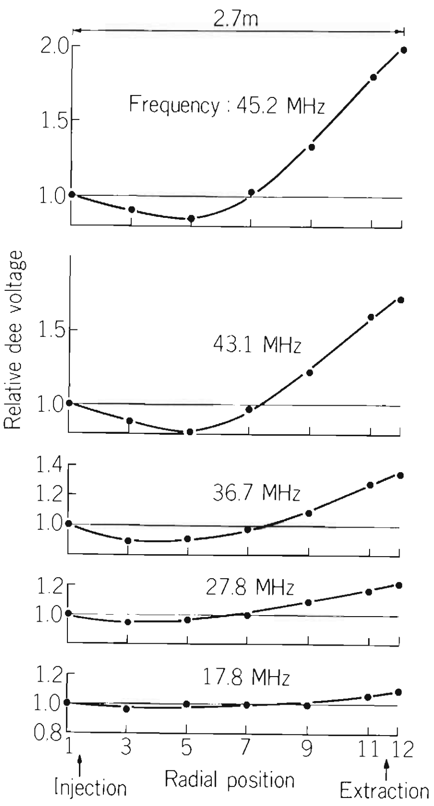

Fig. 3. Relative distributions of RF electric field along the dee gap. The frequency shown is 1/4 times of the measured one.

Impedance matching by capacitive coupler is understood according to an equivalent circuit shown in Fig. 4. The resonator is characterized by three parameters: Q-value, shunt impedance R_s and F_0. F_0 is the resonance frequency of the resonator including the capacitance C_f. At a resonance point, impedance Z_1 in Fig. 4 take a real value and its magnitude is given by

$$|Z_1| = 1 / (2 * \pi * F_0 * C_f)^2 * R_s. \qquad (1)$$

The impedance matching means that Z_1 is equal to real 50 ohms. It is realized by adjusting C_f and tuning the resonator. We applied this procedure to the model resonator and made sure that it is feasible.

The shunt impedance is given by

$$R_s = V_{dee}{}^2 / (2 * P), \qquad (2)$$

where V_{dee} is the dee voltage (peak) and P is the power loss of the resonator. We measured the dee voltage by a calibrated voltage pick-up which gave little effect on the resonator characteristics. RF power fed into the resonator was obtained by measurement of forward and backward power on the feeder.

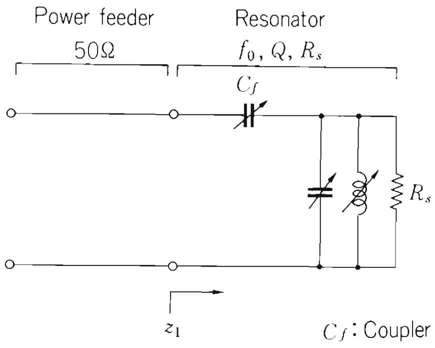

Fig. 4. Equivalent circuit for the capacitive coupler.

The shunt impedance of the model resonator is calculated from these results and that of the actual resonator is estimated by multiplying the model's value by the scale factor of $\sqrt{4}$. The capacitance C_f satisfying impedance matching is deduced by substituting the shunt impedance to Eqn. (1). Figure 5 shows

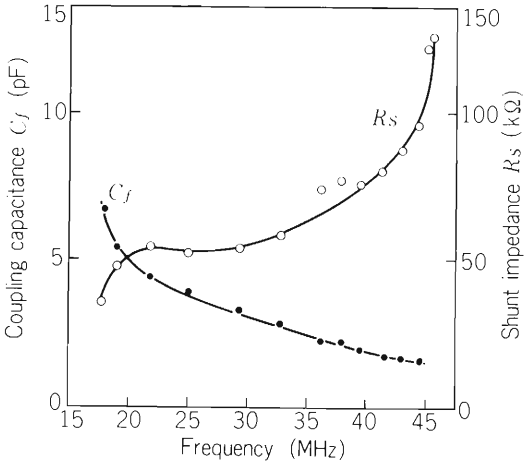

Fig. 5. Shunt impedance and capacitance C_f of the actual resonator estimated by the experimental results.

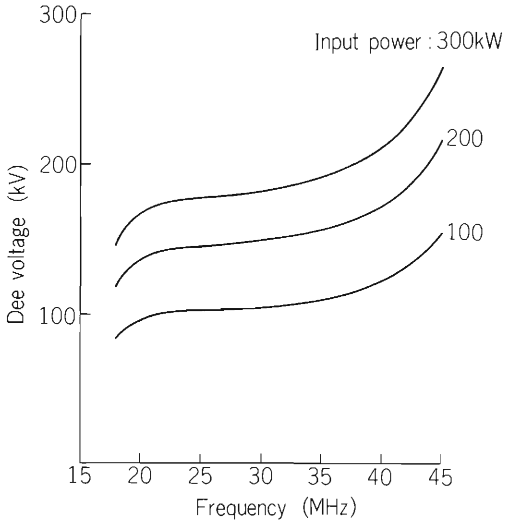

Fig. 6. Estimated dee voltages vs resonant frequency. The parameter is the input power.

the results. Figure 6 gives the dee voltages of the actual resonator estimated from this shunt impedance for input powers of 100, 200, and 300 kW.

Electrical contact involved in the structure of resonator, especially that of sliding contact, is expected to be improved in the actual resonator than in the model; the maximum dee voltage higher than those in Fig. 6 will be obtained in that case.

References

1) T. Fujisawa: RIKEN Accel. Progr. Rep., 15, 196 (1981).
2) K. Ogiwara, T. Fujisawa, and Y. Oikawa: ibid., 16, 217 (1982).
3) L. C. Maier, Jr. and J. C. Slater: J. Appl. Phys., 23, 68 (1952).

IV-6. Grid Tuning Circuit of RF Power Amplifier of the RIKEN SSC

T. Fujisawa, S. Kohara, K. Ogiwara, Y. Oikawa, and Y. Kumata*

A basic design of full wave length (λ) type grid tuning circuit for the power amplifier of the RIKEN SSC has previously been reported.[1] Subsequently it was noticed by experience on the amplifier of RILAC[2] that the plate-grid capacitive coupling inside the tube RCA 4648 at the final stage would cause instability of the amplifier. The grid RF voltage induced by this coupling is proportional to the frequency and the equivalent shunt impedance at the grid. The shunt impedance was set at 50 ohm in the original design. In this case, the induced voltage is estimated to reach a magnitude comparable to the normal grid driving voltage at 45 MHz.[2] Therefore, in order to improve the stability of the amplifier, we took following two measures:

(1) The shunt impedance at the grid is reduced to 12.5 ohm while the input impedance is kept at 50 ohm;

(2) A small variable capacitor between the plate and the tuning capacitor is added for neutrarization.

The performance of the improved circuit was studied on a full sized model equipped with a real tube in cold state. The model of the final stage amplifier and its schematic diagram are shown in Figs. 1 and 2 in Ref. 3. Figure 1 shows the results of measurement for tuning characteristic and input impedance of the grid circuit against the frequency. The intended performance is obtained in a frequency range of 17 to 45 MHz. The effect of the neutralization was studied at 40 MHz by measuring the voltage transmission ratios from the plate to points A and B in Figs. 1 and 2 in Ref. 3. The result is shown in Fig. 2. The voltage induced at point B is very well cancelled by the neutrarization and that at point A is reduced to one fifth of the voltage without the capacitor. Study for the grid tuning circuit is now in progress.

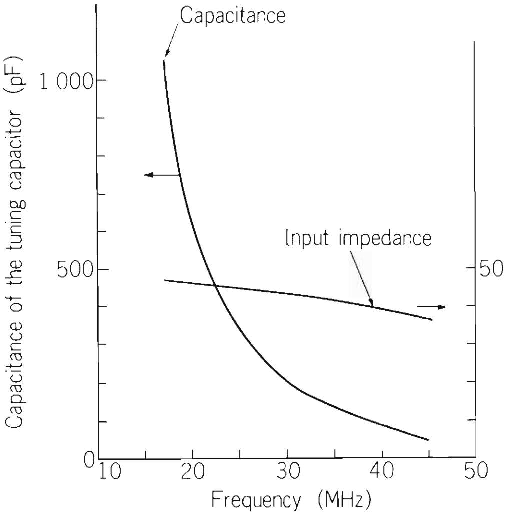

Fig. 1. Capacitance of the tuning capacitor and input impedance of the grid tuning circuit against the resonant frequency.

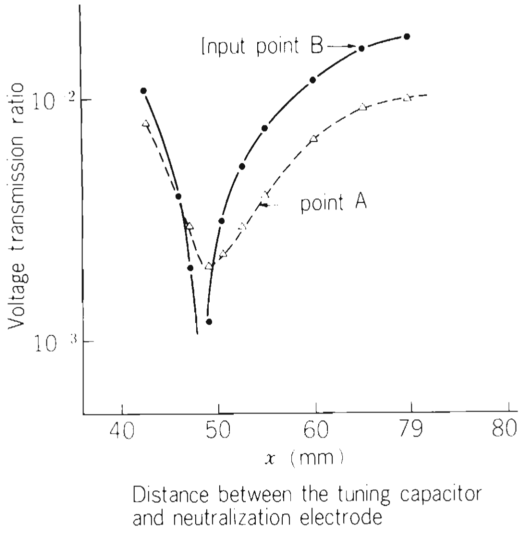

Fig. 2. Voltage transmission ratios from the plate to the grid circuit at 40 MHz. The induced voltages were measured at points A and B in Fig. 2. in Ref. 3.

References

1) S. Kohara and T. Fujisawa: RIKEN Accel. Progr. Rep., 16, 173 (1982).
2) T. Fujisawa and Y. Chiba: ibid., p.169 (1982); S. Kohara, T. Fujisawa, and Y. Chiba: ibid. p. 171.
3) T. Fujisawa, S. Kohara, K. Ogiwara, Y. Oikawa, Y. Kumata, and Y. Chiba: p. 149 in this report.

---

* Sumitomo Heavy Industries, Ltd.

Ⅳ-7. Study of the RF Power Amplifier for the RIKEN SSC

Design of Plate Circuit

T. Fujisawa, S. Kohara, K. Ogiwara, Y. Oikawa, and Y. Kumata*

Each of two resonators of the RIKEN SSC is to be powered by a separate RF amplifier capable of delivering 300 kW in a frequency range of 17 to 45 MHz. A schematic diagram of the final stage of the amplifier is shown in Fig. 1.[1] An RCA 4648 tetrode is used in grounded cathode connection. RF power is fed into the resonator through a 50 Ω coaxial feeder line (~ 1.5 m length) which is coupled with the resonator in good impedance matching by a variable capacitive coupler. Load resistance matching for the tube is made by a variable capacitor (20 ~ 200 pF) inserted in series at the output port of the amplifier.

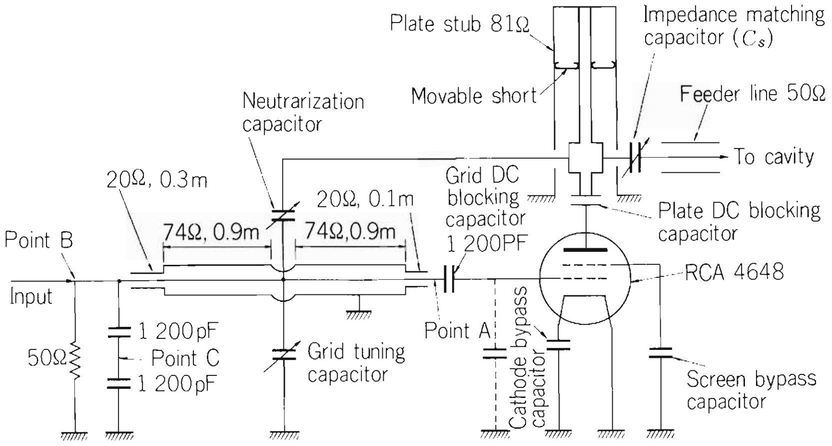

Fig. 1. Schematic drawing of the final stage amplifier of the RIKEN SSC.

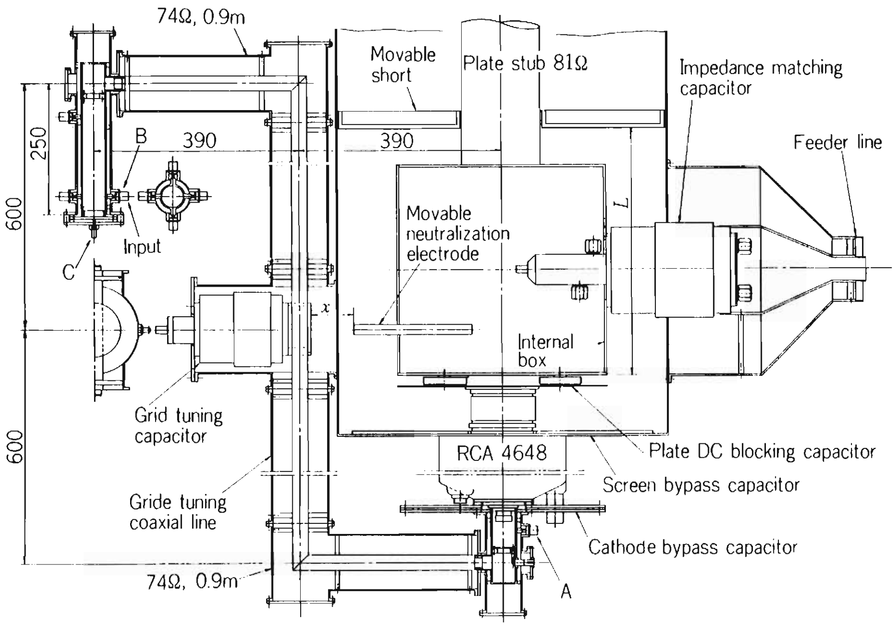

Fig. 2. Full size model of the final stage amplifier.

---

* Sumitomo Heavy Industries, Ltd.

Structure of the plate circuit and its tuning characteristics were investigated on a full sized model. Figure 2 shows a cross sectional view of the model of the final stage amplifier. The plate circuit is tuned by a quarter wave length coaxial stub having a movable short. The center conductor of the plate stub is a 18 cm diam. copper pipe and the outer conductor and the internal box above the plate DC blocking capacitor are square aluminum boxes. Cooling water pipes and DC power line for the tube anode are to pass through the inside of the center conductor of the stub. The internal box is convenient to accomodate joints of cooling water pipes and other equipments. This box is also useful to shorten the length of the stub at the lowest frequency of 17 MHz. Equivalent circuit for this structure is given in Fig. 3(a). The load circuit is replaced by the equivalent resistance R_L and capacitance C_L as shown in Fig. 3(b).

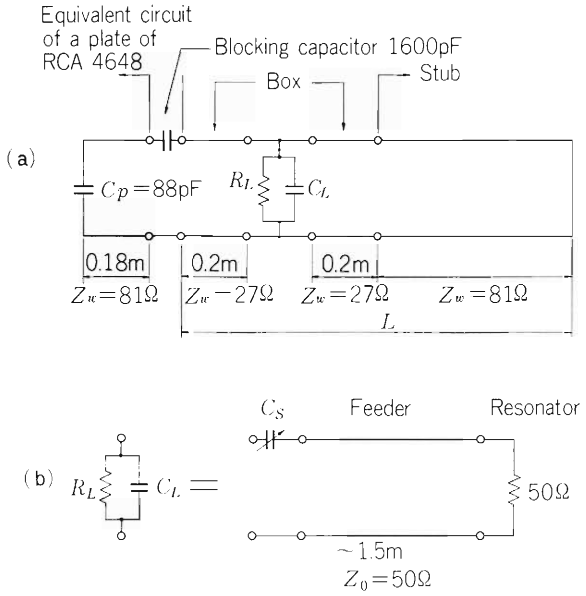

Fig. 3. (a) Equivalent plate circuit, (b) Load and its equivalent circuits.

The capacitance C_L varies from 70 pF at 17 MHz to 26 pF at 45 MHz, if R_L is matched with the optimum load of 300 Ω for the tube by adjusting the capacitance C_S.

Dependence of the resonant frequency of the plate circuit on the length of the stub was measured in order to estimate the stroke of the movable short. In Fig. 4 the results of the measurement are plotted together with calculated curves based on the equivalent circuit in Fig. 3(a). The closed and open circles show the results of measurement without C_L and R_L, and with C_L of 60 pF, respectively. The solid and dotted lines show the results of the calculation. The lowest frequency in the measurement is limited to about 30 MHz because of the saving in length of the model stub. The length of the stub is estimated to be about 1.7 m to cover the lowest frequency without C_L and enough margin is kept for tuning at the highest frequency even if C_L is as large as 60 pF. The dimensions of the plate circuit determined from the present study are listed in Table 1. The impedance matching condition between the tube and feeder line was also investigated on the model whose output port was terminated by an equivalent dumy load of 50 Ω. In Fig. 5, the matching characteristics obtained are shown together with calculated values based on the equivalent circuit in Fig. 3(a). The load impedance can be varied in an sufficiently wide range by adjusting C_s.

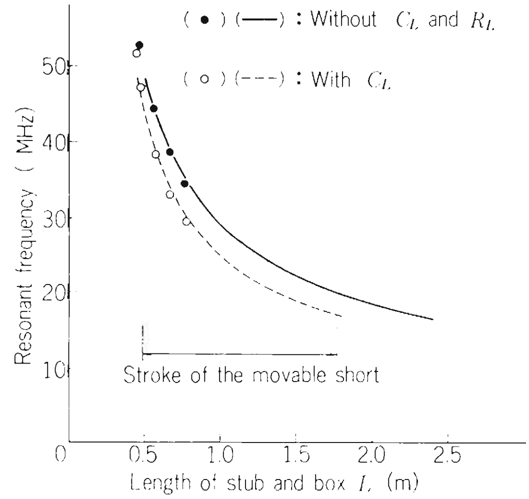

Fig. 4. Measured and calculated resonant frequencies of the plate circuit. See the text.

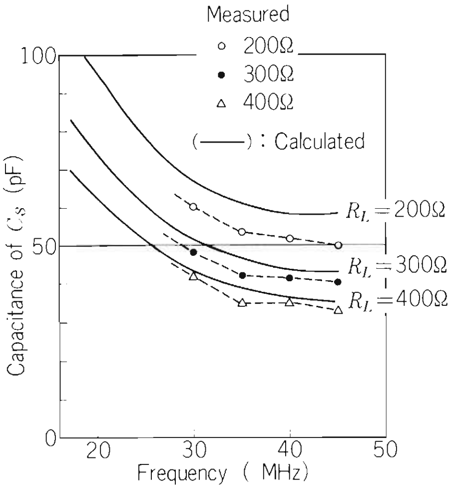

Fig. 5. Measured and calculated impedance matching conditions against the frequency. The parameter is the load impedance.

Table 1. Geometrical parameters of the plate stub designed.

Outer wall of the stub	630 mm(D) x 630 mm(W) x 2400 mm(H)
Diameter of the stem	ϕ180 mm
Internal box	400 mm(D) x 400 mm(W) x 400 mm(H)
Stroke of the movable short	1800 mm

Reference

1) S. Kohara, T. Fujisawa, and Y. Chiba: RIKEN Accel. Progr. Rep., 16, 171 (1982); S. Kohara and T. Fujisawa: ibid., p. 175.

IV-8. Study of the RF Power Amplifier for the RIKEN SSC

DC Blocking Capacitor for Plate Tuning Circuit

S. Kohara, T. Fujisawa, and Y. Chiba

The DC blocking capacitor of plate tuning circuit of power amplifier$^{1)}$ for the RIKEN SSC must sustain DC voltage of 18 kV and high RF current of 220 A(rms) at 45 MHz. Large capacitance is desirable to reduce the RF voltage across the capacitor. Coaxial structure of the plate circuit suggests to use a ring array of capacitors surrounding the cooling pipe of the vacuum tube (See Fig. 2 in Ref. 2). Such an array is expected to have self resonances which disturb normal circuit operation. We made an array composed of four commercially available 400 PF ceramic capacitors (Toshiba RDF110CS) as shown in Fig. 1. and searched for the self resonances. The resonances were found at around 36 and 45 MHz.

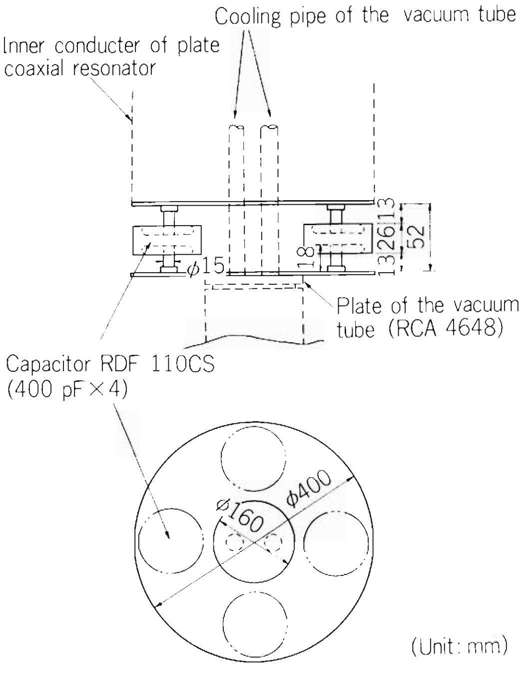

Fig. 1. Capacitor array using four Toshiba RDF110CS.

The modes of resonances are shown in Fig. 2. These resonances are in the operating frequency range of 17 to 45 MHz and are not desirable for the stable operation of the amplifier. Therefore each capacitor was improved in order to raise these resonant frequencies above 45 MHz. The terminal block of the capacitor was made shorter and its diameter larger in order to reduce the inductance as shown in Fig. 3. The resonant frequencies became about 50 and 70 MHz.

The reactive power rating of the blocking capacitor is required to be more than 120 KVA at 45 MHz. That of RDF110CS is specified to be 90 KVA at 1 MHz and 50 °C in the catalog but there is no description at 45 MHz. We are trying to get at least the power rating of 30 KVA at 45 MHz by cooling the improved terminal of the capacitor by water. We are further making an investigation to improve the blocking capacitor array to get higher resonant frequencies and power ratings.

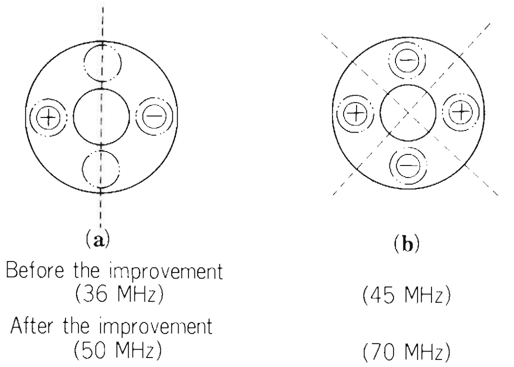

Fig. 2. Resonance modes and frequencies in the capacitor array. Broken lines show the voltage node.

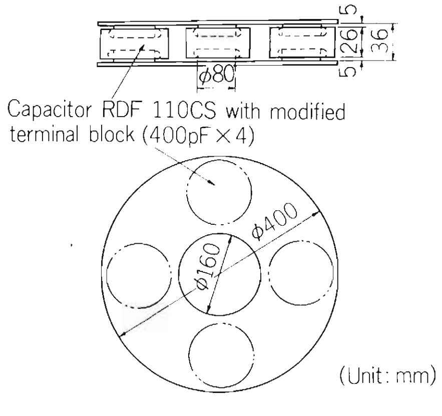

Fig. 3. Improved capacitor array.

References

1) S. Kohara, T. Fujisawa, and Y. Chiba: RIKEN Accel. Progr. Rep., 16, 171 (1982).
2) T. Fujisawa, S. Kohara, K. Ogiwara, Y. Oikawa, and Y. Kumata: p.149 in this report.

IV-9. Calculation of RF Electromagnetic Field by Finite Element Method (III)

F. Kikuchi, M. Hara, T. Wada, and K. Nakahara

Three-dimensional analysis of electro-magnetic field by the finite element method is now considered to be very important in designing the accelerators. Efforts are continued to develop computer codes to calculate electromagnetic fields in cavities. We have already developed two computer codes H2DB and HAX$^{1)}$ which are used for a resonator with constant cross section and for an axisymmetric resonator. We have also given a formulation of three dimensional calculation, in which the electric or magnetic field is chosen as the unknown variables in the finite element formulation.$^{2)}$ Then the boundary conditions imposed on the unknown functions are fairly easy to deal with. The divergence free condition is treated by a penalty method. We have made a computer code MAX3D according to this formulation. But this program did not necessarily give exact resonant frequencies. We made another code to investigate the validity of this method and to obtain basic data for MAX3D.

(1) Program

New code has the following characteristics. (i) Either E or H can be selected as the unknown variable. (ii) Two-dimensional and axisymmetric problems can be solved. (iii) Several types of mesh elements can be used.

(i) Basic equation

Basic equations are given in Ref. 2.

(a) correspondence of Cartesian and cylindrical coordinates.

$(x, y, z) \longleftrightarrow (r, z, \theta)$

(b) shape of function

Ex, Er: Ex (x, y) · (sin (ρz) or cos (ρz))
Ey, Ez: Ey (x, y) · (sin (ρz) or cos (ρz))
Fx, Eθ: Ez (x, y) · (cos (ρz) or sin (ρz))

(c) rot E and div E

rot E:

x or r component

$$\mathrm{sgn} \cdot \left(\frac{\partial E_z}{\partial y} \mp \rho^* E_y\right) \begin{cases} \cos \rho z \\ \sin \rho z \end{cases}$$

y or z component

$$\mathrm{sgn} \cdot \left(-\frac{\partial E_z}{\partial x} - \frac{Ez}{r^*} \pm \rho^* E_x\right) \begin{cases} \cos \rho z \\ \sin \rho z \end{cases}$$

z or θ component

$$\mathrm{sgn} \cdot \left(\frac{\partial E_y}{\partial x} - \frac{\partial E_x}{\partial y}\right) \begin{cases} \sin \rho z \\ \cos \rho z \end{cases}$$

div E:

$$\left(\frac{\partial E_x}{\partial x} + \frac{E_x}{r^*} + \frac{\partial E_y}{\partial y} \mp \rho^* E_z\right) \begin{cases} \sin \rho z \\ \cos \rho z \end{cases}$$

where sgn, ρ*, and 1/r* are given in Table 1.

Table 1. Parameters.

	sgn	ρ*	1/r*
(x, y, z)	1	ρ	0
(r, z, θ)	−1	n/r	1/r

n = 0, 1, 2, ...

(d) In the case of ρ* = 0

In the Cartesian coordinate, ρ* = 0 gives cut-off frequencies. In the cylindrical cooridinate, n = 0 corresponds to the axisymmetric problem. In both cases, following two modes are separable:

$\underline{\underline{Ex, Ey}}$, $\underline{Hz}$ (Ez = Hx = Hy = 0) —— TE mode
$\underline{\underline{Ez}}$, $\underline{Hx, Hy}$ (Ex = Ey = Hz = 0) —— TM mode

Furthermore, in each case either $\underline{\underline{\ \ }}$ or $\underline{\ \ }$ is chosen as unknowns.

(ii) Element and numerical integration

As is shown, a sinusoidal function is used in the z or θ direction. In the (x, y) or (z, r) region, triangular or quadrilateral isoparametric elements can be chosen. Stiffness and mass matrices are calculated using numerical integration technique. Boundary conditions are $E_t = 0$ and $H_n = 0$. Symmetry or antisymmetry conditions are used. Oblique boundary is treated using coordinate rotation. In the finite element calculation, matrix eigenvalue problems must be solved. In this case subspace method is adopted.

(2) Numerical example

Some basic problems are treated.

(i) Unit square region

We solved an eigenvalue problem of Ex and Ey in unit square region. In this case, we can regard that Ex and Ey correspond to Hy and Hx. So it can be seen that the problem is analyzed using Hx and Hy.

(a) Effect of s parameter

Divergence-free condition comes from a penalty term in the functional and s-parameter is a coefficient of that term Dividing unit square region by 4 x 4 grid and using 4 nodes quadrangular element, s-parameter dependence is investigated. The results are shown in Fig. 1. Two kinds of mode are seen. One has little s-dependence. The other has large s-dependence. The former is the physically allowed solution. If s is small, many false modes are mixed. But such modes are pushed away by letting s larger. Divergence check of the numerical solution is useful in judging the modes.$^{2)}$ If the length is given in units of cm, the eigenvalue is given in units of cm^{-2} in our calculations.

(b) Comparision of the elements

We compared the accuracy of five elements for the same problem letting s be 1. The results are shown in Fig. 2.

(ii) Rectangular region with a notch

Next, as a more practical application, we calculated the field in an area with a "notch" shown in Fig. 3.

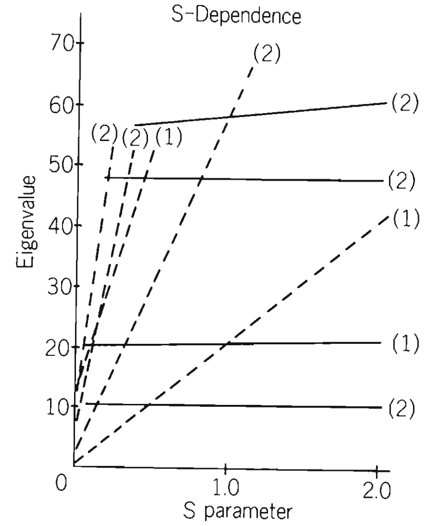

Fig. 1. S-parameter dependence of eigenvalue. The shape of the waveguide is a square of unit side length and NP = 5 x 5. Solid and broken lines show physical and unphysical solutions. Figures in the brackets are the number of degeneracy.

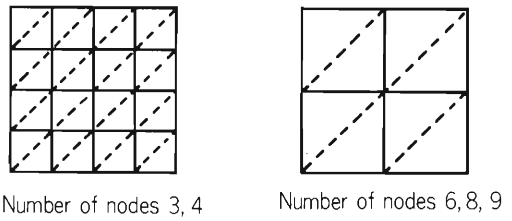

Number of nodes 3, 4　　Number of nodes 6, 8, 9

modes	ELEMENTS (number of nodes)						EXACT
	3	4	4:10x10	6	8	9	
1	10.382	10.387	9.951	9.936	9.944	9.944	9.870
2	10.382	10.387	9.951	9.936	9.944	9.944	9.870
3	22.806	20.773	19.903	20.528	19.957	19.888	19.793
4	22.806	20.773	19.903	20.528	19.957	19.888	19.793
5	47.975	48.000	40.794	40.000	40.000	40.000	39.478
6	47.975	48.000	40.794	40.000	40.000	40.000	39.478
7	60.726	58.387	50.745	56.676	52.000	49.944	49.348
8	60.726	58.387	50.745	56.676	52.000	49.944	49.348
9	73.225	58.387	50.745	59.637	57.944	57.944	49.348
10	73.225	58.387	50.745	59.637	57.944	57.944	49.348

Fig. 2. Comparison of the elements. Underlined modes are false.

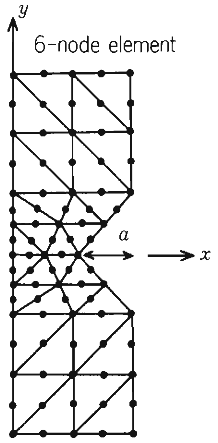

Fig. 3. Mesh of waveguide with notch. Only the upper half region is analyzed imposing a symmetry boundary condition.

Results using E_x and E_y are shown in Fig. 4 varying the notch depth. The same mode can be calculated with H_z. The result with Ex and Ey gives an opposite tendency to that with Hz except the case of small noth. The results using Hz is right. This tendency is the same even if the region is divided more finely. The reason for the occurrence of this phenomenon is not certain, but it originates from the singularity in the corner. In this calculation, the boundary condition at the corner is imposed such that the average tangential component of E is zero. In the case of a smooth notch as shown in Fig. 5, both results agree well as shown in Table 2.

(iii) Cylindrical region

As an axisymmetric region, the cylinder of 1 in radius and 2 in height is analyzed and the results are shown in Table 3.

(3) Conclusion

Our approach works well in problems with sufficiently smooth solutions, but may fail in some problems with non-smooth solutions. From these results, it is found that the penalty method is useful for the area with a smooth boundary.

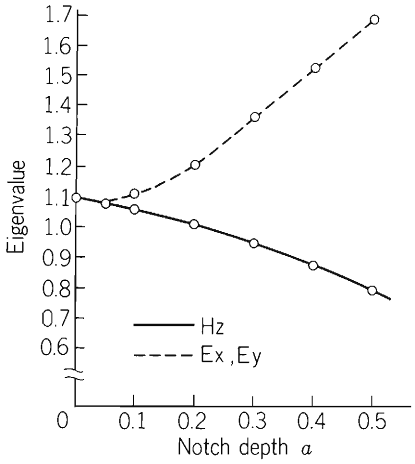

Fig. 4. Notch depth dependence of eigenvalue for the waveguide shown in Fig. 3. The eigenvalue should decrease with the notch depth according to the perturbation theory. Calculation using H_z gives good results. Panalty method using E_x and E_y does not give good results for large notch depths.

Table 2. Lowest eigenvalue λ for waveguide shown in Fig. 5.

Mesh	Hz	Ex, Ey
n_p = 78	0.7115	0.7794
n_p = 119	0.7098	0.7583
n_p = 189	0.7083	0.7368

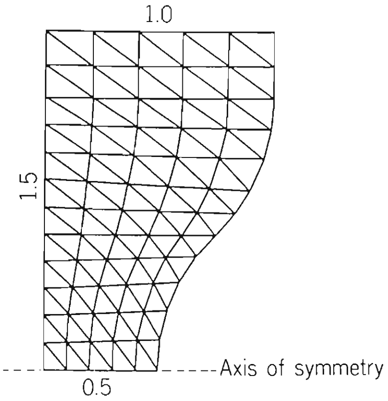

Fig. 5. Mesh of waveguide with smooth notch. A three noded triangular element is used (upper half portion).

Table 3. Eigenvalue λ for cylindrical cavity.

	5 x 10	10 x 20	Exact
n = 0	5.8016	5.7882	5.7840
n = 1	5.8841	5.8641	5.8567

References

1) M. Hara, T. Wada, A. Toyama, and F. Kikuchi: Sci. Papers I.P.C.R., 75, 143 (1981).

2) M. Hara, T. Wada, T. Fukasawa, and F. Kikuchi: RIKEN Accel. Progr. Rep., 16, 227 (1982);
M. Hara, T. Wada, T. Fukasawa, and F. Kikuchi: Proc. of COMPUMAG Genova (1983).

IV-10. Vacuum System of the RIKEN SSC

K. Ikegami, S. Nakajima, S. H. Be, I. Takeshita, Y. Oikawa, and S. Motonaga

The operating pressure of 3 ~ 4 x 10^{-6} Pa is desired in the acceleration chamber of the SSC. The chamber consists of eight separate sections. The flanges between sections are sealed with elastomer O-rings which will be compressed by a "pneumatic expansion seal". Total gas load expected is about 5 x 10^{-4} Pa.m^3/sec. Therefore, total necessary pumping speed amounts to 12 x 10^4 ℓ/sec. Cryogenic-pumps and cryogenic-panels are used as a main pumping system.

(1) Operating pressure

The operating pressure should be 3 ~ 4 x 10^{-6} Pa in order to keep the beam loss less than 10 % for very heavy ions.[1] For light ions an operating pressure of 1 x 10^{-4} Pa is adequate.

(2) Vacuum chamber

The vacuum chamber is divided into eight sections, that is, four magnet chambers, two RF resonator chambers and two valley chambers. The sealing at their interfaces is made by using a pneumatic expansion seal.[2] The pneumatic expansion seal is made of two thin stainless-steel plates cut into a race track shape and welded around the inside and outside edge. The seal is inflated and compresses O-rings by pressurized air. When it is necessary to disassemble the vacuum chamber, the seal is made to shrink back by evacuation and becomes removable from the gaps between the flanges. Figure 1 shows the plane view of the vacuum chamber of the SSC. The RF resonator and valley chambers can be pulled out from the SSC for their overhaul and repair. The RF resonator chamber has a partition wall to shield the cryo-panels installed at the outer side of the chamber from the RF electric field and the thermal radiation of the resonator. The RF resonator is evacuated through many small holes cut in the partition wall. The magnet chamber is surrounded with additional chambers which are evacuated to about 10 Pa to prevent the thin walls of the magnet chamber from collapsing under the atmospheric pressure. Figure 2 shows cross section of the magnet chamber of the SSC. Geometric characteristics of the chamber are as follows:

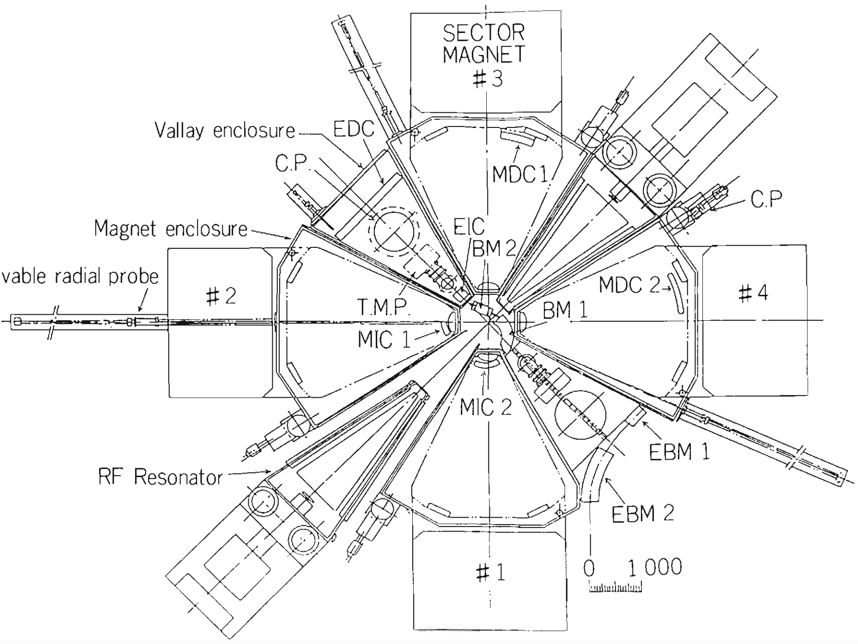

Fig. 1. Plane view of the vacuum chamber of the SSC.

total diameter		9 m
heights:	the valley chamber	60 cm
	the RF resonator chamber	270 cm
	the magnet chamber	5 cm
	the additional chamber	38 cm
total volume		30 m^3
total volume of the additional chambers		2.4 m^3

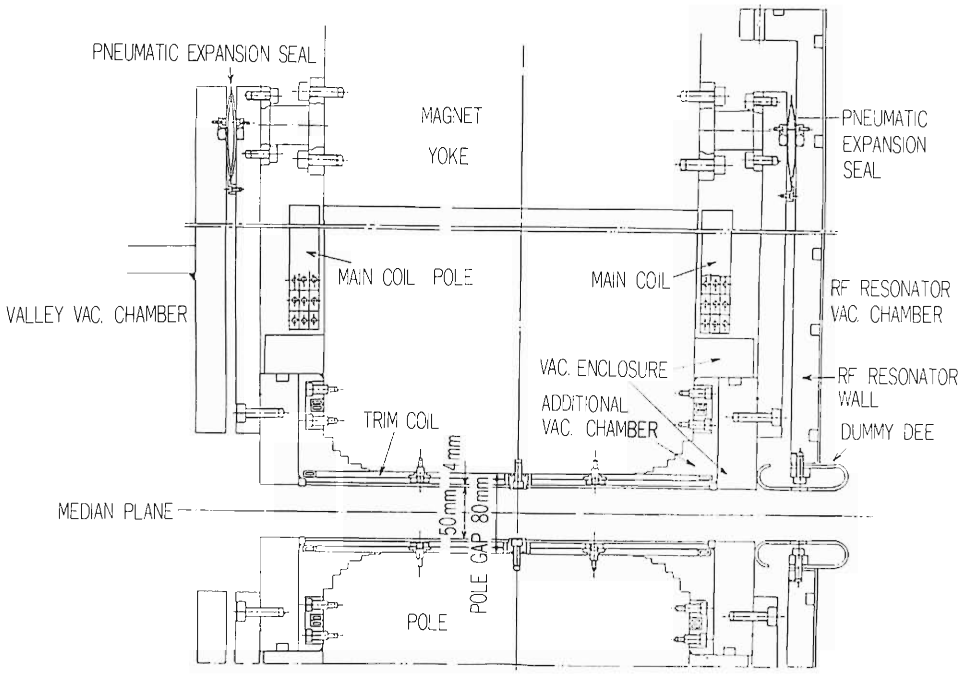

Fig. 2. Cross section of the magnet chamber of the SSC.

Surface areas exposed to high vacuum are as follows:

magnet chambers	80 m^2
valley chambers	30 m^2
RF resonator chambers	240 m^2
total surface area	350 m^2

(3) Gas load

Many parts such as beam diagnostic probes, inflection system, extraction system and other outgassing sources are inserted in the chamber. The main gas loads are those due to the gas given off from the metal surfaces and also that due to the gas given off from, and that permeated through the seals used to connect each chamber. The areas of inner material's surface of the chamber exposed to high vacuum are as follows:

stainless-steel	167 m^2
copper	180 m^2
elastomer	3 m^2

The total outgassing rate is estimated to be about 3.4×10^{-3} Pa.m^3/sec after 20 h pumping. After 100 h pumping it decreases to about 1.6×10^{-3} Pa.m^3/sec. We can expect that, the total outgassing rate will be decreased to about 5×10^{-4} Pa.m^3/sec, by applying the RF power to the resonator, by ECR (electron cyclotron resonance) discharge cleaning[3) supplying hydrogen gas to the magnet chamber, and by baking the valley chamber at mild temperature. The pumping speed of 12×10^4 ℓ/sec is necessary to achieve the aimed pressure.

(4) Pumping system

The pumping system of the SSC consists of two roughing systems, four high vacuum systems and ultra-high vacuum system. The roughing system is composed of a roots pump of 2600 m^3/h and a rotary pump of 3000 ℓ/min. This system is installed at each valley chamber. The pumping down time from atmospheric pressure to 10 Pa is about 20 minutes. High vacuum system is composed of a turbomolecular pump of 5000 ℓ/sec and a rotary pump of 2000 ℓ/min. This system is installed at each RF resonator and valley chamber. The pumping down time from 10 Pa to 3×10^{-4} Pa is about 20 hs. Ultra high vacuum system consist of ten cryogenic pumps of 10^4 ℓ/sec and four cryogenic panels of 5000 ℓ/sec. Two cryogenic pumps are installed at the rear panel of the RF resonator chamber, and two cryogenic panels in the inside of the stems of dee. Three cryogenic pumps are installed at the valley chamber. Ultra high vacuum system starts to operate at a pressure less than 3×10^{-4} Pa. High vacuum system may be operated in parallel to ultra high vacuum systems. The additional vacuum system consists of two rotary pumps of 610 ℓ/min and evacuates the additional chambers to a pressure less than 10 Pa. Figure 3 shows the total pumping system of the SSC.

The pumping system is automatically controlled by a sequence controller with a graphic panel installed at a local control room, and also it is connected to the central control console via. an optical fiber. Information of the pumping systems is sent to the central control console and is displayed on the screen of the CRT set in the control console.

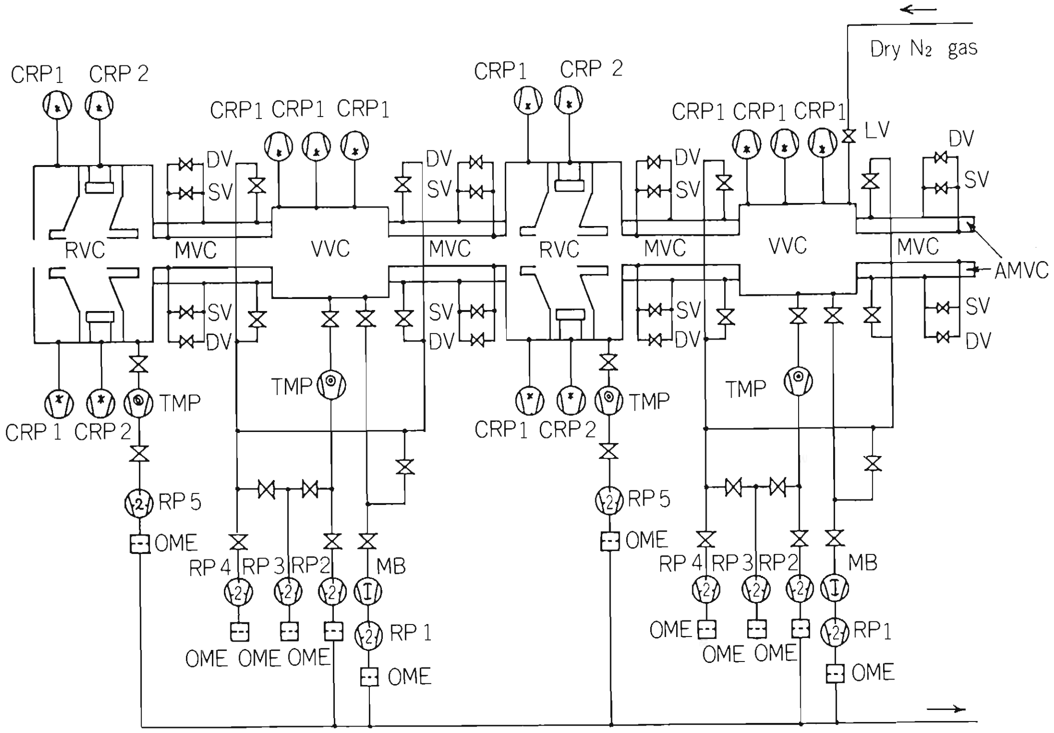

RVC: RF resonator vacuum chamber. MVC: magnet vacuum chamber. VVC: valley vacuum chamber.

AMVC: additional magnet vacuum chamber.

RP: rotary pump, RP1: 3000 ℓ/min, RP2 and RP5: 2000 ℓ/min, RP3: 1000 ℓ/min and RP4: 610 ℓ/min.

MB: roots pump of 2600 m^3/h. TMP: turbomolecular pump of 5000 ℓ/sec.

CRP1: cryogenic pump of 10^4 ℓ/sec. CRP2: cryogenic panel of 5000 ℓ/sec.

SV: safty valve (mechanical). DV: differential valve (air operated). LV: leak valve.

No marked valve: air operated. OME: oil mist eliminator.

Fig. 3. Pumping system of the SSC.

References

1) S. Nakajima and K. Ikegami: 9th Proc. Intern. Conf. on Cyclotron and their Applications, Caen, p. 537 (1981).

2) K. Ikegami, S. Nakajima, Y. Oikawa, M. Hara, S. Motonaga, and H. Kamitsubo: Sci. Papers I.P.C.R., 77, 87 (1982).

3) K. Ikegami, S. Nakajima, Y. Oikawa, Y. Ishibe, H. Oyama, Y. Sakamoto, S. Motonaga, and H. Kamitsubo: ibid., p. 78.

Ⅳ-11. Structure Analysis of a Pneumatic Expansion Seal

M. Hara, K. Ikegami, and T. Ohkuma

A pneumatic expansion vacuum seal is to be used at the interfaces between chambers of the SSC. We have already constructed some scale models and tested the performance.[1] In the present study, we made some calculation using a structure analysis code, in order to understand the stress distribution and to optimize the width and size of the seal. We used the EPIC-IV code[2] which has the following features.

(1) Two dimensional elastic –plastic analysis can be done.

(2) Triangular element with constant stress and strain is used.

(3) In the plastic analysis, element is yielded one by one (r_{min} method).

(4) Material constant is given by $\sigma_x = c\,(\alpha + \epsilon_x^p)^n$.

Following eight kinds of input cards are needed: i) Title card, ii) Control card, iii) Node data cards, iv) Load boundary cards, v) Element data cards, vi) Material data cards, vii) Intermediate load value specification cards, viii) Output information cards.

We calculated a case of free expansion with plane strain assumption. We took a quarter cross section of the seal using the symmetry condition, in order to treat this problem two-dimensionally. In Fig. 1, pneumatic expansion seal and an example of the mesh are shown. The expansion seal is made of thin stainless steel (SUS304). The input material data used give the stress-strain curve shown in Fig. 2. In the numerical analysis, size and shape of mesh give some effect on the results. We investigated the mesh size effect on A type seal in Ref. 1 (W = 100 mm, t = 1.0 mm). In Fig. 3, we show the deformation versus pressure diagram for three kinds of mesh whose element shapes are similar. In Fig. 4, the results for the case of longer element shape are shown. The data with finer mesh give better results. For the case of number 3 in Fig. 3, deformation and yielded elements at several pressures are shown in Fig. 5. In Fig. 6, we show the expansion versus pressure curves for various thickness of stainless steel plate. In these calculations, stress is concentrated on the welded region in our expansion seal.

Next, the O-ring effect is investigated. When O-ring

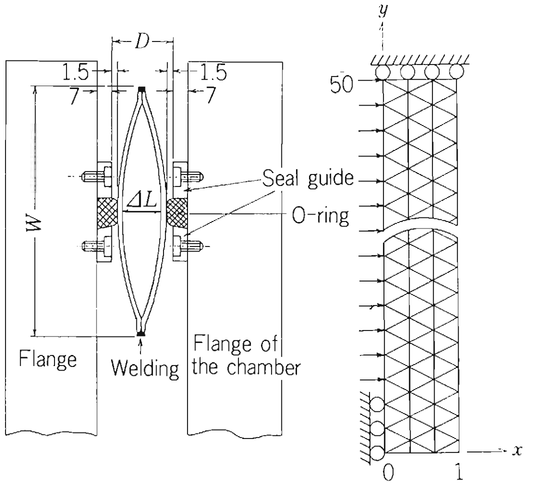

Fig. 1. Pneumatic expansion seal and an example of mesh. A quarter cross section of the expansion seal is analyzed. Arrows show the internal pressure. Deformation at x = 0 and 0 ≦ y ≦ 1 is allowed only in y-direction (welded region) and that at y = 50 only in x-direction.

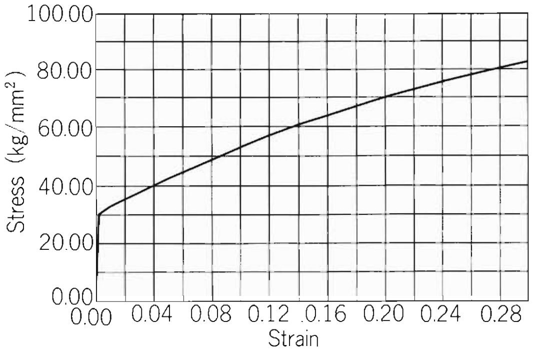

Fig. 2. Stress and strain curve for SUS 304. Stress and strain at yield point are 30.341 kg/mm^2 and 0.00154, respectively.

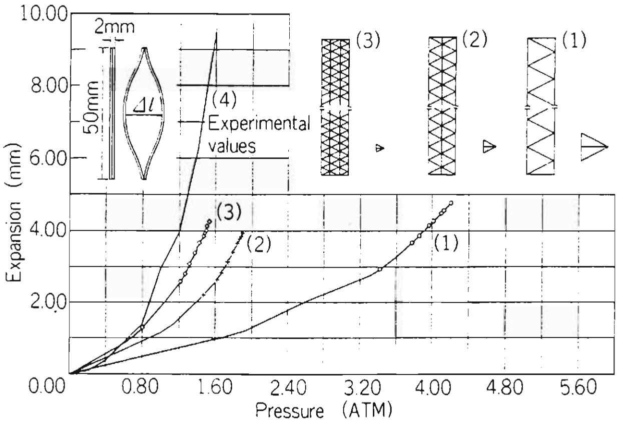

Fig. 3. Expansion vs internal pressure. Free expansion length $\Delta\ell/2$ is calculated for three different meshes of similar shape. The finer mesh gives larger expansion. The number 4 line is the experimental data in Ref. 1.

presses the seal near the top (center) region, the yielded region in the center shifts and expansion length becomes small. Expansion length, deformation and stress are shown in Figs. 7 and 8.

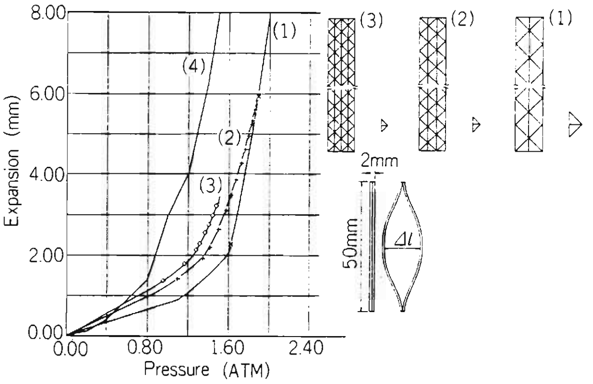

Fig. 4. Expansion vs internal pressure. The ratio of height and base of triangular mesh is different from that of Fig. 3. Mesh shape does not give large effect on the result if the mesh is fine.

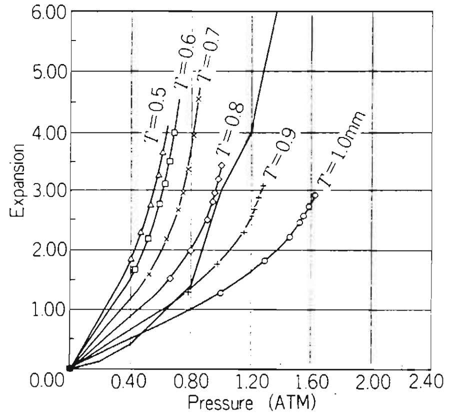

Fig. 6. Thickness dependence of expansion. Thickness of the stainless steel plate is varied from 0.5 mm to 1.0 mm. Non-labeled curve shows the experimental data for the plate with 1.0 mm thickness.

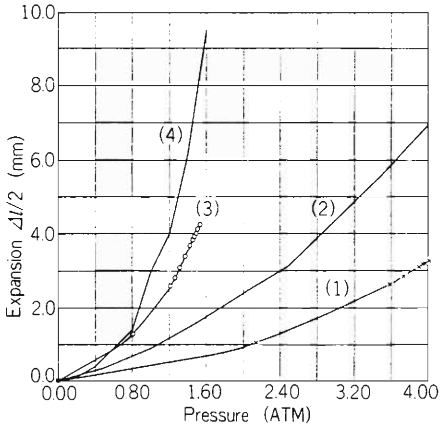

Fig. 8. Expansion vs pressure when reaction of the O-ring is taken into account. (1) Calculation with O-ring force. (2) Experimental data using O-ring. (3) Free expansion calculation. (4) Free expansion experimental data.

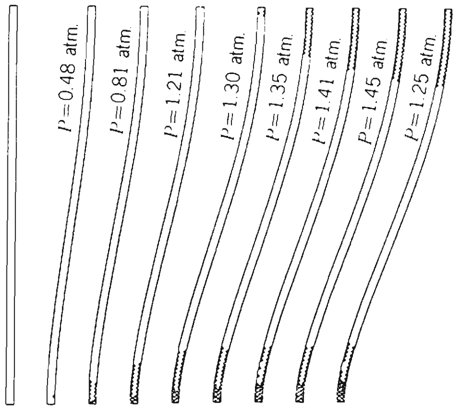

Fig. 5. Deformation and yielded elements. Deformed shapes are shown at some pressure points. The deformation is exaggerated by a factor of 5. The elements which yielded at that pressure are also shown.

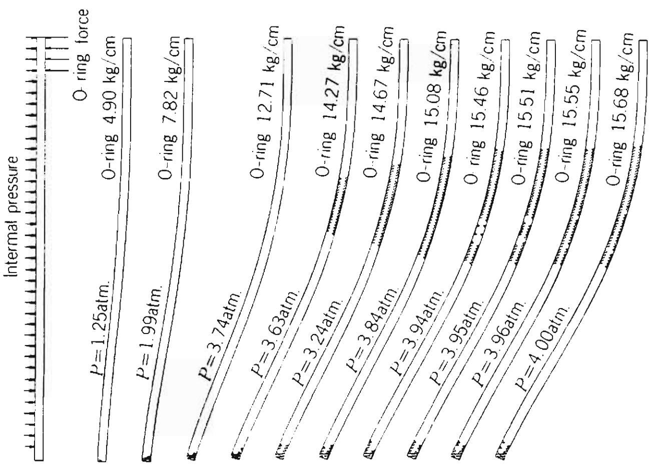

Fig. 7. Deformation and yielded elements when reaction of the O-ring is taken into account.

References

1) K. Ikegami, S. Nakajima, Y. Oikawa, M. Hara, S. Motonaga, and H. Kamitsubo: Sci. Papers I.P.C.R., 77, 87 (1982).

2) Y. Yamada and Y. Yokouchi: Elastic plastic analysis programing by finite element method – Instruction manual of EPIC-IV, (in Japanese), BAIFUUKAN (1981).

IV-12. Numerical Orbit Calculation for a Linac and Improvement of the Transmission Efficiency of a Beam

A. Goto, M. Kase, Y. Yano, Y. Miyazawa, and M. Odera

The transmission efficiency of the accelerated beam in the RILAC was not high compared with the design goal, especially at the low energy stage. In order to study the causes of this low transmission efficiency, we have developed a computer program named LINOR with which beam trajectories are traced by numerically integrating the equation of particle motion in the realistic electro-magnetic fields. LINOR is now used to improve the transmission efficiency and beam quality in the RILAC.

Using the program LINOR the following calculations were made for each of the six tanks constituting the RILAC: 1) the rf phase excursion of an on-axis particle, 2) the acceptance of each tank and 3) a beam behavoir when injected with a certain emittance. In 3) the transmission efficiency through a tank, the energy distribution and the beam profile at the exit of the tank were obtained with the Monte Carlo simulations.

In order to get reliable results with this kind of calculation, it is essential to use an electro-magnetic field distribution as close to the real one as possible. We used the measured magnetic field distribution for the quadrupole magnet. On the other hand, as for the rf electric field, such a distribution is difficult to measure, especially for its radial component. Therefore, an effort was devoted in deducing the electric field distribution which should be used in the calculation.

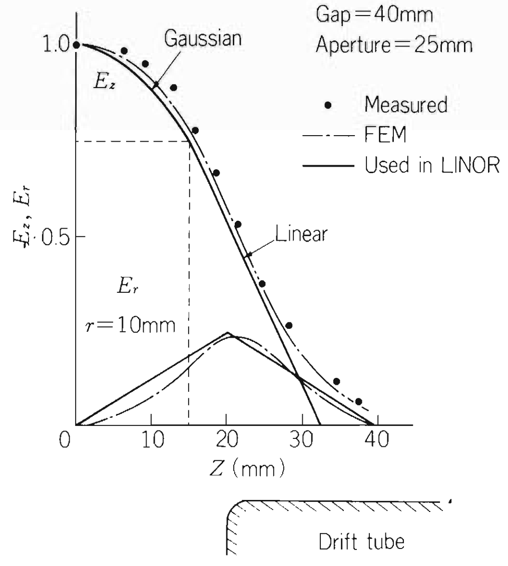

Fig. 1. Example of the distributions of E_z and E_r used in LINOR.

As for the distribution of the axial component of the electric field (E_z), we have the data that were measured using a model cavity. We also made calculations for it by a finite element method (FEM).[1] It was found that the calculated field distribution reproduced well the measured one. Therefore, we decided to use in LONOR the distribution approximated by such a simple function as to fit the above distributions. An example of these distributions is shown in Fig. 1.

It is quite difficult to measure the radial component of the electric field (E_r). As for E_r, we assumed the distribution which has a triangular shape with its top located at the edge of the drift tube. The half-width of the triangle was fixed to the value of 0.78 times the aperture of the drift tube, which was obtained with the calculations by FEM. The height of the triangle E_r^{max} was given by

$$E_r^{max} = \alpha \cdot \left(\frac{1}{2} \frac{\partial E_z}{\partial z} r \right) , \qquad (1)$$

where $\partial E_z/\partial z$ is the gradient of the linear part of E_z–distribution, r the radial coordinate of the particle and α a constant. The value of α was taken to be 1.15 from the result with FEM. An example of the distribution for E_r is also shown in Fig. 1. In order to check the appropriateness of using the above E_r–distribution in LINOR, we made comparison between the calculation and the measurement with respect to the dependence of the transmission efficiency of the beam through the first tank on the rf voltage. For this purpose, a double slit system (the size of both slits is 1 mm x 1 mm) was used. The reason why this narrow double slit system was used is that the uniformity of beam intensity in the emittance defined with it is very good. With this the ambiguity of the calculation with respect to the initial distribution of the emittance can be eliminated. Figure 2 shows the measurement together with the Monte Carlo simulations in two cases: in one case the quadrupole magnets were excited and in the other they were not excited. The simulation was performed for three different values of α. It is seen that the calculation reproduces well the measurement in the case of α = 1.15.

As for the distribution of the rf voltage in each accelerating tank, the data for the model cavity were used.

It is interesting to compare the results of LINOR and those of the calculation using the matrix method. So we calculated with LINOR the phase excursion of an on-axis particle and the acceptance of a tank using the acceleration parameters obtained by the matrix method.

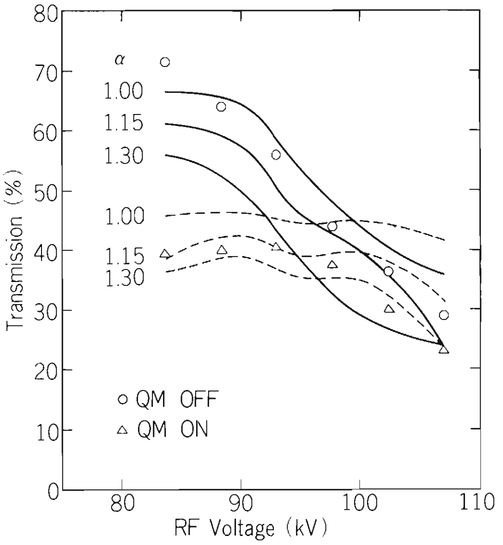

Fig. 2. Transmission efficiencies of an on-axis beam through the first tank in two cases: in one case the quadrupole magnets are excited and in the other they are not. It is noted that the output beam consists of all the particles having different energies.

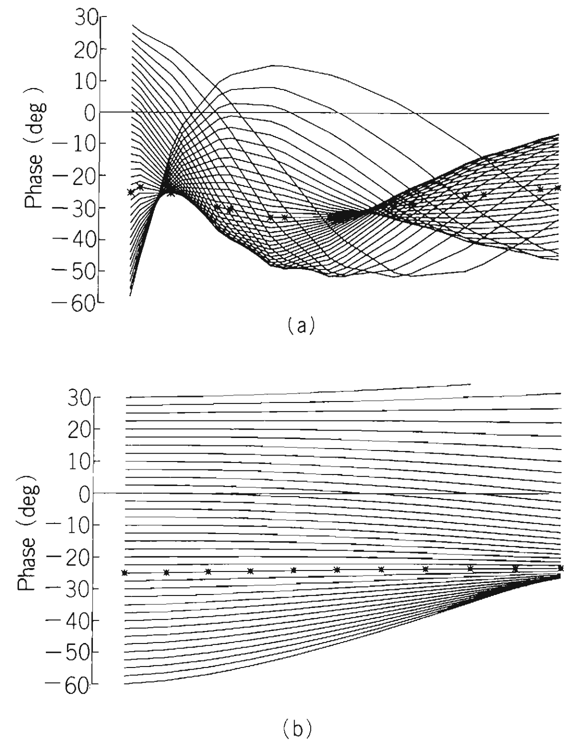

Fig. 3. Phase excursions of an on-axis particle calculated using LINOR: (a) for the first tank and (b) for the fifth tank. Acceleration parameters are those obtained by the matrix method. A star indicates the phase at the center of each acceleration gap for a particle with an injection phase equal to − 25° (the synchronous phase).

The calculation was done for two tanks, the first (low energy stage) and fifth (high energy stage) ones. Results of the calculation are shown in Fig. 3. A star indicates the phase at the center of each acceleration gap for a particle with an injection phase equal to −25°, which is the designed synchronous phase of the RILAC. It is seen that the phase of −25° is indeed synchronous in the fifth tank but there is no complete synchronous phase in the first tank. The beam acceptances of the first and fifth tanks are presented in Fig. 4. As can be seen in the figure, the results of the two kinds of calculation agree quite well with each other for the fifth tank but disagree a little for the first tank. The implication of these results is that the calculation using the matrix method gives proper results in the high energy region but becomes less reliable at the low energy stage.

Using LINOR, we studied the matching of beam emittance and acceptance for the first tank. For this purpose the transmission efficiency was measured when injecting a beam with several shapes of emittances. Figure 5 shows an example of the emittances then measured at the entrance of the RILAC together with the calculated acceptance for a beam with an injection phase of −25°. The measured transmission efficiency through the first tank was 20 % in this case. The Monte Carlo simulation with LINOR, on the other hand, gave a value of 18.7 %, which was very close to the measured value. The injection emittance used in this Monte Carlo simulation was assumed to have a Gaussian distribution. It is presented in Fig. 6, together with the calculated acceptances of the first tank for beams with several initial phases with respect to the rf voltage. The distribution of the initial phase was taken to be uniform in the simulation.

We have not yet obtained the completely optimal operational parameters of the RILAC. LINOR, however, has led to an improvement in the transmission efficiency of the beam. In order to achieve higher transmission efficiency and get better beam quality, we are now developing LINOR to have a function to optimize the currents of quadrupole magnets and the RF voltages.

A more detailed report on the results of the calculation obtained using LINOR is given elsewhere.$^{2)}$

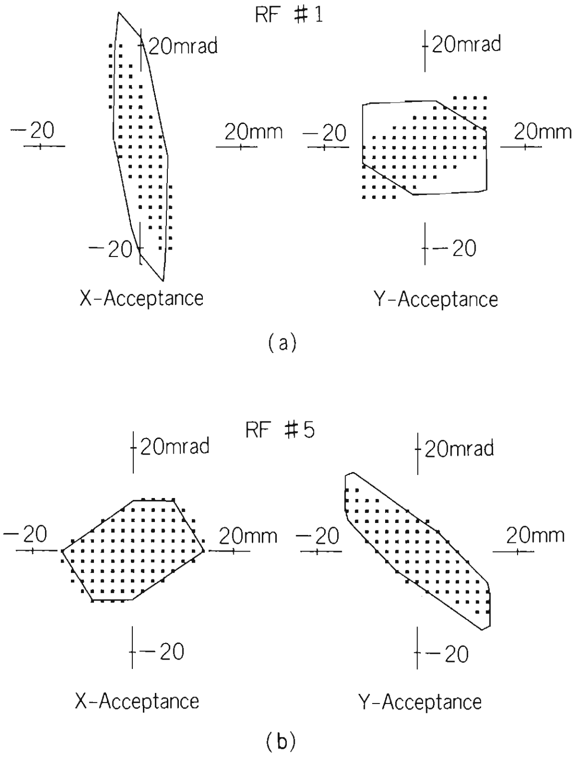

Fig. 4. Comparison between the beam acceptances calculated using LINOR (dots) and those calculated by the matrix method (solid line): (a) for the first tank and (b) for the fifth tank. Injection phase is taken to be − 25°

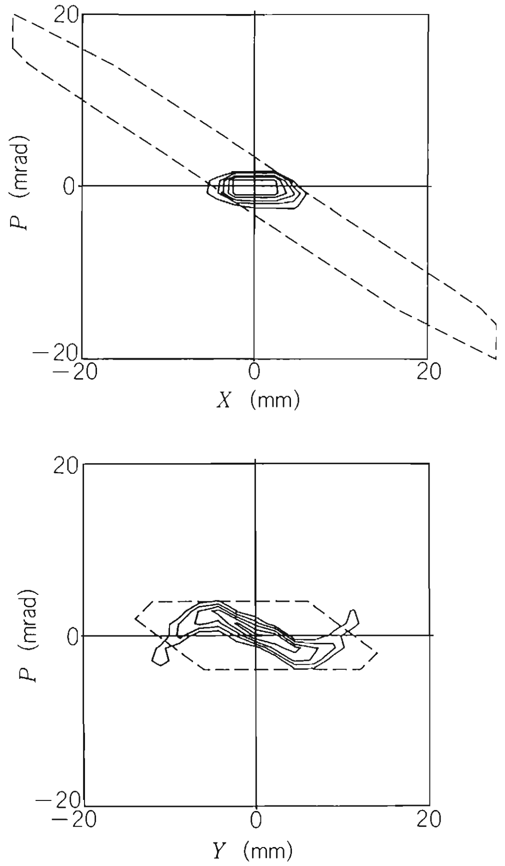

Fig. 5. Measured injection emittances in the case that the transmission efficiency through the first tank was 20 %. The calculated acceptances for a beam with an injection phase of −25° are also presented in this figure (dashed line).

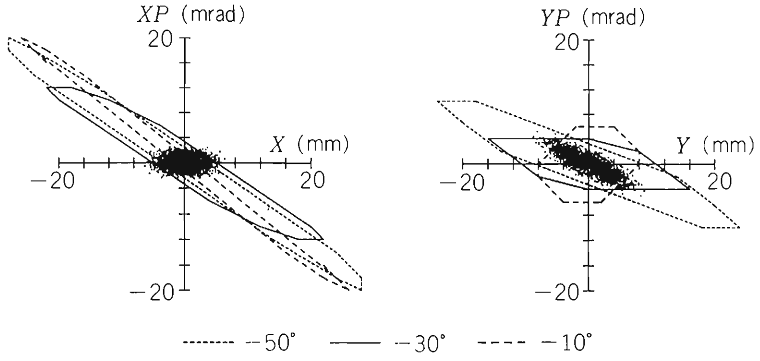

Fig. 6. Injection emittances used in the Monte Carlo simulation and the calculated acceptances of the first tank with different initial phases.

References

1) M. Hara, T. Wada, A. Toyama, and F. Kikuchi: Sci. Papers I.P.C.R., 75, 143 (1981).

2) A. Goto, M. Kase, Y. Yano, Y. Miyazawa, and M. Odera: "Numerical Orbit Calculation for a LINAC and Improvement of Its Transmission Efficiency of a Beam", Proc. of Computing in Accelerator Design and Operation, Europhysics Conference, Berlin (to be published).

IV-13. Energy Tuning and Energy Resolution of RILAC

M. Kase, T. Kambara, T. Tonuma, and M. Odera

At the final acceleration stage of RILAC, two methods are available to change the beam energy continuously without varying the acceleration frequency. One is the phase control method reported previously[1]. The other is the rf voltage control method in which the rf voltage of the final acceleration tank is adjusted and the injection phase is kept nearly constant.

The feasibility of energy tuning by these simple methods at RILAC is due to the following fact. By the technological requirements of the variable frequency scheme, the length of acceleration tank has to be chosen relatively short and the number of drift tubes inside one tank is limited to less than 12 for the last three tanks. Therefore, the rotation angles of the accelerated ions on the energy-phase space diagram around the synchronous point is small in each tank, being less than a quarter of turn for the final two tanks. Such acceleration tanks do not work sufficiently as a velocity filter like an ordinary linac tank. The features relating to acceleration tanks are listed in Table 1, where the comparison with the case of UNILAC Wideroe tanks is made.

Table 1. Parameters of acceleration tank.

Tank No.	Acceleration mode	Tank length	Number of drift tubes	Rotation angle
#1	$\pi/3\,\pi$	3 m	16	380°
#2	π/π	"	18	165°
#3	"	"	14	120°
#4	"	"	12	90°
#5	"	"	11	70°
#6	"	"	10	65°
#1*	$\pi/3\,\pi$	5.5 m	36	
#4*	π/π	7.3 m	26	

* UNILAC Wideroe tanks

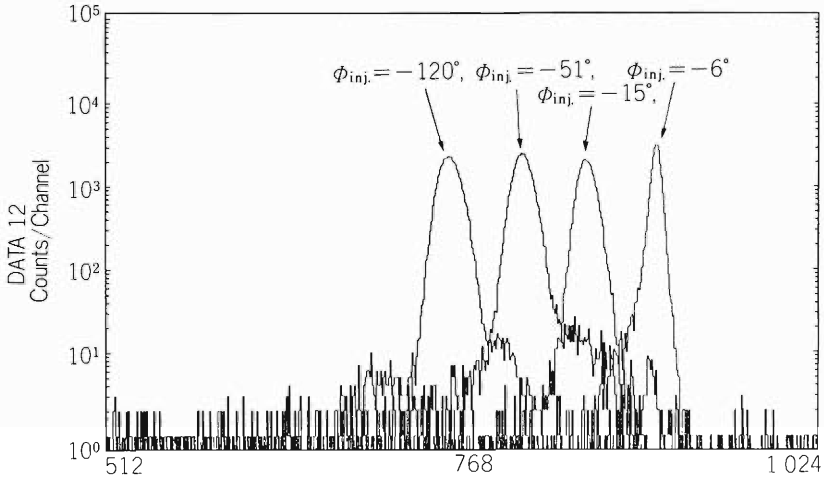

Fig. 1. Energy spectra of beam emerging from tank #5 for four kinds of settings of the injection phase, ϕ_{inj}.

An example of the application of the phase control is shown in Fig. 1, where one can see how the energy spectra of beam emerging from tank #5 varies with change of injection phase. Those spectra were obtained by direct measurement with a surface-barrier-type semiconductor detector set in the beam line. The beam intensity was reduced by using the two sequential charge transfer reactions[2] during the measurement. By changing the injection phase from −6 to −120 deg., the peak position moves to the low energy side and the peak width becomes wider gradually.

We made a computer simulation for the phase motion in RILAC. The results of calculation for five representative points in the longitudinal emittance after tank

#5 for each injection phase are shown in Fig. 2. In the figure, one can see the tendency that, as the injection phase varies from 0 to −100 deg., the beam energy decreases and, at the same time, the energy spread becomes wider. The results are summarized in Fig. 3 together with the experimental ones. The fairly good agreement between calculation and measurement can be seen. However, the minimum value of the obtained energy spread is two times larger than that of calculation. The reason for this difference is not clear at present, but it may be due to the effect of the non-uniform distribution of rf voltage along the beam axis in each tank, the unstability of rf parameters (voltage and/or phase), the coupling of radial and phase motion in the low velocity region, and so on.

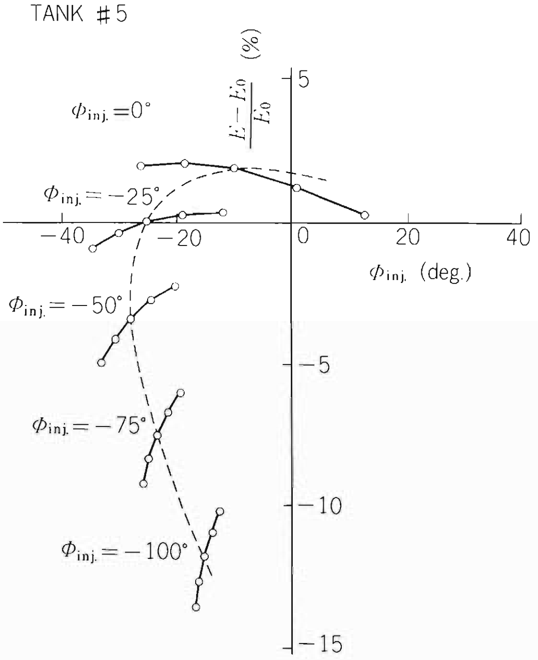

Fig. 2. The results of calculation of longitudinal emittances at the exit of tank #5. The vertical axis is scaled in terms of the relative energy difference from the energy value, E_0, of the synchronous condition. The normal operation was assumed from the injector to tank #4. The rf voltage, $V_{\#5}$, is fixed at the normal value.

Figure 4 shows the results of calculation of the energy variation at the exist of tank #5 against the injection phase. In the figure, the parameter is the acceleration voltage of tank #5 ($V_{\#5}$) and the injection energy is

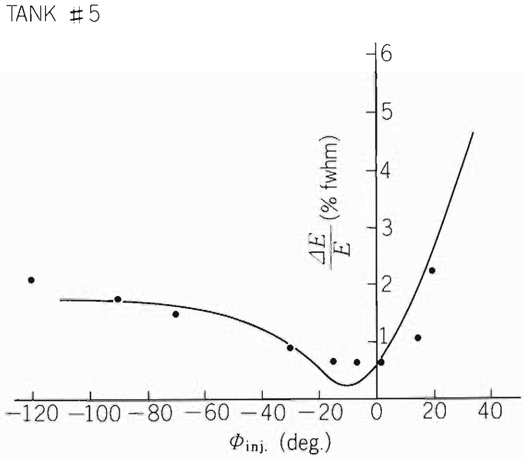

Fig. 3. The variation of energy resolution of beam of tank #5 against the injection phase to the tank. The solid line is the results of calculation in Fig. 2, and the solid circles are the measured energy spreads with the semiconductor detector.

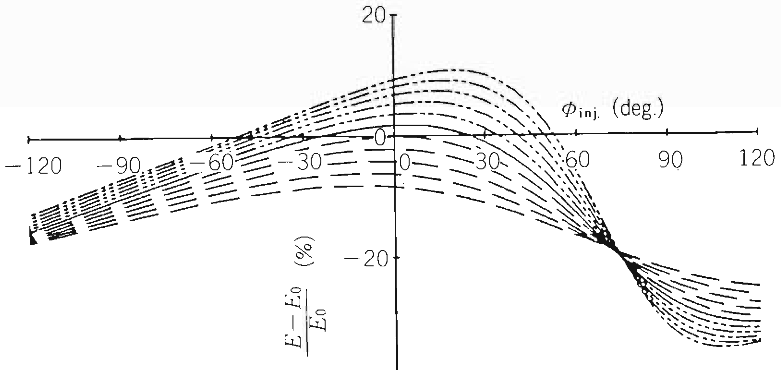

Fig. 4. The calculated relations between the beam energy and the injection phase for tank #5. E_0 is the normal beam energy at the exit of the tank. The rf voltage was changed from 50 to 150 % of the normal value (V_0) by step of 10 %. The solid curve is for V_0, the dashed curves are for the rf voltages less than V_0, and the dot-dash ones for those higher than V_0.

fixed at the designed value. As $V_{\#5}$ goes down from 150 % to 50 % of the designed value, the maximum energy decreases, the undulation of energy curves becomes small and the phase giving the maximum energy shifts slightly to the negative phase side. If the injection phase to tank #5 is always set around the maximum energy point for each $V_{\#5}$ value, energy can be varied without degrading the energy resolution. As shown in Fig. 5, the energy varies linearly and slowly with change of $V_{\#5}$ and goes down toward the normal energy of the previous tank (shown by a dot-dash line in the figure) as $V_{\#5}$ approaches to zero, and, on the other hand, the energy spreads are almost constant against the $V_{\#5}$ adjustment.

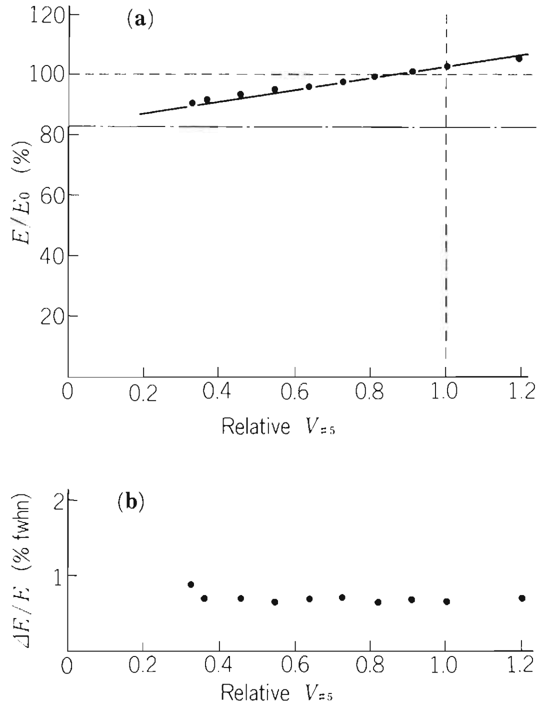

Fig. 5. The variations of energy (a) and energy resolution (b) for tank #5 with change of rf voltage of the tank. The injection phase is adjusted in such way that the beam energy is maximized for each rf voltage. The solid circles in both figures are the experimental data obtained with the semiconductor detector. In figure (a), the energy axis is normalized to the designed energy of tank #5. The solid line shows the results of calculation, and the dot-dash line show the designed energy levels for tank #4.

To tune energy in the routine operation, the method by adjusting the tank voltage is superior to the phase control method from the viewpoint of the constant beam quality. But, when the energy several percent greater than the normal energy of one tank (denoted by tank #N) for a given frequency is required, it is sometimes difficult to apply this voltage control method. In this case, however, there are, in principle, two possible ways for applying the voltage control method. One is to raise the rf voltage of tank #N by 20 – 40 % and turn off the later tanks, and the other is to operate the tank #N normally and to operate the next tank, i.e. tank #(N + 1), at the rf voltage level around 10 % of the normal value. Neither of ways can be used when $V_{\#N}$ is higher than the spark limit and $V_{\#(N+1)}$ is smaller than the lower limit of rf stabilization circuit. In that case, one needs the combination of the voltage and phase control methods or the frequency adjustment.

Even when the beam is accelerated up to the designed energy for a given frequency value, it is preferable to make intentionally a small deviation from the normal acceleration condition by lowering the rf voltage of the final tank to 90 % of the normal value and adjusting the injection phase of the tank to maximize energy (around 0 degree) as shown in Fig. 4. It gives a good energy resolution, and saves the electric power consumption as well.

References

1) M. Kase, T. Kambara, T. Tonuma, and M. Odera: RIKEN Accel. Progr. Rep., 16, 150 (1982).
2) M. Kase and T. Kambara: ibid., p. 147.

IV-14. Change of Longitudinal Phase Motion in the First Tank of RILAC against the Frequency Adjustment

M. Kase, T. Kambara, T. Tonuma, and M. Odera

A question which is of great interest at RILAC, the first linac using the variable frequency scheme, is how to keep a constant beam quality against the frequency adjustment (17 – 45 MHz). In order to do that, it is necessary to maintain the constancy of particle motion in the longitudinal phase space when the frequency is changed, since the beam qualities such as the relative energy spread, the phase spread and the phase acceptance are related closely to the phase motion.

There is, however, an inevitable ununiformity in the distribution of acceleration gap voltage along the beam line in a resonator tank due to the fact that the length of resonator tanks is not sufficiently short as compared with the wave length of radiofrequency. The accelerating voltage drops generally at both ends of tank and this tendency is enhanced as the frequency increases.1),2) This fact causes an undesired frequency dependence of the longitudinal phase motion, since the geometry of drift tubes of RILAC was designed assuming the uniform voltage distribution. As the result, the beam qualities vary with change of frequency. Especially in the first tank, where the $\pi - 3\pi$ mode is employed, these effects are important, because a rotation angle of accelerated particle in the energy-phase space is relatively large and the deviations from the synchronism grows large inside the tank.

Figure 1 shows the longitudinal acceptance of the first resonator tank calculated on the assumption that the distribution of gap voltage is uniform. In the figure, energy is expressed in terms of the relative energy difference given by $(e_i - E_i)/E_i$, where e_i and E_i are the ion energy and the designed energy giving the synchronism at the acceleration stage i, respectively. The vertical axis is the relative energy difference at the entrance of the first tank. The horizontal axis is the phase of rf voltage when an ion is injected to the center of first gap of the first tank. The solid curves in the figure are contour lines of the relative energy difference of the ion at the exit of the first tank, corresponding to the values of –6, –4, –2, 0, and + 2 %. The dashed curves are contour lines of rf phase when the ion reaches the center of the final acceleration gap of the first tank, corresponding to the values of –40, –20, 0, 20, and 40 deg. The synchronism can be seen at the phase of –25 deg. The –4 % energy lines or the 20 deg. phase line shows the typical phase acceptance of a linac with the so-called golf-club shape.

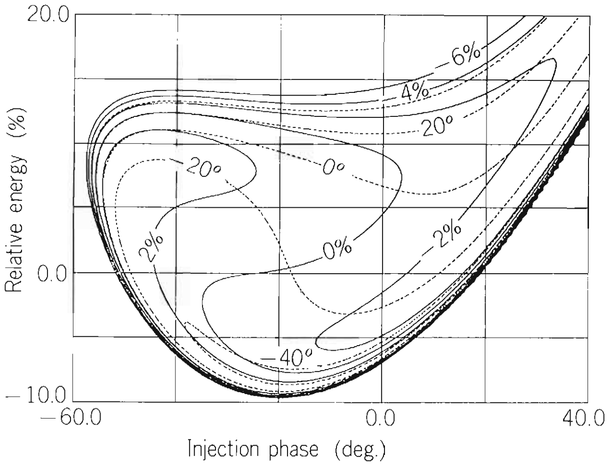

Fig. 1. Result of calculation of the energy and phase contour maps on the injection energy-phase space for the first tank. The gap voltage distribution was assumed to be uniform. The calculation was made using the impulse approximation.3) The solid contour lines give the relative energy difference ranging from –6 to 2 % and the dashed lines show the phase from –40 to 40 deg.

Figures 2 (a) and (b) show the same kind of calculations as that in Fig. 1, but for non-uniform distributions at the frequency of 17 and 45 MHz, respectively. The synchronism at a phase angle of –25 deg. cannot be seen even for the lowest frequency (17 MHz). The higher energy lines are receding as the frequency increases, and 0 % energy line crosses the injection energy level at larger anlge than in the case of the uniform distribution. It can be expected that the longitudinal emittance at the exit of the tank is different from that for the uniform distribution and the average energy of ions become lower than the prescribed value. Moreover, the acceptable region (for example, the region enclosed by –4 % energy line) moves slightly to the higher energy side as the frequency increases, although the area and shape of the region are nearly constant. This fact causes the reduction of phase acceptance for the higher frequency, if the injection energy is set according to the design value.

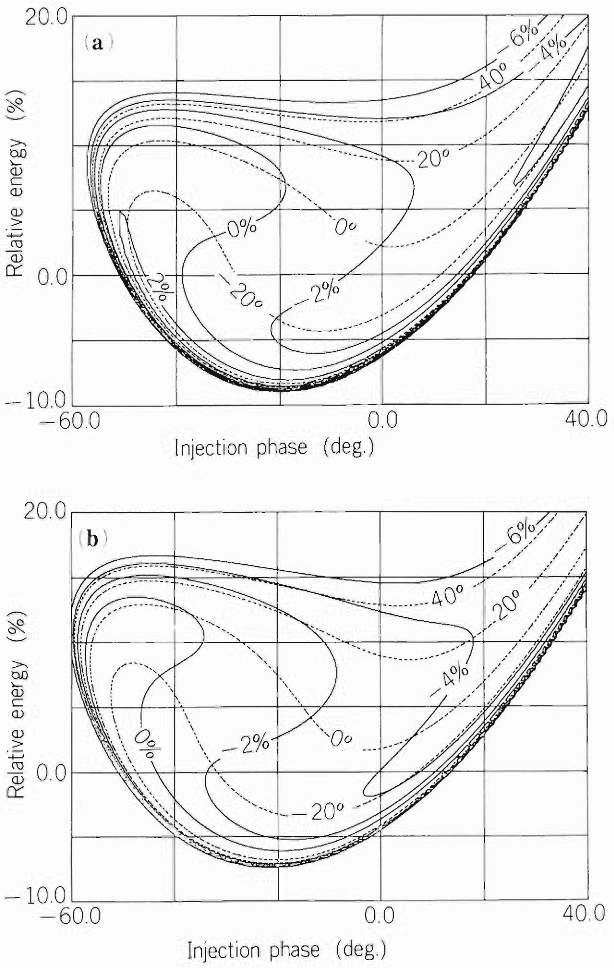

Fig. 2. Results of the same calculation as in Fig. 1 but for the nonuniform gap-voltage distribution. The measured distributions in Ref. 2 were used for the calculation. (a) is for the lowest frequency of RILAC, 17 MHz and (b) for the highest one, 45 MHz. The rf voltage was set in such way that the average value of the distribution will be equal to the prescribed voltage value.

In order to reduce these effects relating to the first tank, the pattern of the energy and phase contour lines around the injection energy level must be identical for any frequency. However, little improvement can be made by adjusting only the rf voltage of the first tank contrary to our early expectation. One has to adjust all the parameters determining the longitudinal phase motion inside the first tank, i.e. the injection voltage V_{inj} and the injection phase ϕ_{inj} as well as the tank voltage $V_{\#1}$. The buncher voltage is also a parameter relating to the phase motion in the first tank but less important in this case. The corrected parameters, V_{inj} and $V_{\#1}$, can be written as follows:

$$V_n = K_n (M/q) f^2 C_n(f) \quad (n = \text{inj and } \# 1),$$

where K_n is a constant, M/q the mass to charge ratio of ions to be accelerated, and f the acceleration frequency. The correction factors $C_n(f)$, which are functions of f, give a value of 1 when the gap voltage distribution is uniform. ϕ_{inj} is also a function of f, although it is a constant (−25 deg.) for the uniform voltage distribution.

When the relative energy difference corresponding to V_{inj} is expressed by ΔE_{inj}, an ion on the point (ϕ_{inj}, ΔE_{inj}) in the injection phase space will be the central particle in the longitudinal phase space after the first tank. The center of injected beam bunch should be located at the point. The resultant phase ϕ_{out} at the exit of the first tank has to be also considered in determing the parameter of the next-stage acceleration, if it depends on the frequency.

Figure 3 shows one of the candidates for these correction factors which were obtained by the computer simulation. They ensure that the pattern of longitudinal emittance at the exit of the first tank and the phase acceptance of the tank is nearly constant over the frequency range. The large correction is required for the injection voltage rather than the rf voltage. The corrections for the parameters of the later-stage acceleration are also necessary but they are smaller than those for the first tank and, in most cases, only the correction for the rf voltage is needed.

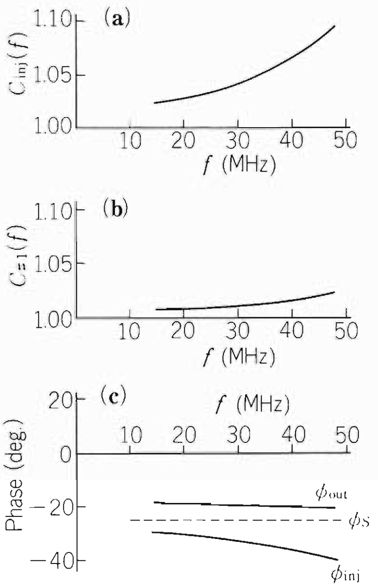

Fig. 3. Calculations of the correction factors for the injector voltage (a), for the tank voltage (b) and for the injection and output phases (c).

References

1) Y. Miyazawa: Private communication.
2) Y. Chiba: IPCR Cyclotron Progr. Rep., 10, 144 (1976).
3) T. Tonuma, F. Yoshida, and M. Odera: Reports I.P.C.R., (in Japanese), 51, 53 (1975).

IV-15. TOF Measurement of Beam Energy

M. Kase, E. Ikezawa, and T. Kambara

At a multi-stage accelerator like RILAC, it is essential to know the beam energy on each acceleration stage for the fine tuning of acceleration parameters. The following three methods are available now at RILAC to estimate the beam energy: the direct measurement with an SSD, the momentum analysis with an NMR-calibrated dipole magnet and the velocity measurement by the time-of-flight method (denoted later by the TOF) using a couple of bunch probes.[1] Among these, the TOF is suitable for a heavy ion linac like RILAC, permitting the precise estimation of the average energy of ions in beam bunch.

The bunch probes used in the TOF are of a capacitive (i.e. beam non-destructive) type, having a ring-shaped electrode matched nearly to 50 ohm impedance. The electrode surface facing to the beam is in the form of a cylinder 30 mm in diameter and 10 mm in length along the beam line. Figure 1 shows the distribution of probes installed along the RILAC beam line. A couple of these probes are used which are located apart from each other at the distance L. If any acceleration devices exist between the two probes, they should be turned off during the measurement. The signals from the probes, which have a bipolar shape as shown in Fig. 2, are sent to the control room via cables with the same time lag.

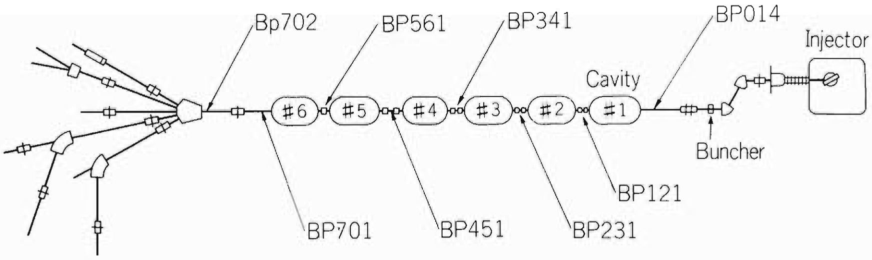

Fig. 1. The distribution of capacitive bunch proves installed along the RILAC beam line. BP denotes the bunch prove.

If one measures the time delay Δt of the signal from the downstream prove relative to that from the upstream probe, the average velocity v of particles in beam bunch is given by[1] $v = [L/(TN + \Delta t)]$, where T is the period of acceleration voltage and N is the number of bunches existing between the two probes, being equal to the largest integer which does not exceed L/(vT). The error in the energy can be reduced to less than 0.2 %, if N is large enough. On the other hand, an error in the knowledge of N leads to a wrong energy value which is different from the real value by 200 n/N % (n = 1,2, ...). In practice, however, since one can easily estimate the beam energy on each acceleration stage with an accuracy within 10 % at RILAC, such an error in N rarely occurs if N is smaller than 20. A combination of probes should be selected so that the N value will be around twenty. When a higher accuracy is required, it is necessary to make a two-step measurement: In the first step, N is set smaller than 20 and larger in the second one. An example of the relation between Δt and E/A is shown in Fig. 3. For N as large as 44, Δt varies almost linearly with E/A.

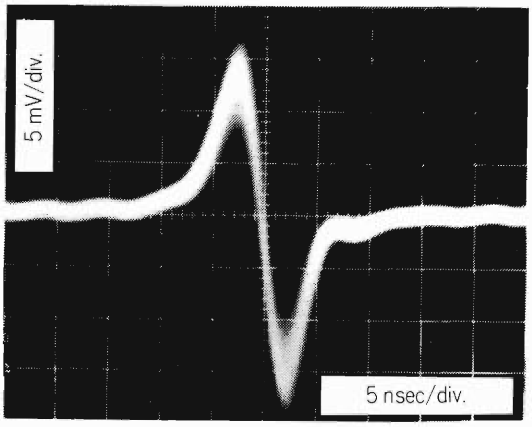

Fig. 2. The signal from the bunch prove BP121. The beam is 1.5 MeV N^{2+} with 1 μA in beam current and the acceleration frequency is 18 MHz. The signal is amplified with a wide-band amplifier (45 dB) and observed on 350 MHz oscilloscope.

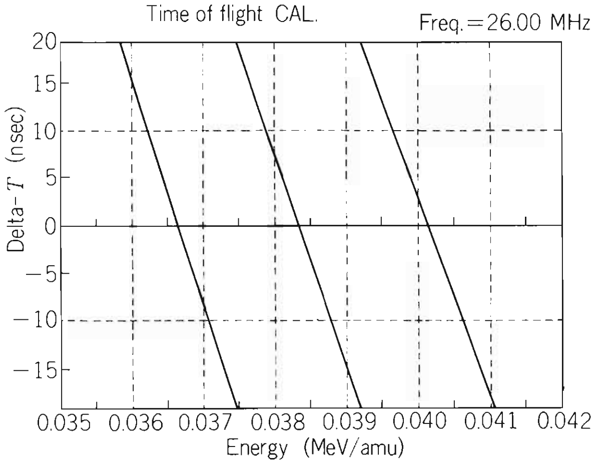

Fig. 3. The relation between the time delay Δt and the energy of beam from the injector, in the case where the frequency is 26 MHz and the probes BP121 and BP231 are used. The length L is 4602 mm and the bunch number N is 45 for the left line, 44 for the middle line and 43 for the right line.

The TOF permits the calibration of accelerating parameters as well as the parameter tuning. Fugure 4 shows the experimental data and the calculations for the energy of beam emerging from the tank #3 when the tank voltage and the injection phase are changed. If one knows the injection phase and the beam energy, the effective voltage for tank #3 can be estimated from the comparison with the calculations. Also a calibration of the injector voltage can be easily done with a buncher if the TOF method is used.

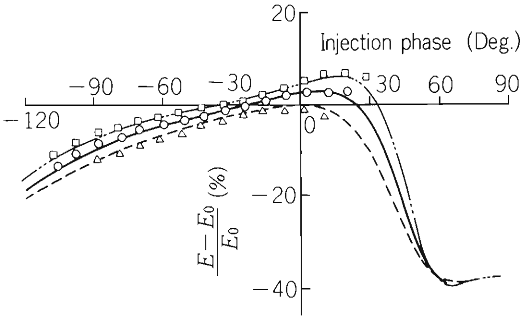

Fig. 4. The beam energy vs the injection phase for the tank #3. The vertical axis is the energy expressed in terms of the relative energy difference (in %) from the normal energy E_0 at the exit of tank #3. The parameter is the tank voltage $V_{\#3}$. The three kinds of curves, that is, dot-dash, solid and dashed curves, are the calculation for $V_{\#3} = 1.1\ V_0$, $1.0\ V_0$ and $0.9\ V_0$, respectively, where V_0 is the normal tank voltage. The open squares, circles and triangles are the results of the TOF for $V_{\#3} = 1.1\ V_m$, $1.0\ V_m$ and $0.9\ V_m$, respectively, where V_m is a meter reading for the tank voltage and is now to be calibrated. The comparison between measurement and calculation permits the decision of the effective tank voltage with an accuracy of a few percents.

Reference

1) J. Glatz, J. Klabunde, and P. Strehl: Proc. of the 1976 Linear Accelerator Conf., p. 306 (1976).

IV-16. Design of a Compact Deflection Magnet

M. Hemmi, Y. Miyazawa, and S. Motonaga

A small deflection magnet named CD was designed, fabricated and set in the course labelled C. The course is in line with the acceleration axis of the linac, so that alignment of the accelerator system such as the beam injection equipments and drift tubes can be checked easily from the end of the course by optical means.

The course was very usefully used at the initial stage of accelerator construction and installation of the experimental apparatuses. However, unwanted neutral or charge changed particles also arrive at the end of course disturbing measurements. Since necessity of rechecking of the alignment has decreased, we decided to add a deflecting magnet in the course to remove the undesired beams from the C course. A small deflection angle is sufficient for that purpose.

The magnet has to be installed in the narrow space

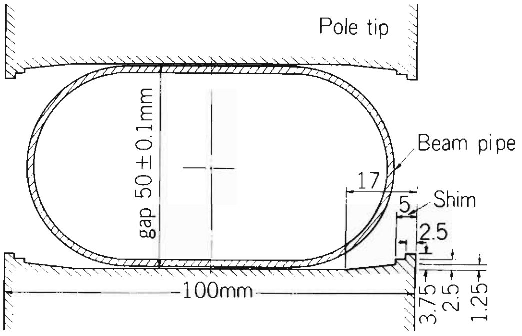

Fig. 1. Pole profile and beam pipe cross section.

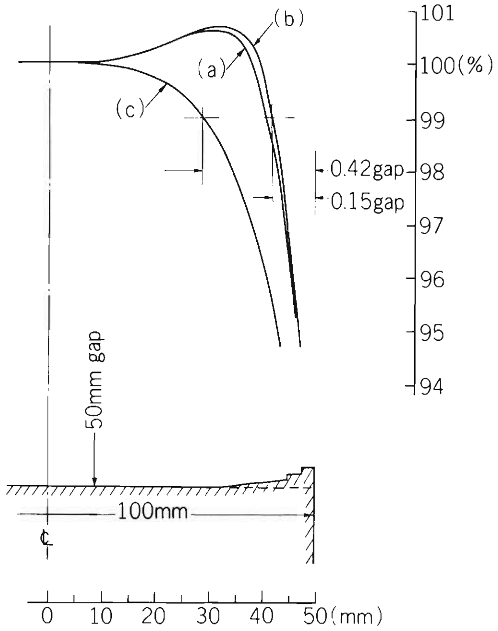

Fig. 2. Comparison of measured (b) and calculated (a), (c) field distributions of the CD magnet. Curves (a) and (b) are for profile shown in Fig. 1. (c) is for a straight pole with flat face.

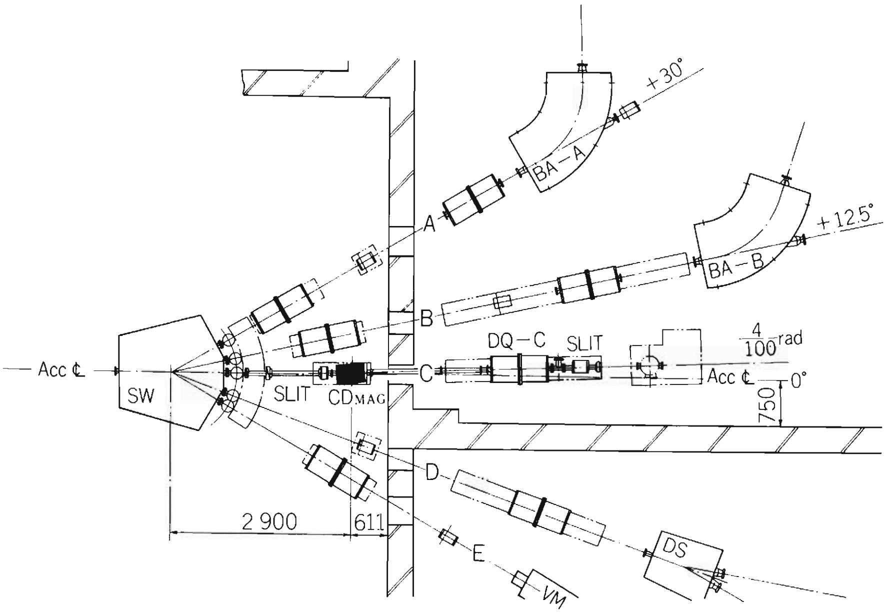

Fig. 3. Layout of the CD magnet in the accelerator vault.

between the beam distributing magnet (SW) and the shielding wall separating the accelerator vault from the experimental areas. Beam pipes of the neighboring courses, B and D run close to the both sides of the pipe of C. The magnet must be made as compact as possible so that it can be fitted in the space. Firstly, we tried to get enough width for beam path with magnet pole having relatively narrow width but moderate gap height by use of iron shim at the pole edge. The pole profile shown in Fig. 1. was determined by TRIM code calculation. In Fig. 2 the result of field measurement (b) of the completed magnet is compared with calculations. (a) is for the profile shown in Fig. 1 and Fig. 2(c) is for a straight pole with flat face. Agreement of (a) with (b) is satisfactory. Also, increase of the useful width in (b) over that in (c) is to be noted. The width for uniformity of 1 % is 83 mm for (b) and is 58 mm for (c), for the pole width of 100 mm and gap height of 50 mm. Since the maximum field required is only 3.5 kG, cross section of the yokes has been reduced to 60 % of the pole surface area to cut weight of the magnet further. No saturation effect was observed in field distribution or in excitation curve. The tape coil cooled by cold plate technique, which has been applied extensively for the magnets of the RILAC, is also used here to reduce the magnet size and its power consumption. Figure 3 shows the position it is installed and Table 1 its specifications.

Table 1. Specifications of CD magnet.

Deflection angle	4/100 rad
Maximum field x Length	3.5 kG x 35 cm
Pole face	100 mmW x 350 mmL
Pole gap	50 ± 0.1 mm
Width within 1 % uniformity of field	83 mm
Effective field boundary	0.52 of pole gap from the edge
Coil (a) type	Tape-coil
(b) Total Amper turns	2 x 70 T x 100 Amp.
(c) Power consumption	8 V x 100 Amp
(d) Cooling water	2 ℓ/min (head loss 0.5 kg/cm^2)
Weight	170 kg

Ⅳ-17. Compact and High Efficiency Arc Pulsing Power Supply for PIG Ion Source of the RILAC

M. Hemmi and Y. Miyazawa

The ion source of the RILAC injector terminal is of an indirectly heated hot cathode PIG type. For these several years after completion of the linac it has been operated in DC mode throughout. This year we designed an arc pulsing power supply and installed it in the high voltage terminal to increase yield of the high charge state ions of heavy elements. Since space, coolant supply and power capacity available for the new equipment in the terminal are limited, the usual ion source pulser which uses a large vacuum tube as a series regulator could not be installed there. Therefore, the arc pulser must be compact and use power efficiently.

We solved the problem by use of a new solid state switching element that recently becomes available in the market, named GTO (Gate Turn Off thyristor). The device has the following characteristics:

(1) It can withstand voltage between anode and cathode as high as 2.5 kV in the off-state.

(2) In the conducting state, the voltage drop within the element is in the range of small value between 1.5 and 2 V. Power dissipation is so small that there is no need of forced cooling of the element. Therefore, power efficiency is good.

(3) In designing power supply, it is not necessary to consider surplus voltage required for the series element in addition to that for the ion source.

(4) The conducting state can be switched off by simply applying a control signal to its gate unlike the ordinary thyristors.

(5) Necessary power to drive the gate is small enough to simplify design and operation of the whole circuit.

On the other hand, there are some drawbacks when compared to the hard tube regulator. One is the slow switching response and the other is possibility of receiving unrecoverable damage when an unexpected voltage spike was generated in the circuit by some reasons.

Table 1 shows specifications of the pulsing power supply and Fig.1 its block diagram. Its characteristics

Table 1. Specification of GTO arc pulsing power supply.

Voltage (peak)	100 ~ 1500 V
Current (peak)	10 A maximum
Polarity	Negative
Pulse width	1 ~ 3 msec
Repetition rate	100 ~ 300 pps
Duty factor	30 % max.
Rise and fall time	10 and 200 μsec respectively
Sag	< 10 %
Power requirements	200V 3 phase, 48 – 50 Hz, 6 kVA max.
Dimensions (W x H x D)	550 x 700 x 800 (m/m)
Weight	Approx. 200 kg

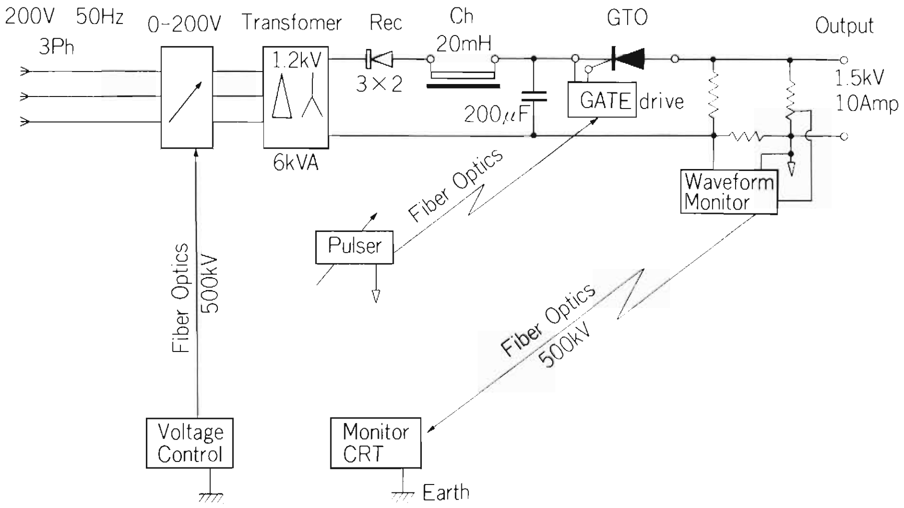

Fig. 1. Schematic diagram of the pulse power supply.

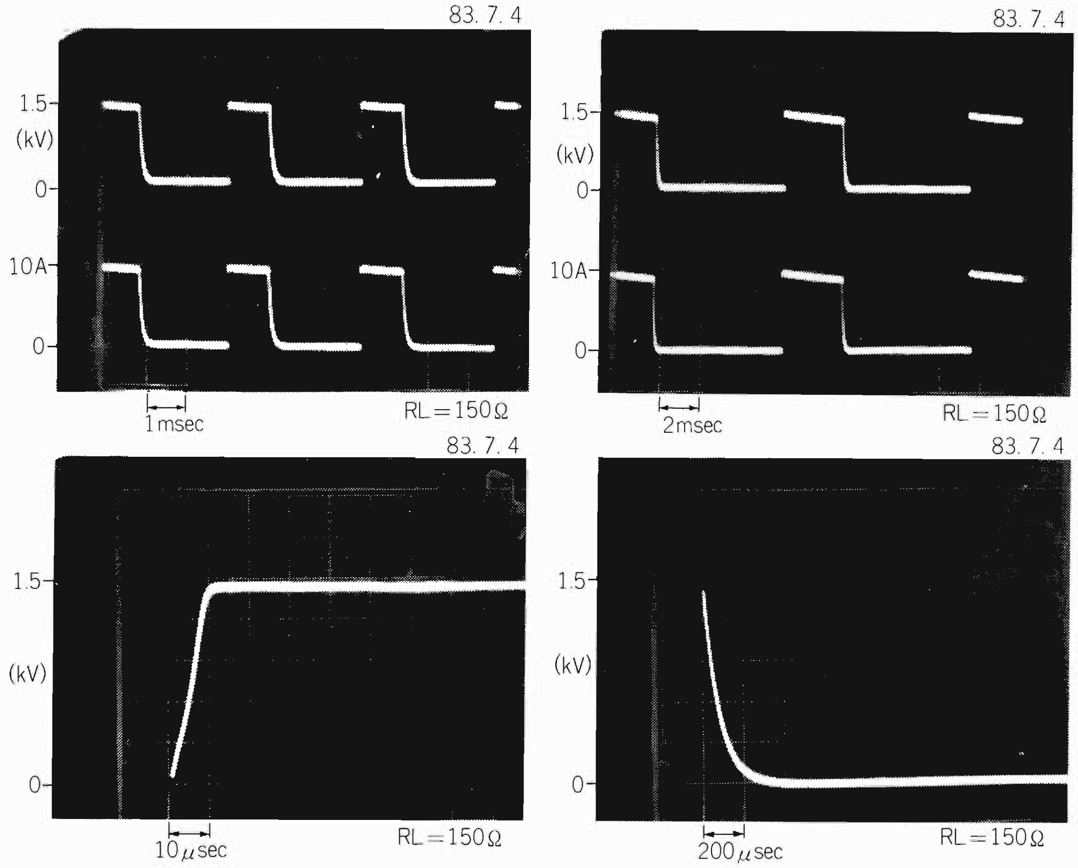

Fig. 2. Photographs of the pulse wave forms at pulse widths of 1 and 3 msec. Lower traces show rising and falling edges of the pulse.

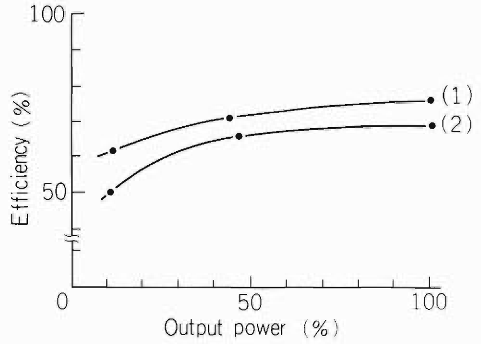

Fig. 3. Measured power efficiency as the ratio of pulse to AC primary.

(1) At pulse width of 3 msec and 30 % duty factor,

(2) At pulse width of 1 msec and 10 % duty factor.

were measured in the terminal. In the upper part of Fig. 2 are the photographs of the wave forms for pulse widths of 1 and 3 msec. In the lower part are shown the leading and trailing edges of the pulse at the high sweeping speed display. The rising and falling time of the pulse are 10 and 200 μsec, respectively, and are satisfactory for ion-source operation.

Power efficiency of the power supply was measured as the ratio of the averaged pulse power to the power drain of the AC line. Figure 3 gives the results. It is 50 % at 10 % duty-factor operation and 76 % at the operation with the maximum duty-factor of 30 %.

Its control is made from the operation console in the central control room of the linac, via optical links used for DC operation of the source. Other optical links are used to transmit analog signals to watch arc discharge condition of the source at the console. Wave forms of voltage or current of the ion source can be displayed on the CRT of the control desk whenever it is necessary.

Ar^{6+}, Kr^{8+}, and Xe^{9+} ions were obtained and accelerated by the linac shortly after installation of the pulser. It was found that charge states higher by 2 than those by DC operation could be obtained for ions of the heavy elements by use of the arc pulsing scheme. We are preparing for acceleration of Au and Al in the beginning of 1984.

IV-18. Design Study of the ECR2

M. Yanokura, S. Ishii, Y. Sakamoto, and M. Odera

We have started developing an ECR ion source which can continuously produce higher charge state ions compared with ordinary PIG ion sources. It is expected to improve performance of our heavy ion linac. Last year we tested a single stage type ECR ion source, and got a few nA Ar^{7+} beam.

We plan to study possibility of using microwave of relatively low frequency to produce enough quantity of highly stripped ions by use of the principle of whistler mode excitation. In the ECR sources developed to date, high frequency (16 GHz) which is available by the most advanced microwave technology has been used. However, in the ECR principle, the higher the frequency, the stronger the magnetic field must be. Power consumption increases rapidly and the microwave source becomes very expensive. Power available on our 500 kV ion source terminal is, however, limited to 50 kVA. Therefore, if the required multiply charged ions could be produced at relatively low frequency by the use of the whistler mode, the ECR source would be more attractive to us. This year, we have designed an ECR ion source of two stage type which we call ECR2. At its first stage, high intensity low charge state ion plasma is formed by whistler mode microwave heating of gas at relatively high pressure, using a 2.45 GHz magnetron. The ion plasma then diffuses into the second stage. At the second stage which is under high vacuum, electrons are excited, and are stripped off from the low-charge state ions by collision with hot free electrons produced by microwave resonance heating. Microwave power source of same frequency is used for the second stage. Higher charge state ions are, therefore, expected to be formed. For the ECR2, we plan to use the coils, the 2.45 GHz microwave power source and the high voltage extraction power supply which have been used for the single stage ECR source to save cost of modification.

In the first stage of the ECR2, microwave is injected along the axis of the mirror field (whistler mode), instead of injecting it perpendicular to the axis as has been done in the first single stage model. We expect this allows to get an overdense plasma in which the electron density n_e is much larger than the critical density and electron plasma frequency ω_{pe} which is proportional to square-root of n_e can become higher than the microwave frequency whereas ω_{pe} can never be larger than ω in the perpendicular injection mode. In fact, we got an electron density of $1.7 \times 10^{13} cm^{-3}$ for 9 GHz in preliminary experiment.[1] This value is ten times larger than the critical density. It is predicted that some instabilities produced in the over-dense plasma will cause trouble. We plan to suppress it by applying a dynamic stabilization method in which modulated microwave[2] is made incident on the plasma.

Outline of the ECR2 is shown in Fig. 1. Total length is about 1.2 m, including extraction system. Most of the vacuum components are made of stainless steel except the second stage cavity. To realize the whistler mode coupling, microwave power is fed through a coaxial wave

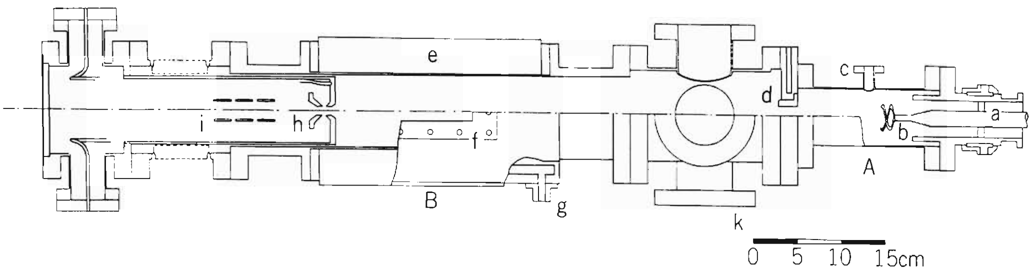

Fig. 1. Design of ECR2 ion source. Letter which shown in this figure means following.
A: first vavity (Whistler mode cavity),
B: second cavity (stripper stage),
a: coaxial wave guide,
b: helical antenna,
c: gas inlet,
d: orifice,
e: hexapole magnet,
g: cooling water inlet,
h: extractor,
i: Einzel lense,
k: pumping port.

guide and is radiated in the axial direction of the cavity by a helical antenna attached to the end of the center conductor of the feeder. The pressure in the first cavity is chosen around 10^{-4} Torr. The reason for choosing this pressure range is due to plasma stability. The second stage is the stripper stage. Length of the second cavity is 30 cm and its inner diameter is 6 cm. This cavity is made of aluminium. Electrons are heated by microwave power and higher charge state ions are formed by successive stripping in the ECR zone. When a hexapole field is added to the mirror field, the length of the ECR zone becomes 20 cm and its maximum diameter will be 3 cm. High vacuum is necessary for this stage to avoid ion loss due to electron capture of the highly stripped ions by collision with the residual gas molecules. The pressure in the stripper stage is designed to be below 10^{-6} Torr, in the gas feed condition. As the pressure of the stripper stage differs from that in the first stage, only a long tube with a small orifice is provided between the two stages to make differential pumping feasible.

Plasma is confined by magnetic mirror field in the axial direction, and by hexapole field in the transversal directions. In order to get hexapole magnetic field, samarium cobalt permanent magnets are used.

Beam extraction system is almost the same as that of the old ECR source. The maximum extraction voltage is 30 kV. The extracted beam is focused by an Einzel lens, and the charge state of ions are analyzed by a bending magnet. Finally the beam current is measured by a Faraday cup.

References

1) S. Ishii: Sci. Papers I.P.C.R., 74. 27 (1979).
2) Y. Sakamoto: Jpn. J. Appl. Phys., 16, 1015 (1977).

IV-19. Production of Highly Charged Ions in a Hexapole-Mirror Magnetic Field

S. Ishii, Y. Sakamoto, and M. Yanokura

High temperature plasmas are important in studying not only plasma physics but also production of highly charged ions. We have developed an efficient method of producing dense plasmas by launching microwaves as whistler waves in a simple-mirror magnetic field.[1),2)] These plasmas are, however, not stable and the electron temperature is too low to produce a sufficient amount of highly charged ions.

In order to obtain hot plasmas we are improving the already-installed mirror device by adopting a hexapole coil and a high-speed pumping assembly. The schematic view of the device is shown in Fig. 1. It consists of a pair of solenoidal coils, a hexapole coil, and an ultra-high vacuum chamber. The solenoidal coils are separated 1.2 m from each other and provide a longitudinal field of 0.33 T at the mirror points (z = ± 600 mm). The mirror ratio is then about 5. The hexapole coil, composed of straight conductors, is placed at r = 110 mm, parallel to the magnetic axis and provides a radial field of 0.09 T at r = 60 mm in the mid-plane (z = 0). The vacuum chamber, 106 mm in diameter and, 1 m in length, is pumped through ten manifolds. An effective pumping speed of 400 ℓ/s can be achieved.

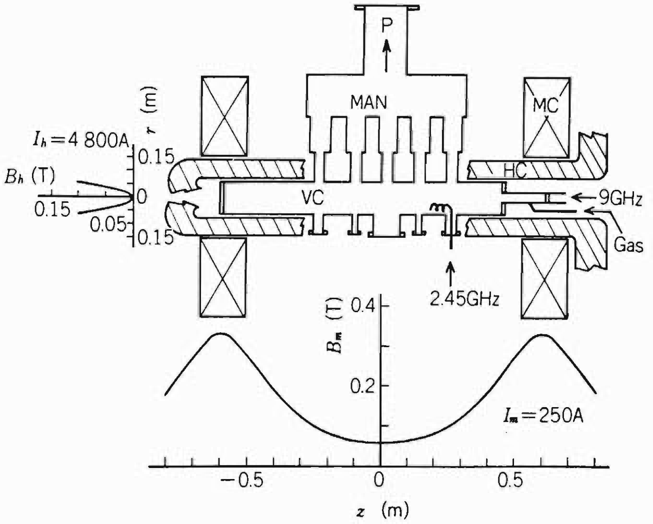

Fig. 1. Schematic view of the hot plasma device. Abbreviations: P, pump; MAN, manifolds; MC, mirror coils; HC, hexapole coil; VC, vacuum chamber.
Spatial variations of the mirror and hexapole magnetic fields, B_m and B_n, are shown together. The hexapole coil is composed of sixfold wound copper pipes.

Cold plasmas are produced by electron cyclotron resonance (ECR) discharge of 9 GHz whistler wave at one of the mirror points (z = 0.6 m). This frequency corresponds to an ECR field of 0.32 T. The effective microwave power of 1 kW can be stationarily delivered. A plasma density of as large as 10^{19} m^{-3} has ever been attained.[1)] The plasmas trapped in the combined field of mirror and hexapole are heated additionally by ECR of 2.45 GHz microwave which is launched as a whistler wave. For this wave the combined field forms a closed ECR surface on which the field intensity is 0.0875 T. The size of this surface can be varied by only changing the coil currents. The typical length and diameter are 400 mm and 40 mm, respectively. By experience a plasma density of 10^{18} m^{-3} is expected in safe stationary operation; the plasmas flow along the magnetic lines of force with a mean ion velocity of 10^3 m/s; the average plasma diameter is about 30 mm. From these parameters we can estimate a plasma flow rate of 3 Pa·ℓ/s which should balance the gas inlet rate. The vacuum chamber would be maintained at a gas pressure of 7×10^{-3} Pa with the pumping speed of 400 ℓ/s. Charge exchange cross-section of, say, Ar^{6+} in argon gas[3)] is in the order of 10^{-18} m^2. Then the mean free path of Ar^{6+} is estimated to be about 10 m. Since this value is large enough compared with the size of the device, confinement of highly charged ions can be expected.

To find optimum conditions for producing the highly charged ions we will measure the plasma parameters, changing the microwave powers, the ECR zone, the gas pressure and so on. Extraction of ion beams will follow achievement of the optimum conditions.

References

1) S. Ishii: Sci. Papers I.P.C.R., 74, 27 (1980).
2) S. Ishii: J. Phys. Soc. Jpn., 50, 1383 (1981).
3) T. P. Grezdanov et al.: Phys. Lett., 66A, 191 (1978).

Ⅳ-20. Circuit for Axial Extraction PIG-Source Power Supply and Control

K. Hoshino

The circuit constructed for supply of power to the ion source and its control is shown in Fig. 1. Figure 2 is the arrangement of the ion source electrodes. In Fig. 2, and electron repelling electrode R is added to the previously described design.[1)]

Electrons are accelerated toward electrode E4 by a potential difference of 1.96 KV. The potential of the electrodes E2 and E3 are given by the Zener diode group (ZD7 → 23) shown in Fig. 1. The electron current emitted from the filament is controlled by an emission

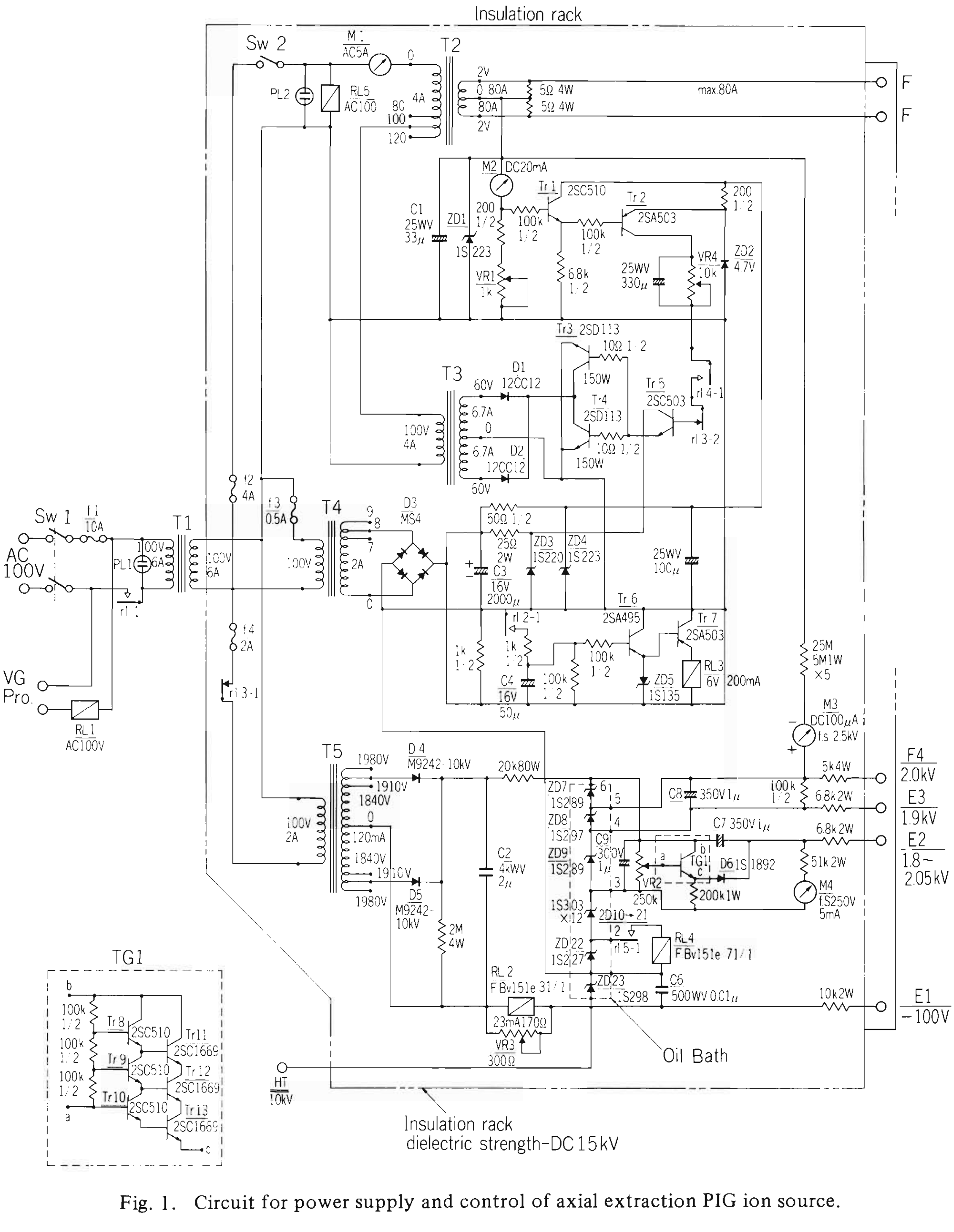

Fig. 1. Circuit for power supply and control of axial extraction PIG ion source.

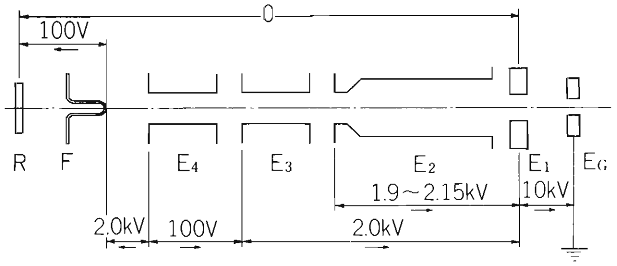

Fig. 2. Potential distribution of electrode of axial extraction PIG ion source.

regulator circuit to which power is supplied by the transformers T2 and T3. VR 1 is a variable resistor to adjust the electron current between 3 mA and 20 mA. VR 4 below Tr 2 in the figure is used for setting an upper limit of the filament heating current to protect the filament from the enormous increase of the filament current some times seen in strong magnetic field operations.

The upper part of lower half of the circuit which draws power from the transformer T4 is a circuit to cut off the power to the transformer T5 for several seconds, when an over current flows in the ion source power supply by the discharge in the source. If a large current flows in RL 2 which is connected to E1, RL 3 is activated by the closing of contact r12-1, which makes Tr 6 and Tr 7 conducting. The contact point r13-1 is opend and cut off power supply to the transformer T5. The electrical current flowing through the closed r12-1 passes through a resistor of 1 kΩ and charges up C4. When r12-1 is opend, C4 begins to be discharged. Potential of base of Tr 7 goes down, and the time to reset RL 3 is determined by product of C4 and 100 kΩ and is 6 seconds.

The potential of the electrode E2 is controlled within a certain range of the potential determined by that of the electrode E3. The lowest is below the potential of E3 by 100 V and the highest above E3 by 150 V. This potential is controlled by VR 2. TG 1 in Fig. 1 is described in detail in the lower part of the figute. As the output voltage of TG 1 is 0 ～ 250 V, and the output current is several mA, TG 1 must be able to control relatively large power.

When the ion source is operated under strong magnetic field with large electron current, intense oscillation is generated. Frequency spectrum of the oscillation is very broad. It is easy to prevent the oscillation at very high frequencies, but suppression of the whole oscillation in the ion source, which includes many frequency components is difficult. The most effective way of suppression of the oscillation is insertion of resistors between the ion control circuit and the ion source terminals. Without the resistors, high frequency current is fed back from the ion source to the power supply, and destroys the semiconductors in the control circuit. C7, C8, and C9 are chemical condensers (350 wV 1 μF) to protect the semiconductors from surge current produced by discharge in the ion source. The condenser C1 and Zener diode ZD 1 shown on the upper part in Fig. 1 also protect the meter M2 from surge current caused by discharge. Five current reading meters are installed in a high voltage insulation box made of acrylic resin, and are used to measure the current in each electrode separately.

Reference

1) K. Hoshino: RIKEN Accel. Progr. Rep., 16, 149 (1982).

IV-21. Modification of Axial Extraction PIG Ion Source

K. Hoshino

Construction of the ion source was already described in a previous report.$^{1)}$ Structure of its central part is shown in Fig. 1. Insulating spacers, which constitute part of cooling channels, were made of steatite. Vacuum seal between the spacer and metal part was made by a small O-ring. The sealing between the O-ring and metal was good, but between steatite and the O-ring was not satisfactory. The vacuum sealing contact obtained by pressing the O-ring on the steatite surface was imperfect, because of roughness of the surface of the steatite. It was tried to make good contact by coating the surface of steatite with silicon compound paste and drying before construction. Though the maximum pressure of cooling water was 10 kg/cm^2, sealing by the O-ring separating the vacuum side and the cooling water was found good enough. Probably a similar good vacuum tightness may by obtained by coating the steatite surface with special chemical plating in place of the paste coating and subsequent polishing.

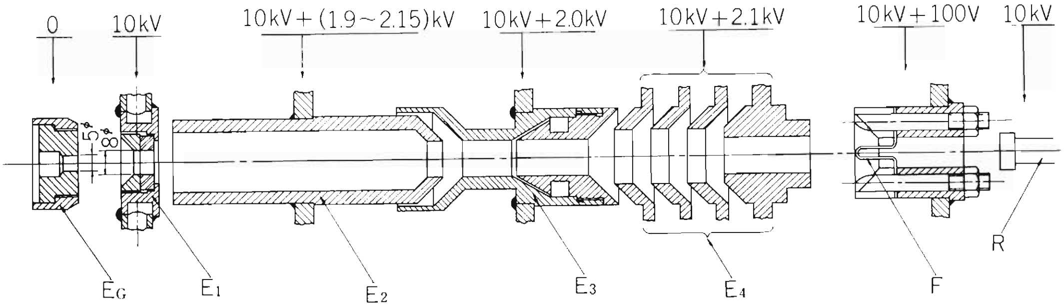

Fig. 1. Schematic diagram of the main part of the reconstructed axial extraction PIG ion source.

Effects of sputtering and evaporation were not considered in the initial design. Films of metal were found formed after operation for a while by the evaporation of the filament material on the surface of the insulators near the filament. Metalic films were also formed on the insulation spacers by sputtering of metal of electrode which forms the extraction aperture. Insulation failure and discharge will be caused as a result of the formation of those films. Shield were, therefore, set around the above mentioned insulators to prevent further film deposition. The distance between the electrodes EG and E1 was chosen as 8 mm in the initial design. Considering the result of the experiments carried out later, the distance was made larger and changed to 14 mm to obtain good focusing by extraction at 10 kV. The result was that the ion beam could be well focused by the extraction voltage of 11 kV. The diameter of the ion extraction aperture in the electrode EG was enlarged to 5 mm and the diameter of the aperture of the electrode E1 to 8 mm.

The electric field, which extracts electrons from the filament, is lowered by space charges in the electron beam of which density is increased by focusing effect of the magnetic field. In order to make its effect smaller, the gap between the filament and the electrode E4 has been made small.

The filament is made of tantalum wire of 1 mm in diameter. The electric resistivity of the tantalum wire is larger, and the heat conductivity is lower than those of tungsten wire, so that the filament wastes less power than the tungsten filament to produce the same electron current. The durability of the tantalum filament has been found sufficient under the condition of use of the ion source controlled by the circuit shown in Fig. 1 shown in another paper.$^{2)}$

In the initial design, ion source chimney formed by E1, E2, E3, and E4 was provided with many gaps for evacuation, as it was considered that the gas pressure in the electrode E2 should not be high. The gap between electrode E2 and E3 was made smaller to increase the gap pressure in the electrode E2.

For the reason of the modification, see the report on operation in this volume.

References

1) K. Hoshino: RIKEN Accel. Progr. Rep., 16, 149 (1982).
2) K. Hoshino: p. 178 in this report.

IV-22. Operation of Axial Extraction PIG Ion Source

K. Hoshino

As the ion current extracted from the ion source is within the range of several tens of micro-amperes to hundreds of micro-amperes, the ion current can be read directly by meters without amplifiers. Because the ion accelerating voltage is about 10 kV and the energies of the secondary electrons produced by collisions of the ions are supposed not large, a simple ion collector is employed. The structure of the ion collector is shown in Fig. 1. Current lead to the collector is introduced into the vacuum vessel by a glass seal at the position distant from the solenoid surrounding the ion source. The ion collector is hung at the end of the lead wire. This method has an advantage of the simple structure, as only one wire is used for measurement of the ion current. But it is impossible to know the effect of the magnet for suppression of the secondary electron emission.

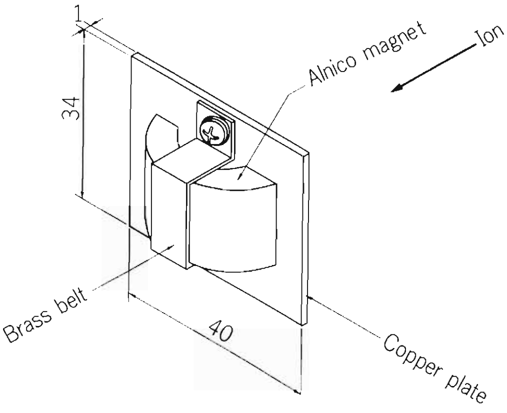

Fig. 1. Ion collector.

The axial extraction type ion source is considered as an ideal one for its small emittance beams. But in practice, the produced ion current is small compared to the electron current for ionization.

An unexpected phenomenon occured in an experiment to increase the ion current. Ion current grew very large when the potential of the electrode E2 was increased higher by about a hundred volts than the potential of the electrode E3 in relatively weak magnetic field. The electrons emitted from the filament oscillated between the filament and E1. See Fig.1 shown in another paper1) for symbols and potentials of each electrode. It was expected that the ions produced by the electron current in the electrode E3 into which gas is fed would be drawn out by the electrode E2, when the potential of E2 is lower than that of E3, and reach the extraction aperture at the electrode E1. If the potential difference is reversed, the ions produced in the high pressure region within E3 would not be extracted. But contrary to the expectation, a large quantity of the ions was obtained by reversing the potential difference. When the magnetic field is increased, the ion current became smaller than that in the weak magnetic field.

The currents of E2 and E3 electrodes were observed during operation of the ion source. When the potential of the electrode E2 was made higher than that of E3, the current to E3 is diminished and that to E2 increased and vice versa. Behavior of current of each electrode was in opposite direction. If the electron current and the potential of the electrode E2 are adjusted to optimize ion current, the current of the electrode E3 decreased rapidly and finally the direction of the current reversed.

Conditions for the reversal of the current of the electrode E3 are as follows: Firstly, the potential of the electrode E2 should be higher than the potential of the electrode E3. Secondly, the ion accelerating voltage should be higher than a certain threshold value, and as the third condition the gas pressure inside of the source should be higher than a certain value. Reversal of the current of E3 means that the electrons are emitted from E3, or the positive ions are captured by E3. The operation of the ion source under the condition, that the potential of the electrode E2 is higher than the potential of the electrode E3, is labeled for the sake of convenience "reverse potential operation" or RPO.

The phenomenon that the ions are produced abundantly by the method of RPO might be explained as follows: The electrons reflected by the electrode E1 impinge on the electrode E2 and E3 directly or indirectly. The electrons which impinge on the electrode E3 produce secondary electrons. The secondary electrons are attracted by the electrode E2, move toward the electrode E1 and produce ions on the path. The secondary electrons produced at the electrode E1 by the impinging ions are accelerated back and bombard the electrode E3 again. The process is cumulative in the RPO. A cylinder of discharge is formed around the central ion beam aixs by the repeated processes. A part of the ions produced in the cylinder is extracted through the extraction aperture increasing ion yield.

The ion current produced by the method of RPO is several times as large as the ion current produced by the normal setting of potentials where the potential of the electrode E2 is lower than that of E3. The gap between E2 and E3 was modified because, by the RPO, the increase of gas pressure in the electrode E2 is effective to obtain larger ion current. The quality of the ion beam must be determined by the mass and charge analysis in future.

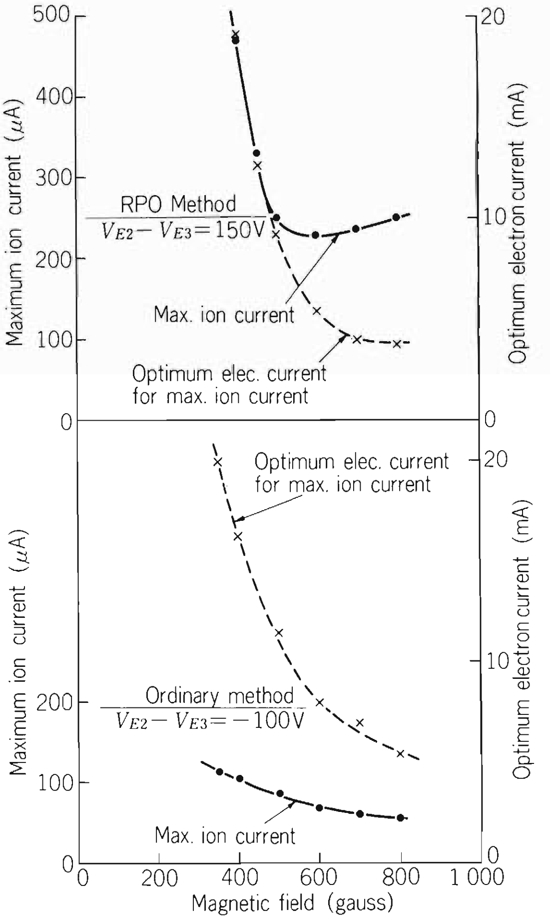

Fig. 2. Ion current produced from Ar vs magnetic field strength.
ion accel. vtg: 11 kV
gas supply rate: 3.9 cc.torr/sec

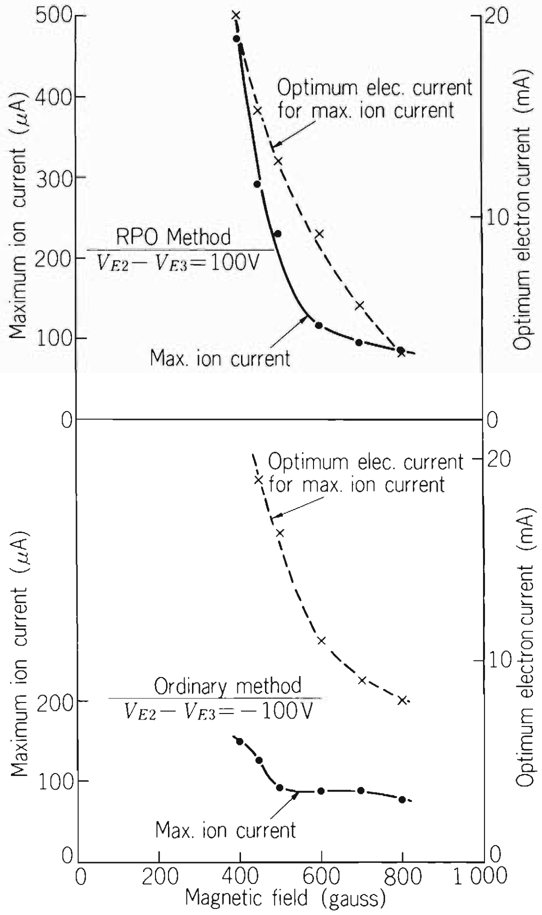

Fig. 3. Ion current produced from nitrogen vs magnetic field strength.
ion accel. vtg: 11 kV
gas supply rate: 8.0 cc. torr/sec

The relations between the ion currents and the strengths of the magnetic field are shown in Fig. 2 and Fig. 3 for the case of Ar and N, respectively. The measurement by the method of RPO is shown in the upper part of each figure, and the measurement with the normal condition in the lower part. The curves show the maximum ion current at the given strength of the magnetic field, and also the optimum electron current for getting the maximum ion current.

Reference

1) K. Hoshino: p.180 in this report.

Ⅳ-23. On a Possible Medium-Beta RFQ Structure II

M. Odera, M. Hemmi, T. Chiba, and E. Ikezawa

We are examining possibility of use of an RFQ linac for medium-beta region of velocity of ions. As a candidate of such RFQ, a structure based on the TM-010 mode of a cylindrical cavity which has been extensively used for the Alvarez linacs is examined.

Satisfactory transit time factor was not obtained for the previously reported open electrode structure.[1)] In that case, a large n = 0 Fourier component in the axial field degraded the transit time factor badly. Therefore, we tried to improve the situation by modifying the electrode configuration. Figure 1 shows a sketch of the electrode array. It is composed of the vertical (a) and horizontal (b) members interlaced as (c). It looks like chain. Therefore, let us call it chain configuration or simply chain. Note that direction of field alternates in the neighboring accelerating gaps and the focusing sections, though the field in TM-010 mode of the cylindrical cavity from which the inter-electrode fields are derived, has the same direction everywhere in the cavity, when it is not loaded by any drift tubes or electrodes. The alternation of the field is expected to decrease the n = 0 Fourier component and to improve the transit time factor. Figure 2 is the result of measurement of the axial field in the chain. Here, cell length corresponding to the phase shift of 2 π of the RF field was chosen to be 48.9 mm. The cell was made to have the same length with that of Ref. 1, in order to facilitate comparison. Accelerating gap is 12.2 mm and bars separating the focusing region from the accelerating gap is 8 mm in thickness. Length of the focusing region between the bars is 20.7 mm. Note that ratio of dimensions was deformed considerably to help understanding of its configuration in Fig. 1. Local maximum in the center of the focusing region suggests weakening of the axial field by increase of the transversal focusing field. Figure 3 gives relative magnitudes of its Fourier components in one period. Though the arrangement is not optimized yet, the DC component is decreased considerably when compared to the previous one, where it was larger by more than 60 % than the amplitude of the component of accelerating frequency.

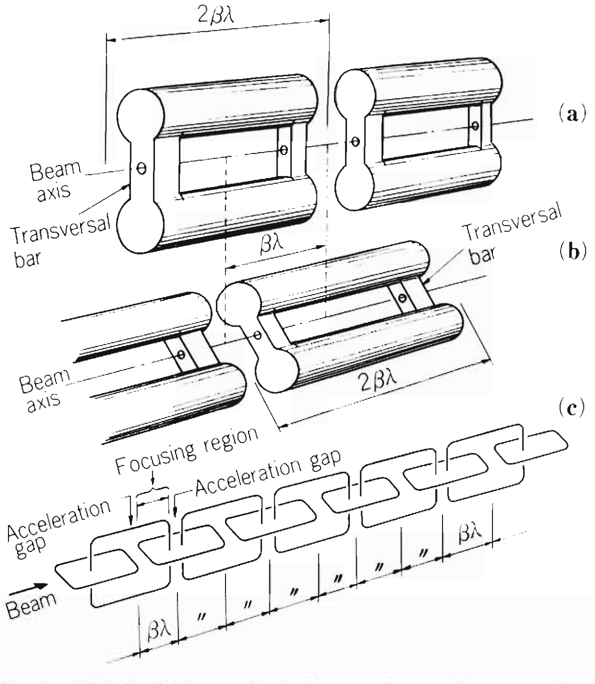

Fig. 1. Chain-like configuration of accelerating electrodes (a) Vertical member electrodes made by connecting two cylindrical bars by two flat bars with beam holes at their center. Distance between the cylindrical bars has been drawn larger than the real proportion of models for convenience of illustration; (b) Horizontal members; (c) Scheme of the chain arrangement made by interlacing (a) and (b). Period between accelerating gaps of the vertical and horizontal electrodes is 2 π or one beta-lambda. Between the gaps there is the region of focusing where radiofrequency quadrupolar field excerts transversal force to the ions. The sign of focusing and defocusing alternates in the next focusing region.

Evaluation of the transit time factors was made by a numerical integration of the measured fields multiplied by a factor of the sinusoidal variation with time. Obtained transit time factors is 90 % for the accelerating gaps and is 63 % for the radiofrequency quadrupolar focusing region. In the normal Alvarez linacs, the region of focusing is enclosed within the drift tubes and no accelerating field exists inside. In the present case, the focusing region has also a π mode-like acceleration effect contributing to energy gain of this structure. In addition, the electric field integrated along the axis at the accelerating gap was found larger than the voltage drop expected by the prescription in which the mean accelerating gradient of the TM-010 mode is multipled with the cell length of 2 π. The method corresponds to the usual procedure of estimation of the gap voltage in the Alvarez linacs. Reason of the larger gap voltage than the ordinary linacs is probably that the distance between the stems supporting the electrodes belonging to the same vertical or horizontal members corresponds to 4 π,

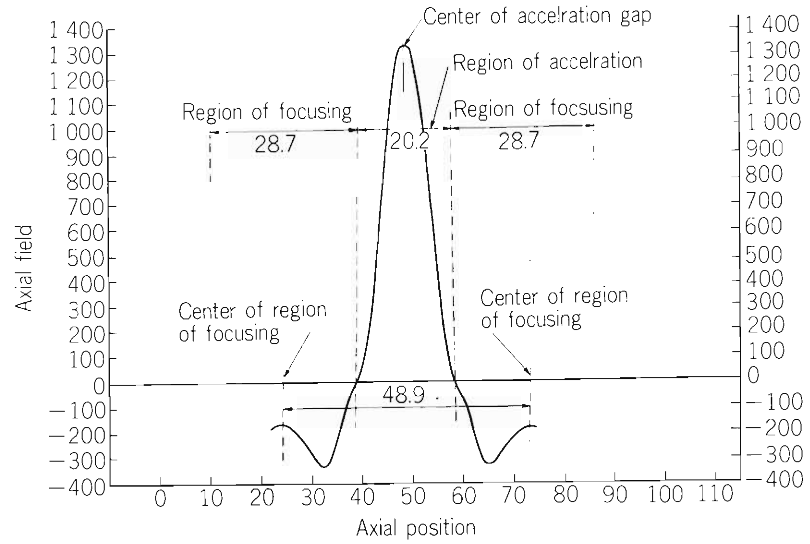

Fig. 2. Measured distribution of axial field by a magnetic analog model. See text for relevant geometrical parameters. Dotted vertical lines show positions of center of the transversal bars. Transit time factors were calculated for accelerating and focusing regions separately between the centers of the bars.

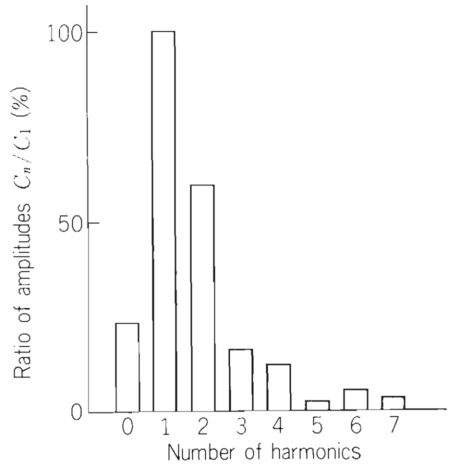

Fig. 3. Amplitude of Fourier components of the axial field distribution shown in Fig. 2.

instead of 2 π in the Alvarez linacs.

When the large effective accelerating voltage in the gaps is added by the additional acceleration effect of the focusing region, there is a possibility for this structure to have an effective shunt impedance larger than those of the Alvarez linacs for the similar velocity region of the accelerated particles. Taking for an example, for field gradient of 1 MV/m for the TM-010 mode of cylindrical cavity, the integrated voltage through the two regions for this structure is 2.6 MV/m which, when multiplied by the transit time factors, results in the effective accelerating voltage gradient of 2 MV/m. That means its effective shunt impedance becomes as high as 4 times of that of the usual Alvarez linacs, if the ohmic loss of the cavity remains constant. Of course, the power loss can not be the same for the structure equipped with electrodes more complicated than the simple drift tubes of the Alvarez. Also the field was obtained by use of the magnetic analog model excited in DC mode and would not perfectly reproduce the radiofrequency field. Re-measurements by a high frequency model are desirable to confirm the obtained results. A reduced scale model is being fabricated for that purpose.

Whether this structure can be a practical linac which has an effective shunt impedance superior to the ordinary linacs or not, must be examined carefully by more detailed study of its electrical and mechanical properties. Especially, beam orbits must be traced numerically by measuring the axial and transversal field distributions in fine steps.

Reference

1) M. Odera, T. Chiba, and M. Hemmi: RIKEN Accel. Progr. Rep., 16, 178 (1982).

Ⅳ-24. A Low-Beta RFQ Structure

M. Odera

Possibility of use of RFQ structures is being studied by us to increase accelerated energies or intensities of ions of heavy elements at the RILAC. One is use of a structure which might be useful in the medium-beta region of velocity of ions.[1] We are also beginning to study a low-beta and low frequency structure as a RILAC injector, which allows acceleration of ions of lower charge states and larger current than those which are being accelerated by the present DC injector. Charge may be increased by stripping before injection into the first cavity of the RILAC.

Its resonant frequency must be equal to or lower than the highest frequency in the frequency range of the main linac in order to make transfer of beam between the RFQ and the main linac with minimum loss. On the other hand, frequencies integer multiple of that of the RILAC can be used for the medium beta RFQ linac mentioned above, which is to be used to boost energy of the RILAC. Operation mode of the RFQs should preferably be continuous to match with that of the main part, though pulse mode is also acceptable if the duty factor is not excessively small.

As such structure, we are planning to try a four-vane type RFQ which has less symmetry with respect to the beam axis than those fabricated to date. Figure 1 shows its cross sections. The reason to choose this configuration is to get relatively low resonant frequencies and to test possibility of frequency tuning. Effect of the asymmetry on separation of the unwanted TE-110 from the wanted TE-210 modes will also be studied. Finally, complete suppression of the TE-110 will be tried by connecting the two longer stems at the point near the open ends. The shorting point is chosen reasonably distant from the central region, to avoid disturbance in the quadrupolar field. As shown in Fig. 1, only two shorting rings will be used to connect the vanes at the entrance and exit ends of the vane structure. It is planned to fabricate a reduced scale model and study its properties.

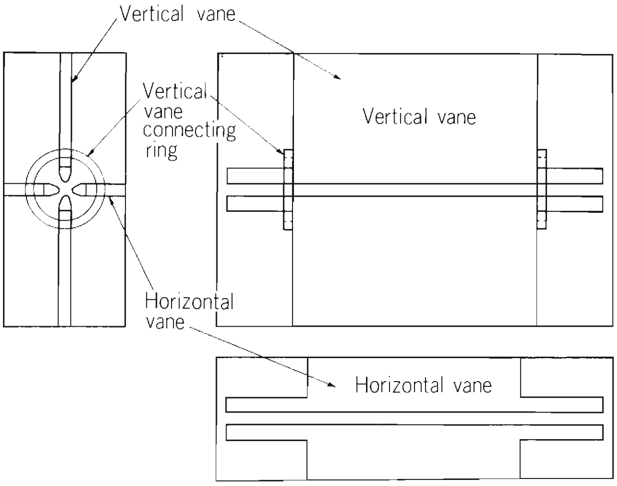

Fig. 1. Cross sections of the planned low frequency RFQ model. The two longer stems may be connected near the open end by metal rings to suppress the unwanted dipole mode.

Reference

1) M. Odera, T. Chiba, and M. Hemmi: RIKEN Accel. Progr. Rep., 16, 178 (1982); M. Odera, M. Hemmi, T. Chiba, and E. Ikezawa: p. 183 in this report.

IV-25. Small Computer System in Operation of the 160 cm Cyclotron

H. Takebe, S. Fujita, and K. Ogiwara

In the 160 cm cyclotron, it is essential to provide the operations staff with fast and easy setting of the operational parameters for any ion species and energy. A small computer was equipped, for this purpose, to the cyclotron control system in July 1983. Using this computer, if we only input the particle name, charge number and the energy, then all the operational parameters are displayed and printed out and all the radio frequency (RF) parameters are set automatically. This system can also stabilize the frequency on line with higher intelligence, monitor the beam current and aquire data of the operation.

Figure 1 shows this small computer control system with the cyclotron. The NEC PC-9801 (CPU; i8086) was purchased at the end of March 1983. We have prepared isolation amplifiers$^{1)}$ to detect the actual positions of the cyclotron moving devices connected to the potentiometer circuits. And we have modified the push button switch units (control units) of the control desk.

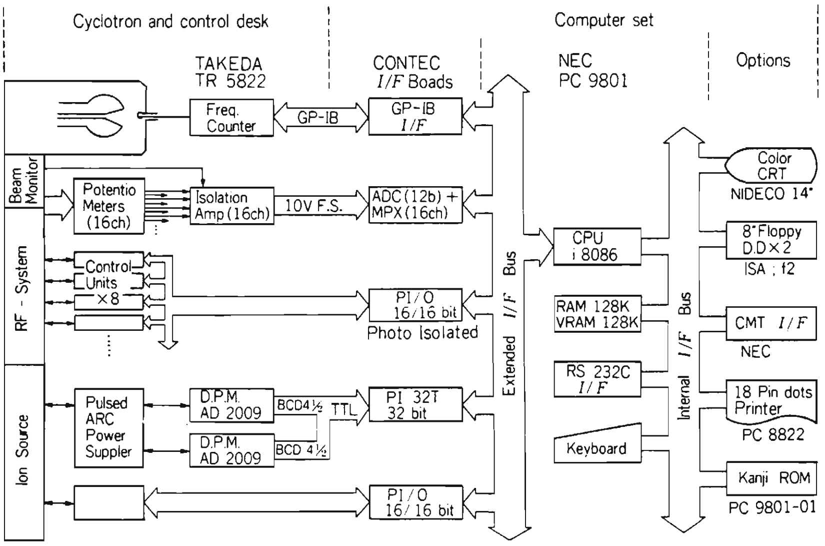

Fig. 1. Block Diagram of the small computer system with the 160 cm cyclotron.

A 14 inch high resolution color graphic display (640 x 400 dots), a dual drive 8-inch floppy disk unit and an 18 pins dot-matrix printer with a 64 kB buffer memory are providing us with faster development of programs. The PC-9801 has a main memory of 128 kB RAM (96 kB is opened for users N88 BASIC program), a 96 kB graphic VRAM, a 32 kB Text VRAM and 32 KB BASIC ROM booter. A frequency counter (Takeda-Riken; TR-5822) measures the cyclotron RF ten times a second and its data output is led to the computer through a GP-IB interface unit. All the external interface boards between cyclotron devices and the CPU are comercial ones. A parallel I/O interface unit (CONTEC Co., Ltd; PI016/16) has photo isolation ICs and driving transisters. We changed those transisters to connect our 48V relay control circuit. Following hardwares of the RF system were changed in order to set the RF parameters using the computer:

(1) Plate capasitor was replaced by a variable vacuum capasitor with motor drive mechanism and its position is detected using a potentiometer.

(2) A heliostat type potentiometer was equipped to the driving system of the shorting plate, instead of a self-synchro meter.

(3) Not only an interlock of the air valve power switch for a contact finger of the shorting plate but also a pressure detection switch of the contact finger were led to an interlock condition of the shorting plate driving system.

Main programs are written in N88-BASIC and some subroutines for I/O control and some graphic commands are written in assembler language. An assembled monitor code is called from the BASIC main program. We basically developed five programs for the cyclotron operation as follows:

i) CYCLO
ii) RF-SET
iii) F-STABILIZE
iv) BEAM-MON
v) LOG.

When we start up the cyclotron, we use the program "CYCLO" and the computer shows us a number of parameters on the CRT display and printed out on paper. Figure 2 shows a flow chart of this program as an example. Seven parameters for the RF system (see Fig. 2) are calculated from the given frequency (F_p) as preset values. Next, the computer sends a signal to turn off the air valve of shorting plate finger and sends a signal to set the above seven parameters through control units until each measured position becomes equal to the preset values within 1 % accuracy. All the parameter calculations were done using first- to sixth-order polynomial equations. Before these programming, we derived the coefficients of those polynomials from the newest data of cyclotron operation using a least squares fitting method.

The program "RF-SET" is used only for the RF parameter setting and has the same function as the latter half of the "CYCLO", independently.

The program "F-STABILIZE" is used for stabilizing the cyclotron radio frequency, more stably than the digital comparating circuit[2)] does, which was used before. The frequency counter sends a frequency datum (F) to the computer 5 to 10 times per second. If the datum is of reasonable value ($6 < F < 12$ MHz, $|F - F_p| < M \times 50$ kHz, etc.), the datum is registered in a F_n data, where n means a data number and M is determined by the particle and a mode of the ion source operation. The averaged frequency data F_a of the past four data is defined by the following equation;

$$F_a = (F_n + F_{n-1} + F_{n-2} + F_{n-3}) / 4.$$

If the F_a exceeds some limitation values, the computer determines a pulse width of the moving command from this value and judges whether it has to send to command to move the upper, lower or both earth plates or not to do. Thus, unnecessary movements of the above frequency compensating devices must be decreased. These procedures also can be done to the dee voltage.

The program "BEAM-MONITOR" is used by all night experimental staff to monitor the beam intensity, dee voltage etc. with a buzzer.

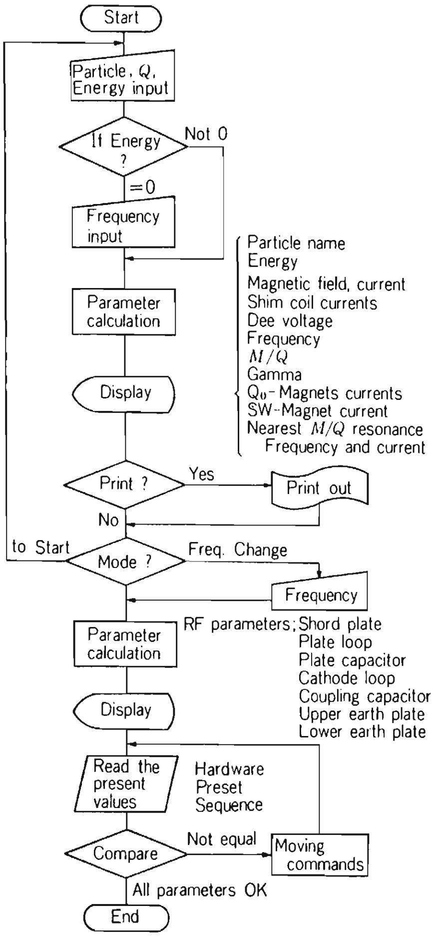

Fig. 2. Flow chart of the program "CYCLO" to calculate the operational parameters for any ion species and energy and automatic setting of the RF parameters.

These programs manage to print out the frequency, dee voltage, and beam currents data in a certain interval of time and show a histogram plot of the above data of past three to sixty minutes on a colour graphic display.

The program "LOG" is to record the cyclotron parameters on a floppy disk.

The interpreter language, BASIC on the 16 bit CPU, is not fast for processing for the on line control program, but good enough to control the mechanical driving system in our cyclotron. Moreover, development of programs using the BASIC interpreter is quite faster than other compiler languages.

References

1) Isolation Amp. (LH0036C) with variable gain and adjustable offset, made by Riken Machine Shop, (M. Fuse and K. Nishi).

2) H. Takebe, K. Ogiwara, and Y. Yamada: IPCR Cyclotron Progr. Rep., 14, 6 (1980).

IV-26. Present Status of the Baby Cyclotron at the Nakano Hospital

T. Karasawa

During this year, the cyclotron has been working satisfactorily for the production of radio-isotopes used in diagnosis and in experiments of labelled compound synthesis. The beam currents at the target box were 15 μA and 10 μA for protons and deuterons, respectively. Change of accelerating particle from proton to deuteron has been simplified. The ion source position with respect to puller is adjusted without change of magnetic field distribution near the center, while the magnetic field distribution was changed previously by narrowing the gap between center plugs at the deuteron acceleration.

When V_0 is half of peak-to-peak dee voltage, energy gain per turn for deuterons and protons are $4V_0\cos\theta$ and $2\sqrt{2}V_0\cos\theta$, respectively. Functional relation between $\sin\theta$ and radius is termed phase history and we can determine $\sin\theta$ by beam fall off radius measured on beam probe. The equation for $\sin\theta$ was reported in the previous report.[1)] The phase histories for deuterons and protons under the present operating condition are shown in Fig. 1 and Fig. 2, respectively.

The ^{15}O labelled molecular oxygen and carbon dioxide were easily produced by deuteron irradiation and used for diagnosis of lung functions, routinely.

A ^{11}C-1-glucose and mannose mixture was synthesized in automatic apparatus from ^{11}C-HCN, which is produced by an in-target recoil method using proton bombardment of mixtures of nitrogen and hydrogen gases. After intravenous injection of the solution of the glucose and mannose to tumor-bearing rabbits, the tumor was specifically visualized on a gamma camera by a computer image processing. It is hoped that ^{11}C-1-glucose-mannose mixture can serve as a valuable radiopharmaceutical for cancer diagnosis in humans.

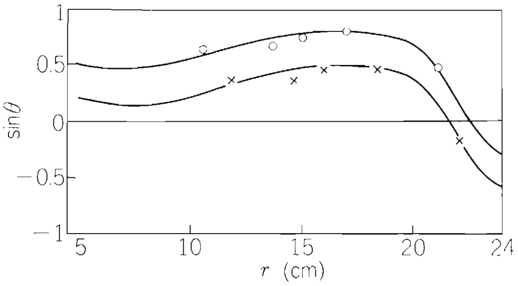

Fig. 1. Phase history of deuterons.

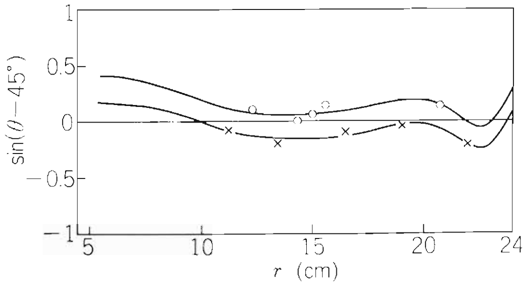

Fig. 2. Phase history of protons.

Reference

1) T. Karasawa: IPCR Cyclotron Progr. Rep., 12, 27 (1978).

V. RADIATION MONITORING

1. Radiation Monitoring Station

M. Okano, M. Nishida, S. Fujita, and H. Kamitsubo

Measurement of Gamma-rays has been continued at the monitoring station located at about 85 m SSE from the cyclotron by using a scintillation detector with a specially designed shield for energy compensation.[1] A monitoring system of the same kind was used as for linac monitoring posts.

The observed results of monitoring during the period from Jan. 1982 to Oct. 1983 are shown in the figure where the radiation level is given in the unit of μR/h. The values include the contribution of soil radioactivity, but the contributions from cosmic rays and detector contamination were subtracted.

In Fig. 1 each bar represents the range of daily variation of the dose rate and dots represent mean values over 24 h. Higher dose rates observed from time to time are due to radon daughters falling down with rain or snow.

No significant leakage radiations from the cyclotron were detected during this period as was always the case since 1975. Contribution of radioactive fallout due to nuclear explosions, which had been observed several times since the station was set up in 1966, had disappeared.

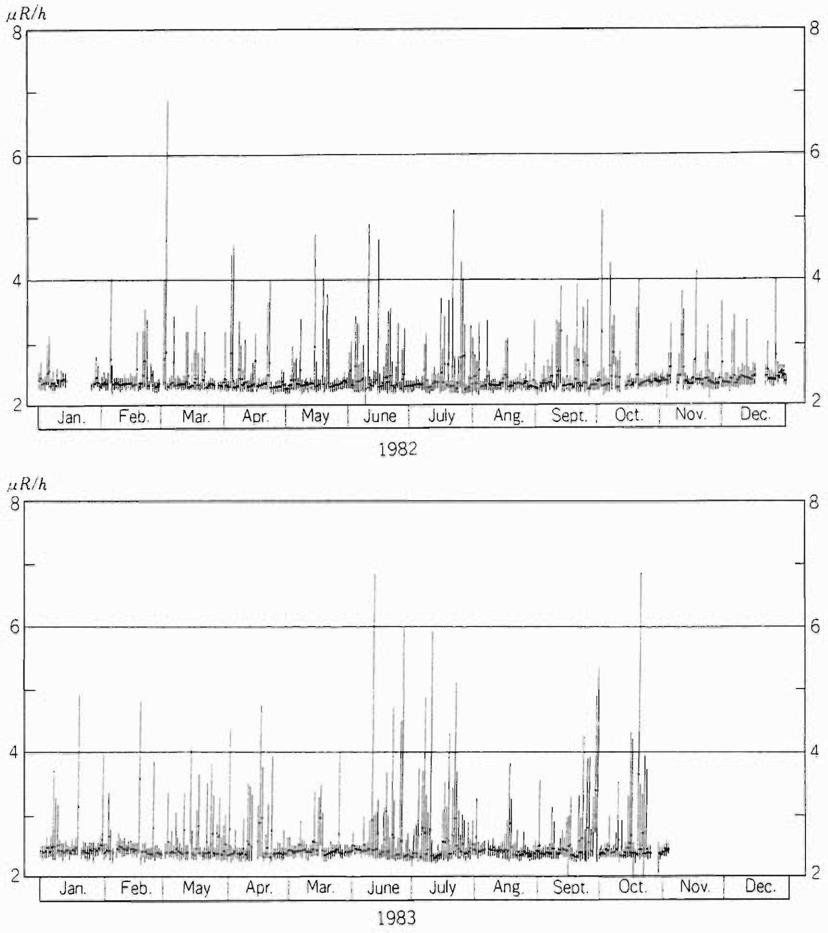

Fig. 1. Record of radiation monitoring at the station 85 m SSE from the cyclotron.

Reference

1) T. Hamada, M. Okano, and M. Ota: IPCR Cyclotron Progr. Rep., 1, 81 (1967).

V-2. Neutron Skyshine from the Cyclotron

T. Nakamura,* A. Hara,* T. Ohkubo,* T. Kosako,* S. Iwai,*
M. Okano, S. Fujita, H. Kamitsubo, I. Kohno, and T. Shikata

Neutron leakage through the cyclotron building into the atmosphere was measured when the cyclotron was operating on 20 MeV deuteron beam acceleration and the beam was bombarding a 4 mm thick beryllium target in a large experimental room, in order to investigate the neutron skyshine effect.

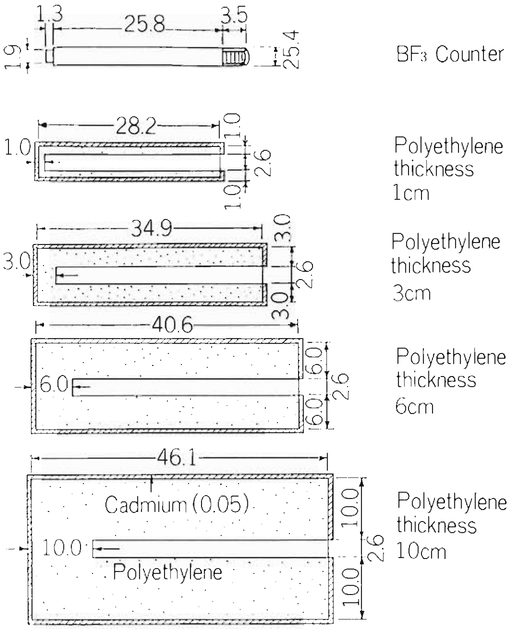

Fig. 1. Cross-sectional view of INS Multi-Moderated Neutron Spectrometer. Dimensions are given in units of cm.

A commercially-available neutron rem counter, Studsvik 2202D, and the multi-moderator neutron spectrometer developed by the Institute for Nuclear Study (INS)$^{1)}$ were used for this measurement. Figure 1 shows the cross-sectional view of INS multi-moderator neutron spectrometer. The distribution of leakage neutrons from the cyclotron building was measured on the roof of the building. The height of the building was 7.7 m. The detector were placed 118 cm above the upper surface of the building roof and moved horizontally for neutron dose mapping. The measurement was carried out twice on August 2 and December 28, 1982. Figure 2 shows the detection points on the roof and Table 1 gives the results of dose mapping. The former measurement was carried out under the average deuteron beam current of 7 μA and the latter under that of 16 μA. In Table 1, the former results normalized to the latter results are also shown. Two separate measurements show very good agreement after the normalization. From Table 1, a strong neutron leakage can be clearly seen at Positions N, S, K, especially at N, in Fig. 2, where the dose was stronger than 10^2 times the dose at Position A which is just above the target. These positions are above the air ducts which go through the concrete

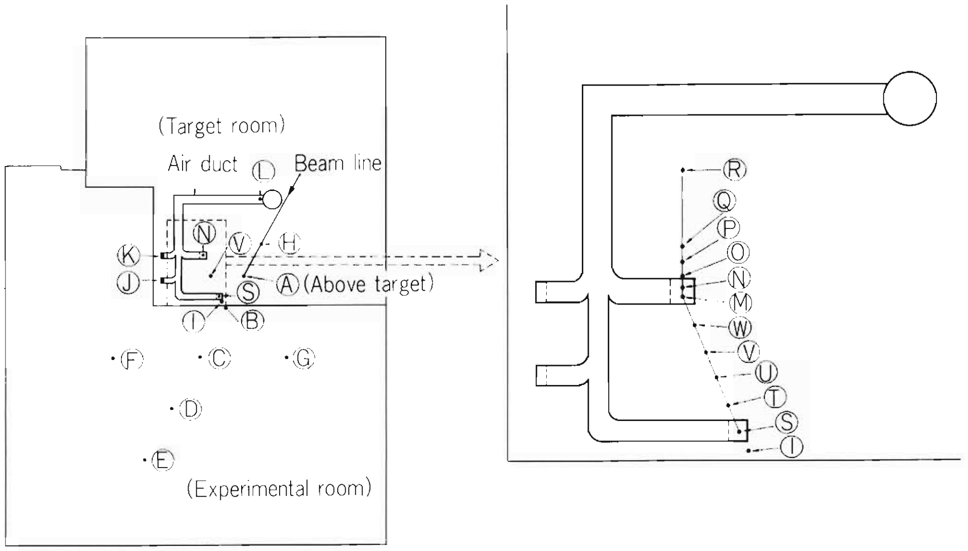

Fig. 2. Detection points on the roof of the cyclotron building.

* Institute for Nuclear Study, University of Tokyo.

Table 1. Neutron dose mapping data 118 cm above the roof of the cyclotron building with the Rem Counter, Studsvik 2202D.

Position[a]	Dose (mrem/h)			Position[a]	Dose (mrem/h)		
	8/2		12/28		8/2		12/28
	7 μA[b]	16 μA[c]	16 μA[b]		7 μA[b]	16 μA[c]	16 μA[b]
A	0.14	0.31	0.31	M	–	–	43.8
B	0.043	0.097	–	N	23.2	53.0	52.5
C	0.013	0.029	–	O	–	–	49.9
D	0.0067	0.015	–	P	–	–	33.0
E	0.0066	0.015	–	Q	–	–	10.7
F	0.0095	0.022	–	R	–	–	1.19
G	0.0085	0.019	–	S	3.75	8.58	7.25
H	0.071	0.16	–	T	–	–	1.45
I	0.82	1.89	–	U	–	–	1.93
J	0.20	0.46	–	V	1.80	4.11	4.28
K	0.95	2.17	–	W	–	–	7.14
L	0.048	0.11	–	X	–	–	0.79

a) Position is indicated in Fig. 2. The dose conversion factor is 3.6 cps per mrem/h given in the instruction manual.

b) Deuteron beam intensity.

The column under c) stands for the numerical values normalized the dose rates measured under the beam current of 7 μA to those for 16 μA.

roof. Detailed mapping was, therefore, done around the air duct as shown in Fig. 2 and Table 1. In parallel with this, rough neutron energy spectra at various points on the roof of the target chamber were measured using the detector described previously.[2] Dose rates and the flux densities of thermal neutrons obtained in this measurement are given in Fig. 3. It can be seen that the areas around the Positions N, S, and K are the main skyshine neutron source from the cyclotron building.

The measurements at Positions N and A and in the field 84 m away from the target in the cyclotron building were performed with INS multi-moderator neutron spectrometer to get the information on the neutron energy spectrum in addition to dose. The neutron spectrum was obtained with the SAND-II unfolding code[3] by using the response function given in Ref. 1. The result is shown in Fig. 4. The dose obtained from the spectrum in Fig. 4 is compared with the dose directly obtained from the rem counter in Table 2. At Position N, the dose by the rem counter is about 30 %

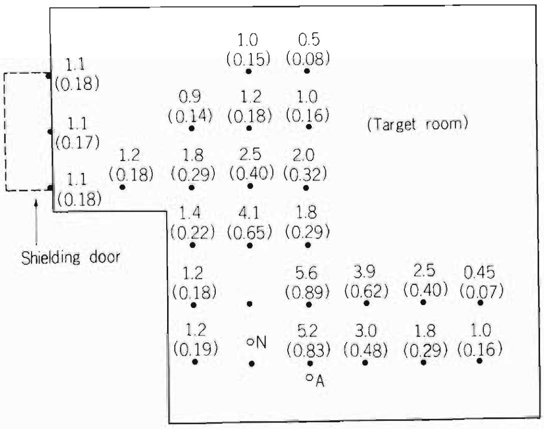

Fig. 3. Detection points on the roof of the target chamber and the flux densities of thermal neutrons (n/cm^2 sec). Estimated dose rate is also given in parentheses (mrem/h).

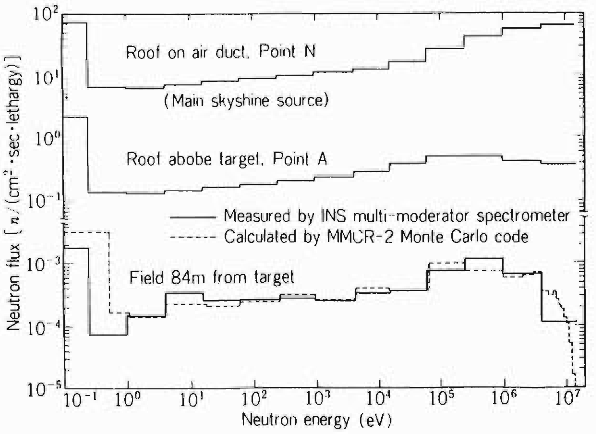

Fig. 4. Neutron-energy spectra of skyshine source and in the environment.

Table 2. Comparison of neutron doses measured by the rem counter and the INS Multi-Moderator Spectrometer.

Position	Dose (mrem/h)		Deuteron beam intensity
	Rem counter Studsvik 2202D	Multi-moderator spectrometer	
N	52.5	38.4	16 μA
A	0.311	0.288	16 μA
84 m in the field	0.352×10^{-3}	0.356×10^{-3}	7 μA
	0.805×10^{-3}	0.814×10^{-3}	16 μA

higher than the dose by the spectrometer, but at Position A and in the field both results show quite good agreement. In Table 2, the dose conversion factor was set to be 3.6 cps per mrem/h given by the maker at Positions A and N on the roof and 4.75 cps per mrem/h in the field point. From Fig. 4, it is seen that the former two spectra are roughly close to 1/E spectra over the whole energy region and the spectrum in the field is about 1/E below 1 MeV and $1/E^2$ above 1 MeV. The number of 4.75 was selected, from the results of our previous paper,$^{4)}$ to be appropriate to the spectrum of $1/E + 1/E^2$, since the sensitivity of the rem counter deviates from the rem response defined in ICRP Publ. 21.

The measured neutron spectrum in the field was analyzed by the MMCR-2 Monte Carlo code developed by Nakamura.$^{5)}$ The source neutron spectrum was set to be the spectrum measured at Position N in Fig. 2, where the major neutron leakage from the cyclotron building occurred. The source neutron flux was 9.6×10^2 n/(cm^2. sec) per 16 μA of deuteron beam. The cross sections for air at a density of 1.293×10^{-3} g/cm^3 consist of 26 energy group constants in a P_8 approximation made from the DLC-2D library.$^{6)}$ The effect of the ground was treated by the albedo Monte Carlo method, and the ordinary concrete albedo data of DLC-57 library$^{7)}$ was used as the albedo data on the ground. The plane mono-directional source which emits neutrons perpendicularly upward was assumed to be placed 7.7 m above the ground. The radius of the plane source r was first put at the size of the air duct, r = 22.6 cm, which is the major skyshine source as shown in Fig. 2, because the distribution of neutron source on the roof given in Table 1 is very complicated. The calculated neutron energy spectrum is compared with the measured neutron spectrum at 84 m away from the source in Fig. 2. The agreement between experimental and calculated spectra is very good. The calculated dose was 0.0456 μrem/h and the ratio to the measured dose of 0.814 μrem/h is 1/17.8. From this ratio, the effective radius of the skyshine neutron source on the roof of the cyclotron building is decided to be 95 cm to get the absolute agreement between measured and calculated neutron spectra and doses.

References

1) T. Kosako, T. Nakamura, S. Iwai, S. Katsuki, and M. Kamata: INS-TS-23, Institute for Nuclear Study, University of Tokyo, (in Japanese), Aug. (1973).
2) T. Hamada, M. Okano, K. Izumo, T. Katou, H. Kumagai, and M. Nishida: Kankyo Hoshano Chosa Kenkyu Seika Ronbun Shorokushu, 22, 147 (1979); ibid., 23, 155 (1980).
3) W. N. McElroy, S. Berg, T. Crockett, and R. G. Hawkins: AFWL-TR-67-41, Vols. I-IV, Air Force Weapons Laboratory (1967).
4) T. Kosako, T. Nakamura, T. Michikawa, K. Katoh, M. Nakazawa, T. Tsujimoto, I. Kimura, and A. Sekiguchi: J. At. Energy Soc. Japan, (in Japanese), 24, 139 (1982).
5) T. Nakamura and T. Kosako: Nucl. Sci. Eng., 77, 168 (1981).
6) RSIC Data Library Collection, DLC-2D, Radiation Shielding Information Center, Oak Ridge National Laboratory (1975).
7) G. L. Simmons: SAI/EPRI Albedo Information Library, EPRI NP-1017, Electric Power Research Institute (1979).

V-3. Routine Monitoring of the Cyclotron

M. Koyama, K. Igarashi, I. Usuba, S. Fujita, and I. Sakamoto

Results of routine radiation monitoring carried out on the cyclotron from April 1982 to March 1983 are described.

No remarkable change in residual activities was observed during this period. Some aspects of the leakage radiation are described in the following report.

(1) Surface and air contamination

The surface contamination has been kept below 10^{-5} μCi/cm^2 on the floor of hot laboratory, and below 10^{-6} μCi/cm^2 in the cyclotron room, experimental areas, underground passage and chemical laboratories. The radioactive nuclides found by the γ-ray spectrometry were ^{65}Zn, ^{185}Os and ^{137}Cs. The contamination was wiped off twice a year, and immediately after this decontamination, the contamination on the floor of the above places had been reduced to a value below 10^{-7} μCi/cm^2.

When the accelerating chamber was opened, slight contamination of the air in the cyclotron room was observed. The value of radioactivity concentration (beta-gamma) was 10^{-12} μCi/cm^3.

(2) Drainage

The radioactivity concentration of the drain water from the cyclotron building was found to be of the order of $10^{-6} - 10^{-7}$ μCi/cm^3. The total quantity of activities in the aqueous effluents in this period was about 17 μCi, and the radioactive nuclides found by the γ-ray spectrometry were mainly ^{147}Gd, ^{60}Co and ^{137}Cs.

(3) Personnel monitoring

The external exposure dose to personnel was measured with γ-ray and neutron film badges. The dose received during the present period by all the cyclotron workers is shown in Table 1. The collective γ-ray dose to all workers was 960 man-mrem, while the collective dose owing to thermal and fast neutron exposures were too small to be detected. The collective dose to the cyclotron workers is about 92 % of the value in the preceding period.

In this period the average annual dose per person was 10.8 mrem, and the maximum individual annual dose was 140 mrem.

Table 1. Annual exposure dose received by the cyclotron workers from April 1982 to March 1983.

Workers	Number of persons			Total	Collective dose (man-mrem)
	Dose undetectable	10 – 100 (mrem)	> 100 (mrem)		
Operators	2	6		8	240
Nuclear physicists	8	1		9	40
Accelerator physicists	15	9		24	140
Physicists in other fields	20	3		23	70
Nuclear chemists	1	5	1	7	460
Radiation chemists	3			3	
Biological chemists	9	1		10	10
Health physicists	5			5	
Total	63	25	1	89	960

Average annual dose per person: 10.8 mrem
Maximum individual annual dose: 140 mrem

V-4. Leakage-Radiation Measurement at the Underground Passage of the Cyclotron Building

I. Sakamoto and S. Fujita

Leakage radiation during operation of the cyclotron at the underground passage of the cyclotron building was measured. Leakage dose received from April 1982 to March 1983 by γ-ray and neutron film badges which were left at the underground passage, are shown in Table 1.

In this period, the machine time allotted for deuteron acceleration was 24 h in August and 52 h in December. Fast neutrons were generated in the beam course No.2 by bombarding a thick beryllium target with 20 MeV deuterons. The beam current was 10~15 μA.

As to the dose values at point No.1 measured every months, the maximum total dose was observed in December. In this case, the values of gamma dose and thermal neutron dose were 15000 mrem and 4340 mrem, respectively. The fast neutron dose could not be measured because the gamma dose was too large.

The radiation levels outside the cyclotron building due to neutrons from the cyclotron were measured in August.[1)]

Table 1. Leakage radiation dose (in mrem) at the underground passage of the cyclotron building from April 1982 to March 1983.

Point of observation * / Radiation	1				2
	August	December	Other months	Total	
γ-rays (mrem)	2170	15000	1270	18440	120
Thermal neutrons (mrem)	590	4340	380	5310	90
Fast neutrons (mrem)	0	undetectable	10	10	0
Total (mrem)	2760	19340	1660	23760	210

* See the figure shown below.

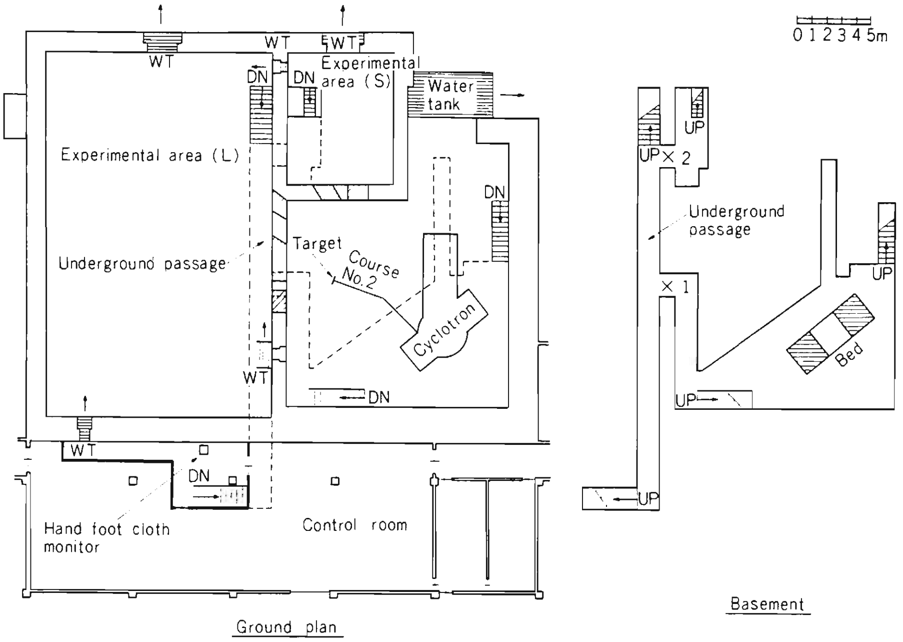

Ground plan

Basement

Reference

1) T. Shikata, S. Fujita, I. Kohno, H. Kamitsubo, M. Okano, T. Nakamura, T. Kosako, A. Hara, and S. Iwai: RIKEN Accel. Progr. Rep., 16, 239 (1982).

VI. LIST OF PUBLICATIONS

1. Accelerator development and accelerator physics
    1) S. Motonaga, H. Takebe, A. Goto, T. Wada, J. Fujita, N. Nakanishi, Y. Yano, N. Kishida, I. Yokoyama, I. Takeshita, H. Kamitsubo, J. Abe, T. Tsukumo, H. Saito, and T. Sato: "Sector Magnets for the RIKEN SSC", Sci. Papers I.P.C.R., 77, 8 (1983).
    2) A. Goto, H. Takebe, S. Motonaga, Y. Yano, N. Nakanishi, and T. Wada: "Trim Coil Field Measurement and Trim Coil Power Supply Specifications for the RIKEN SSC", Sci. Papers I.P.C.R., 77, 54 (1983).
    3) N. Kishida, Y. Yano, and A. Goto: "Beam Extraction System for the RIKEN SSC (I)", Sci. Papers I.P.C.R., 77, 63 (1983).
    4) T. Inamura, N. Kishida, Y. Hata, and H. Kamitsubo: "The RIKEN SSC Beam Handling System (II)", Sci. Papers I.P.C.R., 77,96 (1983).
    5) M. Hemmi, Y. Miyazawa, T. Inoue, and M. Odera: "Design, Fabrication and Performance of the Dipole and Quadrupole Magnets for the RIKEN Heavy-Ion Linear Accelerator", Reports I.P.C.R., (in Japanese), 59, 79 (1983).
    6) M. Odera: "Status of Operation of RIKEN Heavy-Ion Linac, RILAC", J. At. Energy Soc. Japan, 25, 769 (1983).
    7) M. Kase, T. Kambara, A. Goto, Y. Yano, and M. Odera: "Beam Characteristics of the RIKEN Heavy-Ion Linac, RILAC", J. At. Energy Soc. Accelerator Tech., (in Japanese), p. 101 (1983).

2. Nuclear physics and nuclear instrumentation
    1) M. Ishihara: "Direct Reaction with Heavy Ions", Nucl. Phys., A400, 153C (1983).
    2) Y. Itoh, Y. Gono, T. Kubo, M. Sugawara, and T. Nomura: "Excited States in ^{216}Ra", Nucl. Phys., A410, 156 (1983).
    3) T. Fukuda, M. Ishihara, M. Tanaka, H. Ogata, I. Miura, M. Inoue, T. Shimoda, K. Katori, and S. Nakayama: "Correlation between Alpha-Particles and Ejectiles in the 208 MeV ^{14}N on ^{93}Nb Reaction at Three Different Ejectile Angles", Phys. Rev. C, 27, 2029 (1983).
    4) H. Utsunomiya, S. Kubono, M. H. Tanaka, M. Sugitani, K. Morita, T. Nomura, and Y. Hamajima: "Breakup-Fusion of ^{7}Li", Phys. Rev. C, 28, 1975 (1983).
    5) T. Fujisawa: "Analyzing Power-Polarization Inequality in the Inelastic Scattering of Protons on ^{12}C for Incident Energies from 22.0 to 29.0 MeV", Sci. Papers I. P. C. R., 77, 113 (1983).
    6) M. Tohyama and S. Yamaji: "Effects of Two Particle-Two Hole Excitations on the Mass Distribution in Ion-Ion Collisions", Phys. Lett., 123B, 16 (1983).
    7) S. Yamaji and A. Iwamoto: "Friction Coefficients for Deep Inelastic Heavy-Ion Collisions", Z. Phys. A-Atoms and Nuclei, 313, 161 (1983).
    8) M. Ohshima, E. Minehara, M. Ishii, T. Inamura, and A. Hashizume: "Multiple Coulomb Excitation of ^{167}Er", J. Phys. Soc. Japan, 52, 2959 (1983).
    9) T. Inamura: "Spring in Crimea", Butsuri, (in Japanese), 38, 763 (1983).

3. Atomic and solid-state physics
    1) K. Maeda, Y. Sasa, S. Nakamura, and M. Uda: "Particle Induced X-Ray Emission (PIXE) Analysis using RIKEN Heavy Ion Linac", Reports I.P.C.R., (in Japanese), 58, 117 (1982).
    2) J. Mizuno, T. Ishihara, and T. Watanabe: "Energy Exchange between Two Outgoing Electrons in the Post Collision Interaction Processes", Atomic Collision Res. in Japan-Prog. Rep., No. 9, p. 2 (1983).
    3) H. Suzuki, N. Toshima, T. Watanabe: "Exponential Distorted Wave Approximation in Charge Transfer", Atomic Collision Res. in Japan-Prog. Rep., No. 9, p. 33 (1983).
    4) K. Fujiwara, N. Toshima, and T. Watanabe: "Close Coupling Calculation of Electron Capture at High Energies", Atomic Collision Res. in Japan-Prog. Rep., No. 9, p. 36 (1983).
    5) S. Karashima and T. Watanabe: "Stripping Cross Section of Multi-Charged Ions by Neutral Atoms", Atomic Collision Res. in Japan-Prog. Rep., No. 9, p. 39 (1983).
    6) T. Matsuo, J. Urakawa, A. Yagishita, H. Shibata, Y. Awaya, T. Kambara, M. Kase, H. Kumagai, and J. Takahashi: "Ar L-MM Auger Spectra in Ar$^{3,4+}$ Ar Collisions", Atomic Collision Res. in Japan-Prog. Rep., No. 9, p. 83 (1983).
    7) Y. Awaya, T. Kambara, M. Kase, H. Kumagai, H. Shibata, J. Takahashi, J. Urakawa, T. Matsuo, and M. Namiki: "Multiple Inner-Shell Ionization of Argon Ions Impinging on Foils", Atomic Collision Res. in Japan-Prog. Rep., No. 9, p. 86

(1983).

8) J. Takahashi, Y. Awaya, T. Kambra, M. Kase, H. Kumagai, H. Shibata, J. Urakawa, and T. Matsuo: "Angular Distribution of Au L X-Rays by Heavy Ion Impact", Atomic Collision Res. in Japan-Prog. Rep., No.9, p. 89 (1983).

9) T. Kambara, Y. Awaya, M. Kase, A. Hitachi, T. Tonuma, and I. Kohno: "Collisional Quenching of Hydrogen-Like Ne-Ions with Kinetic Energy of 5.5 MeV/amu", Atomic Collision Res. in Japan-Prog. Rep., No. 9, p. 91 (1983).

10) J. Mizuno, T. Ishihara, and T. Watanabe: "Energy Shift of Emitted X-Rays Following Inner Shell Photoionization near Threshold", Atomic Collision Res. in Japan-Prog. Rep., No. 9, p. 136 (1983).

11) K. Fujima, T. Watanabe, and H. Adachi: "The Analysis of Electronic Property of Extremely Condensed Matters by the DV-Xα Method I. Application to Cold and High Density Neon Plasma", Atomic Collision Res. in Japan-Prog. Rep., No. 9, p. 152 (1983).

12) T. Takahashi, Y. Awaya, T. Tonuma, H. Kumagai, K. Izumo, M. Nishida, A. Hitachi, A. Hashizume, S. Uchiyama, and T. Doke: "Stopping Power of Ni, Ag, Au, and Pb for ~ 7 MeV/nucleon α Particles and Carbon Ions. Z_1^3 Deviation from the Bethe Formula", Phys. Rev. A, 27, 1360 (1983).

13) I. Shimamura: "Partial-Sum Rules for and Asymmetry between Rotational Transitions $J \pm \Delta J \leftarrow J$", Phys. Rev. A, 28, 1357 (1983).

14) A. Hitachi, T. Takahashi, N. Funayama, K. Masuda, J. Kikuchi, and T. Doke: "Effect of Ionization Density of Luminescence from Liquid Argon and Xenon", Phys. Rev. B, 27, 5279 (1983).

15) T. Watanabe, T. Ishihara, and J. Mizuno: "Comparison of Threshold Effects in Auger Process Induced by Electron and Photon Impact Ionization", J. Phys. B: At. Mol. Phys., 16, L107 (1983).

16) T. Matsuo, J. Urakawa, A. Yagishita, Y. Awaya, T. Kambara, M. Kase, and H. Kumagai: "Ar L-MM Auger Spectra in Ar^{3+} + Ar Collisions", J. Phys. B: At. Mol. Phys.,16, L239 (1983).

17) K. Nishiyama, K. Nagamine, T. Natsui, S. Nakajima, K. Ishida, Y. Kuno, J. Imazato, H. Nakayama, T. Yamazaki, and E. Yagi: "Critical Phenomena in Nickel Studied with Pulsed μ SR", J. Magn. and Mag. Mater., 31-34, 695 (1983).

18) S. Karashima and T. Watanabe: "Charge Equilibrium of Energetic Heavy Ions in Gaseous Media (Ideal Atomic Hydrogen Gas)", Jpn. J. Appl. Phys., 22, 895 (1983).

19) E. Yagi, T. Kobayashi, S. Nakamura, Y. Fukai, and K. Watanabe: "Lattice Location of Hydrogen in Tantalum as Observed by Channeling Method Using Nuclear Reaction $^1H(^{11}B, \alpha)\alpha\alpha$", J. Phys. Soc. Japan, 52, 3441 (1983).

20) T. Kambara: "Radiative Electron Capture in Heavy Ion-Atom Collisions", Butsuri, 38, 376 (1983).

21) T. Kagawa, T. Kato, T. Watanabe, and S. Karashima: "Atomic Processes in Hot Dense Plasmas", IPPJ-AM-31 Report, Inst. of Plasma Physics, Nagoya Univ. (1983).

22) I. Shimamura: "Electron Collisions with Atoms, Molecules, and Ions. General Review", Basic Researches in Science of Atomic Processes, Published by the Special Research Project Group 'Basic Researches in Science of Atomic Processes', p. 57 (1983).

23) I. Shimamura: "Sum Rules and Partial–Sum Rules for Rotational Transitions of Molecules", Electron-Molecule Collisions and Photoionization Processes, (eds. V. McKoy et al.), Verlag Chemie Intern., Deerfield Beech, Florida, p. 67 (1983).

4. Radiochemistry, radiation chemistry and radiation biology

1) F. Yatagai, T. Takahashi, and S. Kitayama: "W-Reactivation and W-Mutagenesis in Phage φX 174", Adv. Space Res., 3, No. 8, 65 (1983).

2) T. Takahashi, F. Yatagai, and S. Kitayama: "Effect of Heavy Ions on Bacterial Spores", Adv. Space Res., 3, No. 8, 95 (1983).

3) Y. Nagame, M. Watanabe, H. Kudo, K. Sueki, H. Nakahara, and I. Kohno, "Recoil Studies in the Reaction Induced by 115 MeV ^{14}N on ^{62}Ni", Radiochim. Acta, 33, 127 (1983).

4) K. Kimura and J. Hormes: "Roles of the Rydberg Transitions in Fast Excitation Transfer Studied in Cyclohexane and n-Heptane Using Synchrotron Radiation", J. Chem. Phys., 79, 2756 (1983).

5) I. Kaneko: "Current Topics in Potentially Lethal Damage Repair Research", Tissue Culture, 9, 328 (1983).

6) S. Ishii, K. Okazaki, Y. Sakamoto, and K. Yano: "ECR-Discharge Cleaning for Linear Containing Tokamaks", Jpn. J. Appl. Phys., 22, L403 (1983).

7) A. Akanuma, F. Yatagai, K. Igarashi, K. Usuba,

and T. Irifune: "Mouse Skin Reactions to 40 MeV Helium Ion Irradiation", Radiological Medicine (Hoshasenka), 1, 243 (1983).

8) Y. Sakamoto: "ECR Discharge Cleaning of Toroidal Machines", Proc. IX IVC – V ICSS, Invited Papers' Volume (1983, Madrid), p. 716 (1983).

(Papers Presented at Meetings)

1. Accelerator development and accelerator physics
   1) M. Kase, T. Kambara, T. Tonuma, and M. Odera: "Acceleration Test at the RILAC", Symp. on the Next Project of RCNP, Osaka, Jan. (1983).
   2) J. Fujita, T. Kambara, K. Shimizu, T. Wada, Y. Yano, and I. Yokoyama: "Control System for the RIKEN SSC (I)", 6th Symp. on Future Project of RCNP, Osaka, Jan. (1983).
   3) N. Nakanishi: "Beam Dynamics in the RIKEN SSC (1)", 6th Symp. on Future Project of RCNP, Osaka, Jan. (1983).
   4) A. Goto and Y. Yano: "Beam Dynamics in the RIKEN SSC (III)", 6th Symp. on Future Project of RCNP, Osaka, Jan. (1983).
   5) M. Kase, T. Kambara, T. Tonuma, and M. Odera: "Energy Tuning by the Phase Control at the RIKEN Heavy-Ion Linac", 38th Ann. Meeting of the Phys. Soc. Japan, Tokyo, Mar. (1983).
   6) M. Kase, Y. Miyazawa, M. Hemmi, T. Inoue, and T. Chiba: "PIG-Type Heavy-Ion Source for the RILAC", Symp. on Ion Source for Accelerator, Tsukuba, Mar. (1983).
   7) M. Hara, T. Wada, T. Fukasawa, and F. Kikuchi: "Three Dimensional Analysis of RF Electromagnetic Field by Finite Element Method", Particle Accelerator Conf. on Accelerator Engineering and Technology, Santa Fe, U.S.A., Mar. (1983).
   8) M. Hara, T. Wada, T. Fukasawa, and F. Kikuchi: "A Three Dimensional Analysis of RF Electromagnetic Field by the Finite Element Method", COMPUMAG Conf. on Computation of Electromagnetic Fields, Genoa, Italy, May (1983).
   9) M. Kase, T. Kambara, A. Goto, Y. Yano, and M. Odera: "Beam Characteristics of the RIKEN Heavy-Ion Linac", 8th Symp. on Linear Accelerator, Tokyo, July (1983).
   10) F. Kikuchi, M. Hara, and T. Wada: "A Primitive Variable Approach for Finite Element Analysis of Electro-magnetic Waves", JSSC 17th Symp. on Matrix Analysis, Tokyo, July (1983).
   11) A. Goto, M. Kase, Y. Yano, Y. Miyazawa, and M. Odera: "Numerical Orbit Calculation for a Linac and Improvement of Its Transmission Efficiency of a Beam", Computing in Accelerator Design and Operation, Europhys. Conf., Berlin, W. Germany, Sept. (1983).
   12) S. Motonaga, H. Takebe, A. Goto, Y. Yano, T. Wada, and H. Kamitsubo: "Sector Magnet for the RIKEN SSC", 8th Intern. Conf. on Magnet Technology, Grenoble, France, Sept. (1983).
   13) M. Odera: "Operation of RIKEN Variable Frequency Heavy-Ion Linac, RILAC", 2nd Japan-China Joint Symp. on Accel. for Nucl. Sci. and their Applications, Lanzhou, China, Oct. (1983).
   14) T. Wada, J. Fujita, K. Shimizu, I. Yokoyama, and T. Kambara: "Control System of the RIKEN SSC", 2nd Japan-China Joint Symp. on Accel. for Nucl. Sci. and their Applications, Lanzhou, China, Oct. (1983).
   15) M. Hara, T. Wada, T. Nakahara, and F. Kikuchi: "A Three Dimensional Analysis of RF Electromagnetic Field by the Finite Element Method", 2nd Japan-China Joint Symp. on Accel. for Nucl. Sci. and their Applications, Lanzhou, China, Oct. (1983).
   16) N. Nakanishi, A. Goto, and Y. Yano: "Beam Dynamics in the RIKEN SSC", 2nd Japan-China Joint Symp. on Accel. for Nucl. Sci. and their Applications, Lanzhou, China, Oct. (1983).
   17) K. Hayashi, A. Goto, T. Hattori, Y. Oguri, Y. Ozawa, Y. Sato, and E. Arai: "2.5 MeV/u IH Heavy-Ion Linac at TIT – Beam Dynamics", 1983 Fall Meeting of the Phys. Soc. Japan, Kobe, Oct. (1983).

2. Nuclear physics and nuclear instrumentation
   1) E. Minehara, M. Ohshima, S. Kikuchi, T. Inamura, A. Hashizume, and H. Kumahora: "Multiple Coulomb Excitation of ^{163}Dy", 38th Ann. Meeting of the Phys. Soc. Japan, Tokyo, Mar. (1983).
   2) Y. Itoh, Y. Gono, T. Kubo, M. Sugawara, and T. Nomura: "Level Structure of the Ra-Isotopes", 38th Ann. Meeting of the Phys. Soc. Japan, Tokyo, Mar. (1983).
   3) S. Yamaji, A. Iwamoto, K. Harada, and S. Yoshida: "The Effect of the Mass Fragmentation Potential on the Width of the Mass Distribution in the Deep Inelastic Heavy Ion Collision", 38th Ann. Meeting of the Phys. Soc. Japan, Tokyo, Apr. (1983).
   4) T. Inamura: "Fast-Particle Emission in Heavy-

Ion Reactions. Massive Transfer", Intern. School Seminar on Heavy-Ion Physics, Alushta, U.S.S.R., Apr. (1983).

5) T. Inamura, A.C. Kahler, Z.R. Zolnowski, U. Garg, and T.T. Sugihara: "Gamma-Ray Multiplicity Distributions Associated with Massive Transfer", Intern. Conf. on Nuclear Physics, Florence, Italy, Aug. (1983).
6) H. Kudo, T. Nomura, K. Sueki, Y. Gono, and M. Magara: "The Gamma Decay of the 45 sec Isomer in ^{212}Po", 1983 Fall Meeting of the Phys. Soc. Japan, Kobe, Sept. (1983).
7) S. Yamaji and M. Tohyama: "Two-Particle-Two Hole Effects on the Mass Distribution in the ^{16}O + ^{40}Ca Reaction", 1983 Fall Meeting of the Phys. Soc. Japan, Kobe, Oct. (1983).
8) T. Murakami, H. Harada, J. Kasagi, and T. Inamura: "Neutron Multiplicity Filter", 1983 Fall Meeting of the Phys. Soc. Japan, Kobe, Oct. (1983).
9) H. Taketani, M. Adachi, T. Kohno, A. Makishima, T. Suzuki, H. Yamada, S. Fukuda, Y. Gono, and Y. Itoh: "g-Factor Measurements of the Yrast Isomers", 1983 Fall Meeting of the Phys. Soc. Japan, Kobe, Oct. (1983).
10) M. Sugawara, Y. Gono, Y. Itoh, and T. Kubo: "In-Beam Study of ^{215}Fr", 1983 Fall Meeting of the Phys. Soc. Japan, Kobe, Oct. (1983).
11) K. Sueki, M. Magara, Y. Hamajima, H. Nakahara, H. Kudo, and I. Kohno: "Heavy-Ion Reaction in Light-Mass System", 27th Symp. on Radio-Chem., Nagoya, Oct. (1983).
12) K. Sueki, M. Magara, Y. Hamajima, H. Nakahara, H. Kudo, and I. Kohno: "Study on Fission Phenomenon of Heavy-Ion Reaction, Part I", 27th Symp. on Radiochem., Nagoya, Oct. (1983).
13) T. Inamura, A. Hashizume, M. Ohshima, E. Minehara, M. Ishii, S. Kikuchi, and H. Kumahora: "M1 and E2 Transition Probabilities in the Ground-State Rotational Bands of Odd-Mass Nuclei", Intern. Symp. on Electromagnetic Properties of Atomic Nuclei, Tokyo, Nov. (1983).

3. Atomic and solid-state physics

1) J. Takahashi: "The Angular Distribution of X Rays Emitted from Heavy Ion Atom Collisions", 4th Symp. on Atomic Collisions by Using Accelerators, Wako, Feb. (1983).
2) T. Matsuo, J. Urakawa, A. Yagishita, J. Takahashi, T. Kambara, M. Kase, H. Kumagai, and Y. Awaya: "L-MM Auger Electrons in Ar$^{3+,4+}$ + Ar Collisions", 4th Symp. on Atomic Collisions by Using Accelerators, Wako, Feb. (1983).
3) T. Kambara: "Projectile Characteristic X-Rays and Radiative Electron Capture from High Energy Heavy Ion-Atom Collisions", 4th Symp. on the Atomic Collisions by Using Accelerators, Wako, Feb. (1983).
4) S. Karashima and T. Watanabe: "Charge Equilibrium of Multicharged Ions", 4th Symp. on Atomic Collisions by Using Accelerators, Wako, Feb. (1983).
5) K. Hino: "Present Status of the Theory of REC (Radiative Electron Caputre)", 4th Symp. on Atomic Collisions by Using Accelerators, Wako, Feb. (1983).
6) T. Watanabe: "Unitarized and Exponential Distorted Wave Born Approximation-Electrons in Low Z Initial State-Intermediate Velocities", US-Japanese Cooperative Sicnece Seminar on Physics of Highly Ionized Ions Produced in Heavy Ion Collisions, Honolulu, U.S.A., Mar. (1983).
7) T. Kambara, Y. Awaya, M. Kase, H. Kumagai, I. Kohno, T. Tonuma, and A. Hitachi: "Projectile K X Rays in Heavy Ion Atom Collisions(I) – Target Gas Pressure Dependence of K X Rays from 110 MeV Ne Ions", U.S. – Japanese Cooperative Science Seminar on Physics of Highly Ionized Ions Produced in Heavy Ion Collisions, Honolulu, U.S.A., Mar. (1983).
8) Y. Awaya, T. Kambara, M. Kase, H. Kumagai, J. Takahashi, J. Urakawa, T. Matsuo, and M. Namiki: "Projectile K X Rays in Heavy Ion Atom Collisions(II) – High Resolution Measurements of K X Rays from Ar Ions Impinging on Foils", U.S. – Japanese Cooperative Science Seminar on Physics of Highly Ionized Ions Produced in Heavy Ion Collisions, Honolulu, U.S.A., Mar. (1983).
9) M. Uda: "Chemical Effects in X-Rays Satellite Spectra Due to Multiply Ionized States", U.S. – Japanese Cooperative Science Seminar on Physics of Highly Ionized Ions Produced in Heavy Ion Collisions, Honolulu, U.S.A., Mar. (1983).
10) T. Tonuma: "Production of Highly Charged Ions by Heavy-Ion Bombardment of Rare-Gas Targets", U.S. – Japanese Cooperative Science Seminar on Physics of Highly Ionized Ions Produced in Heavy Ion Collisions, Honolulu, U.S.A., Mar. (1983).
11) A. Koyama, T. Shikata, E. Yagi, H. Sakairi, and

M. Uda: "Deviation of Secondary Electron Emission Coefficient from Z_1^2 Proportionality", U.S. – Japanese Cooperative Science Seminar on Physics of Highly Ionized Ions Produced in Heavy Ion Collisions, Honolulu, U.S.A., Mar. (1983).

12) T. Matsuo, J. Urakawa, Y. Awaya, A. Yagishita, T. Kambara, M. Kase, J. Takahashi, and H. Kumagai: "Spectra of Ar L-MM Auger Electrons in Ar^{n+} + Ar Collisions", 38th Ann. Meeting of the Phys. Soc. Japan, Tokyo, Mar. (1983).

13) S. Karashima and T. Watanabe: "Charge Equilibrium of the Fast Heavy Ion in the Medium", 38th Ann. Meeting of the Phys. Soc. Japan, Tokyo, Mar. (1983).

14) N. Toshima and T. Watanabe: "Present Status of the Theories for Extreamly High Energy Region, Symposium on Extreamely High Energy Ion Collisions", 38th Ann. Meeting of the Phys. Soc. Japan, Tokyo, Mar. (1983).

15) K. Fujima and T. Watanabe: "The Electronic State of Higen Dense Ne II", 38th Ann. Meeting of the Phys. Soc. Japan, Tokyo, Mar. (1983).

16) E. Yagi: "Muon Location and Diffusion", 38th Ann. Meeting of the Phys. Soc. Japan, Tokyo, Mar. (1983).

17) E. Yagi, A. Koyama, H. Sakairi, and R. R. Hasiguti: "Lattice Location of Sn Atoms Implanted into Al Crystals", 38th Ann. Meeting of the Phys. Soc. Japan, Tokyo, Mar. (1983).

18) T. Takahashi, Y. Awaya, T. Tonuma, H. Kumagai, K. Izumo, M. Nishida, A. Hashizume, S. Uchiyama, and T. Doke: "The Z_1^3-Dependence of Stopping Power and Effective Charge of 5–7 MeV/amu C and He Ions", 38th Ann. Meeting of the Phys. Soc. Japan, Tokyo, Mar. (1983).

19) T. Kambara: "Experiments of Radiative Electron Capture", 38th Ann. Meeting of the Phys. Soc. Japan, Tokyo, Mar. (1983).

20) T. Kobayashi, E. Yagi, H. Sakairi, and Y. Sasa: "LEC and Sputter Type Ion Source Used in Tandetron", Symp. on Ion Sources Used in Accelerators, Tsukuba, Mar. (1983).

21) S. Karashima and T. Watanabe: "Equilibrium Charge of Heavy Ions in Solid Media", The IPP Symp. on Plasma-Wall Interaction Theories and Particle-Solid Collision Theories in the Initial Processes of Inertial Nuclear Fusion, Nagoya, Mar. (1983).

22) Y. Horino, N. Matsunami, N. Itoh, and K. Kimura: "Effects of Elastic and Nonelastic Collisions by Ions on Reactions at Pd-Si Interface", 30th Ann. Meeting of the Japan Soc. Appl. Phys., Chiba, Apr. (1983).

23) T. Takahashi, S. Konno, and F. Yatagai: "Theories on the Energy Deposition around a Path of a Heavy Charged Particle and Their Application", 30th Spring Meeting of the Japan Soc. Appl. Phys., Chiba, Apr. (1983).

24) K. Aono, M. Iwaki, and S. Namba: "Annealing of Ion Implanted GaP II", 30th Spring Meeting of the Japan Soc. Appl. Phys., Chiba, Apr. (1983).

25) E. Yagi, T. Kobayashi, S. Nakamura, Y. Fukai, and K. Watanabe: "Lattice Location of Hydrogen in Tantalum", 92th Ann. Meeting of Japan Inst. Metals, Tokyo, Apr. (1983).

26) Y. Higashiguchi, H. Kayano, M. Narui, Y. Suzuki, and E. Yagi: "Helium Embrittlement of Nb, V and their Alloys", 92th Ann. Meeting of Japan Inst. Metals, Tokyo, Apr. (1983).

27) S. Karashima and T. Watanabe: "Equilibrium Charge of Incident Heavy Ions in the Medium", Japan-China Binational Radiation Chemistry Symp., Shanghai, China, Apr. (1983).

28) K. Nishiyama, E. Yagi, K. Ishida, T. Matsuzaki, K. Nagamine, and T. Yamazaki: "New Approach in μ^+ SR Study on Critical Phenomena in Ni", 3rd Int. Topical Meeting on μ SR, Shimoda, Apr. (1983).

29) E. Yagi: "Study of Lattice Location of Hydrogen in Metals by Channeling Method", Symp. on Hydrogen in Metals, Tokyo, May (1983).

30) E. Yagi: "Muon Diffusion in Metals", Symp. on Hydrogen in Metals, Tokyo, May (1983).

31) T. Watanabe: "Collision Processes of Atoms by Energetic Multicharged Ions (Experimental Studies in IPCR (RIKEN)", Asia Pacific Physics Conf., Singapore, June (1983).

32) T. Watanabe: "Electron Capture Processes of Multicharged Ions from H and He (Theory)", Asia Pacific Physics Conf., Singapore, June (1983).

33) J. Mizuno, T. Ishihara, and T. Watanabe: "Energy Exchange between Two Outgoing Electrons in the Post Collision Interaction Processes", XIIIth Intern. Conf. on the Phys. of Electron. and Atom. Collisions, Berlin, W. Germany, July (1983).

34) J. Takahashi, Y. Awaya, T. Kambara, M. Kase, H. Kumagai, J. Urakawa, T. Matsuo, and H. Shibata: "Angular Distribution of Au L X-Rays by Heavy Ion Impact", XIIIth Intern. Conf. on the Phys.

of Electron. and Atom. Collisions, Berlin, W. Germany, July (1983).

35) Y. Awaya, T. Kambara, M. Kase, H. Kumagai, J. Takahashi, J. Urakawa, T. Matsuo, and M. Namiki: "High Resolution Measurements of K X-Rays from Ar Ions Impinging on Foils", XIIIth Intern. Conf. on the Phys. of Electron. and Atom. Collisions, Berlin, W. Germany, July (1983).

36) I. Shimamura: "Line-Shape Analysis of Electron Energy-Loss Spectra", XIIIth Intern. Conf. on the Phys. of Electron. and Atom. Collisions, Berlin, W. Germany, July (1983).

37) T. Kambara, Y. Awaya, M. Kase, H. Kumagai, I. Kohno, T. Tonuma, and A. Hitachi: "Target Gas Pressure Dependence of Relative Yields of K X Rays from 110 MeV Ne Ions", XIIIth Intern. Conf. on the Phys. of Electron. and Atom. Collisions, Berlin, W. Germany, July (1983).

38) T. Matsuo, J. Urakawa, A. Yagishita, Y. Awaya, T. Kambara, M. Kase, H. Kumagai, and J. Takahashi, "Ar L-MM Auger Spectra in Ar^{4+} + Ar Collisions", XIIIth Intern. Conf. on the Phys. of Electron. and Atom. Collisions, Berlin, W. Germany, July (1983).

39) J. Urakawa, T. Matsuo, H. Shibata, A. Yagishita, Y. Awaya, T. Kambara, M. Kase, H. Kumagai, and J. Takahashi: "Kr M-NN Auger Spectra in Ar^{4+} + Kr Collisions", XIIIth Intern. Conf. on the Phys. of Electron. and Atom. Collisions, Berlin, W. Germany, July (1983).

40) S. Karashima and T. Watanabe: "Stripping Cross Sections of Multi-Charged Ions by Neutral Atoms", XIIIth Intern. Conf. on the Phys. of Electron. and Atom. Collisions, Berlin, W. Germany, July (1983).

41) S. Karashima and T. Watanabe: "Charge Equilibrium of Fast Heavy Ions Penetrating through Gaseous Media", XIIIth Intern. Conf. on the Phys. of Electron. and Atom. Collisions, Berlin, W. Germany, July (1983).

42) H. Suzuki, N. Toshima, and T. Watanabe: "Exponential Distorted Wave Approximation in Charge Transfer", XIIIth Intern. Conf. on the Phys. of Electron. and Atom. Collisions, Berlin, W. Germany, July (1983).

43) J. Mizuno, T. Ishihara, and T. Watanabe: "Energy Shift of Emitted X-Rays Following Inner Shell Photoionization near Threshold", XIIIth Intern. Conf. on Phys. of Electron. and Atom. Collisions, Berlin, W. Germany, July (1983).

44) K. Fujiwara, N. Toshima, and T. Watanabe: "Close Coupling Calculation of Electron Capture at High Energies", XIIIth Intern. Conf. on the Phys. of Electron. and Atom. Collisions, Berlin, W. Germany, July (1983).

45) M. Uda, A. Koyama, K. Maeda, and Y. Sasa: "Chemical Effects of F KVV Auger Spectra Induced by Photon- and Ion-Impacts", 10th Intern. Conf. on Atomic Collisions in Solids, Bad Iburg, W. Germany, July (1983).

46) A. Koyama, Y. Sasa, T. Shikata, E. Yagi, K. Maeda, H. Sakairi, and M. Uda: "Deviation of Secondary Electron Emission Coefficient from Z_1^2 Proportionality", 10th Intern. Conf. on Atomic Collision in Solids, BadIburg, W. Germany, July (1983).

47) I. Shimamura: "Line-Shape Analysis of Photoelectron Spectra and Electron and Ion Energy-Loss Spectra", Intern. Symp. on Wavefunctions and Mechanisms from Electron Scattering Processes, Roma, Italy, July (1983).

48) H. Muramatsu, T. Miura, H. Nakahara, M. Fujoka E. Tanaka, and A. Hashizume: "Calibration of the Isomer Shift of ^{119}Sn from Internal Conversion Measurements", 6th Intern. Conf. on Hyperfine Interactions, Groningen, The Netherland, July (1983).

49) T. Watanabe: "Extensive Study on the Validity of Atomic Base Treatment – Close Coupling, EDWA, UDWA", VIIIth Intern. Seminar on Ion-Atom Collision, Nijenrode Utrecht, The Netherlands, Aug. (1983).

50) A. Ohsaki: "Resonant Collision in Strong Magnetic Fields", Symp. on Present Status and Future Development of Atomic Collision Theory, Susono, Sept. (1983).

51) S. M. Shafroth: "Comment: Resonant and Non-resonant Electron Transfer and Excitation in Ion-Atom Collision", Symp. on Present Status and Future Development of Atomic Collision Theory, Susono, Sept. (1983).

52) A. C. Roy: "Triple Differential Cross Section Using Glauber Approximation", Symp. on Present Status and Future Development of Atomic Collision Theory, Susono, Sept. (1983).

53) I. Shimamura: "Electron-Molecule Collisions", Symp. on Present Status and Future Development of Atomic Collision Theory, Susono, Sept. (1983).

54) T. Watanabe: "Charge Transfer Processes", Symp. on Present Status and Future Development of Atomic Collision Theory, Susono, Sept.

(1983).

55) K. Aono, M. Iwaki, and S. Namba: "Annealing of Ion Implanted GaP III", 44th Fall Meeting of the Japan Soc. Appl. Phys., Sendai, Sept. (1983).

56) T. Tonuma, M. Kase, H. Kumagai, T. Kambara, H. Shibata, J. Takahashi, I. Kohno, S. Özkök, S. H. Be, J. Urakawa, and T. Matsuo: "Production of Highly-Charged Ions Induced by Heavy-Ion Impact", Intern. Ion Engineering Congr. – ISIAT '83 & IPAT '83 –, Kyoto, Sept. (1983).

57) S. M. Shafroth: "Resonant Transfer and Excitation in High-Energy Multi-Charged Ion-Atom Collisions", 1983 Fall Meeting of the Phys. Soc. Japan, Okayama, Oct. (1983).

58) Y. Awaya, T. Kambara, M. Kase, H. Kumagai, J. Takahashi, H. Shibata, J. Urakawa, T. Matsuo, and M. Namiki: "Multiple Inner-Shell Ionization of Ar Ions Passing through Foils," 1983 Fall Meeting of the Phys. Soc. Japan, Okayama, Oct. (1983).

59) J. Urakawa, T. Matsuo, H. Shibata, A. Yagishita, Y. Awaya, T. Kambara, M. Kase, H. Kumagai, and J. Takahashi: "Kr M-NN Auger Spectra Produced in Collisions with about 0.2 MeV/amu Heavy Ions", 1983 Fall Meeting of the Phys. Soc. Japan, Okayama, Oct. (1983).

60) E. Yagi and S. Nakamura: "Lattice Location of Sn Atoms Implanted into Al Crystals", 1983 Fall Meeting of the Phys. Soc. Japan, Okayama, Oct. (1983).

61) S. Tamada, T. Akioka, A. Hashiba, K. Masuda, A. Hitachi, J. Kikuchi, T. Doke, T. Takahashi, M. Sekiguchi, and E. Shibamura: "LET Dependence of the Light Yield of the Liquefied Rare Gases Induced by Charged Particles", 1983 Fall Meeting of the Phys. Soc. Japan, Okayama, Oct. (1983).

62) K. Maeda, Y. Hayashi, and M. Uda: "An Oxygen Kα Emission Spectrum Free from Multiple-Vacancy Satellites", 1983 Fall Meeting of the Phys. Soc. Japan, Okayama, Oct. (1983).

63) J. Nagakawa, H. Shiraishi, I. Uchiyama, H. Kamitsubo, I. Kohno, and T. Shikata: "Irradiation Creep Experiments of 316 Stainless Steel under 16 MeV Proton Bombardment in a Torsional Creep Apparatus", 93rd Meeting of the Japan Inst. Metals, Akita, Oct. (1983).

64) H. Suzuki, N. Toshima, and T. Watanabe: "The Calculation of Electron Transfer Cross Section to Multicharged Ion by UDWA, II", 1983 Fall Meeting of the Phys. Soc. Japan, Okayama, Nov. (1983).

65) K. Hino, I. Shimamura, and T. Watanabe: "Theory of Radiative Electron Capture", 1983 Fall Meeting of the Phys. Soc. Japan, Okayama, Nov. (1983).

66) S. Karashima and T. Watanabe: "Electron Loss Cross Sections for Projectile Many Electron Ions in the Medium", 1983 Fall Meeting of the Phys. Soc. Japan, Okayama, Nov. (1983).

67) S. M. Shafroth: "Non-Resonant Transfer and Excitation in Ion-Atom Collisions", 5th Symp. on Atomic Collisions by Using Accelerators, Susono, Nov. (1983).

68) T. Matsuo: "Auger Electron Emission in Heavy Ion Atom Collisions", 5th Symp. on Atomic Collisions by Using Accelerators, Susono, Nov. (1983).

69) S. M. Shafroth: "Non-Resonant Electron Transfer and Exitation in Ion-Atom Collision" 5th Symp. on Atomic Collisions by Using Accelerators, Susono, Nov. (1983).

70) T. Watanabe: "Atomic Physics Using High Energy Heavy Ions", RIKEN Symp. on Nuclear Physics Research in the Energy Range of 10–100 MeV/u, Wako, Nov. (1983).

71) T. Watanabe and I. Shimamura: "Properties of High Rydberg State Species", RIKEN Symp. on the Physics of Rydberg States and Their Reaction Processes, Wako, Nov. (1983).

72) A. Ohsaki: "Atomic Collision in Magnetic Fields", 1st Seminar on Elementary Processes in Nuclear Fusions, Kyoto, Nov. (1983).

73) T. Watanabe: "Present Status of the Theories on Charge Exchange Reactions", 1st Seminar on Elementary Processes in Nuclear Fusions, Kyoto, Nov. (1983).

74) S. Karashima, H. Kawagoshi, and T. Watanabe: "Charge Equilibrium Processes of Energetic Incident Ions and Their Range", IPP Symp. on Particle Beam Application to Fusion Research, Nagoya, Nov. (1983).

75) K. Maeda, Y. Sasa, Y. Yokode, M. Maeda, M. Kobayashi, K. Fujima, and M. Uda: "Several Applications of PIXE Analysis", 2nd Symp. on Ion Beam Technology, Hosei University, Tokyo, Dec. (1983).

76) M. Uda, H. Endo, K. Maeda, Y. Sasa, K. Fujima, and K. Fuwa: "Application of Ion Induced X-Ray Emission Spectroscopy to Chemistry", 2nd Symp. on Ion Beam Technology, Hosei University, Tokyo, Dec. (1983).

77) A. Koyama, Y. Sasa, and M. Uda: "Development of Ion Induced Electron Spectroscopy",

2nd Symp. on Ion Beam Technology, Hosei University, Tokyo, Dec. (1983).

4. Radiochemistry, radiation chemistry and radiation biology

1) M. Yanokura, I. Kohno, M. Aratani, and T. Nozaki: "Rutherford Scattering Applied to the Study of Hydrogen in Amorphous Silicon", 30th Spring Meeting of the Japan Soc. Appl. Phys., Chiba, Apr. (1983).
2) Y. Mochizuki, M. Nakamura, S. Koyama, K. Usami, T. Nozaki, and Y. Itoh: "Composition of CVD Silicon Film Doped with Oxygen", 30th Spring Meeting of the Japan Soc. Appl. Phys., Chiba, Apr. (1983).
3) M. Aratani, H. Nagai, T. Nozaki, M. Yanokura, I. Kohno, O. Kuboi, and Y. Yatsurugi: "Rutherford Forward Recoil Measurement Applied to Characterization of Hydrogen", 47th National Meeting of the Chem. Soc. Japan, Kyoto, Apr. (1983).
4) F. Ambe and S. Ambe: "Mössbauer Isomer Shifts of ^{119}Sn Coordinated with Ag – I Atoms", 47th National Meeting of the Chem. Soc. Japan, Kyoto, Apr. (1983).
5) I. Kaneko, T. Ohno, K. Eguchi, T. Inada, and K. Nakano: "Differential Recovery from Potentially Lethal Damage in Human Cultured Cells after Irradiation with Photon and Accelerated N-Ion Beam", GSI Workshop on Heavy Particles in Biology and Medicine, Seeheim, W. Germany, June (1983).
6) K. Eguchi, T. Inada, T. Ohno, S. Satoh, and I. Kaneko: "Recovery from Radiation Damage of Cultured Cells after Irradiation of Photon, Proton, and Nitrogen-Ion", 7th Intern. Congr. Radiat. Res., Amsterdam, The Netherlands, July (1983).
7) K. Kimura, Y. Toda, and M. Imamura: "Effects of LET, Temperature, and Pressure on the Emission Spectra of Helium Excimers Created by Heavy-Ion Irradiation near Critical Temperature", 7th Intern. Congr. of Radiat. Res., Amsterdam, The Netherlands, July (1983).
8) F. Yatagai, T. Takahashi, and T. Katayama: "Effect of Heavy Ions on Bacterial Spores (II)", 2nd Spore Radiation Biology Meeting, Amsterdam, The Netherlands, July (1983).
9) Y. Itoh, T. Nozaki, T. Masui, and T. Abe: "IR Caribration Curve for Nitrogen in Silicon by Charged Particle Activation Analysis", 44th Fall Meeting of the Japan Soc. Appl. Phys., Sendai, Sept. (1983).
10) M. Yanokura, I. Kohno, M. Aratani, and T. Nozaki: "Rutherford Scattering Applied to the Study of Hydrogen in Amorphous Silicon", 44th Fall Meeting of the Japan Soc. Appl. Phys., Sendai, Sept. (1983).
11) K. Kimura and M. Imamura: "Emission Spectra Measured at Different Location of 85 MeV N-Ion Trajectory in He Gas at 5.2K", 26th Congr. of Radiat. Chem., Osaka, Sept. (1983).
12) Y. Sakamoto: "ECR Discharge Cleaning of Toroidal Machines", IX IVC – V ICSS, Madrid, Spain, Sept. (1983).
13) S. Hayashi, H. Nagai, M. Aratani, T. Nozaki, M. Yanokura, I. Kohno, O. Kuboi, and Y. Yatsurugi: "Depth Profiling of Hydrogen with ^{15}N-Induced Resonance Nuclear Reaction", 27th Symp. on Radiochem., Nagoya, Oct. (1983).
14) H. Kudo, T. Nomura, K. Sueki, and M. Magara, "Measurement of Isomeric Transition of ^{212m}Po", 27th Symp. on Radiochem., Nagoya, Oct. (1983).
15) H. Nagai, M. Aratani, S. Hayashi, T. Nozaki, M. Yanokura, I. Kohno, O. Kuboi, and Y. Yatsurugi: "Rutherford Forward Scattering Applied to the Analysis of Hydrogen (II)", 27th Symp. on Radiochem., Nagoya, Oct. (1983).
16) T. Miura, Y. Hatsukawa, K. Endo, H. Nakahara, A. Hashizume, M. Fujioka, and E. Tanaka: "Variation of Intensity on Internal Conversion of Outermost Shell Electrons in ^{125}Te for Various Metal Matrices", 27th Symp. on Radiochem., Nagoya, Oct. (1983).
17) Y. Sakamoto, S. Ishii, K. Okazaki, K. Yano, and et al.: "ECR Discharge Cleaning for TEXTOR Device, II", Japan Vacuum Congr., Tokyo, Oct. (1983).
18) Y. Ishibe, S. Ishii, K. Okazaki, H. Oyama, Y. Sakamoto, K. Yano, T. Nozaki, M. Aratani, S. Hayashi, M. Yanokura, I. Kohno, and et al.: "ECR Discharge Cleaning for JIPPT-II U", Japan Vacuum Congr., Tokyo, Oct. (1983).
19) Y. Sakamoto and H. Oyama: "Interaction of TiC with Hydrogen Plasma", Japan Vacuum Congr., Tokyo, Oct. (1983).
20) S. M. Shafroth: "The ^{1}H(Li, n)^{7}Be Reaction as an Intense MeV Neutron Source", Korean Phys. Soc. Meeting, Jinhae, Korea, Oct. (1983).
21) S. Kitayama, F. Yatagai, A. Shimotsukasa, and K. Tsutsumi: "Repair of DNA Cross-Links in Mitomycin C Sensitive Mutant of *D. radio-*

durans", 55th Ann. Meeting of the Genetics Soc. of Japan, Sendai, Oct. (1983).

22) K. Kimura, S. Kubota, and M. Imamura: "Emission Spectra and Its Decay Measured at Different Location of N-Ion Trajectory in He-Gas under Low Temperature and High Pressure", 1983 Fall Meeting of the Phys. Soc. Japan, Okayama, Oct. (1983).

23) T. Takahashi and F. Yatagai: "Biological Effects of Heavy Ions", 5th Symp. on Atomic Collisions by Using Accelerator, Susono, Nov. (1983).

24) T. Takahashi, F. Yatagai, T. Katayama, M. Inada, and S. Konno: "Track Structure Theories and Their Application for the Interpretation of Biological Effects", 26th Ann. Meeting of the Japan Radiat. Res. Soc., Kyoto, Nov. (1983).

25) M. Aratani, H. Nagai, S. Hayashi, T. Nozaki, M. Yanokura, I. Kohno, O. Kuboi, and Y. Yatsurugi: "Characterization of Surface Hydrogen by the Rutherford Recoil Measurement", 19th Tokyo Conf. on Appl. Spectrosc., Tokyo, Nov. (1983).

26) M. Yanokura, M. Aratani, H. Nagai, S. Hayashi, I. Kohno, T. Nozaki, O. Kuboi, and Y. Yatsurugi: "The Heavy-Ion Probe Rutherford Forward Recoil Measurement Applied to the Characterization of Hydrogen in Solids", 2th Symp. on Ion Beam Technology, Hosei Univ., Tokyo, Dec. (1983).

27) G. Okada, K. Kurita, K. Nakano, and I. Kaneko: "Enhancement of 3-Aminobenzamide on Radiation-Induced Mutation in Chinese Hamster V79 Cells", Ann. Meeting of Japan. Soc. of Radiat. Res., Kyoto, Dec. (1983).

28) K. Nakano, H. Imanishi, G. Okada, and I. Kaneko: "Effect of 3-Aminobenzamide on Sister Chromatid Exchange Frequency in Chinese Hamster V79 Cells Exposed to N-Ion Accelerated in the RIKEN Cyclotron", Ann. Meeting of Japan. Soc. of Radiat. Res., Kyoto Dec. (1983).

VII. LIST OF OUTSIDE USERS AND THEIR THEMES

(Jan. – Dec. 1983)

1)	S. Yoshida and K. Mitsui "Study of Effect by Bombarding High Energy Proton on a GaAs Solar Cell"	LSI R & D Lab. Mitsubishi Electric Co., Ltd.
2)	H. Ueyama "Study of Effect by Bombarding High Energy Proton on a Si Solar Cell"	Sharp Co., Ltd.
3)	H. Nakahara "Production of ^{121}Te"	Faculty of Science, Tokyo Metropolitan Univ.
4)	S. Orito and S. Nakamura "Test of Sensibility of CR39 Track Detector for High Energy Proton"	Faculty of Science, Univ. of Tokyo
5)	T. Abe "Radiochemical Analysis of ^{16}O in Si Crystal"	Shinetsu Semiconductor Co., Ltd.
6)	E. Tohji "Radiochemical Analysis of ^{14}N and ^{16}O in Si Crystal"	Toshiba Ceramics Co., Ltd.
7)	H. Shinyashiki "Radiochemical Analysis of ^{16}O in GaAs"	Central Res. Lab., Mitsubishi Metal Co., Ltd.
8)	H. Yamamoto "Radiation Damage of Cover Glass for a Solar Cell"	R & D Div., Asahi Glass Co., Ltd.
9)	M. Yatsuhashi and T. Suematsu "Study of Effect by Irradiating Fast Neutron on a Insulator Coverning a Cable"	Fujikura Cable Works, Ltd.
10)	A. Morio and M. Harada "Study of Single Event Upset in Microprocessors by Bombarding ^{14}N and ^{20}Ne Particles"	Japan Trust Center for Electronic Parts

VIII. LIST OF SEMINARS

(Jan. – Dec. 1983)

1) T. Ohshima, INS (Tokyo), 13 January
"A Trial of the Determination of Neutrino Mass by the Measurement of β-Ray Spectrum of Triton"

2) H. H. Bolotin, Univ. of Melbourne (Australia), 26 January
"Measurements of Gyromagnetic Ratios of Short-Lived Excited Nuclear States Using the Enhanced Transient Hyperfine Magnetic Field"

3) Y. Torizuka, Tohoku Univ. (Sendai), 1 February
"Prospect of the Study in the Nucleus Using Electron Accelerators"

4) F. Kikuchi, Univ. of Tokyo (Tokyo), 10 February
"Calculation of Electromagnetic Waves by the Finite Element Method"

5) K. Sato, INS (Tokyo), 17 February
"RF Cavity in Cyclotron"

6) B. I. Deutsch, Aarhus Univ. (Denmark), 2 March
"Atomic and Nuclear Polarization by Beam Foil Interaction: Direct Determination via β-Asymmetry"

7) K. Nagatani, INS (Tokyo), 3 March
"Heavy Ion Reaction and Spectroscopy"

8) N. Shikazono, JAERI (Tokai), 14 March
"Present Situation and Heavy Ion Spectrometer at JAERI"

9) H. Morinaga, Tech. Univ. München (West Germany), 22 March
"Mass Spectroscopy by Accelerator"

10) O.W.B. Schult, Inst. für Kernphysik, Jülich(West Germany), 2 April
"Thoughts about Nuclear Physics on the Intense Spallation Source"

11) H. Ejiri, Osaka Univ. (Osaka), 18 April
"Spin-Isospin Mode and Hypernuclei"

12) P. Aguer, CSMSN, Orsay (France), 28 April
"High-Spin States in Er Isotopes"

13) T. Udagawa, Univ. Texas at Austin (USA), 12 May
"A Dynamical Theory of Preequilibrium Reactions"

14) Yu. Ts. Oganessian, JINR, Dubna (USSR), 25 May
"Present Situation of HI Research at JINR"

15) A. Matveenko, JINR, Dubna (USSR), 25 May
"A New Three-Body Equation"

16) J. J. Griffin, Univ. Maryland (USA), 30 May
"Non-Linear Many Body Reaction Theories from Nuclear Mean Field Approximation"

17) K. W. McVoy, Univ. of Wisconsin-Madison (USA), 1 June
"Practical Heavy Ion Optics in the Near/Far Representation"

18) P. Schwandt, ICUF, Indiana Univ. (USA), 3 June
"Optical Potential Phenomenology at Intermediate Energies"

19) K. Kuroda, LAPP (France), 14 June
"Application of Position Sensitive Photomultiplier"

20) H. Ohnuma, Tokyo Inst. Tech. (Tokyo), 24 June
"Recent Topics in 'Nuclear Physics in Intermediate- and High-Energy Regions' "

21) S. Kato, Yamagata Univ. (Yamagata), 7 July
"On Magnetic Spectrograph"

22) B. R. Barrett, Univ. of Arizona (USA), 19 July
"The IBA Model and Its Formulation and Application"

23) A. Matsuyama, Univ. of Tokyo (Tokyo), 28 July
"(π, N) Reaction in the Δ-Hole Model"

24) T. Murakami, INS (Tokyo), 29 July
"$^{12}C(^{16}O,\alpha)$ Reaction: Can 'Molecular Resonance States' be Excited?"

25) N. Takigawa, Tohoku Univ. (Sendai), 4 August
"Coupling of Macroscopic Motion to Intrinsic Oscillators in Heavy Ion Fusion"

26) M. Gai, Yale Univ. (USA), 27 September
"Molecular Dipole States in ^{18}O and ^{218}Ra"

27) J. L. Wood, Georgia Inst. of Tech. (USA), 27 September
"Shape Coexistence in Nuclei"

28) Y. Zhu, IMP, Lanzhou (China), 7 November
"Recent Situation at Institute of Modern Physics"

29) A. Galonsky, MSU (USA), 7 November
"Neutron Emission from ^{165}Ho + ^{14}N Reaction at 35 MeV/nucleon"

30) J. B. McClelland, UCLA (USA), 8 November
"HRS and Focal Plane Polarization at Los Alamos"

31) P. Kleinheinz, KFA, Jülich (West Germany), 16 November
"Aligned Multiparticle Yrast Configurations and Particle-Octupole Coupling Phenomena in the Nuclei around ^{146}Gd"

32) T. Hasegawa, INS (Tokyo), 9 December
"Present Situation at SATURNE"

33) M. Tohyama, Giessen Univ. (West Germany), 16 December
"Subthreshold π-Production"

34) Y. Fujita, INS (Tokyo), 20 December
"Development of PPAC and its Application"

IX. LIST OF PERSONNEL

Members of the Board

HASHIZUME Akira 橋爪 朗
KAMITSUBO Hiromichi 上坪宏道
NOZAKI Tadashi 野崎 正 (Chiarman)
OKADA Shigefumi 岡田重文
SEKIZAWA Hisashi 関沢 尚
UDA Masayuki 宇田応之
IMAMURA Masashi 今村 昌
KOHNO Isao 河野 功
ODERA Masatoshi 小寺正俊
SAKAIRI Hideo 坂入英雄
SHIMA Makoto 島 誠
WATANABE Tsutomu 渡部 力

Cyclotron Operation and Maintenance Group

FUJITA Shin 藤田 新
KAGEYAMA Tadashi 影山 正
KOHNO Isao 河野 功
TAKEBE Hideki 武部英樹
IKEGAMI Kumio 池上九三男
KOHARA Shigeo 小原重夫
OGIWARA Kiyoshi 荻原 清

Linac Operation and Maintenance Group

CHIBA Yoshiaki 千葉好昭
IKEZAWA Eiji 池沢英二
KAMBARA Tadashi 神原 正
KUBO Toshiyuki 久保敏幸
YANOKURA Minoru 矢野倉 実
HEMMI Masatake 逸見政武
INOUE Toshihiko 井上敏彦
KASE Masayuki 加瀬昌之
MIYAZAWA Yoshitoshi 宮沢佳敏

Scientific and Engineering Personnel

Cyclotron Laboratory

BE Suck Hee 裵 碩喜
FUJITA Jiro 藤田二郎
HARA Masahiro 原 雅弘
ISHIHARA Masayasu 石原正泰
KARASAWA Takashi 唐沢 孝
KOHMOTO Susumu 河本 進
KUDO Hisaaki 工藤久昭
NAKAJIMA Shunji 中島諄二
NOMURA Toru 野村 亨
SAKAMOTO Ichiro 坂本一郎
SHIMIZU Kazuo 清水和男
WADA Takeshi 和田 雄
YANO Yasushige 矢野安重
YOSHIDA Nobuaki 吉田宣章
FUJISAWA Takashi 藤沢高志
GOTO Akira 後藤 彰
INAMURA Takashi 稲村 卓
KAMITSUBO Hiromichi 上坪宏道
KISHIDA Norio 岸田則生
KOHNO Isao 河野 功
MOTONAGA Shoshichi 元永昭七
NAKANISHI Noriyoshi 中西紀喜
OIKAWA Yoshifumi 老川嘉郁
SHIKATA Takashi 四方隆史
TAKESHITA Isao 竹下勇夫
YAMAJI Shuhei 山路修平
YOKOYAMA Ichiro 横山一郎

(Visitors)
ROY Amulya C. (Dept. Phys., Univ. of Kalayani)

AGUER Pierre (CSNSM, Orsay)
CHEN Wuzhong 陳 務忠 (Inst. Mod. Phys., Academia Sinica)
INOUE Makoto 井上 信 (RCNP, Osaka Univ.)
KASAGI Jirota 笠木 治郎太 (Dept. Phys., Tokyo Inst. Tech.)
KATORI Kenji 鹿取 謙二 (Dept. Phys., Osaka Univ.)
KIKUCHI Fumio 菊地 文男 (Dept. Math., College of General Education, Univ. of Tokyo)
LEE Wonsik 李 元植 (Dept. Phys., Kyunbook Univ.)
LIU Guo-Xing 劉 国興 (Inst. Mod. Phys., Academia Sinica)
MORINAGA Haruhiko 森永 晴彦 (Dept. Phys., Technische Universität Munchen)
MURAKAMI Takeshi 村上 健 (Dept. Phys., Tokyo Inst. Tech.)
NAGAKAWA Johsei 永川 城正 (Nat. Res. Inst. for Metals)
NAGAMIYA Shoji 永宮 正治 (Dept. Phys., Tokyo Univ.)
NAKAHARA Hiromichi 中原 弘道 (Dept. Chem., Tokyo Metropolitan Univ.)
SATO Kenichi 佐藤 憲一 (Dept. Phys., Tohoku College of Pharmacy)
SHIRAISHI Haruki 白石 春樹 (Nat. Res. Inst. for Metals)
TAKADA Eiichi 高田 栄一 (Dept. Phys., Kyoto Univ.)
TAKEMASA Tadashi 武政 尹士 (Dept. Phys., Saga Univ.)
YOSHIDA Shiro 吉田 思郎 (Dept. Phys., Tohoku Univ.)
ZHU Yongtai 諸 永泰 (Inst. Mod. Phys., Academia Sinica)

(Students)
ANDO Haruhiko 安藤 晴彦 (Fac. Sci. and Eng., Chuo Univ.)
HARADA Hideo 原田 秀郎 (Dept. Phys., Tokyo Inst. Tech.)
HOTATE Yoshiyuki 保立 佳之 (College of Hum. and Sci., Nihon Univ.)
IEKI Kazuo 家城 和夫 (Dept. Phys., Kyoto Univ.)
NAKAHARA Kazuhiko 中原 和彦 (College of Hum. and Sci., Nihon Univ.)
OHKUMA Tsutomu 大熊 勉 (Fac. Sci. and Eng., Chuo Univ.)
SUEKI Keisuke 末木 啓介 (Dept. Chem., Tokyo Metropolitan Univ.)
YOKOYAMA Sachihiro 横山 幸広 (Fac. Sci. and Eng., Chuo Univ.)

Linac Laboratory
CHIBA Toshiya 千葉 利哉
GONO Yasuyuki 郷農 靖之
HOSHINO Kiichi 星野 紀一
ITOH Yoshinori 伊東 芳紀
KASE Masayuki 加瀬 昌之
MIYAZAWA Yoshitoshi 宮沢 佳敏
SHIBATA Hiromi 柴田 裕実
YANOKURA Minoru 矢野倉 実
CHIBA Yoshiaki 千葉 好明
HEMMI Masatake 逸見 政武
INOUE Toshihiko 井上 敏彦
KAMBARA Tadashi 神原 正
KUBO Toshiyuki 久保 敏幸
ODERA Masatoshi 小寺 正俊
TONUMA Tadao 戸沼 正雄

(Visitors)
FUJIWARA Ichiro 藤原 一郎 (Inst. Atomic Energy, Kyoto Univ.)
HAYASHIBE Shogo 林部 昭吾 (Dept. Phys., Tohoku Univ.)
ITO Noriaki 伊藤 憲昭 (Dept. Crystalline Materials, Nagoya Univ.)
MATSUO Takashi 松尾 崇 (Tokyo Medical and Dental Univ.)

MORITA Susumu 森田 右 (College of Eng., Hosei Univ.)
ODA Nobuo 織田暢夫 (Res. Lab. for Nucl. Reactors, Tokyo Inst. Tech.)
OTANI Shunsuke 大谷俊介 (Inst. Plasma Phys., Nagoya Univ.)
SUGAWARA Masahiko 菅原昌彦 (Fund. Sci., Chiba Inst. Tech.)
SUZUKI Hiroshi 鈴木 洋 (Dept. Phys., Sophia Univ.)
TAKEDA Shigeru 竹田 繁 (Nat. Lab. High Energy Phys.)
TAWARA Hiroyuki 俵 博之 (Inst. Plasma Phys., Nagoya Univ.)
URAKAWA Junji 浦川順治 (Nat. Lab. High Energy Phys.)
YAGISHITA Akira 柳下 明 (Nat. Lab. High Energy Phys.)

Radiation Laboratory

HASHIZUME Akira 橋爪 朗
KONNO Satoshi 金野 智
OKANO Masaharu 岡野眞治
TENDOW Yoshihiko 天道芳彦

IZUMO Koichi 出雲光一
KUMAGAI Hidekazu 熊谷秀和
TAKAHASHI Tan 高橋 旦

(Visitors)
DOKE Tadayoshi 道家忠義 (Sci. and Eng. Res. Lab., Waseda Univ.)
FUJIOKA Manabu 藤岡 学 (Dept. Phys., Tohoku Univ.)
ISHII Keizo 石井慶造 (Cyclotron, Tohoku Univ.)
KANG Yung-Ho 姜 栄浩 (Dept. Natural Science, Kyung-Pook Univ.)
MASUDA Kimiaki 増田公明 (School of Sci. Eng., Waseda Univ.)
MIURA Taichi 三浦太一 (Dept. Chem., Tokyo Metropolitan Univ.)
MORITA Susumu 森田 右 (College of Eng., Hosei Univ.)
MURAMATSU Hisakazu 村松久和 (Nat. Lab. High Energy Phys.)
NAGAHARA Teruaki 永原照明 (Inst. Atomic Energy, Rikkyo Univ.)
NAMIKI Masatoshi 並木雅俊 (Div. General Education, Takachiho College)
TAKAHASHI Junzo 高橋純三 (Fac. of Eng., Tohoku Univ.)
TAWARA Hiroyuki 俵 博之 (Inst. Plasma Phys., Nagoya Univ.)
URAKAWA Junji 浦川順治 (Nat. Lab. High Energy Phys.)

(Students)
HATSUKAWA Yuji 初川雄二 (Dept. Chem., Tokyo Metropolitan Univ.)
TAMADA Sakuya 玉田作哉 (Sci. and Eng. Res. Lab., Waseda Univ.)
YANAGA Makoto 矢永誠人 (Dept. Chem., Tokyo Metropolitan Univ.)

Atomic Processes Laboratory

ANDO Kozo 安藤剛三
NISHIDA Masami 西田雅美
SHIMAMURA Isao 島村 勲

AWAYA Yohko 粟屋容子
OHSAKI Akihiko 大崎明彦
WATANABE Tsutomu 渡部 力

(Visitors)
BRIGGS John S. (Fac. of Phy., Univ. Freiburg)
ISHII Keishi 石井慶之 (Dept. Eng. Sci., Kyoto Univ.)

ITOH Yoh 伊藤 陽 (Fac. of Sci., Josai Univ.)
KARASHIMA Shosuke 唐島照介 (Dept. Electr. Eng., Tokyo Univ. of Sci.)
KOIKE Fumihiro 小池文博 (School of Med., Kitasato Univ.)
KOIZUMI Tetsuo 小泉哲夫 (Dept. Phys., Rikkyo Univ.)
ROY Amulya C. (Dept. Phys., Univ. of Kalayani)
SATO Hiroshi 佐藤浩史 (Dept. Phys., Ochanomizu Univ.)
SATO Kuninori 佐藤国憲 (Inst. Plasma Phys., Nagoya Univ.)
SHAFROTH Stephen M. (Dept. Phys. & Astron., Univ. of North Carolina at Chapel Hill)
SHIMAKURA Noriyuki 島倉紀之 (General Educ. Dept., Niigata Univ.)
TOSHIMA Nobuyuki 戸嶋信幸 (Inst. Appl. Phys., Univ. of Tsukuba)
TSURUBUCHI Seiji 鶴淵誠二 (Fac. of Technol., Tokyo Univ. of Agric. Tech.)

(Students)
HINO Kenichi 日野健一 (Dept. Appl. Phys., Univ. of Tokyo)
SEKIYA Masahiro 関谷雅弘 (Dept. Chem., Hokkaido Univ.)

Metal Physics Laboratory

KOYAMA Akio 小山昭雄
YAGI Eiichi 八木栄一
SHIOTANI Nobuhiro 塩谷亘弘

(Student)
NAKAMURA Shiho 中村志保 (School of Sci. Eng., Waseda Univ.)

Magnetic Materials Laboratory

ASAI Kichizo 浅井吉蔵
SAKAI Nobuhiko 坂井信彦
OKADA Takuya 岡田卓也
SEKIZAWA Hisashi 関沢 尚

Plasma Physics Laboratory

ISHIBE Yukio 石部行雄
OKAZAKI Kiyohiko 岡崎清比古
SAKAMOTO Yuichi 坂本雄一
ISHII Shigeyuki 石井成行
OYAMA Hitoshi 大山 等
YANO Katsuki 矢野勝喜

Semiconductors Laboratory

(Visitor)
AONO Keiko 青野桂子 (College of Liberal Arts, Kitasato Univ.)

Solid-State Chemistry Laboratory

KOBAYASHI Masayoshi 小林雅義
SASA Yoshihiko 佐々嘉彦
MAEDA Kuniko 前田邦子
UDA Masayuki 宇田応之

(Visitors)
KUSUYAMA Hiroyuki 楠山弘之 (Cancer Institute Hospital Tokyo)
YOKODE Yutaka 横出 裕 (School of Medicine, Nihon Univ.)

Radiochemistry Laboratory

AMBE Fumitoshi 安部文敏
ARATANI Michi 荒谷美智
ITOH Yoshiko 伊東芳子
MINAI Yoshitaka 薬袋佳孝
TERAI Yoshiro 寺井善郎
AMBE Shizuko 安部静子
HAYASHI Shigeki 林 茂樹
IWAMOTO Masako 岩本正子
NOZAKI Tadashi 野崎 正

(Visitors)
ABE Takao 阿部孝夫 (Shin-Etsu Handotai Co.)
KUBOI Osamu 久保井 収 (Komatsu Electric Metals Co. Ltd.)
MASUI Tsumoru 桝井 積 (Shin-Etsu Handotai Co.)
MOCHIZUKI Yasuhiro 望月康弘 (Hitachi Res. Lab., Hitachi Ltd.)
NAGAI Hisao 永井尚生 (College of Hum. and Sci., Nihon Univ.)
NAKAMURA Minoru 中村 稔 (Hitachi Res. Lab., Hitachi Ltd.)
NOMURA Koichi 野村紘一 (Mitsubishi Metal. Co.)
SHINYASHIKI Hiroshi 新屋敷 浩 (Mitsubishi Metal. Co.)
TAKI Ko 滝 幸 (Dept. Hygen., Kitasato Univ.)
USAMI Katsuhisa 宇佐美 勝久 (Hitachi Res. Lab., Hitachi Ltd.)
YATSURUGI Yoshifumi 八剣吉文 (Komatsu Electric Metals Co. Ltd.)

Radiation Chemistry Laboratory

IMAMURA Masashi 今村 昌
KIMURA Kazuie 木村一宇

(Visitor)
KUBOTA Shinzo 窪田信三 (Dept. Phys., Rikkyo Univ.)

(Students)
KATO Toshiyuki 加藤寿幸 (Dept. Phys., Chuo Univ.)
YAMAZAKI Norio 山崎典夫 (Dept. Phys., Chuo Univ.)

Radiobiology Laboratory

KANEKO Ichiro 金子一郎
NAKANO Kazushiro 中野和城
OKADA Shigefumi 岡田重文
KITAYAMA Shigeru 北山 滋
OKADA Gensaku 岡田源作
YATAGAI Fumio 谷田貝文夫

(Visitors)
INADA Tetsuo 稲田哲雄 (Dept. Medicine, Tsukuba Univ.)
OHNO Tadao 大野忠夫 (Nat. Inst. Radiological Sciences)

(Student)

EGUCHI Kiyomi 江口清美 (Dept. Medicine, Tsukuba Univ.)

Safety Control Affairs Office

IGARASHI Kazui 五十嵐一成

KATOU Takeo 加藤武雄

SAKAMOTO Ichiro 坂本一郎

USUBA Isao 薄葉勲

KAGAYA Satoru 加賀屋悟

MIYAGAWA Makoto 宮川真言

TAKI Kenro 滝剣朗

Beam Analysis Center

IWAKI Masaya 岩木正哉

SAKAIRI Hideo 坂入英雄

KOBAYASHI Takane 小林峰

URAI Teruo 浦井輝夫

AUTHOR INDEX

RIKEN Accelerator Progress Report

理化学研究所加速器年次報告　第17巻（1983）

印　刷　昭和59年（1984）6月25日
発　行　昭和59年（1984）6月30日
発行者　理化学研究所
代表者　宮島龍興
〒351-01　埼玉県和光市広沢2番1号
電話（0484）62－1111
編集者　理化学研究所加速器運営委員会
印刷所　株式会社　日庄印刷
〒130　東京都墨田区亀沢1丁目3番3号

定価　5,000円

理化学研究所

埼玉県　和光市　広沢